Mineral storage of carbon in basaltic rocks at elevated temperatures

A field and experimental study

Deirdre Elizabeth Clark

Faculty of Earth Sciences
University of Iceland
2019

Mineral storage of carbon in basaltic rocks at elevated temperatures
A field and experimental study

Deirdre Elizabeth Clark

Dissertation submitted in partial fulfillment of a
Philosophiae Doctor degree in Geology

PhD Committee
Sigurður Reynir Gíslason
Eric H. Oelkers
Iwona Galeczka
Domenik Wolff-Boenisch

Opponents
Bjørn Jamtveit
Gregory M. Dipple

Faculty of Earth Sciences
School of Engineering and Natural Sciences
University of Iceland
Reykjavik, October 2019

Mineral storage of carbon in basaltic rocks at elevated temperatures
A field and experimental study

Dissertation submitted in partial fulfillment of a *Philosophiae Doctor degree in Geology*

Faculty of Earth Sciences
School of Engineering and Natural Sciences
University of Iceland
Sturlugata 7
102 Reykjavík
Iceland

Telephone: 525-4000

Bibliographic information:
Deirdre Elizabeth Clark, 2019, Mineral storage of carbon in basaltic rocks at elevated temperatures. A field and experimental study, PhD dissertation, Faculty of Earth Sciences, University of Iceland, 183 pp.

Author ORCID: 0000-0002-1278-6229
ISBN: 978-9935-9473-8-3

Printing: Háskólaprent
Reykjavík, Iceland, October 2019

Abstract

The reduction of carbon dioxide (CO_2) emissions in the atmosphere is currently one of the main challenges facing humanity. One solution is carbon capture from concentrated sources and directly from the atmosphere, and long term storage in rocks. Basaltic rocks are rich in divalent cations, Ca^{2+}, Mg^{2+} and Fe^{2+}, which react with the dissolved CO_2 to form stable carbonate minerals. Mineralization of water-dissolved CO_2 injected into basaltic rocks at 20–50 °C occurs within two years in field-scale settings.

In this study, a high-pressure column flow-through experiment was run to simulate CO_2 injection into glassy basaltic rocks at 50 °C. The aim of this experiment was to investigate the proportions of injected dissolved CO_2 and high-pH groundwater needed to reach a "sweet spot" in the reacted fluid composition that favors the saturation of carbonates rather than zeolites and clays at pH 5.2–6.5 at 50 °C, as all compete for divalent cations and pore space. Results highlighted the importance of initial pCO_2 and pH values to obtain a balance between the formation of carbonates versus clays and zeolites. Moreover, modelling indicates that pauses in CO_2 injection while still injecting water can result in enhanced large molar volume Ca-Na-zeolite and Mg-Fe-clay formation that consumes pore space within the rocks.

Parallel to the laboratory experiment, industrial-scale testing of a CO_2-H_2S gas mixture injection commenced in 2014 at the Hellisheiði geothermal power plant in Iceland. By the end of 2017, 23,200 metric tons of CO_2 and 11,800 metric tons of hydrogen sulfide (H_2S) had been injected to a depth of 750 m into fractured, hydrothermally altered basalts at > 250 °C. We collected over 80 water and gas samples from monitoring and injection wells, before and during injection. Major, minor, and trace element geochemical data were compiled to assess the magnitude of carbon and sulfur mineralization in the subsurface in relation to relevant primary and secondary minerals in the geothermal reservoir and to evaluate the potential scavenging and mobility of trace metals.

During the first phase of the CarbFix2 injection (June 2014 to July 2016), over 50% of injected carbon and 76% of sulfur mineralized within four to nine months. Four months after the doubling of gas injection rates in July 2016, the decrease in injected fluid pH led to increased mineralization during the second phase (July 2016 to December 2017), resulting in over 60% of the injected carbon and over 85% of the sulfur mineralizing. Doubling the gas injection rate brought the gas-charged fluids closer to the "sweet spot" of mineralization. The Ca release from the reservoir rocks to the fluid phase is a potential limiting factor for calcite ($CaCO_3$) precipitation, although dolomite ($Ca,Mg(CO_3)_2$) and thus aqueous Mg may also play a role in the mineralization of

the injected carbon. The mineralization rates are accelerated by the high temperatures (> 250 °C) of the formation rocks, but this is the upper temperature limit for carbon storage via the mineral carbonation of basalts due to decarbonation reactions. However, the injectivity of the injection well has remained stable throughout the study period confirming that the host rock permeability has been essentially unaffected by 3.5 years of mineral carbon and sulfur reactions.

Basalt rock dissolution is also known to release trace elements, having been extensively studied in Icelandic geothermal systems. Yet, little is known with regards to their mobility as a consequence of gas injection into basaltic rocks. The results here reveal the mobilization and uptake of several trace elements, particularly Ba, Sr, As, and Mo. Carbonates, sulfides, and secondary minerals such as epidote and actinolite likely incorporated these elements, among others. Notably, although these geothermal fluids are not meant for consumption, the trace elements were generally not above the drinking water standards set by the World Health Organization, the European Union, and Iceland, with the main exception of As. However, while As was significantly elevated before and during the first year of gas injection, concentrations have since been greatly reduced over time to levels at or below drinking water standards.

Ágrip

Eitt af höfuðvandamálum þeim, sem mannkynið stendur frammi fyrir um þessar mundir, er hvernig draga megi úr losun koltvíoxíðs (CO_2) til andrúmsloftsins. Ein lausnin væri að fanga koltvíoxíðið úr útblæstri iðju- og orkuvera, eða þá beint úr andrúmslofti, og binda það til frambúðar í bergi. Basalt er auðugt af tvígildum katjónum, Ca^{2+}, Mg^{2+} og Fe^{2+}, sem geta leyst úr bergi og hvarfast við koldíoxíð, og myndað þannig stöðugar karbónatsteindir. Koldíoxíð, sem leyst er upp í vatni og dælt niður í basaltsvæði, steinrennur á innan við tveimur árum.

Í rannsókn þessari var gerð rennslistilraun í háþrýstihvarfasúlu, sem svo er kölluð, til að herma dælingu koltvíoxíðs í glerað basalt við 50°C. Var þetta gert í því augnamiði að kanna hver hlutföll koltvíoxíðsins og vatnsins, sem það væri leyst í, þyrftu að vera til þess að skapa kjöraðstæður til útfellingar karbónata, fremur en zeólíta eða leirsteinda, við 50°C og pH-gildi á bilinu 5,2 til 6,5, en allar þessar steindir keppa um tvígildar katjónir og holrými í berginu. Niðurstöðurnar sýna glöggt, að upphaflegt pH-gildi og styrkur koltvíoxíðs í niðurdælingarvatninu skipta mestu um að þessar kjöraðstæður náist. Líkanreikningar sýna enn fremur, að ef hlé er gert á innstreymi koltvíoxíðs en niðurdælingu vatns haldið áfram, aukast líkur á myndun rúmmálsfrekra Ca-Na-zeólíta og Mg-Fe-leirsteinda, sem taka upp holrými í berginu.

Samhliða tilraunum á rannsóknarstofu hófst niðurdæling blöndu koltvíoxíðs og brennisteinsvetnis árið 2014 í svonefndu CarbFix2 verkefni við Hellisheiðarvirkjun. Í árslok 2017 hafði 23.200 tonnum af koltvíoxíði og 11.800 tonnum af brennisteinsvetni verið dælt niður á 750 m dýpi, í sprungið og ummyndað basalt, heitara en 250°C. Safnað var meira en 80 sýnum af vatni og gasi úr vöktunar- og niðurdælingarholum, bæði fyrir niðurdælingu og meðan á henni stóð. Styrkur aðal-, auka- og snefilefna var mældur í þeim tilgangi að leggja mat á hlut steinrunninna gasa, reikna mettunarstig frum- og ummyndunarsteinda í berginu, og til að kanna hreyfanleika og upptöku snefilefna.

Í fyrsta áfanga CarbFix2 niðurdælingarinnar, frá júní 2014 til júlí 2016, steinrunnu meira en 50% af koltvíoxíðinu og 76% af brennisteinsvetninu á fjórum til níu mánuðum. Niðurdælingin var tvöfölduð í öðrum hluta verkefnisins, frá júlí 2016 til desember 2017, og jókst þá steinrenningin á fjórum mánuðum, þannig að 60% koltvíoxíðsins og meira en 85% brennisteinsvetnisins bundust í bergi. Tvöföldun innstreymis gass hafði þá lækkað pH-gildi vökvans og fært hann nær kjöraðstæðum útfellingar. Leysing Ca úr bergi er væntanlega sá þáttur sem takmarkar útfellingu kalsíts, en dólómít og uppleyst Mg skipta trúlega einnig máli fyrir steinrenningu koltvíoxíðsins. Hár hiti bergsins, yfir 250°C, flýtir steinrenningu, en hann er við efri mörk þess að leyfa steinrenningu

koltvíoxíðs, því karbónatsteindir vilja brotna niður við hærri hita. Ádælingarstuðull niðurdælingarholunnar hélst stöðugur á því hálfu fjórða ári sem tilraunin stóð yfir, sem sýnir að steinrenningin hefur enn ekki spillt lekt bergsins svo neinu nemi.

Uppleysing basalts losar einnig snefilefni, sem talsvert hafa verið rannsökuð í íslenskum jarðhitakerfum. Lítið er samt vitað um hreyfanleika þeirra í kjölfar niðurdælingar gasa í basalt. Niðurstöður þessa verkefnis sýna fram á losun og upptöku nokkurra snefilefna, einkum Ba, Sr, As og Mo. Þessi efni, og fleiri, eru væntanlega tekin upp af karbónötum, súlfíðum svo og ummyndunarsteindum eins og epídóti og aktínólíti. Þótt þessi jarðhitavökvi sé ekki ætlaður til drykkjar, er engu að síður eftirtektarvert að styrkur snefilefna í honum er yfirleitt undir þeim mörkum sem neysluvatnsstaðlar Alþjóðaheilbrigðismálastofnunarinnar, Evrópusambandsins og íslenskra stjórnvalda setja. Helsta undantekningin er þó styrkur arsens. Hann var umtalsvert hærri áður en niðurdæling hófst, svo og á fyrsta ári hennar, en lækkaði síðan mikið með tímanum, og það niður fyrir mörk téðra neysluvatnsstaðla.

To my uncles

Dr. Alexander Henning Borchers & Gordon "Roy" Clark

"In every conceivable manner, the family is a link to our past, bridge to our future."

- Alex Haley

basalt eyes

by cubs the poet

hot water tears.
the northern lights
are the dreams left behind.
we take nature
and nurture the
process of turning
gas into gems.
iceland
and fire in hand
emitting the
escape of
carbon we
decide to
drive
the gas into the ground.
power plants
blossom
like black roses.

we are the ones
chosen to create
a way.

Table of Contents

List of Figures

List of Tables

Acknowledgments

First and foremost, I would like to thank Siggi. I could not have asked for a better supervisor, especially for his enthusiasm and encouragement. I am especially grateful for his commitment towards my career development here in Iceland. Certainly who else could look at my numerous figures and then immediately proclaim the data as beautiful? Thank you for believing in me and giving me this wonderful opportunity!

To the rest of my PhD committee, it has been a pleasure to work and get to know you all. Domenik, hopefully one day we can physically meet, although the early morning Skype meetings discussing the column experiments were quite enjoyable. Eric, thank you for your assistance, especially for the time you invested to help improve my manuscripts. I shall miss all the instances you popped into my office here in Iceland for a chat or the discussions over food and drink at the CO2-React network meetings. Iwona, thank you for your guidance and support, especially during my first years in Iceland. I sincerely look forward to working with you as a colleague.

I am eternally grateful for the CarbFix group and Reykjavík Energy. It is amazing to be a part of such timely and vital research in carbon storage and on top of it, working with a fantastic bunch of people based in Iceland and abroad. Special thanks to Doddi, for being the best fieldwork partner and accompanying me on the majority of our sampling trips at Hellisheiði. I look forward to what the future lies in store as the CarbFix method is utilized by other countries and sectors!

The Bambi group also deserves special thanks (including the honorary members). It is wonderful to get together over various lunches and dinners, and that so many of us are still in Iceland (we miss you Becca)! Eydís, Iwona, Gabby, Helgi, Becca, Snorri, and Sandra - your successes have given me the courage to think beyond the PhD, thank you! Tobias, I know you can do it too!

To those based in Askja over the years - in particular, Gro, Maja, Hannah, Barbara, Sydney, Jan, Vincent, Paavo, Jed, Mary, Kate, Rob, Will, Águst, the Daniels, Oli, Maria, Ríkey, Mona, Siqi, Quinten, Ed, Revathy, Eemu, Matylda, Joí, Kalina, Mariel, Cécile, Ragnheiður, Habba, Águstá, Talfan, Hrönn - I will miss the sense of community you have all given me these past five years. Without your friendships, I really would not have been able to push forward on top of the dark stormy Icelandic winters. Special thanks goes to Jón Örn Bjarnason, your discussions at all times of the day and night were always a pleasure. Thank you for always taking the time to answer my questions. I would also like to thank Steini, who was essential in the preparation and dismantling of the column experiments and Giulia Alessandrini, for being the best intern and assistant in running the column experiment.

Little did I know when I traveled one February day to the Canary Islands, how much I would enjoy the company and friendship of some wonderful people based across Europe as a part of the

CO2-React and MINSC networks. I honestly cannot thank our supervisors enough for selecting us to randomly become instant friends, what are the odds? Thank you for your support and for reminding me that life existed outside of doing a PhD in Iceland. Martin and Chiara - I am so happy that we have been able to collaborate post CO2-React, and thank you for being wonderful (physical and virtual) officemates these last years.

To my family in the United States, Canada, and England - I thank you all for your genuine interest in my research. So many of you took the time to visit me, to not only experience Iceland, but to learn more about my work in CarbFix. I will forever cherish these memories, especially those of Roy and Alex, who had both actively encouraged me to pursue a career in science. With chemists, engineers, and earth scientists on all sides of the family, I guess it only made sense to combine it all and take part in some geochemical engineering! Mom, Dad, and Gillian - thank you for your love and support ever since I first moved away from New Jersey. I know Iceland was not as close you would have liked, but thank you for understanding the wonderful chance that came my way.

Thank you to my friends from Háskólákórinn, singing with you helped keep me grounded. I am looking forward to singing with you all in other choirs!

To the Dutchies in Utrecht - It is wonderful to know that I have a city filled with friends, with whom I instantly feel at home with. I feel incredibly lucky and I thank you for your enduring friendships.

To my friends from back home in New Jersey - Although I am never there for long, I sincerely thank you for always taking the time to meet up! Know that I miss you all dearly, and that wherever I end up, you are always welcome.

Joaquín - What a journey we have been on so far, from getting to know you on my first day in Iceland and beginning the PhDs, to finishing our degrees and starting our careers! I am extremely grateful for the love and support you have shown me in the final stages. Thank you. I cannot wait to see what lies in store for us, though perhaps we should stop moving apartments at the same time as defending doctoral degrees?

Last but not least, I would like to thank Iceland. Throughout my ups and downs, Iceland has always reminded me to stop and just live, whether it be to look up and enjoy the Northern Lights, relax and soak in the many hotpots, or listen to the wind while playing board games inside a cosy cabin. Takk fyrir mig, Ísland!

This work was financially supported from the European Commission through the projects CarbFix (EC Project 283148), CO2-React (EC Project 317235), CarbFix2 (EC Project 764760), and S4CE (EC Project 764810) in addition to Reykjavík Energy and the first CarbFix team, who without their interest and investment in the original CarbFix project, none of the subsequent research would have been possible.

1 Introduction

1.1 Brief history of climate change science

> *"The establishment and progress of human societies, the action of natural forces, can notably change, and in vast regions, the state of the surface, the distribution of water and the great movements of the air. Such effects are able to make to vary, in the course of many centuries, the average degree of heat; because the analytic expressions contain coefficients relating to the state of the surface and which greatly influence the temperature."*
>
> - Joseph Fourier, 1827
> Translation by W.M. Connolley

Fourier (1824; 1827) deduced the existence of the greenhouse effect and its importance for the Earth's climate. Experiments by Foote (1856) and Tyndall (1861) determined that water vapor and carbon dioxide are the primary contributors to the trapping of infrared radiation in the atmosphere, thus regulating the temperature of the Earth's surface. Arrhenius (1896) was the first to quantify the effect of varying the carbon dioxide in the atmosphere; he suggested that by doubling the atmospheric CO_2, the average global temperature would increase by 5–6 °C.

Arrhenius (1896) had not considered carbon emission rates from industrial sources substantial enough compared to natural sources of carbon and suggested that any warming would occur over thousands of years. But by the 1950s, concern over the rising CO_2 emissions was growing. During this time, Charles Keeling joined the Scripps Institute of Oceanography (California, USA) to head the Atmospheric Carbon Dioxide Program. From March 1958 onwards, he took the first frequent regular measurements of atmospheric CO_2 concentrations at the South Pole and on Mauna Loa, Hawaii. This was the first concrete evidence of increasing CO_2 in the atmosphere (Keeling et al., 2001). Meanwhile, by assuming exponentially increasing industrial production, Bolin and Eriksson (1959) had estimated that the atmospheric CO_2 would rise around 25% (and possibly larger) by the year 2000. Measurements of atmospheric CO_2 at Mauna Loa continue to this day and the subsequent graph is known as the "Keeling Curve", as seen in Fig. 1.1 (Keeling et al., 2001).

With the advent of digital computers, numerical calculations and modelling were utilized to further investigate the climatic impact of increasing CO_2. Wigley and Jones (1981) compared the best computer models at the time to natural surface temperature fluctuations, concluding that effects from CO_2 may not be detectable until the turn of

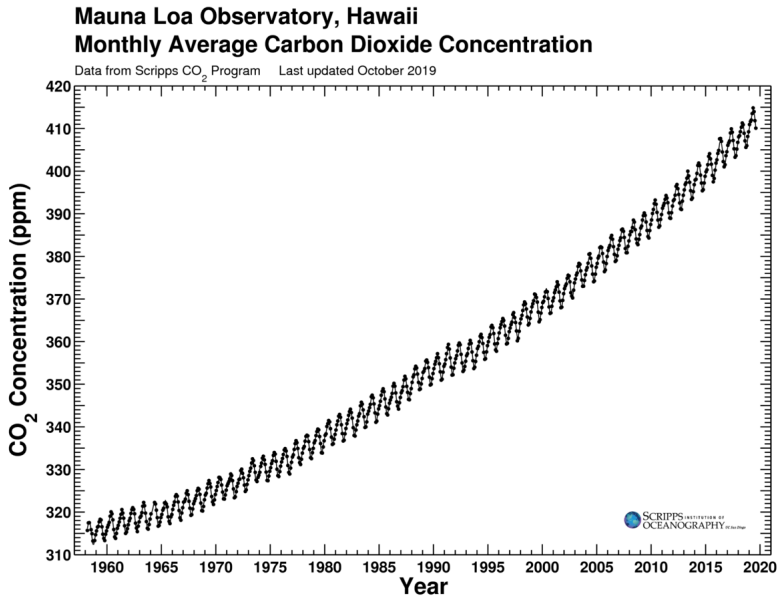

Figure 1.1. A daily record of atmospheric carbon dioxide from Scripps Institute of Oceanography, known as the "Keeling Curve" (Keeling et al., 2001; Keeling and Keeling, 2017).

the 21st century, yet immediate action should be made to avert a climatic change as atmospheric CO_2 concentrations were only increasing.

Further evidence of rising atmospheric CO_2 was confirmed with the drilling of an ice core at Vostok Station in central Antarctica. The two kilometer long core carried a 150,000-year record of the last climatic cycle and confirmed the relationship between atmospheric CO_2 levels and atmospheric temperatures (Lorius et al., 1985). With the completion of drilling, the record was extended to 420,000 years, which revealed that the climate has been in a state of change, although within stable bounds (Petit et al., 1999). Soon after, the European Project for Ice Coring in Antarctica drilled an ice core at Concordia Station (Dome C) that produced a record back to 800,000 years. The new core confirmed and extended the atmospheric CO_2 concentration from the Vostok core (Jouzel et al., 2007; Lüthi et al., 2008; Siegenthaler et al., 2005). Moreover, Marzeion et al. (2014) demonstrated that the world's glaciers were losing mass from 1851 to 2010 with increasing anthropogenic contribution during 1991 to 2010.

With the historical data from ice cores and a better understanding of different climate feedback loops, computer models simulating the Earth's climate could no longer discount the apparent global warming. The work by Levitus et al. (2001; 2000) demonstrated that the oceans around the world were experiencing a net warming since the 1950s as a result of anthropogenic sources of greenhouse gases (e.g. CO_2, CH_4). Climate models soon corroborated that the addition of new heat energy was being stored

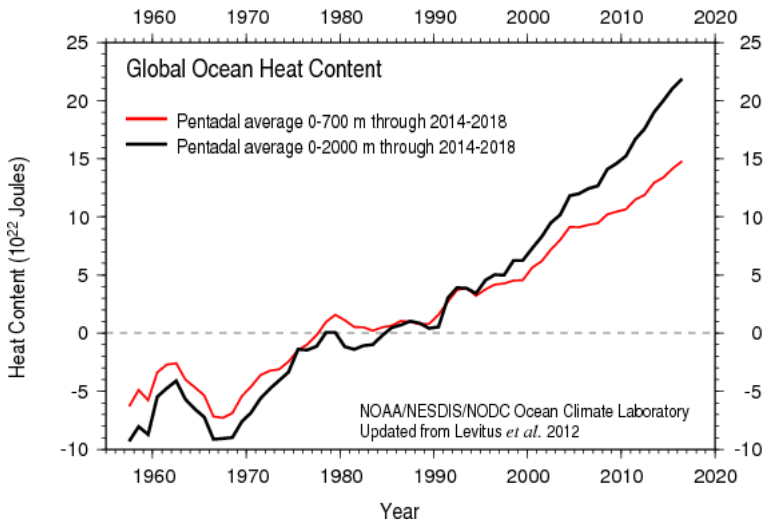

Figure 1.2. Comparison of the global heat content of 0–700 layers and 0–2000 layers of the world's oceans (Levitus et al., 2017; 2012).

in the oceans rather than in the atmosphere (Barnett et al., 2005; Hansen et al., 2005). Thus to accurately measure the changes in global temperatures, it was better to monitor the global ocean heat content (OHC) in the upper layers of the world's oceans. Figure 1.2 shows these estimates of the global OHC down to 2000 m based on 5-year (pentadal) average temperatures (Boyer et al., 2018). This clearly depicts that the OHC is steadily rising since 1955 and at faster rates in the 0–2000 m layer than 0–700 m (Levitus et al., 2017; 2012). Research has since shown that global surface temperatures would remain elevated centuries later, even if CO_2 emissions immediately ceased and atmospheric CO_2 levels stabilized (Matthews and Caldeira, 2008; Tyrrell et al., 2007).

1.2 Status of the climate

In 1988, James Hansen, the Director of the NASA Goddard Institute for Space Studies (New York, USA) gave a congressional testimony to the United States Senate on climate change (Hansen, 1988). The following is an excerpt from his statement:

> *"Number one, the earth is warmer in 1988 than at any time in the history of instrumental measurements. Number two, the global warming is now large enough that we can ascribe with a high degree of confidence a cause and effect relationship to the greenhouse effect. And number three, our computer climate simulations indicate that the greenhouse effect is already large enough to begin to effect the probability of extreme events such as summer heat waves."*

The World Meteorological Organization and the United Nations Environmental Programme established the Intergovernmental Panel on Climate Change (IPCC) that very

year. Since 1990, IPCC Assessment Reports have been released, with the Fifth Assessment Report in 2014 and the Sixth Assessment Report to be released in 2022. These reports contribute to the work of the United Nations Framework Convention on Climate Change, whose objective is to "stabilize greenhouse gas concentrations in the atmosphere at a level that would prevent dangerous anthropogenic interference with the climate system" (United Nations, 1992).

Each report provides an update on scientific, technical, and socio-economic aspects of climate change, and thereby a status of the climate. Key findings from the Fifth Assessment Report determined a clear human influence on the climate system with the resulting changes having widespread impacts on human and natural systems, which would be sustained if greenhouse gas emissions continued (see Fig. 1.3). Considerable reductions in emissions over the next decades can reduce climate risks in the coming century and beyond, but many adaptation and mitigation strategies must be implemented in order to achieve this goal (IPCC, 2014). In every major sector – energy supply, transport, buildings, industry, human settlements and infrastructure, and agriculture, forestry and other land use (AFOLU) – there are available mitigation strategies that can reduce greenhouse gas emissions, improve energy intensity, and enable structural changes, the most cost-effective being systemic and cross-sectoral. An essential component is to decarbonize electricity generation and thus the energy supply sector through low- and zero-carbon technologies. One such option is CO_2 capture and storage (CCS), of which an IPCC special report on the topic was published in 2005. The process involves separating CO_2 from industrial and energy-related sources and transporting to a storage location to sequester from the atmosphere (IPCC, 2005).

With the 2018 release of the IPCC Special Report on Global Warming of 1.5°C, further emphasis has been placed on CO_2 removal via CCS. Such technologies will be imperative to achieve deep emissions reductions and limit global warming to 1.5 °C in three of the four pathways proposed to reach 1.5 °C (Fig. 1.4). Current mitigation strategies under the Paris Agreement put the climate on pathways consistent with a warming of about 3 °C by 2100 (IPCC, 2018).

1.3 Carbon capture and storage (CCS)

The level of future emissions (the baseline) and the chosen target for long-term CO_2 concentrations will dictate the magnitude of the required emissions reductions to stabilize the atmospheric CO_2 concentration – the higher the baseline and the lower the target, the larger the necessary reductions in CO_2 emissions (Fig. 1.3). As previously mentioned, CCS is one of the viable mitigation options to help achieve the target CO_2 concentration in the atmosphere, especially considering the worldwide reliance on fossil fuels. Three main components make up the CCS process – capture, transport, and storage; however the focus here will be on carbon storage, of which there are three types – ocean storage, geological storage, and mineral carbonation (Bickle, 2009; IPCC, 2005).

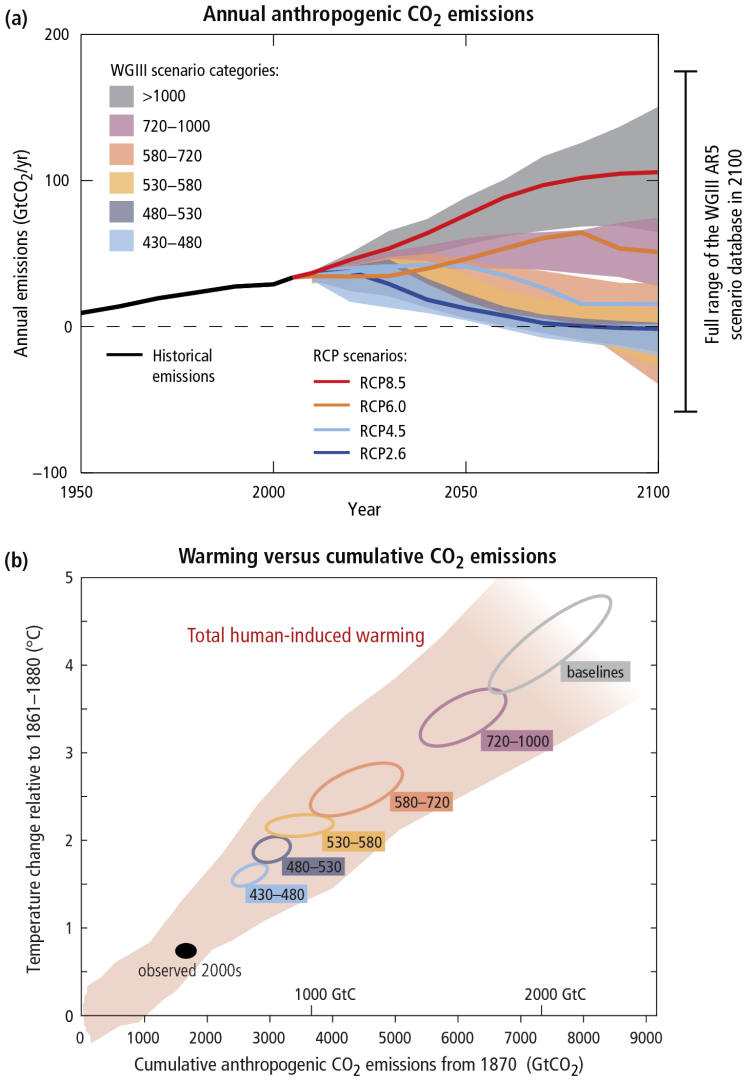

Figure 1.3. (a) CO_2 emissions in the Representative Concentration Pathways (RCPS) and their associated scenario categories. These categories summarize the wide range of emission scenarios published on the basis of CO_2-eq concentration levels (in ppm) in 2100. (b) Global mean surface temperature increase at the time global CO_2 emissions reach a given net cumulative total, plotted as a function of that total, from various lines of evidence. Ellipses show total anthropogenic warming in 2100 versus cumulative CO_2 emissions from 1870 to 2100 under the scenario categories. The filled black ellipse shows observed emissions to 2005 and observed temperatures in the decade 2000-2009 with associated uncertainties (IPCC, 2014).

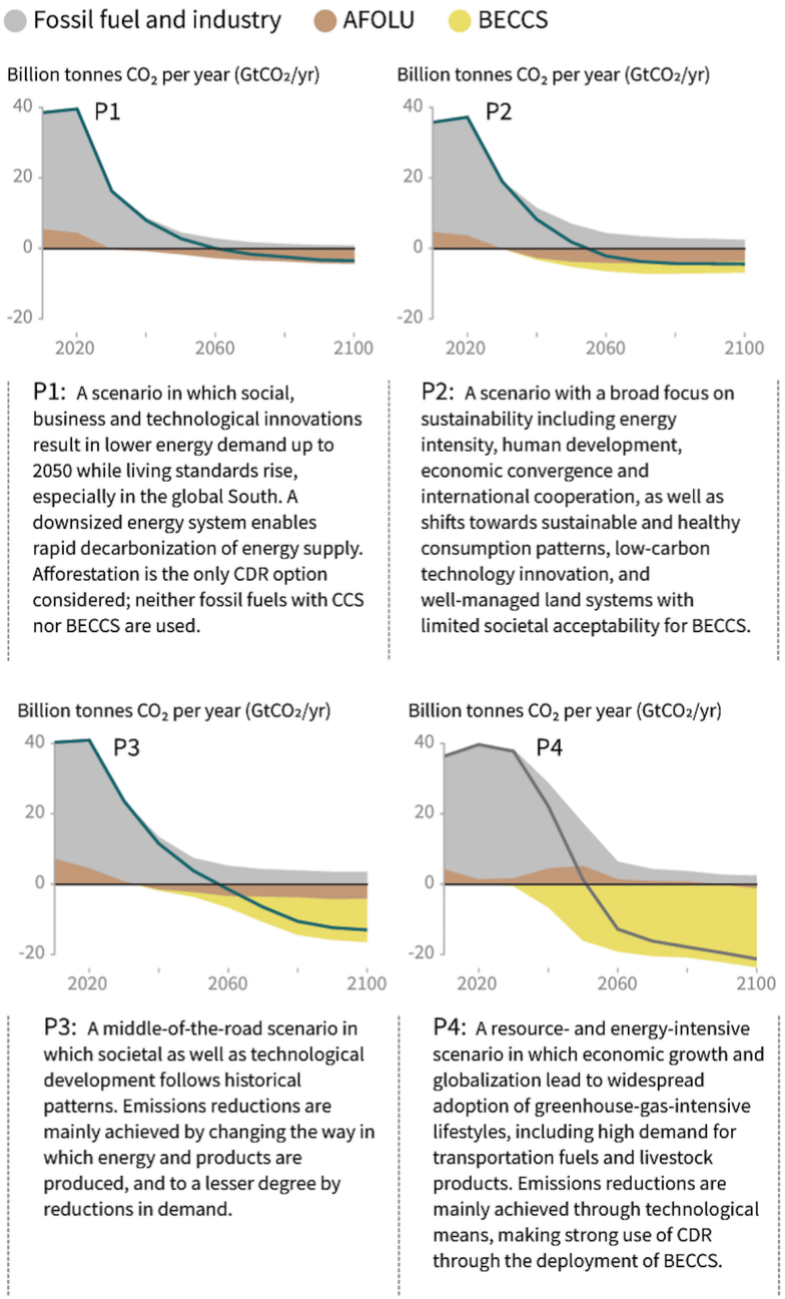

Figure 1.4. Different mitigation strategies can achieve the net emissions reductions that would be required to follow a pathway that limits global warming to 1.5 °C with no or limited overshoot. All pathways use Carbon Dioxide Removal (CDR), but the amount varies across pathways, as do the relative contributions of Bioenergy with Carbon Capture and Storage (BECCS) and removals in the Agriculture, Forestry and Other Land Use (AFOLU) sector (IPCC, 2018).

The first option, ocean storage, entails transporting CO_2 via pipelines or ships to an ocean storage site and injecting at depths greater than 1,000 m into the ocean's water column or at the sea floor (Adams and Caldeira, 2008; Haugan, 2005; Marchetti, 1977; Ohsumi, 1995). CO_2 would subsequently dissolve and disperse in the deep ocean waters. However, while the injection of a few $GtCO_2$ would only have a regional effect on the ocean chemistry, the injection of hundreds of $GtCO_2$ would ultimately affect the chemistry of the entire ocean volume. Moreover, the elevated CO_2 levels can harm marine organisms, e.g. reduced rates of calcification, reproduction, and mobility, and increased mortality over time (IPCC, 2005; Pörtner et al., 2005; Sato and Sato, 2002). As the increased acidity of the sea water from the addition of CO_2 would be mostly neutralized by the slow natural dissolution of carbonate minerals in seafloor sediments (Archer et al., 1997), another approach to ocean storage was proposed to promote carbonate dissolution using limestone (Kheshgi, 1995; Rau and Caldeira, 1999). Several small-scale laboratory experiments and numerical models have been reported (Brewer et al., 1999; Brewer et al., 2005; Caldeira and Rau, 2000; Caldeira and Wickett, 2005), yet proposed large scale field tests were not approved (de Figueiredo et al., 2002; Giles, 2002).

The engineered geological storage of CO_2 has many natural analogues (Benson et al., 2002; Güleç and Hilton, 2016; Heinemann et al., 2013; Jeandel et al., 2010; Power et al., 2013) as well as industrial analogues (Benson et al., 2002; Jeandel et al., 2010; Perry, 2005; Wilson et al., 2003) and has been extensively researched since the 1970s (Aminu et al., 2017; Baes et al., 1980; Benson and Cole, 2008; Friedmann, 2007; Leung et al., 2014; Marchetti, 1977; Michael et al., 2010; Orr, 2009; Schrag, 2009). CO_2 can be stored underground for long periods of time by injecting into deep geological formations, such as depleted oil and gas reservoirs, coal formations, and saline formations. The injected CO_2 becomes less mobile over time as a result of multiple trapping mechanisms, structural and stratigraphic trapping followed by solubility and mineral trapping (Fig. 1.5a). Thus it is considered likely that 99% or more of the injected CO_2 will be retained for 1000 years (IPCC, 2005). Currently there are 23 large-scale projects in operation or under construction (Global CCS Institute, 2018), including the Sleipner project, Norway in a saline formation (Furre et al., 2017) and the Weyburn pilot project, Canada in an oil reservoir (Hutcheon et al., 2016; Whittaker et al., 2011).

The third option, and the main subject of this thesis, is mineral carbonation, or the fixation of CO_2 as stable carbonate minerals upon the reaction with metal oxide bearing materials, like silicate minerals (Broecker and Kunzig, 2008; Dunsmore, 1992; Lackner et al., 1995; Matter and Kelemen, 2009; Oelkers et al., 2008; Power et al., 2013; Seifritz, 1990). The consumption of atmospheric CO_2 during weathering of Ca-Mg-silicates already occurs naturally, albeit over large timescales (Dessert et al., 2003; Gíslason et al., 1996; Gíslason and Eugster, 1987), thus for the practical application of anthropogenic sources of CO_2 this process needs to be accelerated. One way to accomplish this is to mine and grind up silicates to increase the mineral surface area with which a CO_2-rich fluid reacts with. However, the immense amount of material in addition to the required energy for the transportation, preparation, and storage of said material to capture small amounts of CO_2 makes this type of *ex situ* mineral carbonation impractical (Gerdemann

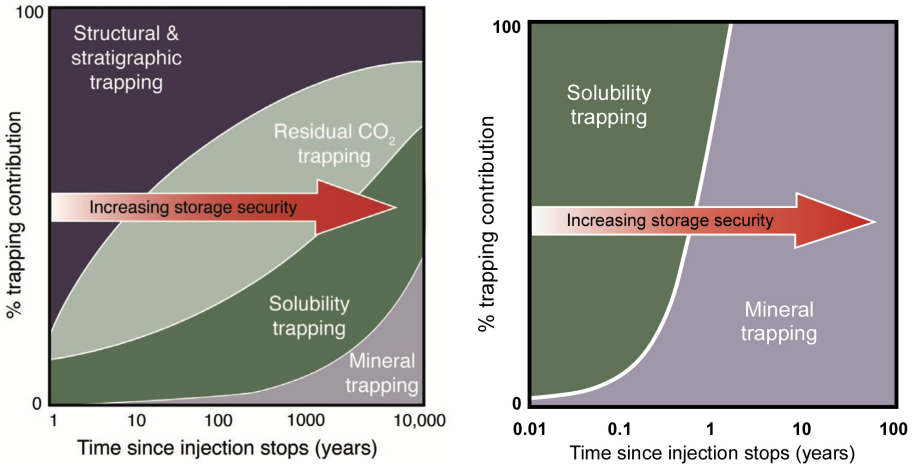

Figure 1.5. Schematic illustration depicting the evolution of trapping mechanisms as a function of time in (a) geological storage (Benson and Cole, 2008), and (b) mineral carbonation in basaltic rocks via the CarbFix method (Snæbjörnsdóttir et al., 2017).

et al., 2007; Oelkers et al., 2008). On the other hand, *in situ* carbonation involves the direct injection of CO_2 into the subsurface, where it then reacts with the silicate minerals in, for example, basaltic rocks. This has been successfully demonstrated at the Wallula Basalt Pilot site, USA (McGrail et al., 2017a; 2017b) and the CarbFix Pilot site, Iceland (Matter et al., 2016; Snæbjörnsdóttir et al., 2017). The latter also injected a gas mixture of CO_2 and H_2S and was subsequently upscaled at the Hellisheiði geothermal power plant in Iceland, where CO_2-H_2S gas injection has been ongoing since 2014 (Gunnarsson et al., 2018).

1.4 CarbFix

The CarbFix group was created in 2006 with the goal to implement a demonstration project of *in situ* mineral carbonation in an economically feasible way (Gíslason et al., 2018). Figure 1.6 summarizes the various stages of CarbFix from its inception to the current industrial scale injection.

The mineral storage of CO_2 occurs in a series of chemical reactions. The CarbFix approach either dissolves the CO_2(g) in water during its injection into the subsurface basaltic rocks (Gíslason and Oelkers, 2014; Sigfússon et al., 2015) or in a scrubbing tower adjacent to the gas source before subsequent injection (Gunnarsson et al., 2018; Sigfússon et al., 2018); both results in the formation of carbonic acid and lowers the pH of the fluid:

$$CO_2(g) + H_2O \rightleftharpoons H_2CO_3 \tag{1.1}$$

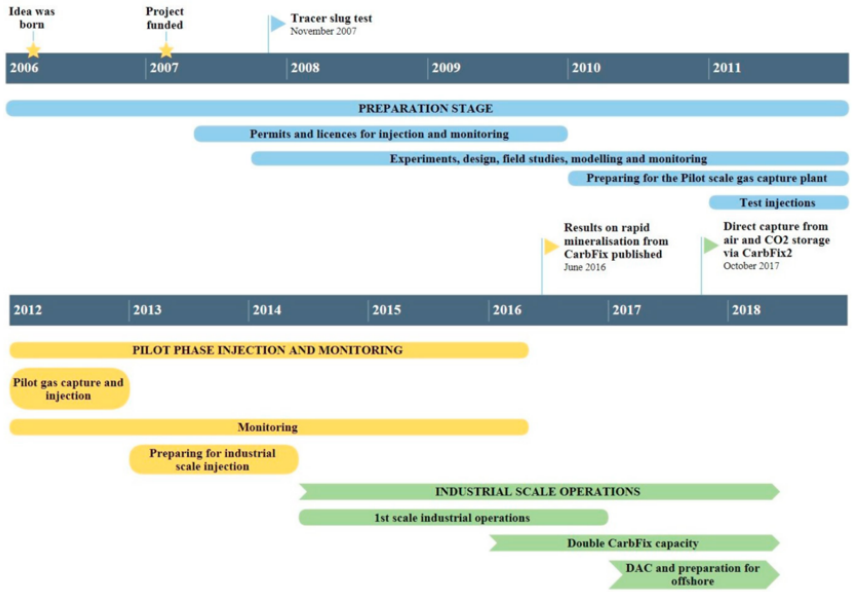

Figure 1.6. A timeline for CarbFix, including the preparation stage, the CarbFix pilot project from 2012–2016, and the industrial scale CarbFix2 project from 2014–2018 (Gíslason et al., 2018).

$$H_2CO_3 \rightleftharpoons HCO_3^- + H^+ \tag{1.2}$$

During the capture and injection process, solubility trapping of CO_2 occurs within five minutes, which adds the security of no potential gas leaks (Sigfússon et al., 2015), thereby omitting the need for physical trapping mechanisms (Fig. 1.5). Upon injection, the injected CO_2 reacts with the minerals in basaltic rocks such as anorthite (plagioclase), diopside (pyroxene), and forsterite (olivine), which release the divalent cations Ca^{+2}, Mg^{+2}, and Fe^{+2} (Gíslason and Oelkers, 2014; Gíslason et al., 2010):

$$CaAl_2Si_2O_8 + 8H^+ \rightleftharpoons Ca^{2+} + 2Al^{3+} + 2SiO_2 + 4H_2O \tag{1.3}$$

$$CaMgSi_2O_6 + 4H^+ \rightleftharpoons Ca^{2+} + Mg^{2+} + 2SiO_2 + 2H_2O \tag{1.4}$$

$$Mg_2SiO_4 + 4H^+ \rightleftharpoons 2Mg^{2+} + SiO_2 + H_2O \tag{1.5}$$

These cations then react with the dissolved CO_2 to form stable carbonate minerals like calcite, magnsite, and siderite (Gíslason and Oelkers, 2014):

$$CaCO_3 + H^+ \rightleftharpoons Ca^{2+} + HCO_3^- \tag{1.6}$$

$$MgCO_3 + H^+ \rightleftharpoons Mg^{2+} + HCO_3^- \tag{1.7}$$

$$FeCO_3 + H^+ \rightleftharpoons Fe^{2+} + HCO_3{}^- \tag{1.8}$$

Within the CarbFix group, natural analogues for sequestration of CO_2 within basalts have been studied (Flaathen et al., 2009; Galeczka et al., 2015; Olsson et al., 2014) and numerous experiments conducted (Gudbrandsson et al., 2014; 2011; Gysi and Stefánsson, 2012a; 2012b; Stockmann et al., 2014; 2013; 2012; 2011) including a high pressure column flow reactor to bridge the gap between field and laboratory scale studies (Galeczka et al., 2013; 2014). Then a 2012 field injection at a pilot site next to the Hellisheiði geothermal power plant in Iceland resulted in the successful mineralization of CO_2 within two years of injection (Matter et al., 2016; Snæbjörnsdóttir et al., 2017).

Yet given the high CO_2 capture costs in addition to the strict Icelandic regulations regarding H_2S emissions from geothermal power plants, H_2S capture and storage was researched and determined feasible (Aradóttir et al., 2014; Gunnarsson et al., 2015; 2011). The dissolution of H_2S in water is similar to that of the dissolution of CO_2 in Reactions 1.1 and 1.2:

$$H_2S\,(g) \rightleftharpoons H_2S\,(aq) \tag{1.9}$$

$$H_2S\,(aq) \rightleftharpoons HS^- + H^+ \tag{1.10}$$

The formation of stable sulfide minerals (pyrite, pyrrhotite) is also expected to occur upon reaction with minerals in the basaltic rocks:

$$FeS_2 + H_2O \rightleftharpoons Fe^{2+} + 0.25\,H^+ + 0.25\,SO_4{}^{2-} + 1.75\,HS^- \tag{1.11}$$

$$FeS + H^+ \rightleftharpoons Fe^{2+} + HS^- \tag{1.12}$$

The mixed gas injection of CO_2 and H_2S emissions captured from the Hellisheiði geothermal power plant into subsurface basalts began in 2014 (Gunnarsson et al., 2018; Sigfússon et al., 2018) and is ongoing. The industrial injection stage of CarbFix has thus far been successful with over 50% of the injected CO_2 and 76% of the injected H_2S mineralized within nine months of injection. Moreover, significant reductions in gas capture costs relative to conventional technologies have been made (Gunnarsson et al., 2018).

Using the CO_2 sequestration rates suggested by Weise et al. (2008), up to 5,200 Mt CO_2 could be stored in the Hellisheiði geothermal reservoir, while H_2S sequestration rates from Přikryl et al. (2018) estimate 2.6 Mt H_2S. Given that Iceland's total CO_2 emissions (without AFOLU) in 2017 was 7.1 Mt CO_2 (Keller et al., 2019) and total H_2S emissions from the country's geothermal energy sector amounted to 19,000 tonnes in 2016 (Sigfússon et al., 2018), much less than 1% of the storage potential at Hellisheiði could be utilized each year for Icelandic emissions only. Consequently, the CarbFix method could be a realistic mitigation option for Iceland to achieve CO_2 emissions reductions. This has been highlighted by the Letter of Intent signed in June 2019 between the Prime Minister of Iceland, Reykjavík Energy, the Aluminium and Silicon Industry in Iceland, the Ministry for the Environment and Natural Resources, the Ministry of Industries and Innovation, and the Ministry of Education, Science and Culture.

1.5 Summary of scientific contributions

The first paper in Chapter 2, *Experimental observations of CO_2-water-basaltic glass interaction in a large column reactor at 50 °C*, used the experimental design of Galeczka et al. (2013; 2014) while building on the geochemical observations and modelling results from the first phase of pure CO_2 injection of the CarbFix Pilot Project (Matter et al., 2016; Snæbjörnsdóttir et al., 2018; 2017). It investigates the proportions of injected dissolved CO_2 and high pH groundwater needed to reach a "sweet spot" in the reacted fluid composition that favors the saturation of carbonates rather than zeolites and clays. Additionally, it explores the possible sequence of carbonate minerals' saturation states and studies the consequences of discontinuous gas injection (Clark et al., 2019). Supplementary Material and trace element data are in Appendices A and B, respectively.

The papers in Chapters 3–5 focuses on the 2014–2017 geochemical data of the upscaled CarbFix2 mixed gas injection at the Hellisheiði geothermal power plant. The second paper in Chapter 3, *The chemistry and potential reactivity of the CO_2-H_2S charged injected waters at the basaltic CarbFix2 site, Iceland*, presents the injected fluid geochemistry and investigates the stability of primary and secondary minerals at the injection well outlet (Clark et al., 2018). The third paper in Chapter 4, *CarbFix2: CO_2 and H_2S mineralization after 3.5 years of continuous injection at more than 250 °C*, lengthens and expands the monitoring data originally presented by Gunnarsson et al. (2018) of dissolved CO_2 and H_2S and major element chemistry, and assesses the magnitude of carbon and sulfur storage in the subsurface. The fourth paper in Chapter 5, *Mobility of trace metals following the injection of CO_2-H_2S gas mixture into basaltic rock at 250°C*, reports the trace metal concentrations from the monitoring fluids, and evaluates the potential effects from carbon and sulfur storage. Supplementary Material for the latter two papers in Chapters 4 and 5 are contained in Appendices C and D, respectively.

Two co-authored papers have been included in the Appendices as they have been instrumental for the completion of this thesis. The paper in Appendix E, *Evaluation and refinement of thermodynamic database for mineral carbonation*, describes the updates to a thermodynamic database necessary to process the geochemical data for all four papers mentioned above (Voigt et al., 2018). Lastly, the paper in Appendix F, *The rapid and cost-effective capture and subsurface mineral storage of carbon and sulfur at the CarbFix2 site*, details the injection method and monitoring of the dissolved CO_2 and H_2S at the CarbFix2 site from 2014 until 2015 (Gunnarsson et al., 2018).

1.6 References

Adams, E.E. and Caldeira, K. (2008) Ocean Storage of CO_2. *Elements* 4, 319–324.

Aminu, M.D., Nabavi, S.A., Rochelle, C.A. and Manovic, V. (2017) A review of developments in carbon dioxide storage. *Applied Energy* 208, 1389–1419.

Aradóttir, E.S.P., Gunnarsson, I., Sigfússon, B., Gunnarsson, G., Júliusson, B.M., Gunnlaugsson, E., Sigurdardóttir, H., Arnarson, M.Th. and Sonnenthal, E. (2014)

Toward Cleaner Geothermal Energy Utilization: Capturing and Sequestering CO_2 and H_2S Emissions from Geothermal Power Plants. *Transport in Porous Media* 108, 61–84.

Archer, D., Kheshgi, H. and Maier-Reimer, E. (1997) Multiple timescales for neutralization of fossil fuel CO_2. *Geophysical Research Letters* 24, 405–408.

Arrhenius, S. (1896) On the Influence of Carbonic Acid in the Air upon the Temperature of the Ground. *Philosophical Magazine and Journal of Science* 41, 237–276.

Baes, C.F., Beall, S.E., Lee, D.W. and Marland, G. (1980) The collection, disposal, and storage of carbon dioxide. In: Bach, W., Pankrath, J., William, J. (Eds.), Interaction of Energy and Climate. D. Reidel Publishing Co., pp. 495–519.

Barnett, T.P., Pierce, D.W., AchutaRao, K.M., Gleckler, P.J., Santer, B.D., Gregory, J.M. and Washington, W.M. (2005) Penetration of Human-Induced Warming into the World's Oceans. *Science* 309, 284–287.

Benson, S.M. and Cole, D.R. (2008) CO_2 sequestration in deep sedimentary formations. *Elements* 4, 325–331.

Benson, S.M., Hepple, R., Apps, J., Tsang, C.-F. and Lippmann, M. (2002) Lessons learned from natural and industrial analogues for storage of carbon dioxide in deep geological formations. Lawrence Berkeley National Laboratory.

Bickle, M., J. (2009) Geological carbon storage. *Nature Geoscience* 2, 815–818.

Bolin, B. and Eriksson, E. (1959) Changes in the Carbon Dioxide Content of the Atmosphere and Sea Due to Fossil Fuel Combustion. In: Bolin, B. (Ed.), The Atmosphere and the Sea in Motion. Rockefeller Institute Press, New York, pp. 130–142.

Boyer, T.P., Baranova, O.K., Coleman, C., Garcia, H.E., Grodsky, A., Locarnini, R.A., Mischonov, A.V., O'Brien, T.D., Paver, C.R., Reagan, J.R., Seidov, D., Smolyar, I.V., Weathers, K. and Zweng, M.M. (2018) World Ocean Database 2018.

Brewer, P.G., Friederich, G., Peitzer, E.T. and Orr Jr., F.M. (1999) Direct experiments on the ocean disposal of fossil fuel CO_2. *Science* 284, 943–945.

Brewer, P.G., Peltzer, E.T., Walz, P., Aya, I., Yamane, K., Kojima, R., Nakajima, Y., Nakayama, N., Haugan, P. and Johannessen, T. (2005) Deep oceans experiments with fossil fuel carbon dioxide: Creation and sensing of a controlled plume at 4 km depth. *Journal of Marine Research* 63, 9–33.

Broecker, W.S. and Kunzig, R. (2008) Fixing climate: what past climate changes reveal about the current threat–and how to counter it. Hill and Wang.

Caldeira, K. and Rau, G.H. (2000) Accelerating carbonate dissolution to sequester carbon dioxide in the ocean: Geochemical implications. *Geophysical Research Letters* 27, 225–228.

Caldeira, K. and Wickett, M.E. (2005) Ocean model predictions of chemistry changes from carbon dioxide emissions to the atmosphere and ocean. *Journal of Geophysical Research* 110(C9).

Clark, D.E., Galeczka, I.M., Dideriksen, K., Voigt, M.J., Wolff-Boenisch, D. and Gíslason, S.R. (2019) Experimental observations of CO_2-water-basaltic glass interaction in a large column reactor experiment at 50 °C. *International Journal of Greenhouse Gas Control* 89, 9–19.

Clark, D.E., Gunnarsson, I., Aradóttir, E.S., Arnarson, M.Þ., Þorgeirsson, Þ.A., Sigurðardóttir, S.S., Sigfússon, B., Snæbjörnsdóttir, S.Ó., Oelkers, E.H. and Gíslason,

S.R. (2018) The chemistry and potential reactivity of the CO_2-H_2S charged injected waters at the basaltic CarbFix2 site, Iceland. *Energy Procedia* 146, 121–128.

de Figueiredo, M.A., Reiner, D.M. and Herzog, H.J. (2002) Ocean carbon sequestration: A case study in public and institutional perceptions, Sixth International Conference on Greenhouse Gas Control Technologies, Kyoto, Japan.

Dessert, C., Dupré, B., Gaillardet, J., François, L.M. and Allegre, C.J. (2003) Basalt weathering laws and the impact of basalt weathering on the global carbon cycle. *Chemical Geology* 202, 257–273.

Dunsmore, H. (1992) A geological perspective on global warming and the possibility of carbon dioxide removal as calcium carbonate mineral. *Energy Conversion and Management* 33, 565–572.

Flaathen, T.K., Gíslason, S.R., Oelkers, E.H. and Sveinbjörnsdóttir, Á.E. (2009) Chemical evolution of the Mt. Hekla, Iceland, groundwaters: A natural analogue for CO_2 sequestration in basaltic rocks. *Applied Geochemistry* 24, 463–474.

Foote, E.N. (1856) Circumstances affecting the Heat of the Sun's Rays. *The American Journal of Science and Arts* 22, 382–383.

Fourier, J. (1824) Remarques Générales Sur Les Températures Du Globe Terrestre Et Des Espaces Planétaires. *Annales de Chimie et de Physique* 27, 136–167.

Fourier, J. (1827) Mémoire sur la température du globe terrestre et des espaces planétaires. *Mémoires de l'Académie Royale des Sciences* 7, 569–604.

Friedmann, S.J. (2007) Geological carbon dioxide sequestration. *Elements* 3, 179–184.

Furre, A.-K., Eiken, O., Alnes, H., Vevatne, J.N. and Kiær, A.F. (2017) 20 Years of Monitoring CO_2-injection at Sleipner. *Energy Procedia* 114, 3916–3926.

Galeczka, I., Eiriksdóttir, E.S., Harðardóttir, J., Oelkers, E.H., Torssander, P. and Gíslason, S.R. (2015) The effect of the 2002 glacial flood on dissolved and suspended chemical fluxes in the Skaftá river, Iceland. *Journal of Volcanology and Geothermal Research* 301, 253–276.

Galeczka, I., Wolff-Boenisch, D., Jonsson, T., Sigfússon, B., Stefánsson, A. and Gíslason, S.R. (2013) A novel high pressure column flow reactor for experimental studies of CO_2 mineral storage. *Applied Geochemistry* 30, 91–104.

Galeczka, I., Wolff-Boenisch, D., Oelkers, E.H. and Gíslason, S.R. (2014) An experimental study of basaltic glass–H_2O–CO_2 interaction at 22 and 50°C: Implications for subsurface storage of CO_2. *Geochimica et Cosmochimica Acta* 126, 123–145.

Gerdemann, S.J., O'Connor, W.K., Dahlin, D.C., Penner, L.R. and Rush, H. (2007) Ex situ aqueous mineral carbonation. *Environmental Science & Technology* 41, 2587–2593.

Giles, J. (2002) Norway sinks ocean carbon study. *Nature* 419, 6.

Gíslason, S.R., Arnórsson, S. and Armannsson, H. (1996) Chemical weathering of basalt in southwest Iceland: Effects of runoff, age of rocks and vegetative/glacial cover. *American Journal of Science* 296, 837–907.

Gíslason, S.R. and Eugster, H.P. (1987) Meteoric water-basalt interactions. II: A field study in N.E. Iceland. *Geochimica et Cosmochimica Acta* 51, 2841–2855.

Gíslason, S.R. and Oelkers, E.H. (2014) Carbon Storage in Basalt. *Science* 334, 373–374.

Gíslason, S.R., Sigurðardóttir, H., Aradóttir, E.S. and Oelkers, E.H., 2018. A brief history of CarbFix: Challenges and victories of the project's pilot phase. *Energy*

Procedia 146, 103–114.

Gíslason, S.R., Wolff-Boenisch, D., Stefánsson, A., Oelkers, E.H., Gunnlaugsson, E., Sigurðardóttir, H., Sigfússon, B., Broecker, W.S., Matter, J.M. and Stute, M. (2010) Mineral sequestration of carbon dioxide in basalt: A pre-injection overview of the CarbFix project. *International Journal of Greenhouse Gas Control* 4, 537–545.

Global CCS Institute (2018) The Global Status of CCS: 2018, Australia.

Gudbrandsson, S., Wolff-Boenisch, D., Gíslason, S.R. and Oelkers, E.H. (2011) An experimental study of crystalline basalt dissolution from $2 \leq \text{pH} \leq 11$ and temperatures from 5 to 75°C. *Geochimica et Cosmochimica Acta* 75, 5496–5509.

Gudbrandsson, S., Wolff-Boenisch, D., Gíslason, S.R. and Oelkers, E.H. (2014) Experimental determination of plagioclase dissolution rates as a function of its composition and pH at 22°C. *Geochimica et Cosmochimica Acta* 139, 154–172.

Güleç, N. and Hilton, D.R. (2016) Turkish geothermal fields as natural analogues of CO_2 storage sites: gas geochemistry and implications for CO_2 trapping mechanisms. *Geothermics* 64, 96–110.

Gunnarsson, I., Aradóttir, E.S., Oelkers, E.H., Clark, D.E., Arnarson, M.Þ., Sigfússon, B., Snæbjörnsdóttir, S.Ó., Matter, J.M., Stute, M., Júlíusson, B.M. and Gíslason, S.R. (2018) The rapid and cost-effective capture and subsurface mineral storage of carbon and sulfur at the CarbFix2 site. *International Journal of Greenhouse Gas Control* 79, 117–126.

Gunnarsson, I., Júlíusson, B.M., Aradóttir, E.S., Sigfússon, B. and Arnarson, M.Þ. (2015) Pilot Scale Geothermal Gas Separation, Hellisheiði Power Plant, Iceland, World Geothermal Congress, Melbourne, Australia.

Gunnarsson, I., Sigfússon, B., Stefásson, A., Arnórsson, S., Scott, S.W. and Gunnlaugsson, E. (2011) Injection of H_2S from Hellisheiði Power Plant, Iceland, Thirty-Sixth Workshop on Geothermal Reservoir Engineering, Stanford University, Stanford, California.

Gysi, A.P. and Stefánsson, A. (2012a) CO_2-water-basalt interaction. Low temperature experiments and implications for CO_2 sequestration into basalts. *Geochimica et Cosmochimica Acta* 81, 129–152.

Gysi, A.P. and Stefánsson, A. (2012b) Mineralogical aspects of CO_2 sequestration during hydrothermal basalt alteration — An experimental study at 75 to 250°C and elevated pCO_2. *Chemical Geology* 306–307, 146–159.

Hansen, J., Nazarenko, L., Ruedy, R., Sata, M., Willis, J., Del Genio, A., Koch, D., Lacis, A., Lo, K., Meno, S., Novakov, T., Perlwitz, J., Russell, G., Schmidt, G.A. and Tausnev, N. (2005) Earth's Energy Imbalance: Confirmation and Implications. *Science* 308, 1431–1435.

Hansen, J.E. (1988) The Greenhouse Effect: Impacts on Current Global Temperature and Regional Heat Waves, NASA Goddard Institute for Space Studies.

Haugan, P.M. (2005) Turbulent diffusion and transport from a CO_2 lake in the deep ocean. *Journal of Geophysical Research* 110(C9).

Heinemann, N., Wilkinson, M., Haszeldine, R.S., Fallick, A.E. and Pickup, G.E. (2013) CO_2 sequestration in a UK North Sea analogue for geological carbon storage. *Geology* 41, 411–414.

Hutcheon, I., Shevalier, M., Durocher, K., Bloch, J., Johnson, G., Nightingale, M. and Mayer, B. (2016) Interactions of CO_2 with formation waters, oil and minerals and

CO_2 storage at the Weyburn IEA EOR site, Saskatchewan, Canada. *International Journal of Greenhouse Gas Control* 53, 354–370.

IPCC (2005) IPCC Special Report on Carbon Dioxide Capture and Storage, IPCC, New York.

IPCC (2014) Climate Change 2014: Synthesis Report. Contribution of Working Groups I, II and III to the Fifth Assessment Report of the Intergovernmental Panel on Climate Change, IPCC, Geneva, Switzerland.

IPCC (2018) Global Warming of 1.5°C. An IPCC Special Report on the impacts of global warming of 1.5°C above pre-industrial levels and related global greenhouse gas emission pathways, in the context of strengthening the global response to the threat of climate change, sustainable development, and efforts to eradicate poverty, IPCC.

Jeandel, E., Battani, A. and Sarda, P. (2010) Lessons learned from natural and industrial analogues for storage of carbon dioxide. *International Journal of Greenhouse Gas Control* 4, 890–909.

Jouzel, J., Masson-Delmotte, V., Cattani, O., Dreyfus, G., Felourd, S., Hoffmann, G., Minster, B., Nouet, J., Barnola, J.-M. and Chappeliaz, J. (2007) Orbital and millennial Antarctic climate variability over the past 800,000 years. *Science* 317, 793–796.

Keeling, C.D., Piper, S.C., Bacastow, R.B., Wahlen, M., Whorf, T.P., Heimann, M. and Meijer, H.A. (2001) Exchanges of atmospheric CO_2 and $^{13}CO_2$ with the terrestrial biosphere and oceans from 1978 to 2000. I. Global Aspects, UC San Diego: Scripps Institute of Oceanography.

Keeling, R.F. and Keeling, C.D. (2017) Atmospheric Monthly In Situ CO_2 Data - Mauna Loa Observatory, Hawaii. In: Scripps CO_2 Program Data (Editor). UC San Diego Library Digital Collections.

Keller, N., Stefani, M., Einarsdóttir, S.R., Helgadóttir, Á.K., Guðmundsson, J., Snorrason, A., Þórsson, J. and Tinganelli, L. (2019) National Inventory Report, The Environment Agency of Iceland.

Kheshgi, H.S. (1995) Sequestering atmospheric carbon dioxide by increasing ocean alkalinity. Energy 20, 915–922.

Lackner, K.S., Wendt, C.H., Butt, D.P., Joyce Jr, E.L. and Sharp, D.H. (1995) Carbon dioxide disposal in carbonate minerals. *Energy* 20, 1153–1170.

Leung, D.Y.C., Caramanna, G. and Maroto-Valer, M.M. (2014) An overview of current status of carbon dioxide capture and storage technologies. *Renewable and Sustainable Energy Reviews* 39, 426–443.

Levitus, S., Antonov, J., Boyer, T., Baranova, O., Garcia, H., Lcarnini, R., Mischonov, A., Reagan, J., Seidov, D., Yarosh, E. and Zweng. M. (2017) NCEI ocean heat content, temperature anomalies, salinity anomalies, thermosteric sea level anomalies, halosteric sea level anomalies, and total steric sea level anomalies from 1955 to present calculated from in situ oceanographic subsurface profile data In: Information, N.N.C.f.E. (Editor).

Levitus, S., Antonov, J.I., Boyer, T.P., Baranova, O.K., Garcia, H.E., Locarnini, R.A., Mishonov, A.V., Reagan, J.R., Seidov, D., Yarosh, E.S. and Zweng, M.M. (2012) World ocean heat content and thermosteric sea level change (0-2000 m), 1955–2010. *Geophysical Research Letters* 39.

Levitus, S., Antonov, J.I., Boyer, T.P. and Stephens, C. (2000) Warming of the World Ocean. *Science* 287, 2225–2229.

Levitus, S., Antonov, J.I., Wang, J., Delwork, T.L., Dixon, K.W. and Broccoli, A.J. (2001) Anthropogenic Warming of Earth's Climate System. *Science* 292, 267–270.

Lorius, C., Jouzel, J., Ritz, C., Merlivat, L., Barkov, N.I., Korotkevich, Y.S. and Kotlyakov, V.M. (1985) A 150,000-year climatic record form Antarctic ice. *Nature* 316, 591–596.

Lüthi, D., Le Floch, M., Bereiter, B., Blunier, T., Barnola, J-M., Siegenthaler, U., Raynaud, D., Jouzel, J., Fischer, H. and Kawamura, K. (2008) High-resolution carbon dioxide concentration record 650,000–800,000 years before present. *Nature* 453, 379.

Marchetti, C. (1977) On Geoengineering and the CO_2 Problem. *Climate Change* 1, 59–68.

Marzeion, B., Cogley, J.G., Richter, K. and Parkes, D. (2014) Attribution of global glacier mass loss to anthropogenic and natural causes. *Science* 345, 919–921.

Matter, J.M. and Kelemen, P.B. (2009) Permanent storage of carbon dioxide in geological reservoirs by mineral carbonation. *Nature Geoscience* 2, 837.

Matter, J.M., Stute, M., Snæbjörnsdóttir, S.Ó., Oelkers, E.H., Gíslason, S.R., Aradóttir, E.S., Sigfússon, B., Gunnarsson, I., Sigurðardóttir, H., Gunnlaugsson, E., Alfredsson, H.A., Wolff-Boenisch, D., Mesfin, K., Fernandez de la Reguera Taya, D., Hall, J., Dideriksen, K. and Broecker, W.S. (2016) Rapid carbon mineralization for permanent disposal of anthropogenic carbon dioxide emissions. *Science* 352, 1312–1314.

Matthews, H.D. and Caldeira, K. (2008) Stabilizing climate requires near-zero emissions. *Geophysical Research Letters* 35.

McGrail, B.P., Schaef, H.T., Spane, F.A., Cliff, J.B., Qafoku, O., Horner, J.A., Thompson, C.J., Owen, A.T. and Sullivan, C.E. (2017a) Field Validation of Supercritical CO_2 Reactivity with Basalts. *Environmental Science & Technology Letters* 4, 6–10.

McGrail, B.P., Schaef, H.T., Spane, F.A., Horner, J.A., Owen, A.T., Cliff, J.B., Qafoku, O., Thompson, C.J. and Sullivan, E.C. (2017b) Wallula Basalt Pilot Demonstration Project: Post-injection Results and Conclusions. *Energy Procedia* 114, 5783–5790.

Michael, K., Golab, A., Shulakova, V., Ennis-King, J., Allinson, G., Sharma, S. and Aiken, T. (2010) Geological storage of CO_2 in saline aquifers—A review of the experience from existing storage operations. *International Journal of Greenhouse Gas Control* 4, 659–667.

Oelkers, E.H., Gíslason, S.R. and Matter, J. (2008) Mineral Carbonation of CO_2. *Elements* 4, 333–337.

Ohsumi, T. (1995) CO_2 storage options in the deep sea. Marine Technology Society Journal, 29, 58–66.

Olsson, J., Stipp, S.L.S., Makovicky, E. and Gíslason, S.R. (2014) Metal scavenging by calcium carbonate at the Eyjafjallajökull volcano: A carbon capture and storage analogue. *Chemical Geology* 384, 135–148.

Orr, F.M. (2009) Onshore Geologic Storage of CO_2. *Science* 325, 1656–1658.

Perry, K.F. (2005) Natural gas storage industry experience and technology: potential application to CO_2 geological storage. *Carbon dioxide capture for storage in deep geologic formations* 2, 815–825.

Petit, J.R., Jouzel, J., Raynud, D., Barkov, N.I., Barnola, J.-M., Basile, I., Benders, M., Chappeliaz, J., Davis, M., Delaygue, G., Delmotte, M., Kotlyakov, V.M., Legrand, M., Liepnkov, V.Y., Lorius, C., Pépin, L., Ritz, C., Saltzman, E. and Stievenard, M. 1999 Climate and atmospheric history of the past 420,000 years from the Vostok ice core, Antarctica. *Nature* 399, 429–436.

Pörtner, H., Langenbuch, M. and Michaelidis, B. (2005) Effects of CO_2 on marine animals: Interactions with temperature and hypoxia regimes. *Journal of Geophysical Research-Oceans* 110.

Power, I.M., Harrison, A.L., Dipple, G.M., Wilson, S.A., Keleman, P.B., Hitch, M. and Southam, G. (2013) Carbon Mineralization: From Natural Analogues to Engineered Systems. *Reviews in Mineralogy and Geochemistry* 77, 305–360.

Přikryl, J., Marieni, C., Gudbrandsson, S., Aradóttir, E.S., Gunnarsson, I. and Stefánsson, A. (2018) H_2S sequestration process and sustainability in geothermal systems. *Geothermics* 71, 156-166.

Rau, G.H. and Caldeira, K. (1999) Enhanced carbon dissolution: a means of sequestering waste CO_2 as ocean bicarbonate. *Energy Conversion and Management* 40, 1803-1813.

Sato, T. and Sato, K. (2002) Numerical prediction of the dilution process and its biological impacts in CO_2 ocean sequestration. *Journal of Marine Science and Technology* 6, 169–180.

Schrag, D.P. (2009) Storage of Carbon Dioxide in Offshore Sediments. *Science* 325, 1658–1659.

Seifritz, W. (1990) CO_2 disposal by means of silicates. *Nature* 345, 486.

Siegenthaler, U., Stocker, T.F., Monnin, E., Lüthi, D., Schwander, J., Stauffer, B., Raynaud, D., Barnola, J.-M., Fischer, H. and Masson-Delmotte, V. (2005) Stable carbon cycle–climate relationship during the late Pleistocene. *Science* 310, 1313–1317.

Sigfússon, B., Arnarson, M.Þ., Snæbjörnsdóttir, S.Ó., Karlsdóttir, M.R., Aradóttir, E.S. and Gunnarsson, I. (2018) Reducing emissions of carbon dioxide and hydrogen sulphide at Hellisheidi power plant in 2014-2017 and the role of CarbFix in achieving the 2040 Iceland climate goals. *Energy Procedia* 146, 135–145.

Sigfússon, B., Gíslason, S.R., Matter, J.M., Stute, M., Gunnlaugsson, E., Gunnarsson, I., Aradóttir, E.S., Sigurðardóttir, H., Mesfin, K., Alfredsson, H.A., Wolff-Boenisch, D., Arnarsson, M.T. and Oelkers, E.H. (2015) Solving the carbon-dioxide buoyancy challenge: The design and field testing of a dissolved CO_2 injection system. *International Journal of Greenhouse Gas Control* 37, 213–219.

Snæbjörnsdóttir, S.Ó., Gíslason, S.R., Galeczka, I.M. and Oelkers, E.H. (2018) Reaction path modelling of in-situ mineralisation of CO_2 at the CarbFix site at Hellisheidi, SW-Iceland. *Geochimica et Cosmochimica Acta* 220, 348–366.

Snæbjörnsdóttir, S.Ó., Oelkers, E.H., Mesfin, K., Aradóttir, E.S., Dideriksen, K., Gunnarsson, I., Gunnlaugsson, E., Matter, J.M., Stute, M. and Gíslason, S.R. (2017) The chemistry and saturation states of subsurface fluids during the in situ mineralisation of CO_2 and H_2S at the CarbFix site in SW-Iceland. *International Journal of Greenhouse Gas Control* 58, 87–102.

Stockmann, G.J., Shirokova, L.S., Pokrovsky, O.S., Bénézeth, P., Bovet, N., Gíslason, S.R. and Oelkers, E.H. (2012) Does the presence of heterotrophic bacterium

Pseudomonas reactans affect basaltic glass dissolution rates? *Chemical Geology* 296, 1–18.

Stockmann, G.J., Wolff-Boenisch, D., Bovet, N., Gíslason, S.R. and Oelkers, E.H. (2014) The role of silicate surfaces on calcite precipitation kinetics. *Geochimica et Cosmochimica Acta* 135, 231–250.

Stockmann, G.J., Wolff-Boenisch, D., Gíslason, S.R. and Oelkers, E.H. (2011) Do carbonate precipitates affect dissolution kinetics? 1: Basaltic glass. *Chemical Geology* 284, 306–316.

Stockmann, G.J., Wolff-Boenisch, D., Gíslason, S.R. and Oelkers, E.H. (2013) Do carbonate precipitates affect dissolution kinetics? 2: Diopside. *Chemical Geology* 337–338, 56–66.

Tyndall, J. (1861) On the absorption and radiation of heat by gases and vapours, and on the physical connexion of radiation, absorption, and conduction. *Philosophical Transactions of the Royal Society of London* 151, 1–36.

Tyrrell, T., Shepherd, J.G. and Castle, S. (2007) The long-term legacy of fossil fuels. *Tellus B: Chemical and Physical Meteorology* 59, 664–672.

United Nations (1992) United Nations Framework Convention on Climate Change.

Voigt, M., Marieni, C., Clark, D.E., Gíslason, S.R. and Oelkers, E.H. (2018) Evaluation and refinement of thermodynamic databases for mineral carbonation. *Energy Procedia* 146, 81–91.

Weise, F., Fridriksson, T. and Armannsson, H. (2008) CO_2 fixation by calcite in high-temperature geothermal systems in Iceland. ÍSOR.

Whittaker, S., Rostron, B., Hawkes, C., Gardner, C., White, D., Johnson, J., Chalaturnyk, R. and Seeburger, D. (2011) A decade of CO_2 injection into depleting oil fields: monitoring and research activities of the IEA GHG Weyburn-Midale CO_2 Monitoring and Storage Project. *Energy Procedia* 4, 6069–6076.

Wigley, T.M.L. and Jones, P.D. (1981) Detecting CO_2-induced climatic changes. *Nature* 292, 205–208.

Wilson, E.J., Johnson, T.L. and Keith, D.W. (2003) Regulating the Ultimate Sink: Managing the Risks of Geologic CO_2 Storage. *Environmental Science & Technology* 37, 3476–3483.

2 Paper I

Experimental observations of CO_2 – water – basaltic glass interaction in a large column reactor experiment at 50 °C

Deirdre E. Clark, Iwona M. Galeczka, Knud Dideriksen, Martin J. Voigt, Domenik Wolff-Boenisch, and Sigurður R. Gíslason

International Journal of Greenhouse Control 89, 9–19, 2019.
doi.org/10.1016/j.ijggc/2019.07.007

Abstract

Mineralization of water dissolved carbon dioxide injected into basaltic rocks occurs within two years in field-scale settings. Here we present the results from a CO_2-water-basaltic glass laboratory experiment conducted at 50 °C and 80 bar pressure in a Ti high-pressure column flow reactor. We explore the possible sequence of saturation with Fe-Mg-Ca-carbonate minerals versus Fe-Mg-clay and Ca-zeolite saturation states, which all compete for divalent cations and pore space during injection of CO_2 into basaltic rocks.

Pure water (initially with atmospheric CO_2) – basaltic glass reactions resulted in high pH (9–10) water saturated with respect to Mg-Fe-clays (saponites), Ca-zeolites, and Ca-carbonate. As CO_2-charged water ($\sim$20 mM) entered the column and mixed with the high pH water, all the Fe-Mg-Ca-carbonates became temporarily supersaturated along with clays and zeolites. Injected waters with dissolved CO_2 reached carbonate mineral saturation within 12 hours of fluid-rock interaction. Once the pH of the outflow water stabilized below 6, siderite was the only thermodynamically stable carbonate throughout the injection period, although no physical evidence of its precipitation was found. When CO_2 injection stopped while continuing to inject pure water, pH rose rapidly in the outflow and all carbonates became undersaturated, whereas zeolites became more saturated and Mg-Fe-saponites supersaturated. Resuming CO_2 injection lowered the pH from > 8 to about 6, resulting in an undersaturation of the clays and Na-zeolites.

These results along with geochemical modelling underscore the importance of initial pCO_2 and pH values to obtain a balance between the formation of carbonates versus clays and zeolites. Moreover, modelling indicates that pauses in CO_2 injection while still injecting water can result in enhanced large molar volume Ca-Na-zeolite and Mg-Fe-clay formation that consumes pore space within the rocks.

2.1 Introduction

The CarbFix CO_2 storage pilot project in Iceland (Alfredsson et al., 2013; Aradóttir et al., 2012; Gíslason et al., 2010; Matter et al., 2011, Khaalilabad et al., 2008; Oelkers et al., 2008) was established to investigate the potential of mineral carbon storage in basalt to reduce CO_2 concentration in the atmosphere. Conceptually, CO_2-saturated water enhances basalt dissolution due to their low pH, thus releasing primarily divalent cations into the solution. Stable carbonate minerals, such as calcite, magnesite, siderite, and mixtures thereof, then precipitate during the CO_2-water-basalt reactions (Daval, 2018; Gysi and Stefánsson, 2012a; Gysi 2017; Kanakiya et al., 2017; Matter and Kelemen, 2009; McGrail et al., 2017; Schaef et al., 2010; Snæbjörnsdóttir et al., 2018; Xiong et al., 2017).

Carbon dioxide dissolved in water had mineralized within two years of field injection into reactive basaltic rocks at the CarbFix site in SW-Iceland (Matter et al., 2016; Snæbjörnsdóttir et al., 2017) and some of the supercritically injected CO_2 has also mineralized after two years at the Wallula Basalt Pilot Project in Washington, USA (McGrail et al., 2017). The rapid mineralization at the CarbFix site is attributed to the dissolution of CO_2 into water during injection, enhanced dissolution of the basaltic minerals and glass at low pH, as well as the mixing of the injected fluid with high pH groundwater that is further explored in this experiment (Snæbjörnsdóttir et al., 2017). Reaction path modelling of the fluid in the first phase of pure CO_2 injection reveals that basaltic glass dissolution drives the mineralization of the bulk of the injected CO_2 along a slower, pervasive flow path, while a faster, high permeability flow path (the first breakthrough) is dominated by crystalline basalt dissolution. Modelling results of this first breakthrough ($\sim$3% of the injected fluid) from the first monitoring well suggests that the initial carbon mineralization at the lowest pH ($\sim$5) begins with siderite ($FeCO_3$), and as pH increases, mixtures of Fe-, Mg-, and Ca-carbonates take over; finally, at the highest pH, calcite is predicted to be the dominant alteration product (Snæbjörnsdóttir et al., 2018). This sequence had not been directly observed in the field as the pH was already too high (up to 8.2) in the first monitoring well with calcite being the final mineral product at pH > 8 (Snæbjörnsdóttir et al., 2017). Nevertheless, the modelled carbonate sequence is in agreement with (a) natural analogue studies (Rogers et al., 2006), (b) the observed well fluid chemical composition, and (c) the ^{14}C isotopic composition of the fluid within the first monitoring well (Matter et al., 2016). Additionally, the pilot project continued to inject water in between and after the two phases of gas injections and also had some operational complications to troubleshoot, leading to periods of discontinuous gas injection during the second phase of CO_2-H_2S-H_2 injection, which in turn resulted

in pH fluctuations and elevated saturation states of secondary minerals like analcime and smectite (Gíslason et al., 2018, Snæbjörnsdóttir et al., 2017).

Besides field test injections, numerous laboratory experiments have been conducted to examine sequestration of CO_2 within basalts by studying carbonation on basalt powders and grains (e.g. Gysi and Stefánsson, 2012a; 2012b; Hellevang et al., 2017; Rosenbauer et al., 2012; Schaef et al., 2010; Stockmann et al., 2011; 2013; Wolff-Boenisch and Galeczka, 2018) or basalt cores (e.g. Andreani et al., 2009; Adeoye et al., 2017; Kanakiya et al., 2017; Luhmann et al., 2017a; 2017b; Menefee et al., 2018; Xiong et al., 2017; 2018) as well as its inhibition by carbonate coatings and bacteria (e.g. Stockmann et al., 2012; 2014). From these studies, physical evidence of siderite, ankerite, and/or Mg-Fe-carbonates have been reported by Adeoye et al. (2017), Gysi and Stefánsson (2012a), Kanakiya et al. (2017), Menefee et al. (2018), Rosenbauer et al. (2012), Schaef et al. (2010), and Xiong et al. (2017). Of note is the residence time of these batch experiments, which lasted from a minimum of 12 days up to 182 days; this provides ample time for basalt dissolution and accumulation of enough divalent cations in the fluid to precipitate Fe-carbonates. Flow through experiments using basalt cores conducted by Andreani et al. (2009) identified minor amounts of siderite in a dead end fracture after a total run time of 450 minutes. On the other hand, a series of flow through experiments using basalt cores run by Luhmann et al. (2017b) for up to 33 days was unable to produce detectable siderite despite the saturation or supersaturation of the fluid with respect to siderite and reaction path modelling that had suggested siderite formation at low pH.

A 2.3 m long Ti high-pressure column flow reactor has been designed for CO_2-water-basalt experiments (Galeczka et al., 2013) to bridge the gap between field and laboratory-scale experiments. In addition to its large scale, this setup permits the sampling of a pressurized gas-charged liquid along a flow path and *in situ* monitoring of dissolved inorganic carbon and pH. The experiment described in this study utilized this column reactor but modified it with a high pressure syringe pump; this provided slower flow rates and increased residence times of the fluid within the column, thereby enabling longer water-rock interaction before the fluid exited the column. Galeczka et al. (2014) had previously conducted an experiment at 22 and 50 °C set at 22 bar pCO_2 aimed at studying CO_2-charged fluid-basalt interaction, however as the pH did not rise much above 4.5 after the first arrival of the CO_2-charged waters at 22 °C, saturation with carbonates (and precipitation) was unable to occur.

The aim of this experiment is to further investigate the proportions of injected dissolved CO_2 and high pH groundwater needed to reach a "sweet spot" in the reacted fluid composition that favors the saturation of carbonates rather than zeolites and clays at pH 5.2–6.5 (Snæbjörnsdóttir et al., 2018). In addition, this study explores the possible sequence of carbonate minerals' saturation states in the first phase of pure CO_2 injection of the CarbFix pilot project, and to study the consequences of discontinuous gas injection.

2.2 Materials and methods

2.2.1 Experimental design

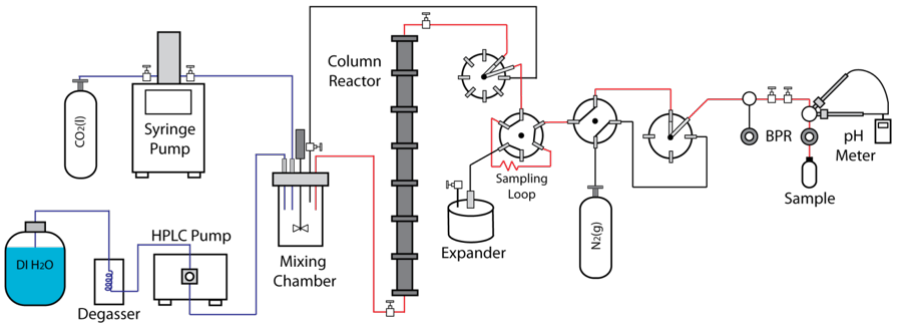

Figure 2.1. Drawing of the experimental design, which is shown for both normal flow and the sampling mode. The CO_2 is mixed with H_2O and pumped through a 2.34 long column that is wrapped with heating tape. The inlet pathways are in blue. The reacted solution (in red) flows through a multi-position 8-port stream selector followed by a 2-position 6-port valve with a 5 mL sampling loop. Filtrated samples are collected once also passing a 2-position 4-port valve, a 4-port stream selector, a set of pH electrodes, and a back pressure regulator (BPR). The mixing chamber fluid can be sampled by changing the settings of the 8-port stream selector and closing off the valves to and from the column reactor (pathway in black). For more detailed descriptions and drawings of the various settings, refer to Galeczka et al. (2013).

This study used the Ti high-pressure column flow reactor (HPCFR) designed by Galeczka et al. (2013), where a detailed description can be found. One significant modification has been made to the setup; a high pressure syringe pump (VINCI Technology, BTSP-03-050) was used instead of a supercritical fluid pump to provide slower flow rates and longer residence times of fluids within the column, allowing for longer water-rock interaction. As depicted in Fig. 2.1, the syringe pump was connected to both a liquid CO_2 cylinder source and a 'mixing chamber' (mixed-flow-through Ti-Parr-reactor) with valves between each. The syringe compartment was first filled to its capacity with CO_2(l). Once filled and the valve closed off from the cylinder, the volume of the syringe was adjusted to obtain a pressure of $\sim$80 bar. Subsequently, the valve between the 'mixing chamber' and syringe pump was opened so that the liquid CO_2 was allowed to mix with the degassed deionized (DI) water (18.2 MΩ x cm^{-1}) delivered by a high pressure liquid chromatography pump (HPLC). The stirring rate in the mixing chamber was 300 rpm and the average residence time of the CO_2-water mixture within the 100 mL chamber was $\sim$30 min to assure full dissolution. The CO_2-charged water from the 'mixing chamber' was pumped through the column filled with basaltic glass powder (see Section 2.2.2). This starting solution could also be sampled when closing off the valve between the mixing chamber and the column reactor, thereby bypassing the reactor. This column measured 234 cm in length, 5.0 cm in inner diameter, and held a total volume of 4.78 L.

Initial conditions were set to be similar to that of the CarbFix pilot project (Sigfússon et al., 2015; Matter et al., 2016; Snæbjörnsdóttir et al., 2017). As groundwater temperatures at the field site ranged from 20–50 °C, the experiment was set to 50 ± 0.5 °C using heating tape. The starting *in situ* pH of the flowing fluid in the filled column before CO_2 injection was 9.8, which was analogous to the area's groundwater pre-injection where the pH ranged from 8.9–9.8 (Alfredsson et al., 2013) as a result of DI water-rock interaction. The experiment CO_2(l) and water pump flow rates were fixed to 0.004 and 3.5 mL/min, respectively, giving an average fluid residence time of 12 hours in the column. Based on these rates, the dissolved inorganic carbon (DIC) concentration and pH of the CO_2-charged inlet fluid were ∼20 mM (mmol/kg water) and ∼4.0, respectively. For comparison, the DIC and pH in the CarbFix injection well were 823 mM and 3.85, respectively (Sigfússon et al., 2015). The lower pCO_2 (0.60 bar) in the laboratory experiment would limit the formation of zeolites and clays, but still promote carbonate formation as the expected pH was computed to be within the "sweet spot" of 5.2 to 6.5 (Snæbjörnsdóttir et al., 2018). Stagnation of the CO_2-charged fluids within the HPCFR occurred several times in the latter half of the experiment due to refilling of CO_2 in the syringe pump, the HPLC pump stopping, or the sampling of compartments along the column (of which a detailed description can be found in Galeczka et al., 2013).

2.2.2 Material

Stapafell basaltic glass was used as the filling material for the column, which originated from the Stapafell Mountain located in SW Iceland. This material has been widely used and characterized in previous experiments on glass dissolution kinetics (Galeczka et al., 2014; Gysi et al., 2012a; 2012b; Gudbrandsson et al., 2011; Gíslason and Oelkers, 2003; Oelkers and Gíslason, 2001; Stockmann et al., 2011; Wolff-Boenisch et al., 2011). Its major element chemical composition, normalized to one Si atom, was $Si_{1.000}Ti_{0.024}Al_{0.358}Fe_{0.188}Mg_{0.281}Ca_{0.264}Na_{0.079}K_{0.008}O_{3.370}$ (Oelkers and Gíslason, 2001). The material preparation procedure can be found in Appendix A.

The BET specific surface area (A_{BET}) before the experiment was 1240 cm^2/g, as measured by six-point N_2 adsorption using a Quantachrome Gas Sorption system, and the specific geometric surface area (A_{geo}) calculated was 286 cm^2/g, assuming the glass powder to be composed of identical cubes and based on the particle density and equations reported by Wolff-Boenisch et al. (2006). The total BET surface area in the column amounted thus to 8,358,000 cm^2 and the corresponding geometric surface area was 1,927,000 cm^2, yielding a geometric surface area to solution volume ratio of 760 cm^{-1}. The difference in BET surface area compared to previous experiments using Stapafell basaltic glass can most likely be attributed to different particle size distributions and surface roughness (Wolff-Boenisch et al., 2016). It is most similar to the Stapafell glass of Stockmann et al. (2011) and Wolff-Boenisch et al. (2011), which has a A_{BET} of 5880 cm^2/g.

2.2.3 Analysis

To chemically characterize the H_2O-CO_2 system, pH was measured in-line at the outlet of the column (Fig. 2.1) using high pressure temperature stainless steel pH electrodes (Corr instruments, Texas) with a precision of ±0.1 pH unit. The pH electrodes were calibrated at the start, during, and end of the experiment. DIC was recalculated using the measured *in situ* pH and concentrations of the major elements excluding carbon, assuming charge balance, or from the alkalinity, which started to be measured after 20 days of experiment duration. The geochemical modelling software, PHREEQC (Parkhurst and Appelo, 1999), was used for these calculations, further described in Section 2.2.4.

Fluids were sampled from the outlet of the column (Fig. 2.1) for analysis of their major elemental composition by inductively-coupled plasma optical emission spectrometry (ICP-OES) and ion chromatography. After the completion of the experiment, the solid material was analyzed by scanning electron microscopy (SEM), X-ray diffraction (XRD), and X-ray photo electron spectroscopy (XPS). A detailed description of the fluid sample analysis along with the procedures for preparation and analysis of the solid material is located in Appendix A.

Many techniques exist for characterizing solids and the changes to them that occur during water-mineral interaction. Some, such as computed tomography, are able to probe large volumes, but suffer from poor spatial resolution; others, such as transmission electron microscopy of thin foils cut with a focused ion beam, have outstanding spatial resolution, but probes only extremely small volumes of sample. As a compromise between investigated volume and spatial resolution, the suite of techniques employed probes relatively large portions of samples and provides information on structure within larger volumes of samples. However, XRD is unlikely to detect changes affecting only small volumes of material at the grain surface. XPS is highly surface sensitive, yielding information on the composition of the top 10 nm of materials. This technique is particularly useful for detection of thin surface coatings, and an area $\sim$300 µm by $\sim$700 µm of the packed sample is irradiated during analysis. Finally, through repeated EDXS mapping and SEM imaging at variable magnification, the composition at an area of approximately 250 µm by 250 µm was probed. The spatial resolution of EDXS at our operating conditions means that significant compositional variation can be detected only with $\sim$1 µm resolution or so in all three dimensions. Thus, thin surface coatings will be unseen, but even fairly rare occurrences of micrometre sized particles or aggregates with highly contrasting chemical composition should be identifiable (e.g. carbonate minerals on top of the basaltic glass).

2.2.4 Geochemical calculations & modelling

Aqueous speciation, mineral saturation states, and reactive transport modelling were performed using the PHREEQC 3.4.0 geochemical code (Parkhurst and Appelo, 2013) and the *carbfix.dat* database (Voigt et al., 2018), which is based on the *core10.dat* database (Neveu et al., 2017); relevant mineral phases and further additions are listed in Table A.1.

For aqueous speciation and mineral saturation index (SI, defined as the base-10 logarithm of the saturation state, which is the ratio of the ion activity product to the equilibrium constant of the precipitation reaction) calculations, chemical compositions of the sampled fluid together with pH measured in-line (corrected to the experimental temperature) at the outlet were used. As described earlier, PHREEQC calculations based on pH, measured concentrations, and charge balance constraints were performed to estimate DIC concentrations used for further calculations, which were then verified with corresponding alkalinity measurements and no charge balance constraint. Aqueous speciation and saturation state calculations used measured Fe^{II} and Fe^{III} concentrations as redox indicators for the CO_2-charged water experiments.

The fluid chemistry in the reactor was modelled using a one-dimensional reactive transport simulation with seven cells, similar to that of Galeczka et al. (2014). The advective flow of the fluid was simulated in PHREEQC by moving the reactive fluids to the subsequent cell after each time step, which corresponded to its residence time within each cell. The fluid phase was allowed to react with basaltic glass, whose dissolution rate was taken from Gíslason and Oelkers (2003) and assumed to dissolve stoichiometrically. The basaltic glass surface area used in the model was set to approximately one-tenth of the A_{geo}, like that of simulations run by Aradóttir et al. (2012), Beckingham et al. (2016, 2017), Galeczka et al. (2014), and Gysi and Stefánsson (2012a). The Fe redox state of the fluid was effectively controlled by the amounts of Fe^{II} and Fe^{III} released from the basaltic glass and then taken up by secondary minerals. Several mineral phases were allowed to precipitate by constraining them to local equilibrium with the fluid (i.e. assuming fast precipitation kinetics relative to fluid residence times) based on experimental results and common secondary minerals found in natural basaltic systems (Alfredsson et al., 2013; Rogers et al., 2006).

2.3 Results

In the beginning of the experiment, high pH pore water (9.8) resulted from a continuous flow of DI water deprived of CO_2 through the column of basaltic glass grains, followed by a CO_2-water injection at a pCO_2 of 0.60 bar, or 20 mM, for 108 days, of which 66 days (132 pore volumes) are discussed here. Stagnation of the CO_2-charged fluids within the HPCFR occurred several times in the latter half of the experiment due to refilling of CO_2 in the syringe pump, the HPLC pump stopping, or the sampling of compartments along the column (of which a detailed description can be found in Galeczka et al., 2013). The resulting disturbances to the pH and DIC thus altered the steady state behavior of several mineral saturation states.

Each sample taken from the outlet represents water-rock interaction during the 12-hour passage through the column reactor. This experimental setup simulates sampling of the injected fluid from a single monitoring well downstream from an injection well, where each water sample represents a single passage between the injection and

monitoring well. See Table A.2 for the chemical compositions of the fluid samples.

2.3.1 Outlet fluid chemistry

Measured outlet pH, major element concentrations, calculated DIC, and mineral saturation states during the experimental runtime of 66 days are shown in Figs. 2.2 and 2.3, with a more detailed evolution of the outlet fluid compositions during the first 13 days shown in Fig. A-1 (Appendix A). Within 18 hours of the initial CO_2 injection and 1.5 PV of CO_2-fluid-rock interaction, the pH decreased from 10 (resulting from the initial DI water-basalt interaction) to 6–6.5 while DIC increased and briefly reached the 20 mM inlet concentration (Fig. A.1). This simulates the mixing of injected fluid with high pH groundwater during field injections. All major elements increased in concentration within 1–2 PV, with the exception of Al and K. All the Ca-Mg-Fe-carbonates became supersaturated with respect to the pore fluids around pH 8.8 with the first arrival of the CO_2-charged water after 12 hours of interactions.

The pH was mostly stable at ∼5.6 from days 4 to 52 while DIC fluctuated. Concentrations of major elements stabilized after four days, while Ca and Mg stabilized after six days. Siderite was at or slightly above saturation and the other carbonates undersaturated until day 53. The majority of total dissolved Fe was also observed as Fe^{II} rather than Fe^{III} (Fig. A.2).

After approximately 56 days, the syringe pump failed for an estimated 100 hours and no new CO_2 entered the 'mixing chamber' and thereby only DI water was pumped through the column from the HPLC (Fig. 2.1). This mimics the geochemical consequences of alternating water and CO_2-charged water injections during field-scale carbon capture and storage. It took about 10 PV (5 days) for the pH to peak at 8.7. During this time, carbonate mineral saturation indices and major element concentrations changed with a slight delay, with a significant undersaturation with respect to siderite and decreased concentrations of aqueous Si, Ca, and Mg concentrations.

Once the pump was running again (day 61), it took 6 PV (3 days) for the outlet pH to restabilize at ∼5.7 and the DIC to increase. In response, outlet concentrations of all elements, besides K, Al, and Fe, also increased and returned to previous levels once the pH re-stabilized.

Changes in mineral saturation indices for zeolites (Fig. 2.3) reflected the changes in dissolved constituents and the composition of the zeolites, for instance the fluid was reaching saturation with respect to the Na-zeolite (analcime) only when the pH was above 7. The clay minerals, Fe-saponite and Mg-saponite ($Fe/Mg_{3.175}Al_{0.35}Si_{3.65}O_{10}(OH)_2$), very common alteration minerals in basaltic terrain at low temperature < 100°C (Alfredsson et al., 2013; Schiffman and Fridleifsson, 1991), also reached supersaturation only when pH was higher than 7, with Fe-saponite mostly at saturation. The fluids were supersaturated with respect to most of the Fe-oxides, Al-oxides, and silica phases for the duration of the experiment. All minerals reflected major changes in pH and DIC concentrations.

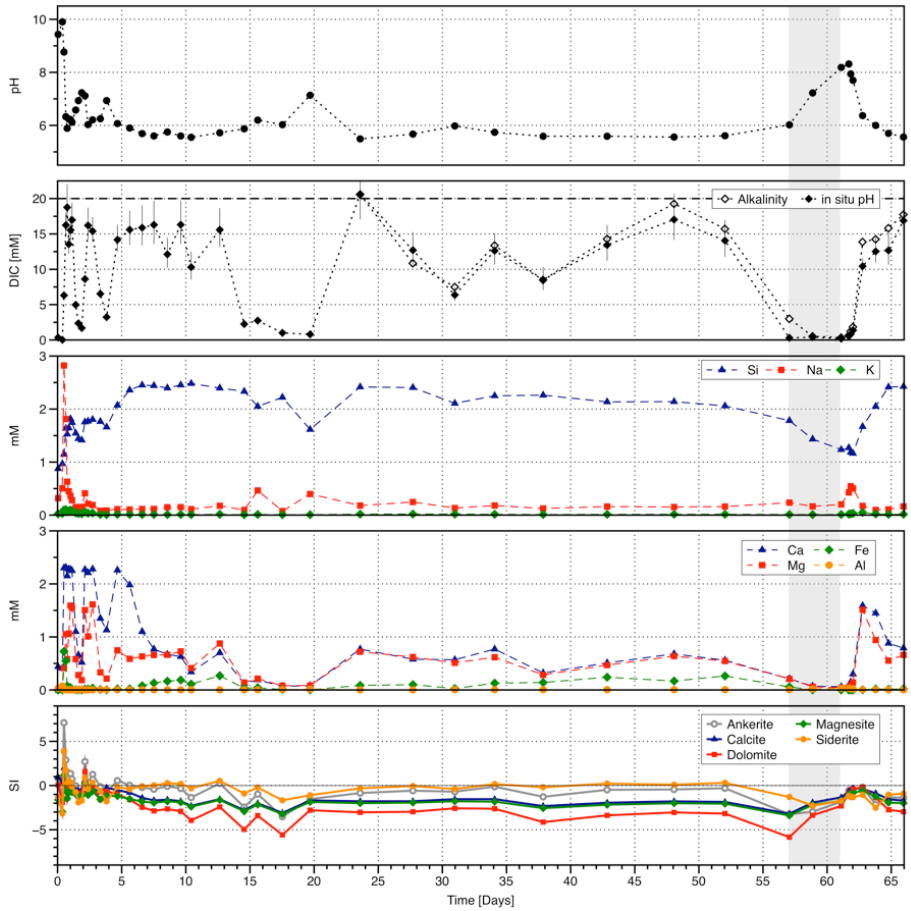

Figure 2.2. Outlet pH, DIC, major element concentrations, and mineral saturation indices (SI) of carbonates during the 66 days of experimental duration. The light gray shaded area represents the approximate 100 hours when the syringe pump failed and no new CO_2 entered into the 'mixing chamber'. Error bars for DIC concentrations were calculated from only varying pH ± 0.10. The dotted line represents the input DIC.

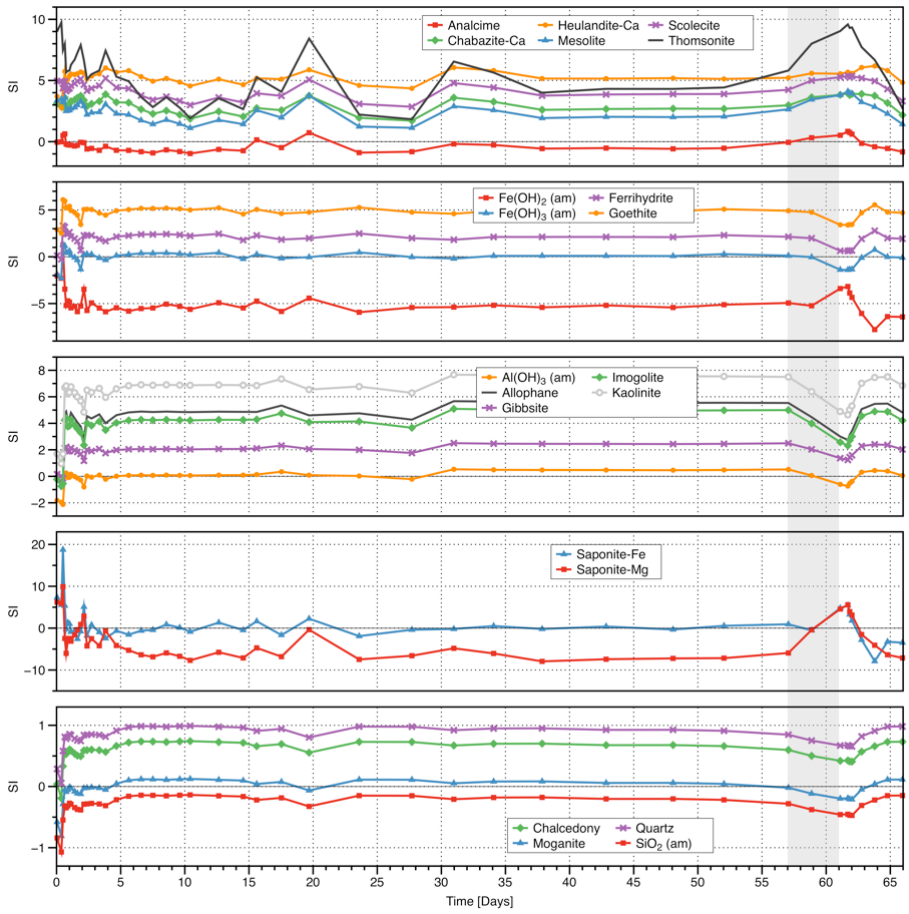

Figure 2.3. Mineral saturation states of zeolites, Fe-oxides, Al-oxides, clay minerals, and silica phases during the experiment after 66 days. The light gray shaded area represents the approximate 100 hours when the syringe pump failed and no new CO_2 entered the 'mixing chamber'.

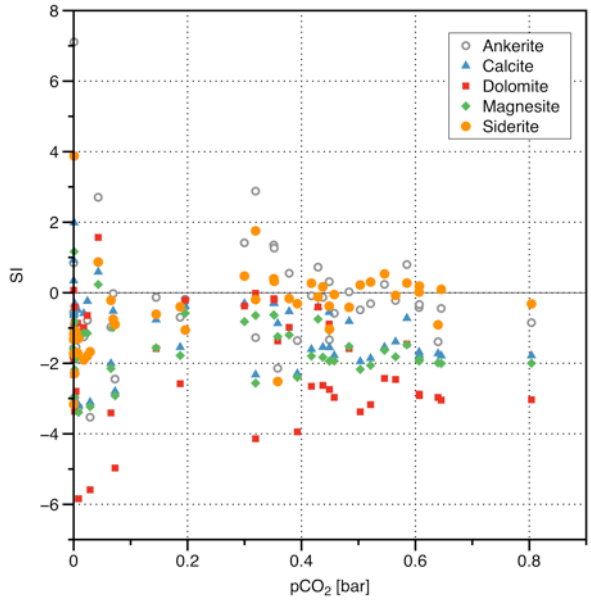

Figure 2.4. Mineral saturation indices of carbonates against pCO_2 during the experiment.

The relationship between pCO_2 and the saturation states of carbonate minerals in Fig. 2.4 depicts the supersaturation of siderite and ankerite when pCO_2 values were between 0.3 and 0.7 bar with the highest saturation levels between 0.3 and 0.4 bar. Note that the supersaturation of all carbonate minerals at pCO_2 of < 0.05 bar occurred during the initial arrival of CO_2-charged fluids.

Sodium was chosen as a reference element to evaluate element mobility because it was considered the closest representation of a mobile element under the present experimental conditions, though it should be noted that some Na might have been incorporated into secondary minerals. The results are shown in Fig. 2.5 relative to the stoichiometry of the Stapafell basaltic glass. Aluminum and Fe indicate either non-stoichiometric dissolution and/or precipitation into secondary minerals. The latter was expected considering the saturation or supersaturation of various Al minerals, clay minerals, zeolites, and siderite (Figs. 2.2 and 2.3). Potassium showed the opposite behavior by dissolving stoichiometrically relative to Na, independent of any changes in DIC. There was both stoichiometric and non-stoichiometric dissolution of the divalent cations, Ca and Mg, as well as Si, reflecting experimental changes in pH leading to the formation of relevant secondary minerals. The greatest element mobility occurred during the initial arrival of the CO_2-charged waters within the column after 1 PV.

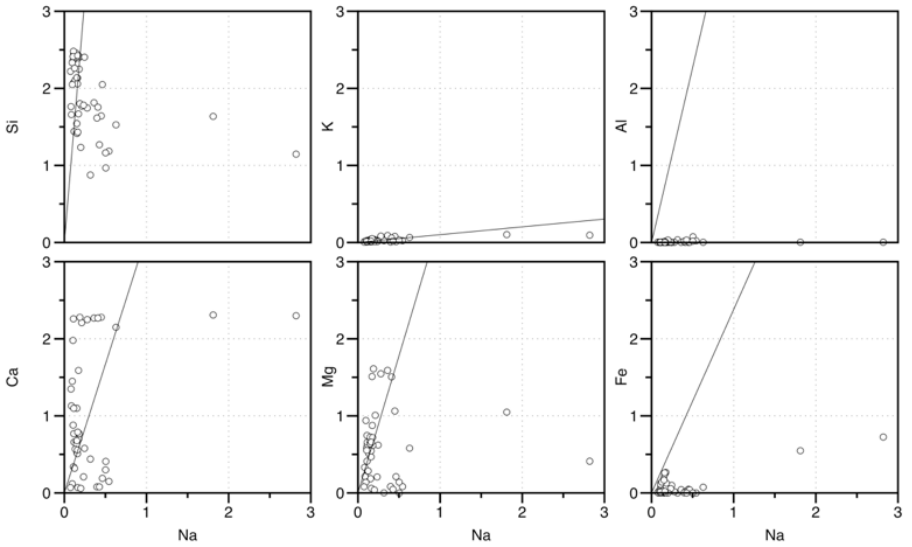

Figure 2.5. Element mobility relative to Na. Values plotted on the line represent stoichiometric dissolution of basaltic glass whereas values to the right indicate secondary mineral formation.

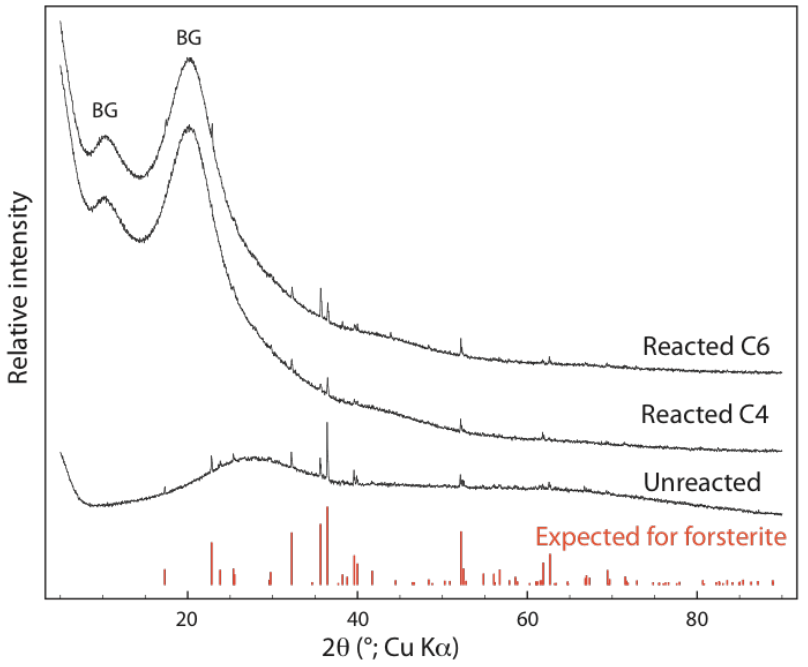

Figure 2.6. XRD of the unreacted Stapafell basaltic glass and samples from compartments 4 (C4) and 6 (C6) after 108 days of reaction. Red bars indicate peaks expected for forsterite based on Birle et al. (1968).

2.3.2 Solid chemistry

XRD of the unreacted material shows a broad background centered at about 30° 2Θ as well as smaller peaks for forsterite (Fig. 2.6). Apart from two broad peaks from the dome protecting the sample from oxidation, only the peaks from forsterite were discernible for the reacted material. Thus, crystalline secondary phases were not present in amounts allowing detection with XRD (> 0.5% or so).

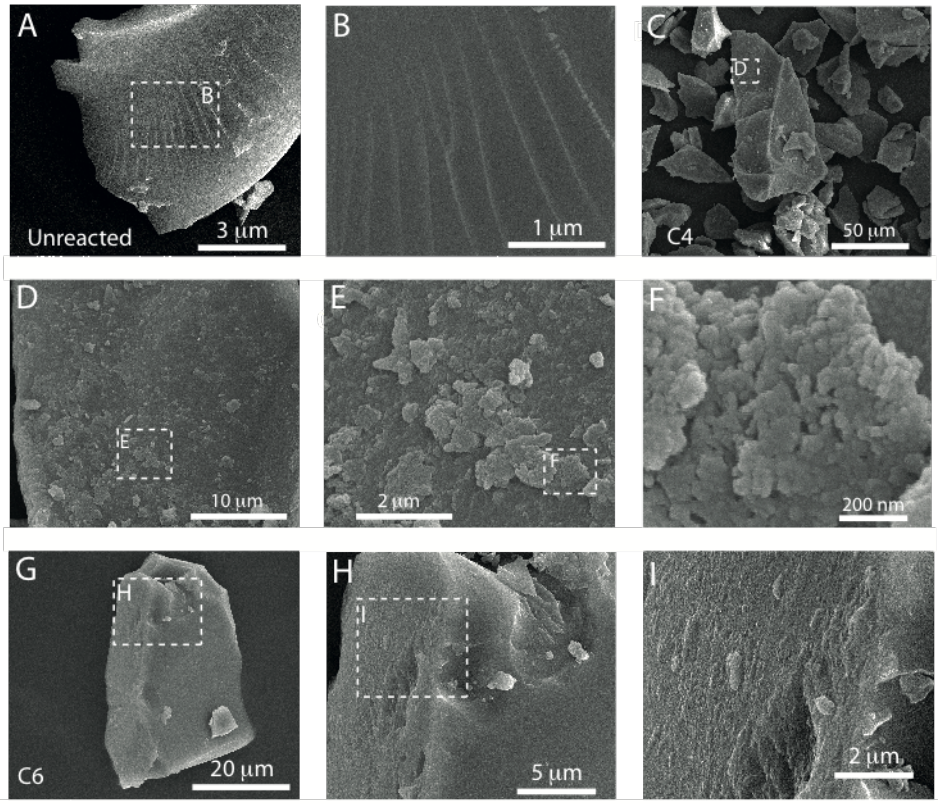

Figure 2.7. SEM of unreacted Stapafell basaltic glass (A and B), of sample from compartments 4 (C4; C-F) and 6 (C6; G-I)) after 108 days of reaction.

SEM of the initial material often shows < 50 nm protrusions on the glass surface. At times, these adorn conchoidal fractures, indicating that they formed after the crushing of the material (Fig. 2.7A). Presumably they have formed as a result of reactions occurring during the washing of the material prior to use and/or from reaction mediated by the thin water layer covering ionic compounds in air. After reaction with CO_2-charged water, the surfaces appeared more altered, in particular for material from compartment 4 (C4), where the original glass surface often cannot be discerned (Fig. 2.7D to 2.7F; more images in Appendix A). Here, the surface region was composed dominantly of ∼40 nm spherical or semi-spherical particles, whose exact morphology cannot be determined

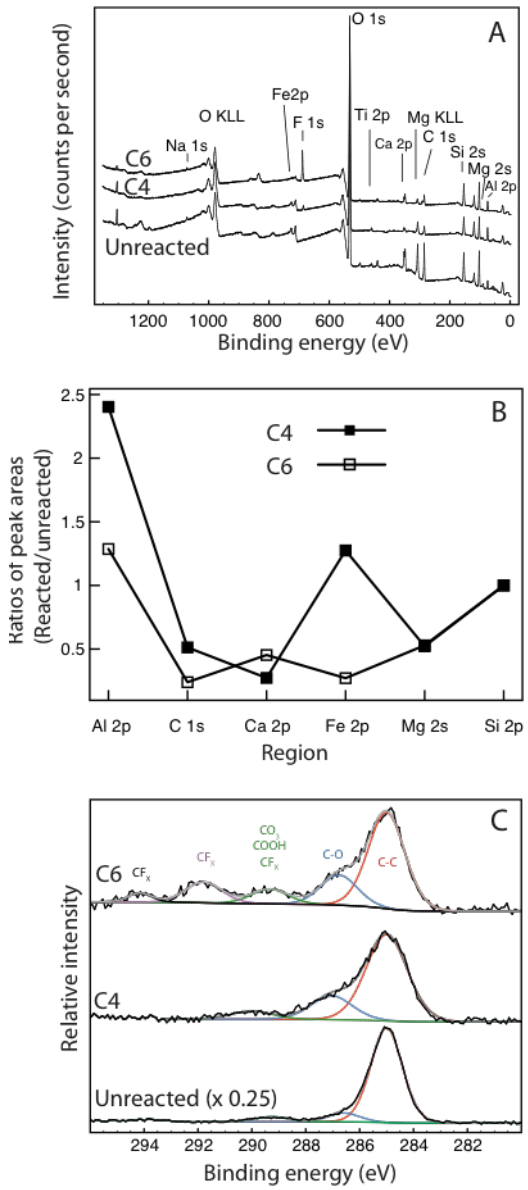

Figure 2.8. XPS of the unreacted and reacted Stapafell basaltic glass from compartments 4 and 6 (C4 and C6): (A) survey scan, (B) ratios between the integrated numbers of counts of unreacted and reacted material normalised to those for Si, and (C) detail scan for C1s.

because of the spatial resolution and the presence of a ∼10 nm gold coating. Often such particles appeared organized in flakes (Fig. 2.7E, 2.7F). In addition, platy particles with variable widths, sometimes reaching > 1 um, were common in the images. Overall, the topographical relief had increased significantly because of spatially uneven dissolution and/or secondary phase formation. During the imaging, we conducted ∼20 EDXS spot analysis of particles, whose morphology might resemble siderite, chukanovite, or amorphous iron carbonate, and made ∼20 maps to probe larger areas for abnormal concentrations of Ca, Mg, Fe, C, and Si. Neither of the datasets showed signs that could be attributable to carbonates. Thus, we conclude that carbonate minerals did not occur as single or aggregated particles with dimensions large enough for EDXS detection (∼1 um with the settings used).

XPS survey scan of the unreacted materials contains peaks for O, Si, Mg, Ca, Fe, Ti, Na, and C (Fig. 2.8A). After reaction, peak intensity decreased significantly for Na, Ca, and Mg, and to lesser degree for Si and Mg. In contrast, peaks for Fe were similar in intensity and the peak for Al was more pronounced. For the sample from compartment 6 (C6), the intensities of the Fe peaks were significantly lowered. Figure 2.8B shows the integrated peak area quantified from detail scans as ratios between the values determined for the reacted material divided by those for the unreacted material and normalized to the counts for Si. For Al, the ratio was well above 1, indicating its surface enrichment compared to Si. In contrast, Ca and Mg showed low ratios, signifying significant depletion. For Fe, ratios were similar for the unreacted material and the sample from C4, whereas the sample from C6 revealed significant depletion in Fe compared to Si. Inspection of the detailed scan for the Fe 2p region (Fig. A.3) shows that little difference exists between the spectra for the unreacted material and the sample from C4, indicating that little change occurred in the Fe surface concentration and its valency as a result of reaction. For C6, the low Fe concentration complicated determination of Fe valency.

During reaction, the overall peak intensity decreased significantly for carbon. The detail scan for C1s had been fitted with three or more components (Fig. 2.8C). The component at low binding energy was assumed to represent adventitious carbon. This peak had been assigned a value of 285 eV in the calibration of all spectra. The component at the slightly higher binding energy most likely represented C-O bonds, whereas the small component at binding energy of ∼290 eV may be attributable to carboxylate groups or carbonates. Thus, XPS provides no evidence for carbonate phases existing commonly as surface coatings or more evenly distributed, small particles, which would have gone unnoticed in EDXS. Based on this data, we conclude that carbonate solids occurred only very rarely, if at all, in the sampled material after 108 days of reaction. However, the data indicate that Fe was not leached to the same degree as other divalent cations from the central part of the column.

2.3.3 Reactive transport modelling

In the 1D reactive transport model to simulate the experiment, CO_2 addition to the water flowing through the basaltic glass system was active for 57 days or 114 PV, stopped

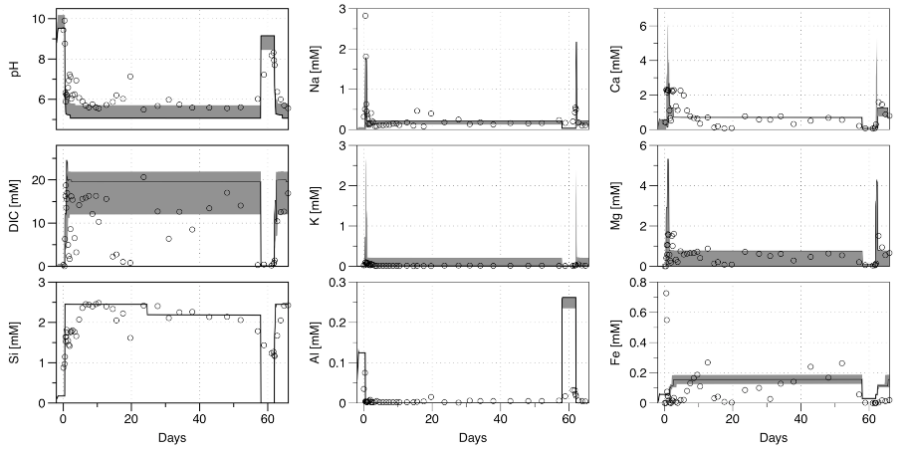

Figure 2.9. Comparison of reactive transport modelling results (black line) with measured experimental outlet fluid concentrations (open circles). The gray shaded area represents the effect of a variability of 15–25 mM in input DIC concentrations.

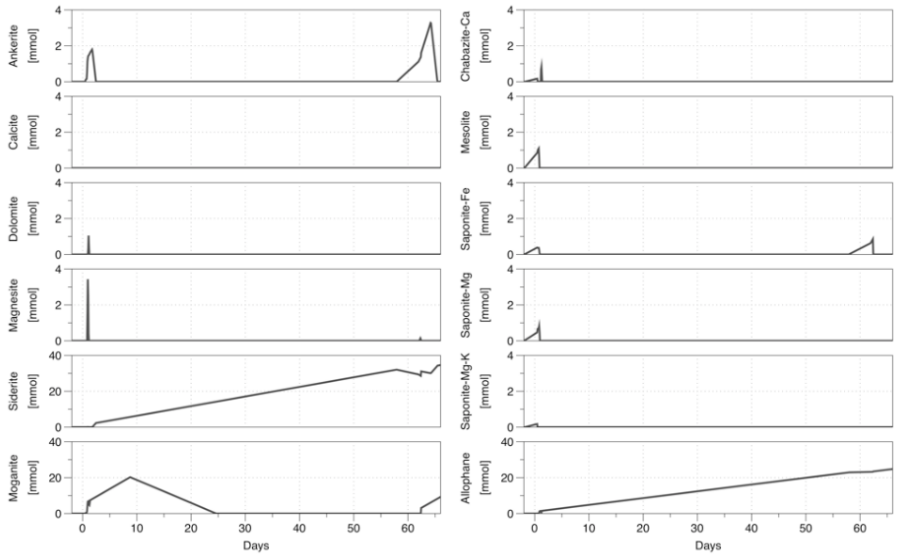

Figure 2.10. Cumulative amount (millimoles) of selected minerals allowed to precipitate in the reactive transport model. Note the variable scale on the y-axis.

for four days (8 PV), and then active again for an additional five days (10 PV), making a total of 66 days. Many phases in the fluid phase were supersaturated during the experiment (Fig. 2.4), therefore several were allowed to precipitate at local equilibrium in the model: moganite, allophane, Mg- and Fe-saponites, Ca-chabazite, and mesolite in addition to the carbonate minerals – ankerite, calcite, dolomite, magnesite, and siderite. It was found that reducing the geometric surface area of the basaltic glass in the model to approximately one tenth of that estimated from the mass of basalt used in the experiment resulted in a good agreement of modelled major elemental concentrations in the outlet fluids in comparison with the corresponding experimental data. Furthermore, moganite's saturation index was adjusted to 0.1 to better reflect the experimental results shown in Fig. 2.3. The results of the simulations were compared to the experimental results (Fig. 2.2) in Fig. 2.9.

Predicted pH, DIC and major element concentrations are generally comparable to that of the experimental results (Fig. 2.9): Modelled results were within or close to the range of measured values before the addition of CO_2. When 20 mM of CO_2 was added to the simulation, results showed peaks in Ca, Mg, and Na in addition to the increased concentrations of DIC, Si, and Fe and decreased pH and Al values, similar to the experimental data. During the simulated stop of CO_2 addition, the modelled results reflected the changes in expected increased or decreased concentrations, with the exception of K, Na, and a small peak in Fe. By varying the amount of CO_2 added to the simulation from 15 to 25 mM, the changes to the modelled major element chemistry were minimal with the expected exception of DIC, which shows a variation similar to that in the experiments, suggesting that injected CO_2 may have varied within these limits.

According to the reactive transport model, the initial arrival of CO_2 (1–2 PV) would enable ankerite, dolomite, and magnesite precipitation, though this was soon taken over by siderite and rapidly forming Al/Si phases (moganite and allophane in this model, Fig. 2.10). After 57 days, around 5750 mmols of CO_2 had been injected into the system, while only 32 mmols of siderite was predicted to have been precipitated (less than 1% of the injected CO_2). When no new CO_2 was added after this, allophane and siderite began to slowly dissolve and ankerite and Fe-saponite started precipitating. However, as soon as CO_2 re-entered the system, ankerite rapidly precipitated and re-dissolved, magnesite briefly formed while allophane, moganite, and siderite all started to precipitate again. With this second "plume" of CO_2-charged fluids, only ankerite and siderite were able to precipitate, ankerite for at least 1 PV with siderite continuing to form as before. Due to its relatively large molar volume, the allophane predicted to form has by far the largest cumulative volume, as shown in Fig. A.4, followed by siderite and moganite.

2.4 Discussion

Both the immediate change in pH and subsequent supersaturation of carbonates were previously noted during the first arrival of CO_2-charged waters at the CarbFix field injec-

tion site (Snæbjörnsdóttir et al., 2017) and preceding HPCFR experiments (Galeczka et al., 2014). These cases did have significantly higher injected DIC concentrations of 823 and 300 mM, respectively, compared to this experiment. Siderite was the first carbonate mineral to become saturated at the lowest pH during the first phase of the CarbFix field injection of pure CO_2, and the monitoring solutions remained supersaturated with respect to siderite and ankerite weeks after the injection was stopped. Furthermore, calcite was oversaturated before injection and was a common alteration mineral in the subsurface rocks, but became undersaturated after days of injection (Alfredsson et al., 2013; Snæbjörnsdóttir et al., 2017). Calcite and dolomite reached supersaturation several days after injection and remained so to the end of the monitoring close to 600 days after the initial CarbFix injection (Snæbjörnsdóttir et al., 2017). Furthermore, Mg-saponite, a smectite, was oversaturated in all samples, except for the samples taken during and shortly after the two CarbFix injections where pH was < 8 (Snæbjörnsdóttir et al., 2017). Smectite is one of the most abundant secondary minerals in basaltic rocks at < 100 °C and had been identified in all wells drilled at the CarbFix site in Hellisheiði, SW-Iceland (e.g. Schiffman and Fridleifsson 1991).

This sequence of carbonate and Mg-saponite saturation stages was explored in the present study by lowering the injected DIC concentration to 20 mM, forty-fold more dilute than the injected DIC concentration in the pure CO_2 injection phase of the CarbFix pilot study, considered the "sweet spot" for carbonation (Snæbjörnsdóttir et al., 2018). This was necessary because of the short reaction time (12 hours) within the HPCFR. The sequence of carbonation varied throughout the experimental run, as shown in Figs. 2.2 and A.1. The rapid rise in Ca and Mg concentrations at the start of the experiment suggests that high pH mineral phases, like calcite, Mg-saponite, and Ca-zeolites, had previously formed before the addition of CO_2 and were immediately dissolving. This is supported by the supersaturation of these minerals during the first day (Figs. 2.2 to 2.3). In addition, the quick dissolution of calcite during the first four days would clarify Ca's deviation from stoichiometric dissolution observed in Fig. 2.5. At the lowest pH (30–45 days), siderite was at saturation followed by, in sequence of lowest to highest undersaturation, ankerite, calcite, magnesite and dolomite. When CO_2 injection stopped after 57 days, the sequence changed, not only dictated by pH and pCO_2, but by the relative activity of the Fe, Mg, and Ca dissolved species (Fig. 2.2). Once pH stabilized below 6, Mg-saponite was undersaturated throughout the CO_2 injection (Fig. 2.3), and after the CO_2 injection was terminated, Mg-saponite became supersaturated. This mimics the first phase of the CarbFix field injection, as described above.

Despite the thermodynamic stability of siderite for at least 24 days, based on mass balance calculations approximately 45–70 cm^3 of siderite (2–3% of the total material) could have precipitated, but in this case 25–50 cm^3 of it would have re-dissolved before the pump failure as siderite never went much above saturation. Its complete dissolution would have been ensured when the syringe pump failed and afterwards. This is in agreement with the lack of Fe-carbonates among the detected alteration products on the surfaces of the basaltic grains; energy dispersive X-ray spectroscopy was unable to determine compositions of any potential alteration product from the thin alteration layer. Conceivably if the saturation indices of siderite and ankerite had been higher (>

1), homogenous nucleation could likely occur as opposed to surface-controlled growth, as observed from the calcite precipitation experiments conducted by Stockmann et al. (2014). This, in turn, could provide the seeds, or nuclei, for further surface-controlled growth of carbonates at lower saturation levels provided that the pH is not too low, in which case carbonates would re-dissolve. However, this study demonstrates that already at pH 5.7 most of the carbonates become undersaturated. Yet, if pH is > 7, then Fe- and Mg-saponites become oversaturated with many zeolites always saturated, especially when pH is higher than 6. Consequently, this reveals an even narrower "sweet spot" for efficient carbonation than the suggested 5.2 to 6.5 (Snæbjörnsdóttir et al., 2018).

Reactive transport modelling of the experimental conditions provided insight to the possible mineral groups competing for the divalent cations. Fe-rich saponite, rather than iron oxides, was competing with siderite for Fe^{II}, which was similarly observed for Mg between Mg-rich carbonates and saponite (Fig. 2.10). On the other hand, Ca-rich zeolites like chabazite would have been competing for Ca with calcite instead of clays. However, there was little competition between the carbonates and the clays/zeolites when CO_2 injection was occurring (Fig. 2.10) due to the fluids being undersaturated with Ca-carbonates. Most likely the formation of Al/Si-containing solids like allophane and moganite prevented the precipitation of any zeolites due to the limited availability of Si and Al and their relative thermodynamic stabilities at low pH. Notably though, only a few carbonates besides siderite were predicted to briefly precipitate with each arrival of new CO_2 to the water-basaltic glass system, while siderite was able to form during the entire CO_2 injection time.

While inadvertent, important observations were made when the syringe pump for CO_2 failed, especially as discontinuous injections will always occur at the industrial-scale (Gíslason et al., 2018). The discontinuous injection was characterized by a rapid increase in pH and decrease in DIC (similar to the trends seen during CarbFix after the injection of pure CO_2 in March 2012; Matter et al., 2016), which in turn suggests that a brief failure of the pump transpired around days 15 to 20 (Fig. 2.2). In addition, the pump failure in the experiment led to prompt changes in mineral saturation states, particularly the supersaturation with respect to clays/zeolites like Mg/Fe-saponites, analcime, and thomsonite as well as the decrease in saturation with respect to the carbonates. This was also observed during CarbFix during the two month period between the pure CO_2 and the gas mixture injections, where only water was injected; a perfect example to observe the natural state of the fluids reacting with the basaltic rocks (Snæbjörnsdóttir et al., 2017). Based on these field observations, in the event of a gas injection stoppage in the field, for example due to routine maintenance, it is important to note that the injected water would still have some alkalinity. This lack of alkalinity in the DI water injected in the experiment had led to immediate undersaturation of all carbonates, which would not be the case in the field. However, during long periods of no gas injection, the stability fields of saponites and zeolites would change to favor their precipitation, thereby consuming valuable pore space for carbonates. Further research on a site-by-site basis will be necessary to anticipate any potential complications for this scenario in addition to a complete shutoff of gas and water injection.

These experimental results, as well as results from the subsequent reactive transport model, demonstrate how sensitive the fluid chemistry and mineralization are to any abrupt changes in pCO_2 input. The sensitivity of calculated DIC concentrations to uncertainties in measurements also highlights the challenge of monitoring the injected fluid chemistry during experiments when changes in DIC between the inlet and outlet are small. One suggestion to further improve the precision is to include another set of pH probes in-line, between the mixing chamber and the column, thereby allowing to calculate injected DIC (Rendel et al., 2018). However, it is important to note that inferred DIC concentrations are sensitive to uncertainties in such pH measurements.

2.5 Conclusions

Water dissolved CO_2 was injected into a 234 cm long titanium HPCFR at 50 °C and 80 bar pressure that was already filled with basaltic glass grains and DI-water. The experimental outlet fluids reached carbonate mineral saturation within 12 hours of fluid-rock interaction.

As the CO_2-charged water ($\sim$20 mM) entered the column and mixed with the high pH water (9–10), the outlet fluid with respect to Fe-, Mg-, and Ca-carbonates all became temporarily supersaturated along with clays and zeolites. Once the pH of the outflow water stabilized below 6, siderite ($FeCO_3$) was the only stable carbonate along with Fe-, Al-, and Si- oxides and hydroxides, Fe-saponite, and Ca-zeolites. When CO_2 injection was terminated while continuing to inject pure water, pH rose rapidly in the outflow and all carbonates became temporarily undersaturated, while zeolites became more saturated and Mg-saponite more supersaturated along with Fe-saponite. Comparable observations were also reflected in the reactive transport model.

The sequence of carbonate and clay saturation in this experimental study was dependent on pCO_2 and pH. The Fe-rich carbonates were stable at the highest pCO_2 and the Ca-rich carbonates at the lowest pCO_2. This is in agreement with observations from low temperature natural analogues in basaltic terrains (Rogers et al., 2006), the pure CO_2 phase of the CarbFix field injection site (Snæbjörnsdóttir et al., 2017), and our study's reactive transport model of the experiment. Similarly to CarbFix, the high molar volume Mg-saponite was undersaturated throughout the CO_2 laboratory injection once pH stabilized below 6. Fe- and Mg-saponites became supersaturated when the CO_2 injection was terminated and pH rose to about 8, while again confirmed by the reactive transport model though only Fe-saponite briefly formed when CO_2 injection began the second time.

Thus, during CO_2 injection into basaltic rocks one should aim at sufficiently low pH to start carbonate mineralization at the lowest possible pH to maximize the use of divalent cations for carbonization and create porosity near the injection well. Siderite saturation would therefore be at the center of the plume (i.e. injection of CO_2-charged fluid), followed by the sequence of Fe-, Mg-, and finally Ca-carbonates in the most

dilute edges of the "plume" at the lowest pCO_2 and highest pH. This low pH carbonation has been referred to as the "sweet spot" of efficient carbonation (Snæbjörnsdóttir et al., 2018).

Discontinuous injection will always occur during industrial-scale carbon capture and storage due to equipment failure and/or overall service breaks. This experiment shows rapid alteration in the mineral saturation stages when CO_2 injection is terminated. Saturation states of large molar volume clays and zeolites increases along with one of the Ca-carbonates (calcite), while Fe-carbonates' saturation state decreases. Therefore for efficient use of the pore space in the subsurface during carbon storage, service breaks should be kept at a minimum during injection.

Acknowledgements

This publication has been produced with support from the European Commission through the projects CarbFix (EC Project 283148), CO2-React (EC Project 317235), and S4CE (EC Project 764810). Special thanks to Giulia Alessandrini for her indispensable assistance in running the experiment, Sydney Gunnarson for material preparation, and Þorsteinn Jónsson for preparing, setting up, and taking apart the column. We would also like to acknowledge Rebecca Neely and Tobias Linke for their help in the laboratory in addition to Eric Oelkers, Peter Rendel, and the CarbFix group for their support.

2.6 References

Adeoye, J.T., Menefee, A.H., Xiong, W., Wells, R.K., Skemer, P., Giammar, D.E. and Ellis, B.R. (2017) Effect of transport limitations and fluid properties on reaction products in fractures of unaltered and serpentinized basalt exposed to high pCO_2 fluids. *International Journal of Greenhouse Gas Control* 63, 310–320.

Alfredsson, H.A., Oelkers, E.H., Harðarsson, B.S., Franzson, H., Gunnlaugsson, E. and Gíslason, S.R. (2013) The geology and water chemistry of the Hellisheidi, SW-Iceland carbon storage site. *International Journal of Greenhouse Gas Control* 12, 399–418.

Aradóttir, E.S.P., Sonnenthal, E.L., Björnsson, G. and Jónsson, H. (2012) Multidimensional reactive transport modeling of CO_2mineral sequestration in basalts at the Hellisheidi geothermal field, Iceland. *International Journal of Greenhouse Gas Control* 9, 24-40.

Beckingham, L.E., Mitnick, E.H., Steefel, C.I., Zhang, S., Voltolini, M., Swift, A.M., Yang, L., Cole, D.R., Sheets, J.M., Ajo-Franklin, J.B., DePaolo, D.J., Mito, S. and Xue, Z., 2016. Evaluation of mineral reactive surface area estimates for prediction of reactivity of a multi-mineral sediment. *Geochimica et Cosmochimica Acta* 188, 310–329.

Beckingham, L.E., Steefel, C.I., Swift, A.M., Voltolini, M., Yang, L., Anovitz, L.M., Sheets, J.M., Cole, D.R., Kneafsey, T.J., Mitnick, E.H., Zhang, S., Landrot, G.,

Ajo-Franklin, J.B., DePaolo, D.J., Mito, S. and Xue, Z. (2017) Evaluation of accessible mineral surface areas for improved prediction of mineral reaction rates in porous media. *Geochimica et Cosmochimica Acta* 205, 31–49.

Birle, J.D., Gibbs, G.V., Moore, P.B. and Smith, J.V. (1968) Crystal structures of natural olivines. *American Mineralogist* 53, 807–824.

Daval, D. (2018) Carbon dioxide sequestration through silicate degradation and carbon mineralisation: promises and uncertainties. *npj Materials Degradation* 2.

Galeczka, I., Wolff-Boenisch, D., Jonsson, T., Sigfússon, B., Stefánsson, A. and Gíslason, S.R. (2013) A novel high pressure column flow reactor for experimental studies of CO_2 mineral storage. *Applied Geochemistry* 30, 91–104.

Galeczka, I., Wolff-Boenisch, D., Oelkers, E.H. and Gíslason, S.R. (2014) An experimental study of basaltic glass–H_2O–CO_2 interaction at 22 and 50°C: Implications for subsurface storage of CO_2. *Geochimica et Cosmochimica Acta* 126, 123–145.

Gíslason, S.R. and Oelkers, E.H. (2003) Mechanism, rates, and consequences of basaltic glass dissolution: II. An experimental study of the dissolution rates of basaltic glass as a function of pH and temperature. *Geochimica et Cosmochimica Acta* 67, 3817–3832.

Gíslason, S.R., Wolff-Boenish, Sigurðardóttir, H., Aradóttir, E.S. and Oelkers, E.H. (2018) A brief history of CarbFix: Challenges and victories of the project‘s pilot phase. *Energy Procedia* 146, 103–114.

Gíslason, S.R., Wolff-Boenisch, D., Stefánsson, A., Oelkers, E.H., Gunnlaugsson, E., Sigurðardóttir, H., Sigfússon, B., Broecker, W.S., Matter, J.M. and Stute, M. (2010) Mineral sequestration of carbon dioxide in basalt: A pre-injection overview of the CarbFix project. *International Journal of Greenhouse Gas Control* 4, 537–545.

Gudbrandsson, S., Wolff-Boenisch, D., Gíslason, S.R. and Oelkers, E.H. (2011) An experimental study of crystalline basalt dissolution from $2 \leq$ pH ≤ 11 and temperatures from 5 to 75°C. *Geochimica et Cosmochimica Acta* 75, 5496–5509.

Gysi, A.P. (2017) Numerical simulations of CO_2 sequestration in basaltic rock formations: Challenges for optimizing mineral-fluid reactions. *Pure and Applied Chemistry* 89, 581–596.

Gysi, A.P. and Stefánsson, A. (2012a) Experiments and geochemical modeling of CO_2 sequestration during hydrothermal basalt alteration. *Chemical Geology* 306–307, 10–28.

Gysi, A.P. and Stefánsson, A. (2012b) Mineralogical aspects of CO_2 sequestration during hydrothermal basalt alteration — An experimental study at 75 to 250°C and elevated pCO_2. *Chemical Geology* 306–307, 146–159.

Hellevang, H., Haile, B.G. and Tetteh, A. (2017) Experimental study to better understand factors affecting the CO_2 mineral trapping potential of basalt. *Greenhouse Gases: Science and Technology* 7, 143–157.

Kanakiya, S., Adam, L., Esteban, L., Rowe, M.C. and Shane, P. (2017) Dissolution and secondary mineral precipitation in basalts due to reactions with carbonic acid. *Journal of Geophysical Research: Solid Earth* 122, 4312–4327.

Khalibad, M.R., Axelsson, G. and Gíslason, S.R. (2008) Aquifer characterization with tracer test technique; permanent CO_2 sequestration into basalt, SW Iceland. *Mineralogical Magazine* 72, 121–125.

Luhmann, A.J., Tutolo, B.M., Bagley, B.C., Mildner, D.F.R., Seyfried, W.E. and Saar, M.O. (2017a) Permeability, porosity, and mineral surface area changes in basalt cores induced by reactive transport of CO_2-rich brine. *Water Resources Research* 53, 1908–1927.

Luhmann, A.J., Tutolo, B.M., Tan, C., Moskowitz, B.M., Saar, M.O. and Seyfried, W.E. (2017b) Whole rock basalt alteration from CO_2-rich brine during flow-through experiments at 150 °C and 150 bar. *Chemical Geology* 453, 92–110.

Matter, J.M., Broecker, W.S., Gíslason, S.R., Gunnlaugsson, E., Oelkers, E.H., Stute, M., Sigurðardóttir, H., Stefánsson, A., Alfreðsson, H.A., Aradóttir, E.S., Axelsson, G., Sigfússon, B. and Wolff-Boenisch, D. (2011) The CarbFix Pilot Project–Storing carbon dioxide in basalt. *Energy Procedia* 4, 5579–5585.

Matter, J.M. and Kelemen, P.B. (2009) Permanent storage of carbon dioxide in geological reservoirs by mineral carbonation. *Nature Geoscience* 2, 837–841.

Matter, J.M., Stute, M., Snæbjörnsdóttir, S.Ó., Oelkers, E.H., Gíslason, S.R., Aradóttir, E.S., Sigfússon, B., Gunnarsson, I., Sigurðardóttir, H., Gunnlaugsson, E., Axelsson, G., Alfredsson, H.A., Wolff-Boenisch, D., Mesfin, K., Fernandez de la Reguera Taya, D., Hall, J., Dideriksen, K. and Broecker, W.S. (2016) Rapid carbon mineralization for permanent disposal of anthropogenic carbon dioxide emissions. *Science* 352, 1312–1314.

Menefee, A.H., Giammar, D.E. and Ellis, B.R. (2018) Permanent CO_2 Trapping through Localized and Chemical Gradient-Driven Basalt Carbonation. *Environmental Science & Technology* 52, 8954–8964.

McGrail, B.P., Schaef, H.T., Spane, F.A., Cliff, J.B., Qafoku, O., Horner, J.A., Thompson, C.J., Owen, A.T. and Sullivan, C.E. (2017) Field Validation of Supercritical CO_2 Reactivity with Basalts. *Environmental Science & Technology Letters* 4, 6–10.

Neveu, M., Desch, S.J. and Castillo-Rogez, J.C. (2017) Aqueous geochemistry in icy world interiors: Equilibrium fluid, rock, and gas compositions, and fate of antifreezes and radionuclides. *Geochimica et Cosmochimica Acta* 212, 324–371.

Oelkers, E.H. and Gíslason, S.R. (2001) The mechanism, rates and consequences of basaltic glass dissolution: I. An experimental study of the dissolution rates of basaltic glass as a function of aqueous Al, Si and oxalic acid concentration at 25°C and pH = 3 and 11. *Geochimica et Cosmochimica Acta* 65, 3671–3681.

Oelkers, E.H., Gíslason, S.R. and Matter, J. (2008) Mineral Carbonation of CO_2. *Elements* 4, 333–337.

Parkhurst, D.L. and Appelo, C.A.J. (1999) User's Guide to PHREEQC (Version 2) - A Computer Program for Speciation, Batch-Reaction, One-Dimensional Transport, and Inverse Geochemical Calculations, Water-Resources Investigations Report. U.S. Department of the Interior.

Parkhurst, D.L. and Appelo, C.A.J. (2013) Description of Input and Examples for PHREEQC Version 3 - A Computer Program for Speciation, Batch-Reaction, One-Dimensional Transport, and Inverse Geochemical Calculations, in: Survey, U.S.G. (Ed.), Techniques and Methods, p. 497.

Rendel, P.M., Wolff-Boenisch, D., Gavrieli, I. and Ganor, J. (2018) A novel experiment system for the exploration of CO_2-water-rock intereactions under conditions relevant to CO2 geological storage. *Chemical Engineering Journal* 334, 1206–1213.

Rogers, K.L., Neuhoff, P.S., Pedersen, A.K. and Bird, D.K. (2006) CO_2 metasomatism in a basalt-hosted petroleum reservoir, Nuussuaq, West Greenland. *Lithos* 92, 55–82.

Rosenbauer, R.J., Thomas, B., Bischoff, J.L. and Palandri, J. (2012) Carbon sequestration via reaction with basaltic rocks: Geochemical modeling and experimental results. *Geochimica et Cosmochimica Acta* 89, 116–133.

Schaef, H.T., McGrail, B.P. and Owen, A.T. (2010) Carbonate mineralization of volcanic province basalts. *International Journal of Greenhouse Gas Control* 4, 249–261.

Schiffman, P. and Fridleifsson, G.Ó. (1991) The smectite-chlorite transition in drillhole NJ-15, Nesjavellir geothermal field, Iceland: XRD, BSE and electron microprobe investigations. *Journal of Metamorphic Geology* 9, 679–696.

Sigfússon, B., Gíslason, S.R., Matter, J.M., Stute, M., Gunnlaugsson, E., Gunnarsson, I., Aradóttir, Sigurðardóttir, H., Mesfin, K., Alfredsson, H.A., Wolff-Boenisch, D., Arnarsson, M.T. and Oelkers, E.H. (2015) Solving the carbon-dioxide buoyancy challenge: The design and field testing of a dissolved CO_2 injection system. *International Journal of Greenhouse Gas Control* 37, 213–219.

Snæbjörnsdóttir, S.Ó., Gíslason, S.R., Galeczka, I.M. and Oelkers, E.H. (2018) Reaction path modelling of in-situ mineralisation of CO_2 at the CarbFix site at Hellisheidi, SW-Iceland. *Geochimica et Cosmochimica Acta* 220, 348–366.

Snæbjörnsdóttir, S.Ó., Oelkers, E.H., Mesfin, K., Aradóttir, E.S., Dideriksen, K., Gunnarsson, I., Gunnlaugsson, E., Matter, J.M., Stute, M. and Gíslason, S.R. (2017) The chemistry and saturation states of subsurface fluids during the in situ mineralisation of CO_2 and H_2S at the CarbFix site in SW-Iceland. *International Journal of Greenhouse Gas Control* 58, 87–102.

Stockmann, G.J., Shirokova, L.S., Pokrovsky, O.S., Bénézeth, P., Bovet, N., Gíslason, S.R. and Oelkers, E.H. (2012) Does the presence of heterotrophic bacterium Pseudomonas reactans affect basaltic glass dissolution rates? *Chemical Geology* 296–297, 1–18.

Stockmann, G.J., Wolff-Boenisch, D., Bovet, N., Gíslason, S.R. and Oelkers, E.H. (2014) The role of silicate surfaces on calcite precipitation kinetics. *Geochimica et Cosmochimica Acta* 135, 231–250.

Stockmann, G.J., Wolff-Boenisch, D., Gíslason, S.R. and Oelkers, E.H. (2011) Do carbonate precipitates affect dissolution kinetics? 1: Basaltic glass. *Chemical Geology* 284, 306–316.

Stockmann, G.J., Wolff-Boenisch, D., Gíslason, S.R. and Oelkers, E.H. (2013) Do carbonate precipitates affect dissolution kinetics? 2: Diopside. *Chemical Geology* 337–338, 56–66.

Voigt, M., Marieni, C., Clark, D.E., Gíslason, S.R. and Oelkers, E.H. (2018) Evaluation and refinement of thermodynamic databases for mineral carbonation. *Energy Procedia* 146, 81–91.

Wolff-Boenisch, D. and Galeczka, I.M. (2018) Flow-through reactor experiments on basalt-(sea)water-CO_2 reactions at 90°C and neutral pH. What happens to the basalt pore space under post-injection conditions? *International Journal of Greenhouse Gas Control* 68, 176–190.

Wolff-Boenisch, D., Galeczka, I.M., Mesfin, K.G. and Gíslason, S.R. (2016) A foray into false positive results in mineral dissolution and precipitation studies. *Applied*

Geochemistry 71, 9–19.

Wolff-Boenisch, D., Gíslason, S.R. and Oelkers, E.H. (2006) The effect of crystallinity on dissolution rates and CO_2 consumption capacity of silicates. *Geochimica et Cosmochimica Acta* 70, 858–870.

Wolff-Boenisch, D., Wenau, S., Gíslason, S.R. and Oelkers, E.H. (2011) Dissolution of basalts and peridotite in seawater, in the presence of ligands, and CO_2: Implications for mineral sequestration of carbon dioxide. *Geochimica et Cosmochimica Acta* 75, 5510–5525.

Xiong, W., Wells, R.K., Horner, J.A., Schaef, H.T., Skemer, P.A. and Giammar, D.E. (2018) CO_2 Mineral Sequestration in Naturally Porous Basalt. *Environmental Science & Technology Letters* 5, 142–147.

Xiong, W., Wells, R.K., Menefee, A.H., Skemer, P., Ellis, B.R. and Giammar, D.E. (2017) CO_2 mineral trapping in fractured basalt. *International Journal of Greenhouse Gas Control* 66, 204–217.

3 Paper II

The chemistry and potential reactivity of the CO_2-H_2S charged injected waters at the basaltic CarbFix2 site, Iceland

Deirdre E. Clark, Ingvi Gunnarsson, Edda S. Aradóttir, Magnús Þ. Arnarson, Þorsteinn A. Þorgeirsson, Sigrún S. Sigurðardóttir, Bergur Sigfússon, Sandra Ó. Snæbjörnsdóttir, Eric H. Oelkers, and Sigurður R. Gíslason

Energy Procedia 146, 121–128, 2018.
doi.org/10.1016/j.egypro.2018.07.016

Abstract

The CarbFix2 project aims to capture and store the CO_2 and H_2S emissions from the Hellisheiði geothermal power plant in Iceland by mineral storage through its injection into subsurface basalts. The gas mixture is captured directly by its dissolution into water at elevated pressure. This fluid is then injected along with effluent geothermal water into subsurface basalts to mineralize the dissolved acid gases as carbonates and sulfides. Sampled effluent and gas-charged injection waters were analyzed and their mixing geochemically modeled using PHREEQC. Results suggest that carbonates, sulfides and any secondary minerals would only precipitate from the fluid after it has substantially reacted with the host basalt; the fluid is undersaturated with the most common primary and secondary minerals at the injection well outlet, suggesting that the risk of clogging fluid flow paths near the injection well is limited.

3.1 Introduction

Reykjavik Energy, the largest geothermal power company in Iceland, alongside the CarbFix group has developed a pioneering method to capture their carbon dioxide (CO_2) and hydrogen sulfide (H_2S) emissions and store as minerals in subsurface basalts. The emission of these geothermal gases in addition to hydrogen (H_2), nitrogen (N_2), methane (CH_4), and argon (Ar) are associated with high-temperature geothermal systems.

Carbon capture and storage is one solution to reduce CO_2 emissions into the atmosphere. This approach was successfully tested as a part of the original CarbFix CO_2 storage project at the Hellisheiði geothermal power plant in Iceland. Basaltic rocks, like those found at Hellisheiði, are rich in divalent cations, Ca^{+2}, Mg^{+2} and Fe^{+2}, which react with CO_2 dissolved in water to form stable carbonate minerals. Results from injection experiments at the original CarbFix low temperature site (20–50 °C) showed mineralization of injected dissolved acid gases had occurred in less than two years (Gíslason and Oelkers, 2014; Matter et al., 2016; Snæbjörnsdóttir et al., 2017).

The Government of Iceland passed a regulation in 2010 restricting atmospheric H_2S emissions. This regulation required the geothermal industry in Iceland to reduce their H_2S emissions substantially (Aradóttir et al., 2015; Hallsdóttir et al, 2010; Júliusson et al., 2015) H_2S abatement by sulfur mineral storage was proposed by Stefánsson et al. (2011) and preliminary efforts were made through gas capture and injection tests in 2012 (Aradóttir et al, 2015; Gunnarsson et al., 2015).

These initial efforts were upscaled starting in June 2014 as part of the CarbFix2 project where a mixture of CO_2 and H_2S is injected to a depth of 750 m with temperatures of 240–250 °C (Gunnarsson, et al. 2018). By the end of 2017, 23,104 tons of CO_2 and 11,853 tons of H_2S had been injected, accounting for approximately 34% of CO_2 and 68% of the H_2S 2017 emissions of the Hellisheiði power plant. Once in the geothermal reservoir, heat exchange and host rock dissolution neutralizes the gas-charged water and saturates the injected fluid with respect to carbonate and sulfur minerals.

The waters injected into the CarbFix2 site are a combination of gas-charged water obtained from the capture plant and effluent geothermal water from the powerplant. To better characterize the long-term behavior of the CarbFix2 acid gas storage effort, specifically the conditions within the injection wells, the gas-charged and effluent waters were sampled from the head of the injection wells. The mixing of these two waters at more than 750 m depth was geochemically modeled using PHREEQC to calculate the changes in pH, temperature and fluid composition. The stability of the primary and secondary minerals at the injection well outlet was also assessed as the fluids mixed and heated up to the geothermal reservoir temperature.

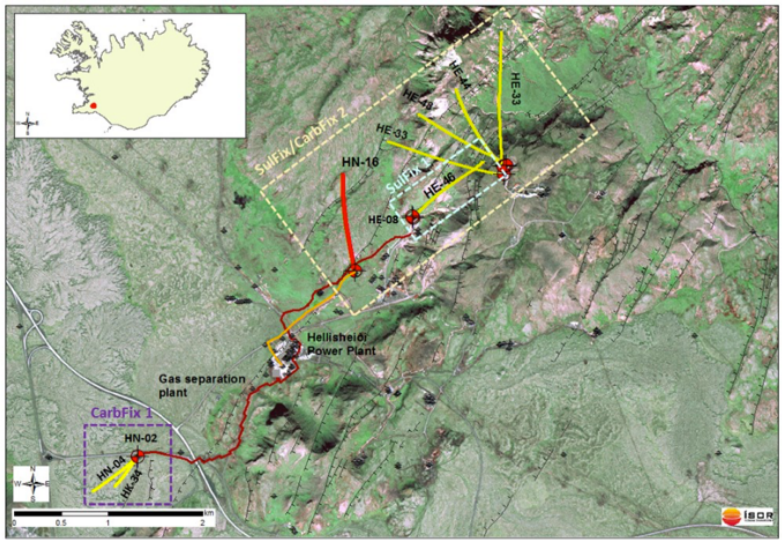

Figure 3.1. Aerial map of the original CarbFix and the CarbFix 2 injection sites and the HN-16 injection well (shown in bright red). Taken from Aradóttir et al. (2015).

3.2 Materials and methods

3.2.1 Capture and injection

The CarbFix2 injection site is located adjacent to the Hellisheiði Geothermal Power Plant, 25 km east of Reykjavik, Iceland (Fig. 3.1). The Hellisheiði geothermal field is a part of the southern Hengill volcanic system, which consists of fractured, hydrothermally altered basalts. Further details describing the geology of the site are reported by Gunnarsson et al. (2018) and Franzson et al. (1988; 2010).

Table 3.1. Dissolution reactions of gases.

Gas	Reactions
CO_2	$CO_2(g) + H_2O \rightleftharpoons H_2CO_3$
	$H_2CO_3 \rightleftharpoons HCO_3^- + H^+$
	$HCO_3^- \rightleftharpoons CO_3 - 2 + H^+$
H_2S	$H_2S(g) \rightleftharpoons H_2S(aq)$
	$H_2S(aq) = HS^- + H^+$
	$HS^- \rightleftharpoons S_2^- + H^+$

About 40,000 tonnes of CO_2 and 9,000 tonnes of H_2S are produced out from the geothermal reservoir annually along with a minor amounts of H_2, N_2, Ar, and CH_4. A scrubbing tower was used to dissolve a CO_2 and H_2S dominated gas mixture under anoxic conditions from the exhaust gas stream into pure water (condensate), in accord with the reactions shown in Table 3.1. This approach allows for immediate solubility trapping with the added security of no potential gas leaks during the injection of this

fluid into the subsurface (Aradóttir et al., 2015; Gunnarsson et al., 2018). Note that the dissolution of these gases liberate H^+ leading the gas-charged fluids becoming acidic and thus reactive when in contact with basalts.

Starting in June 2014, approximately 25% of the exhaust gas from the power plant was processed through the scrubbing tower that operated at a pressure of 5 bars. Flow rates were optimized to recover 56% of the CO_2 and 97% of the H_2S from the processed exhaust stream. The gas-charged condensate water at a temperature of 20 °C was then pressurized to 9 bars and transported 1.5 km to injection well HN-16 (Fig. 3.1) where it was injected into the subsurface at a rate of 30 to 36 kg/s together with a known flux of effluent water (Gunnarsson et al., 2018). From 16 July 2016 the scrubbing tower gas capture capacity was doubled and operated at 6 bars before being transported to HN-16 and co-injected with the effluent water. This change in capture rate altered somewhat the composition of the gas-charged fluid at this time. In addition, starting at this time, a minor quantity of acid gases were added to the effluent water to prevent pipe clogging. Prior to the addition of the acid gases, the effluent geothermal water had an average pH of 9.13, but after it was 7.5. As such two sets of calculations are presented below, one for the compositions of the fluids before and one for after July 2016. The co-injected effluent water had a temperature ranging from 55 to 140 °C and was injected at a rate of 10 to 130 kg/s.

These fluids were injected into the HN-16 and HN-14 injection wells. HN-16 was directionally drilled, 2206 m long and 0.311 m wide with the top 660 m encased in carbon steel. The two fluids (acid gas-charged condensate and effluent geothermal water) were injected separately to a depth of 700 m (Fig. 3.2) where they mixed and flowed into the main target aquifer at a depth between 1900 and 2200 m and a temperature range from 220 to 260 °C (Gunnarsson et al., 2018). Table 3.2 lists the primary and secondary minerals expected to be present within this aquifer (Snæbjörnsdóttir et al., 2011).

3.2.2 Sampling and analysis

The effluent and gas-charged waters were sampled at the HN-16 injection well. The dissolved inorganic carbon (DIC) and H_2S concentrations in the gas-charged pure water was determined from collected water samples. The effluent water samples were analyzed for DIC, H_2S, and SO_4^{2-}. The sampling and analysis methods are described by Gunnarsson et al. (2018). Major elements of the effluent water were also measured either by Ion Chromatography (Dionex ICS-1100 or ICS-2000 chromatography system), Inductively Coupled Plasma Optical Emission Spectrometer (ICP-OES) or Inductively Coupled Plasma Mass Spectrometer (ICP-MS). Fluids were acidified with concentrated supra-pure HNO_3 (1.0 vol %) prior to analysis by ICP-OES and ICP-MS while no preparation was required for IC analysis. Analytical uncertainties of these analyses were on the order of $\leq 5\%$.

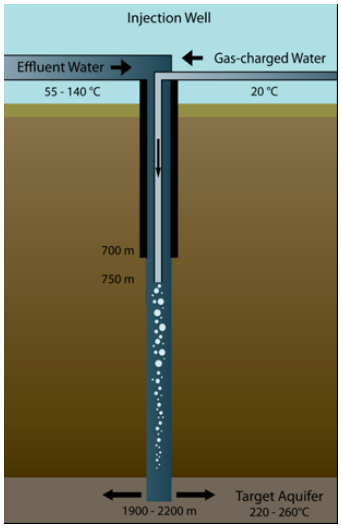

Figure 3.2. Schematic diagram of the injection well. Within the casing of each well is a 4" stainless steel pipe that reaches 750 m, thus preventing any contact between the carbon steel and the gas-charged water. The two fluids, effluent water and gas-charged water, were injected separately, mixing at the exit of the stainless steel pipe. The main aquifer receiving the water mixture was located at a depth between 1900 and 2200 m with a temperature of 220–260 °C.

Table 3.2. Dissolution reactions of primary and secondary minerals present in the target basaltic reservoir.

Minerals		Dissolution reaction
Primary	Basalt	$SiAl_{0.35}O_2(OH)_{1.05} + 1.05\,H^+ \rightleftharpoons 0.35\,Al^{+3} + SiO_2 + 1.05\,H_2O$
	Albite	$NaAlSi_3O_8 + 4\,H^+ \rightleftharpoons Al^{+3} + Na^+ + 3\,SiO_2 + 2\,H_2O$
	Anorthite	$CalAl_2Si_2O_8 + 8\,H^+ \rightleftharpoons Ca^{+2} + 2\,Al^{+3} + 2\,SiO_2 + 4\,H_2O$
	Diopside	$CaMgSi_2O_6 + 4\,H^+ \rightleftharpoons Ca^{+2} + Mg^{+2} + 2\,SiO_2 + 2\,H_2O$
	Enstatite	$MgSiO_3 + 2\,H^+ \rightleftharpoons Mg^{+2} + SiO_2 + H_2O$
	Fayalite	$Fe_2SiO_4 + 4\,H^+ \rightleftharpoons 2\,Fe^{+2}\,SiO_2 + 2\,H_2O$
	Ferrosilite	$FeSiO_3 + 2\,H^+ \rightleftharpoons Fe^{+2} + SiO_2 + H_2O$
	Forsterite	$Mg_2SiO_4 + 4\,H^+ \rightleftharpoons 2\,Mg^{+2} + SiO_2 + H_2O$
	Magnetite	$Fe_3O_4 + 8\,H^+ \rightleftharpoons Fe^{+2} + 4\,H_2O$
Secondary	Calcite	$CaCO_3 + H^+ \rightleftharpoons Ca^{+2} + HCO_3{}^-$
	Clinchlore	$Mg_5Al_2Si_3O_{10}(OH)_8 + 16\,H^+ \rightleftharpoons 5\,Mg^{+2} + 2\,Al^{+3} + 3\,SiO_2 + 12\,H_2O$
	Daphnite	$Fe_5Al_2Si_3O_{10}(OH)_8 + 16\,H^+ \rightleftharpoons 5\,Fe^{+2} + 2\,Al^{+3} + 3\,SiO_2 + 12\,H_2O$
	Epidote	$Ca_2FeAl_2Si_3O_{12}(OH) + 13\,H^+ \rightleftharpoons 2\,Ca^{+2} + Fe^{+2} + 2\,Al^{+3} + 3\,SiO_2 + 7\,H_2O$
	Ferroactinolite	$Ca_2Fe_5Si_8O_{22}(OH)_2 + 14\,H^+ \rightleftharpoons 2\,Ca^{+2} + 5\,Fe^{+2} + 8\,SiO_2 + 8\,H_2O$
	Prehnite	$Ca_2\,Al_2Si_3O_{10}(OH)_2 + 10\,H^+ \rightleftharpoons Ca^{+2} + 2\,Al^{+3} + 3\,SiO_2 + 6\,H_2O$
	Pyrite	$FeS_2 + H_2O \rightleftharpoons Fe^{+2} + 0.25\,H^+\,0.25\,SO_4 - 2 + 1.75\,HS^-$
	Pyrrhotite	$FeS + H^+ \rightleftharpoons Fe^{+2} + HS^-$
	Tremolite	$Ca_2Mg_5Si_8O_{22}(OH)_2 + 14\,H^+ \rightleftharpoons 2\,Ca^{+2} + 5\,Mg^{+2} + 8\,SiO_2 + 8\,H_2O$
	Wairakite	$CaAl_2Si_4O_{10}(OH)_4 + 8\,H^+ \rightleftharpoons Ca^{+2} + 2\,Al^{+3} + 4\,SiO_2 + 6\,H_2O$
	Wollastonite	$CaSiO_3 + 2\,H^+ \rightleftharpoons Ca^{+2} + SiO_2 + H_2O$

3.2.3 Modeling

The goal of the modeling is to determine the potential of secondary minerals that might precipitate in and near the well prior to substantial dissolution of the host rock. The geochemical speciation program PHREEQC 3.4.0 was used together with its *core10.dat* database and additional modifications (Neveu et al., 2017; Parkhurst and Appelo, 2013; Voigt et al., 2018) to determine the pH, temperature and geochemical speciation of the injection mixture in addition to the saturation index of the primary and secondary minerals expected to be present or potentially forming during the injection. The saturation index is defined as $SI \equiv \log_{10} \Omega$; saturation state, Ω, is calculated from $\Omega \equiv Q/K_{SP}$, where K_{SP} is the equilibrium constant of the mineral dissolution reaction, and Q is the corresponding reaction quotient of a specific solution. A solution is oversaturated with a mineral if a saturation index is greater than zero and undersaturated if less than zero.

The average DIC, H_2S, and major element concentrations of the measured gas-charged and effluent water were adopted to model the chemistry of the mixed injection fluid. The original temperature of the gas-charged water was 20 °C but that of the effluent water ranged from 55 to 140 °C. We have modeled the saturation state of the gas-charged and effluent water mixture as a function of temperature as this fluid was heated to 260 °C during its descent in the well and its arrival into the main target reservoir. No dissolution or precipitation was allowed to occur during the simulation. The fluid pressure was fixed at 81.6 bars to reflect that of the target reservoir.

Table 3.3. Average geochemical compositions of injected effluent geothermal and gas-charged waters before and after July 2016. Average concentrations reported for the first injection scenario (June 2014 – July 2016) are taken from Gunnarsson et al. (2018). Values given in mmol/kg.

Injection Scenario		June 2014 - July 2016	July 2016 - Dec 2017
Gas-charged water	pH	3.65	3.54
	DIC	102	101
	H_2S	72.9	166
Effluent water	pH	9.13	7.5
	DIC	0.424	1.53
	H_2S	0.442	1.21
	SO_4	0.246[a]	0.110[b]
	Si	8.17	7.88
	Na	6.13	5.65
	K	0.616	0.600
	Ca	0.0143	0.0101
	Mg	< 0.002	0.003
	Fe	< 0.001[c]	0.0005[d]
	Al	0.047	0.041
	Cl	3.36[a]	3.66[b]
	F	0.051[a]	0.049[b]

[a]Measured by ICS-1100.
[b] Measured by ICS-2000.
[c] Measured by ICP-OES.
[d] Measured by ICP-MS.

3.3 Results

The average DIC, H_2S, and major element concentrations of the gas-charged and effluent water are reported in Table 3.3. Values from the June 2014 – July 2016 injection period are averaged from results in Gunnarsson et al. (2018).

Changes in the calculated pH and temperature of the injection fluids having different mixing ratios of the effluent and gas-charged waters were calculated. Saturation state results are presented in Fig. 3.3 for the target fluid mixing ratio of 30% gas-charged condensate and 70% effluent water, and initial fluid temperature mixture of 80 °C. The pH of the mixed injection fluids were 5.4 and 4.7, respectively, for the fluid mixture before and after July 2016.

For both sets of fluid compositions, the fluids were substantially undersaturated with the most potential secondary phases at temperatures to at least 260 °C (Fig. 3.3). Siderite was the only carbonate close to saturation at the highest temperatures, others undersaturated at all temperatures. Pyrite was at saturation and pyrrhotite below. Daphnite, the Fe endmember of chlorite, became supersaturated; ferroactinolite, also the Fe endmember of actinolite, showed a similar pattern, although in the second scenario it did not reach saturation.

3.4 Conclusions

The results summarized above suggest that little to no mineral precipitation would be expected to occur from the fluids injected into the CarbFix2 storage site during its descent within the injection wells and immediately following its release to the main basaltic target reservoir. Secondary minerals are only expected to precipitate after significant basalt has dissolved into the injected fluids as it moves away from its injection point. These results suggest that there is minimal risk to clog injection wells and pore space close to the injection wells. The major reactions will be the dissolution of the host basalt in the vicinity of the well increasing the rock permeability. Furthermore, doubling the CO_2 and H_2S injection rates and adding gas to the effluent water before injection lowers the saturation state of most primary and secondary minerals within and close to the injection wells.

Acknowledgements

This publication has been produced with support from Reykjavik Energy and the European Commission through the projects CarbFix (EC coordinated action 283148) and CO2-REACT (EC Project 317235). Special thanks to Martin Voigt for his help and support.

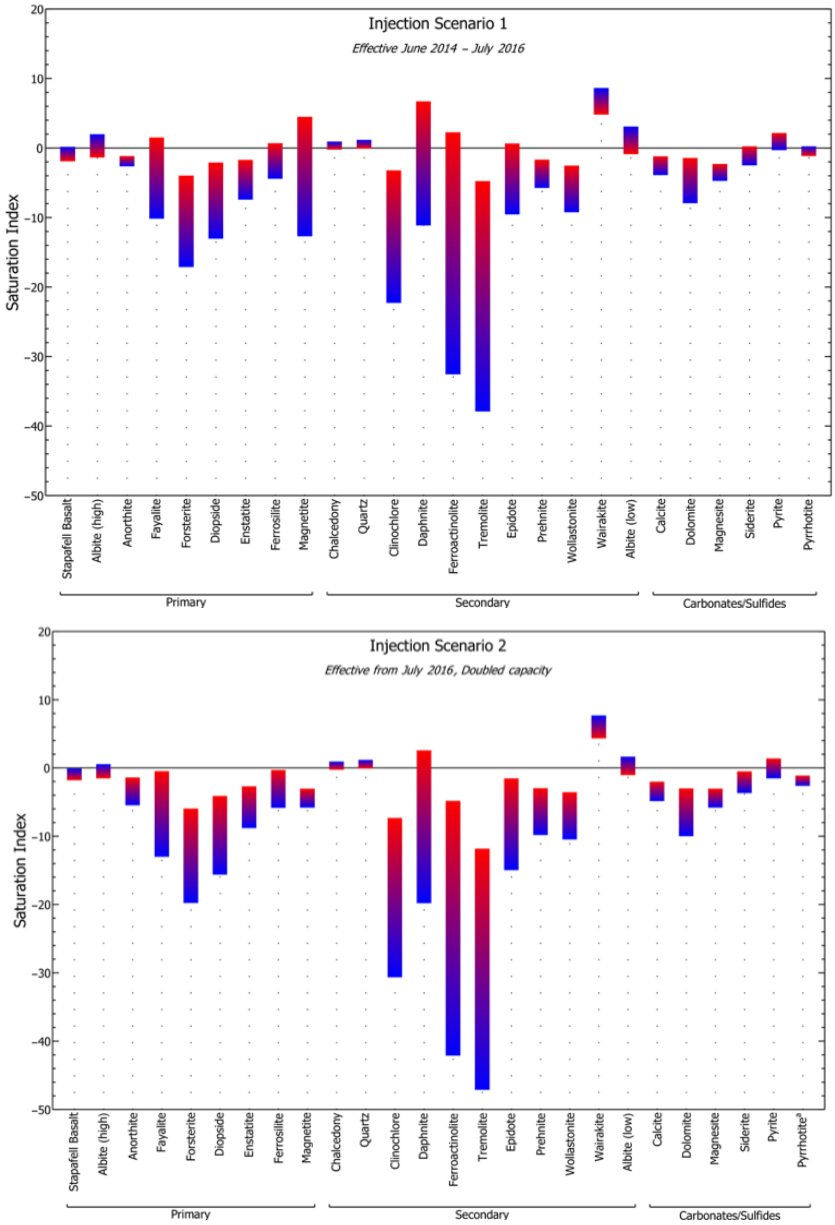

Figure 3.3. The calculated saturation index of primary and secondary minerals during Injection Scenario 1 and 2 over a temperature range of 60 to 260 °C, which occurs as the injected fluids heat within and close to the injection wells. The coolest temperature is represented by the blue, but the warmest by red part of each column. Note that these waters reflect a starting effluent water temperature of 80 °C.

[a]The saturation state of pyrrhotite during Scenario 2 does not increase continuously with temperature; it is closest to saturation at 150 °C.

3.5 References

Aradóttir, E.S., Gunnarsson, I., Sigfússon, B., Gíslason, S.R., Oelkers, E.H., Stute, M., Matter, J.M., Snæbjörnsdóttir S.Ó., Mesfin, K., Alfredsson, H.A., Hall, J., Arnarson, M.Th., Dideriksen, K., Júliusson, B.M., Boecker, W.S. and Gunnlaugsson, E. (2015) Towards Cleaner Geothermal Energy: Subsurface Sequestration of Sour Gas Emissions from Geothermal Power Plants. World Geothermal Congress, Melbourne, Australia.

Franzson, H. (1988) Nesjavellir, Borholujardfraedi, Vatnsgengd i jardhitageymi (Nesjavellir, Borehole geology, Geothermal Fluid Type). Orkustofnun, OS-88046/JHD-09.

Franzson, H., Gunnlaugsson, E., Árnason, K., Sæmundsson, K., Steingrímsson, B., Harðarson, B. (2010) Hengill geothermal system, conceptual model and thermal evolution. Proceedings, World Geothermal Congress, Bali, Indonesia.

Gíslason, S.R. and Oelkers, E.H. (2014) Carbon Storage in Basalt. *Science* 344, 373–374.

Gunnarsson, I., Aradóttir, E.S., Oelkers, E.H., Clark, D.E., Arnarson, M.Th., Sigfússon, B., Snæbjörnsdóttir, S.Ó., Matter, J.M., Stute, M., Júlíusson, B.M. and Gíslason, S.R. (2018) Rapid and cost-effective capture and subsurface mineral storage of carbon and sulfur. *International Journal of Greenhouse Gas Control* 79, 117–126.

Gunnarsson, I., Júlíusson, B.M., Aradóttir, E.S., Sigfússon, B. and Arnarson, M.Th. (2015) Pilot Scale Geothermal Gas Separation, Hellisheiði Power Plant, Iceland. Proceedings, World Geothermal Congress, Melbourne, Australia.

Júliusson, B.M., Gunnarsson, I., Matthíasdóttir, K.V., Markússon, S.M., Bjarnason, B., Sveinsson, Ó.G., Gíslason, Th. and Thorsteinsson, H. (2015) Tackling the Challenge of H_2S Emissions. Proceedings, World Geothermal Congress, Melbourne, Australia.

Matter, J.M., Stute, M., Snæbjörnsdóttir, S.Ó., Oelkers, E.H., Gíslason, S.R., Aradóttir, E.S., Sigfússon, B., Gunnarsson, I., Sigurðardóttir, H., Gunnlaugsson, E., Axelsson, G., Alfredsson, H.A., Wolff-Boenisch, D., Mesfin, K., Fernandez de la Reguera Taya, D., Hall, J., Dideriksen, K. and Broecker, W.S. (2016) Rapid carbon mineralization for permanent disposal of anthropogenic carbon dioxide emissions. *Science* 352,1312–1314.

Neveu, M., Desch S.J. and Bastillo-Rogez, J.C. (2017) Aqueous geochemistry in icy world interiors: Equilibrium fluid, rock, and gas compositions, and fate of antifreezes and radionuclides. *Geochimica et Cosmochimica Acta* 212, 324–371.

Parkhurst, D.L. and Appelo, C.A.J. (2013) Description of input and examples for PHREEQC. Version 3-a computer program for speciation, batch-reaction, one-dimensional transport, and inverse geochemical calculations. U.S. Geological Survey Techniques. Methods Report, Book 6, chapter A43, 1–497.

Snæbjörnsdóttir, S.Ó., Oelkers, E.H., Mesfin, K., Aradóttir, E.S., Dideriksen, K., Gunnarsson, I., Gunnlaugsson, E., Matter, J.M., Stute, M. and Gíslason, S.R. (2017) The chemistry and saturation states of subsurface fluids during the in-situ mineralization of CO_2 and H_2S at the CarbFix site in SW-Iceland. *International Journal of Greenhouse Gas Control* 58, 87–102.

Stefánsson, A., Arnórsson, S., Gunnarsson, I., Kaasalainen, H. and Gunnlaugsson, E. (2011) The geochemistry and sequestration of H_2S into the geothermal system at Hellisheidi, Iceland. *Journal of Volcanology and Geothermal Research* 202, 179–188.

Snæbjörnsdóttir, S.Ó. (2011) The Geology and Hydrothermal Alteration at the Western Margin of the Hengill Volcanic System. University of Iceland, Master's Thesis.

Voigt, M., Clark, D.E., Marieni, C., Gíslason, S.R. and Oelkers, E.H. (2018) Evaluation and refinement of thermodynamic databases for mineral carbonation. *Energy Procedia* 146, 81–91.

4 Paper III

CarbFix2: CO_2 and H_2S mineralization during 3.5 years of continuous injection into basaltic rocks at more than 250°C

Deirdre E. Clark, Eric H. Oelkers, Ingvi Gunnarsson, Bergur Sigfússon, Sandra Ó. Snæbjörnsdóttir, Edda S. Aradóttir, and Sigurður R. Gíslason

Submitted to Geochimica Cosmochimica Acta

Abstract

The CarbFix method was upscaled at the Hellisheiði geothermal power plant to inject and mineralize the plant's CO_2 and H_2S emissions in June 2014. This approach first captures the gases by their dissolution in water, and the resulting gas-charged water is injected into subsurface basalts. The dissolved CO_2 and H_2S then react with the basaltic rocks liberating divalent cations, Ca^{2+}, Mg^{2+} and Fe^{2+}, increasing fluid pH, and precipitating stable carbonate and sulfide minerals. By the end of 2017, 23,200 metric tons of CO_2 and 11,800 metric tons of H_2S had been injected to a depth of 750 m deep into fractured, hydrothermally altered basalts at > 250 °C. The *in situ* fluid composition, as well as saturation indices and predominance diagrams of relevant secondary minerals at the injection and monitoring wells, indicate that sulfide precipitation is not limited by the availability of Fe or by the consumption of Fe by other secondary minerals; Ca release from the reservoir rocks to the fluid phase, however, is a potential limiting factor for calcite precipitation, although dolomite and thus aqueous Mg may also play a role in the mineralization of the injected carbon.

During the first phase of the CarbFix2 injection (June 2014 to July 2016) over 50% of injected carbon and 76% of sulfur mineralized within four to nine months, but these percentages increased four months after the amount of injected gas was doubled during the second phase of CarbFix2 (July 2016 – December 2017) at over 60% of carbon and over 85% of sulfur. The doubling of the gas injection rate decreased the pH of the injection water and liberating more cations for gas mineralization. Notably, the injectivity of the injection well has remained stable throughout the study period confirming that the host rock permeability has been essentially unaffected by 3.5 years of mineralization

reactions. Lastly, although the mineralization reactions are accelerated by the high temperatures (> 250 °C), this is the upper temperature limit for carbon storage via the mineral carbonation of basalts as higher temperatures leads to potential decarbonation reactions.

4.1 Introduction

Upon the successful rapid subsurface mineral storage of carbon and sulfur at the original CarbFix site (Matter et al., 2016; Snæbjörnsdóttir et al., 2017), the CarbFix method was upscaled at the Hellisheiði geothermal power plant, which emits about 41,000 metric tons of CO_2 and 10,000 metric tons of H_2S annually as a by-product of geothermal energy production (Gunnarsson et al., 2018). Icelandic regulations, stricter than WHO guidelines, have been in effect to cut down H_2S emissions of the geothermal industry since 2010 (Aradóttir et al., 2015). These regulations motivated the development of H_2S abatement techniques by mineral storage (Aradóttir et al., 2015; Gunnarsson et al., 2015a), in conjunction with carbon mineralization, the latter deemed the safest way of storing carbon in the subsurface (Benson and Cook, 2005; Gíslason and Oelkers, 2014; McGrail et al., 2006). By combining these efforts, a mixed CO_2–H_2S gas injection has been pursued at Hellisheiði to reduce both the CO_2 and H_2S emissions of the power plant, with the advantage of significantly decreasing the cost of their capture and storage (Aradóttir et al., 2015; Gunnarsson et al., 2018).

The CarbFix method first captures CO_2 and H_2S in water either during its injection (Gíslason and Oelkers, 2014; Andresdóttir et al., 2015) or in a scrubbing tower adjacent to the gas source (Gunnarsson et al., 2018). The resulting gas-charged injection water is acidic. Upon its injection into basalts, this acidic water accelerates the dissolution of the basaltic rocks releasing divalent cations, Ca^{2+}, Mg^{2+}, and Fe^{2+}, to the injected waters. These cations react with the dissolved CO_2 and H_2S to form stable carbonate and sulfide minerals (Gíslason and Oelkers, 2014; Power et al, 2013; Stefánsson et al., 2011). From January to August 2012, 175 metric tons of pure CO_2 and 73 metric tons of a gas mixture (75% CO_2 – 24% H_2S – 1% H_2) were injected into basaltic rocks at the original CarbFix site in Iceland, having a temperature of 20–50 °C. This pilot study demonstrated that 95% of the CO_2 was mineralized in less than two years predominantly as calcite and essentially all of the H_2S within four months as pyrite (Matter et al., 2016; Oelkers et al., 2019a, 2019b; Pogge von Strandmann et al., 2019; Snæbjörnsdóttir et al., 2017). In a different effort, 1000 tons of supercritical CO_2 was injected into Columbia River Basalts during July – August 2013 at the Wallula Basalt pilot site, USA. Results validated the rapid rates of carbonate mineralization with both calcite and ankerite identified in sidewall core samples extracted from the injection zone two years post-injection (McGrail et al., 2017a, 2017b). Research has also begun to evaluate the feasibility of collecting and storing 50 million metric tons of CO_2 in basalt formations offshore from Washington, USA and British Columbia, Canada (Goldberg et al., 2018).

The CarbFix2 project upscaled the original CarbFix project by capturing and injecting a portion of the CO_2 and H_2S emissions of the Hellisheiði geothermal power plant into geothermally altered basalts at temperatures ∼260 °C beginning in June 2014. By the end of 2017, 23,200 metric tons of CO_2 and 11,800 metric tons of H_2S had been injected to a depth of 750 m. Four previous reports of this mixed gas injection in Iceland have been published thus far: 1) a detailed description of the injection method and the monitoring of the dissolved CO_2 and H_2S in the wells downstream from the injection well until 2015 by Gunnarsson et al. (2018), 2) an account of the mixed gas capture method by Sigfússon et al. (2018), 3) geochemical data from the injection well by Clark et al. (2018), and 4) a description of the hydrology and the alteration of the rocks before the CarbFix2 injection by Snæbjörnsdóttir et al. (2018b).

This study expands the geochemical monitoring data originally presented by Gunnarsson et al. (2018) by extending the previously reported measured concentrations and mass balance calculations of dissolved inorganic carbon (DIC) and dissolved sulfur (DS) by two years (2016–2017), and presenting the major element (Al, Na, K, Cl, F, B) and cation (Ca, Mg, Fe) concentrations and mass balance calculations from the start of the CO_2–H_2S injection in 2014 until the end of 2017. Mineral saturation states and predominance diagrams of primary and secondary minerals (e.g. carbonates, sulfides, epidote) in the Hellisheiði geothermal system were then generated from the results presented using a revised thermodynamic database by Voigt et al. (2018a). This expanded chemical dataset allows assessment of the magnitude of carbon and sulfur mineralization in the subsurface in relation to other relevant primary and secondary minerals in the geothermal reservoir.

4.2 CarbFix2 project

The CarbFix2 injection site (Fig. 4.1) is located 1.5 km north of the Hellisheiði geothermal power plant in Húsmúli, a part of the southern Hengill volcanic system that consists of fractured, hydrothermally altered basalts. Studies of the Hellisheiði geothermal field reveal sequences of alteration mineral assemblages as a function of increased depth and temperature (Franzson et al., 2010; 2005). The alteration phases of the original CarbFix site, located about two km southwest of the power plant (Fig. 4.1) at a depth of 500 m and a temperature of 20–50 °C, were chalcedony, smectites, calcite, and Ca-rich and Na-rich zeolites (Alfredsson et al., 2013). The main aquifer of the CarbFix2 storage site, however, is located below the end of the cased section of the injection well at depths greater than 1300 m with temperatures > 250 °C. At these conditions the major alteration minerals are chlorite, epidote, and prehnite. Actinolite is anticipated at temperatures around 280 °C. Other commonly observed secondary minerals at the CarbFix2 site include wollastonite, wairakite, albite, calcite, pyrite, and pyrrhotite. In addition, quartz rather than chalcedony is present at > 180 °C (Snæbjörnsdóttir et al., 2018b). It is important to highlight that geothermal systems are characterized by their hydrothermal convection. Fluid circulation is essentially density-driven when temperatures at the base of the circulation are above ∼150 °C. Therefore as primary geothermal fluids rise

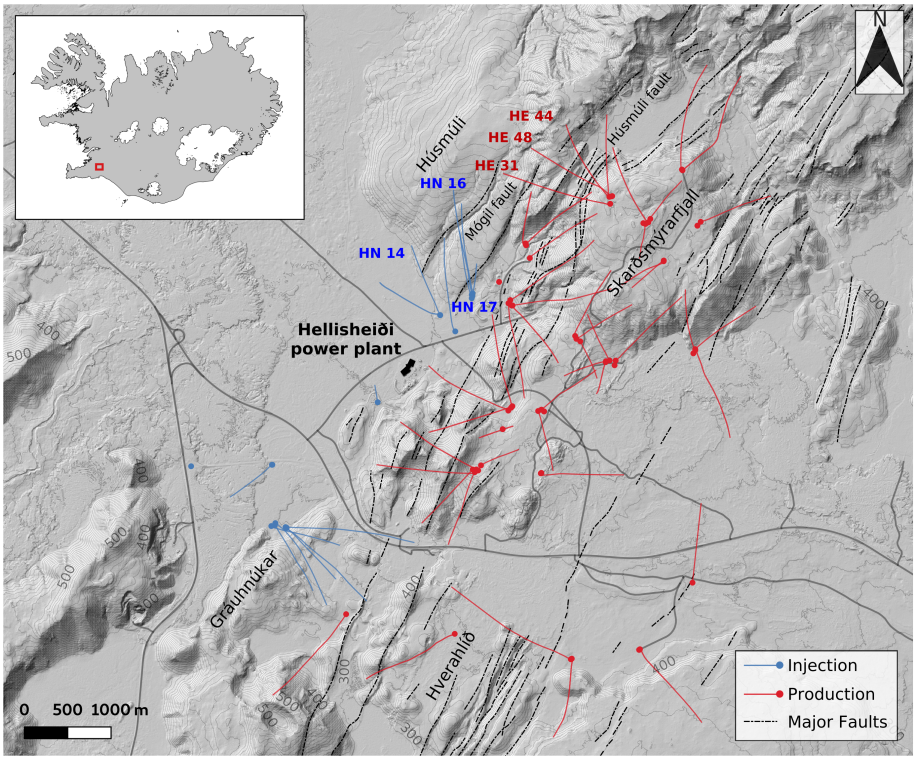

Figure 4.1. An overview of the CarbFix2 injection site. The gas separation plant is located at the Hellisheiði power in the center of the figure. A 1.5 km long, gas-charged water pipe connects the gas capture plant to the injection wells. Injection was into wells HN-16 and HN-14, which are directionally drilled as shown by the line from the surface location. The three monitoring wells (HE-31, HE-48, and HE-44), also directionally drilled, are located from one to two km down gradient from the injection well.

towards the surface, the formation of secondary geothermal fluids occurs due to fluid phase segregation and fluid mixing with shallower and cooler groundwater (Arnórsson et al., 2007).

There have been two distinct phases of gas injection in CarbFix2, as described in more detail by Clark et al. (2018) and Sigfússon et al. (2018). During the first phase, effective from 23 June 2014 to 15 July 2016, approximately 25% of the exhaust gas of the powerplant comprised of 63 vol% CO_2, 21 vol% H_2S, 14 vol% H_2, and 2 vol% of other gases, predominantly Ar, CH_4, and N_2, from the power plant was dissolved into 20 °C condensate (condensed steam from the power plant turbines) in a single step in a scrubbing tower at 5 bar pressure and 30–36 l/s. The CO_2 and H_2S charged condensate water was then pressurized to 9 bar and transported 1.5 km to injection wells HN-16 or HN-14 (Gunnarsson et al., 2018). Due to unrelated repairs to an inner pipe in injection well HN-16, gas injection was switched to HN-14 from 15 July 2015 to 15 March 2016. From 15 July 2016, the scrubbing tower gas capture capacity was doubled with the pressure raised to 6 bar and its resulting gas-charged condensate water, pressurized to 9 bar and subsequently injected into well HN-16. This injection well is directionally drilled, as shown in Fig. 4.1, 2204 m long, and 0.311 m wide with the top 660 m encased in carbon steel; HN-14 is of similar design at 2039 m long with the top 690 m encased. Effluent water is injected into the wells at a rate of 15 to 130 l/s, the gas-charged water from the scrubbing tower was injected separately into a 4” stainless steel pipe within the carbon steel casing at a rate of 30 to 60 l/s (Fig. 4.2). Injection well flow rates are a function of the temperature, pressure, and the amount of water injected into other injection wells in the vicinity, injection rates during this study are shown in Fig. 4.2. Nevertheless, despite these minor variations, the injection flow rates have not decreased with time and the injection pressure has remained close to constant, indicating that the permeability of the system has not degraded over the 3.5 year study period. The flow rates of both injection wells as well as the operation status of the gas capture compressors from 2014 to 2017 are reported in Sigfússon et al. (2018); note that condensate water flow in HN-16 began on 22 April 2014 before the gas capture plant was in operation two months later. The gas-charged condensate water takes two to four minutes to reach the end of this stainless steel pipe within the injection wells, and then mixes with the effluent water while taking an additional 10 to 45 minutes to reach high permeability fractures at depths below 1300 m. Three geothermal production wells, HE-31, HE-48, and HE-44 (Fig. 4.1), were used as monitoring wells. These wells are located 984, 1356, and 1482 m, respectively, from HN-16, and are directionally drilled down to depths of 2703 m, 2248 m, and 2606 m (Gunnarsson et al., 2018; Snæbjörnsdóttir et al., 2018b).

Since the start of the gas-charged condensate water injection on 23 June 2014 through the end of 2017, 23,200 metric tons of CO_2 and 11,800 metric tons of H_2S had been injected. Based on average flow rates of the effluent and gas-charged fluids reported by Sigfússon et al. (2018), Clark et al. (2018) geochemically modelled the fluid exiting the injection well, which consisted of 70% geothermal effluent water at 80 °C and 30% gas-charged condensate water at 20 °C. The combined fluids had a temperature of 62 °C, while the calculated temperatures of the combined fluids throughout the study period

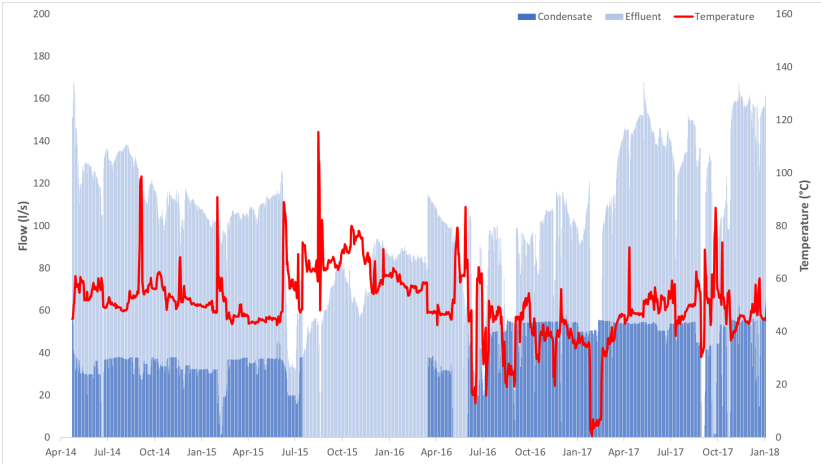

Figure 4.2. Temporal evolution of the effluent water flow (light blue area) and condensate water flow (dark blue area), and the calculated temperature of the combined fluids (red line) in the HN-16 injection well. Note that condensate flow began on 22 April 2014, while the gas capture plant was in operation from 23 June 2014. The injected condensate water was gas charged after this date. Note that the gas-charged condensate water was injected into HN-14 from 15 July 2015 to 15 March 2016, therefore this gas-charged water does not appear in this figure. Modified from Sigfússon et al. (2018).

are shown in Fig. 4.2. During the first phase of gas injection, the fluid mixture had an average pH of 5.4, DIC of 30.9 mM, and DS of 22.3 mM; after the gas injection was doubled in July 2016, the pH decreased to 4.7, but the DIC increased to 50.6 mM, and DS to 31.3 mM. Geochemical calculations also determined that most common basaltic primary and secondary minerals are undersaturated in the injected fluids at the well outlet, although sulfides are supersaturated and siderite close to saturation after the mixed injection fluid is heated to 260 °C. As the acidic gas-charged injected waters react with the host basalts, carbonates, sulfides, and other secondary minerals likely precipitate as the fluids move away from the injection point. The likely dissolution of the host rock minerals close to the injection wells indicates a minimal risk of pore clogging close to the wells. During the second phase of gas injection, when CO_2 and H_2S injection rates were doubled, the saturation states of most primary and secondary minerals are further lowered within and adjacent to the injection well (Clark et al., 2018).

Comprehensive tracer tests were conducted during 2013–2015 to constrain the connection between the injection and production wells in the Hellisheiði geothermal field, including HE-31, HE-48, and HE-44, and the HN-17 injection well. Note HN-17 is next to and has the same trajectory as HN-16 (see Fig. 4.1). All three monitoring wells lie on a major fault zone on the western flanks of the Hengill volcanic system with HE-44 having the highest enthalpy of the three (Gunnarsson et al., 2016). Using these tracer test results, Tómasdóttir (2018) developed a simplified TOUGH2 model of the injection system to model the flow channels between the HN-17 injection well and the three monitoring wells using a multi-channel approach. This model set the

permeability to 1×10^{-12} m^2 and assigned porosity values of 0.2–3.5% to different flow channels. The study concluded that flow paths are lengthened by the sinking of cool injected fluids, thus increasing the water-rock interaction and reducing potential cooling effect of the injected fluids on the fluids collected from the monitoring wells.

Once in the geothermal reservoir, heat exchange and host rock dissolution saturates the injected gas-charged fluid with respect to various carbonate and sulfur minerals. The mass of carbonate and sulfate minerals precipitated from these waters was quantified using an inert chemical tracer. In total, 405 kg of a thermally stable inert tracer, 1-naftalenesulfonic acid (1-ns), was mixed into the injected gas-charged condensate water stream to monitor the subsurface transport, dilution, and mixing, and to assess the degree of subsurface carbonation and sulfide precipitation from 23 June 2014 to 15 March 2016. The first arrival of the tracer from the HN-16 injection well to the HE-31, HE-48, and HE-48 was observed after 15, 30, and 94 days, respectively, after the injection of the tracer. Note that the flow path from injection well HN-16 is north/northeast towards the three monitoring wells, while the flow path of injection well HN-14 deviates more towards the northwest. Consequently, the gas mixture and tracer injected into HN-14 from 15 July 2015 to 15 March 2016 flowed outside the CarbFix2 site and was not observed in the monitoring wells.

The first monitoring results of the CarbFix2 site were published by Gunnarsson et al. (2018) who reported that the permeability of the target injection reservoir remained stable throughout the first year and a half of the injection. This observation was attributed to 1) the acidic injected gas-charged fluids tendency to dissolve material close to the injection well but only precipitate minerals away from the injection well, and 2) the relatively small amount of mineral precipitates compared to the size of the reservoir, it is estimated that calcite and pyrite filled no more than 0.001 vol percent of the pore space in the target aquifer during the first 1.5 years of the injection.

4.3 Methods

4.3.1 Sampling and analysis

A total of 76 samples were collected from the three monitoring wells at the Hellisheiði geothermal power plant (Fig. 4.1). The steam and water phases of the samples were collected using a Webre separator. The pH of the water phase was measured on site with an estimated uncertainity of ± 0.1 using a flow cell connected to a cooling spiral to prevent degassing of CO_2 and influx of O_2 and H_2S. All water samples were filtered on site through 0.2 µm Millipore cellulose acetate filters using a 142 mm Sartorius filter holder. Samples for 1-ns tracer measurements were filtered into 60 mL amber glass bottles and analyzed using a Thermo Ultimate 3000 High Pressure Liquid Chromatography with a BetaBasic C-18 column and fluorimetric detection. The detection limit for 1-ns is 5×10^{-7} mM (Gunnarsson et al., 2018).

Major dissolved elements and anions, other than carbon- and sulfide- derived anions, of

the water samples were measured using a Dionex ICS-2000 Ion Chromatography (IC), a Spectro Ciros Vision Inductively Coupled Plasma Optical Emission Spectrometer (ICP-OES), and a Thermo Scientific iCAPQc Inductively Coupled Plasma Mass Spectrometer (ICP-MS). Water subsamples to be analyzed by ICP-OES and ICP-MS were acidified on site with concentrated supra-pure HNO_3 (1.0 vol %) while no preparation was required for IC analysis of Cl^- and F^-. For the determination of sulfate (SO_4^{2-}), water subsamples were treated on site with Zn acetate to precipitate sulfide (S^{2-}) as zinc sulfide preventing H_2S oxidation to SO_4 upon storage. These subsamples were then filtered again through 0.2 µm cellulose acetate filters before analysis by IC. Water samples for DIC determination were filtered and collected in 300 mL amber glass bottles and analyzed by alkalinity titration, while a 0.5 mL water sample of H_2S was titrated on site using 0.001 M mercuric acetate; both analysis methods are described in detail by Arnórsson et al. (2006). Analytical uncertainties of these analyses were on the order of $\leq 5\%$ and the detection limits listed in Appendix C.

Steam samples were collected into 250 mL pre-evacuated gas bulbs containing a 5–10 mL 50% aqueous KOH solution. The composition of these samples were measured using an Agilent Technologies 7890 A gas chromatography system using a HP-Molesieve (19095P-MSO) column and Thermal Conductivity Detector for H_2, O_2, N_2, and CH_4. The H_2S in the steam phase, after its dissolution into the KOH rich aqueous solution, was analyzed by titration with silver nitrate and silver electrode endpoint detection (Metrohm 905 Titrando), while the CO_2 in the steam samples was analyzed by alkalinity titration (Arnórsson et al., 2006), but used argon instead of nitrogen. Analytical uncertainties of these analyses were on the order of $\leq 5\%$.

4.3.2 Geochemical calculations

The WATCH speciation program (Arnórsson et al., 1982; Bjarnason and Arnórsson, 2010) was used to calculate the major element concentrations of the original geothermal reservoir fluids before its phase separation during sampling. As the three monitoring wells are liquid enthalpy wells (Gunnarsson et al., 2018), the steam fraction at the sample collection pressure was determined assuming adiabatic boiling from the reservoir temperature to the sampling pressure (Arnórsson et al., 2007). The pH at the reservoir temperature was calculated from the sum of the concentrations of the anions of the weak acids and their complexes (a measure of alkalinity) of both the steam and liquid phases. This sum of concentrations is assumed to be constant for a given sample, independent of temperature (Bjarnason and Arnórsson, 2010).

Studies of Icelandic geothermal fields concluded that local chemical equilibrium is closely approached between the fluids and hydrothermal minerals at temperatures as low as 50 °C for all major components, except Cl. Thus geothermal fluid compositions can be estimated with the help of geothermometers that are based on certain elements (Arnórsson et al., 2008). Based on the previously measured downhole temperatures and characterization of the Hellisheiði geothermal reservoir (Franzson et al., 2010; 2005; Gunnarsson et al., 2018), the reservoir temperature was calculated assuming equilibrium with quartz (Gunnarsson and Arnórsson, 2000) using a silica geothermometer equation

derived from experimental data on the solubility of quartz in water for temperatures (°C) up to 330 °C:

$$T_{quartz}°C = -42.198 + 0.28831 \cdot [Si] - 3.6686 \cdot 10^{-4} \cdot [Si]^2 + 3.1665 \cdot 10^{-7} \cdot [Si]^3 + 77.034 \cdot \log[Si] \quad (4.1)$$

where [Si] represents the silica concentration in mg/kg (Fournier and Potter, 1982). Temperatures estimated in this manner are referred to as 'quartz temperatures' below and are estimated to have an uncertainty < 2%.

The geochemical speciation program PHREEQC 3.4.0 (Parkhurst and Appelo, 2013) was then used together with the *carbfix* database (Voigt et al., 2018a), which itself was modified from the *core10* database (Neveu et al., 2017) to determine the saturation index of the sampled fluids with respect to relevant primary and secondary minerals (Clark et al., 2018; Snæbjörnsdóttir et al., 2018b) (Table C.1). The saturation index is defined as SI $\equiv \log_{10} \Omega$; the saturation state, Ω, is calculated from $\Omega \equiv Q/K_{SP}$, where K_{SP} represents the equilibrium constant of the mineral dissolution reaction, and Q denotes the corresponding reaction quotient of the combined fluid sample. A sample is supersaturated with a mineral if a saturation index is greater than zero and undersaturated if less than zero.

To create mineral predominance diagrams, the computer program PhreePlot (Kinniburgh and Cooper, 2011), which is embedded with PHREEQC, was used along with the *carbfix* database and the average deep fluid concentrations and temperatures from the monitoring wells. Pourbaix diagrams were generated using the Geochemist's Workbench Version 12, the *LNLL thermo* database, and the average deep fluid concentrations and temperatures. As wells HE-31 and HE-48 had similar compositions and the same average reservoir temperature, these monitoring wells were grouped together in the mineral predominance and Pourbaix diagrams and a separate set of diagrams created for HE-44.

4.3.3 Mass balance and mineralization calculations

The concentrations of the major elements, if no mineral-fluid reactions occurred after the injection of fluids $C_{i,predicted}$, were determined assuming the non-reactive mixing of the injected and formation waters. The mixing ratio of these fluids was determined from the measured concentrations of the injected non-reactive tracers $C_{1\text{-}ns}$. Taking account of mass balance constraints, $C_{i,predicted}$ was determined from Matter et al. (2016) (see the Appendix C for the derivation of this equation):

$$C_{i,predicted} = \frac{C_{i,background} \cdot (C_{1-ns,injected} - C_{1-ns}) + A \cdot C_{1-ns,injected} \cdot (C_{1-ns} - C_{1-ns,background})}{C_{1-ns,injected} - C_{1-ns,background}} \quad (4.2)$$

where C_i designates the concentration of the component i, and A the molar ratio between the element and the tracer, 1-ns, in the gas-charged injection water (Table C.2); these were calculated using the average injection fluid compositions and averaged injection well flow rates (Clark et al., 2018; Sigfússon et al., 2018). The background

concentrations of the elements in the reservoir fluids $C_{i,background}$, were calculated by averaging the concentrations of the reservoir fluid of the monitoring wells before the arrival of the gas-charged injection water (the samples averaged are italicized in Tables C.3 to C.8 in Appendix C). As 1-ns had been used in the previous tracer tests, a dilute background concentration of 1-ns was present in the reservoir fluid ($C_{1\text{-}ns,background}$). This background concentration in wells HE-31, HE-48, and HE-44 was determined to be 6.95×10^{-7} mM. The average amount of 1-ns tracer injected ($C_{1\text{-}ns,injected}$) in HN-16 is 1.15×10^{-3} mM in the gas-charged condensate water and 3.35×10^{-4} mM in fluid mixture (gas-charged condensate + effluent water).

Since no further tracer was injected into HN-16 after 15 July 2015, to quantify the effects of doubling the gas injection, the tracer recovery results at the monitoring wells of the 2014–2015 tracer test were extrapolated and applied from 15 July 2016. This extrapolation was performed by first fitting a third degree polynomial curve to each monitoring well's tracer concentrations over time starting from when the tracer first appeared (Figs. C.2 to C.4). Thus by knowing the start date of the original tracer injection, 23 June 2014, it was assumed that the same proportion of tracer was injected with the gas-charged water from 15 July 2016. For each monitoring well, tracer concentrations relative to the sampling dates after July 2016 were determined using the respective polynomial curves and added to the measured tracer remaining from the first phase; this total is $C_{1\text{-}ns}$ in Eqn.4.3. This approach requires the assumption that the flow channels between HN-16 and the monitoring wells remained identical throughout this study's monitoring period, which is consistent with the near constant permeability observed in the system.

Comparison of the measured (C_i) and calculated non-reactive DIC and DS concentrations in the monitoring wells allows for the calculation of the fraction of gases mineralized in the subsurface, using the following equation from Gunnarsson et al. (2018):

$$Fraction\ Mineralized = \frac{C_{i,predicted} - C_i}{C_{i,predicted} - C_{i,background}} \tag{4.3}$$

4.4 Results

The composition of all collected liquid and steam samples are presented in Tables C.3 to C.8 in the Appendix C. The recalculated compositions before phase separation are shown in Figs. 4.3 to 4.5.

4.4.1 Major element concentrations in the deep fluid

Sampling of the liquid and steam phases at the three monitoring wells for this study began on 29 April 2014, prior to the gas-charged water injection starting on 23 June. The pre-gas injection samples are highlighted in gray in Figs. 4.3 to 4.9. Injection of gas-charged water occurred mainly into well HN-16, except from 14 July 2015 to 15

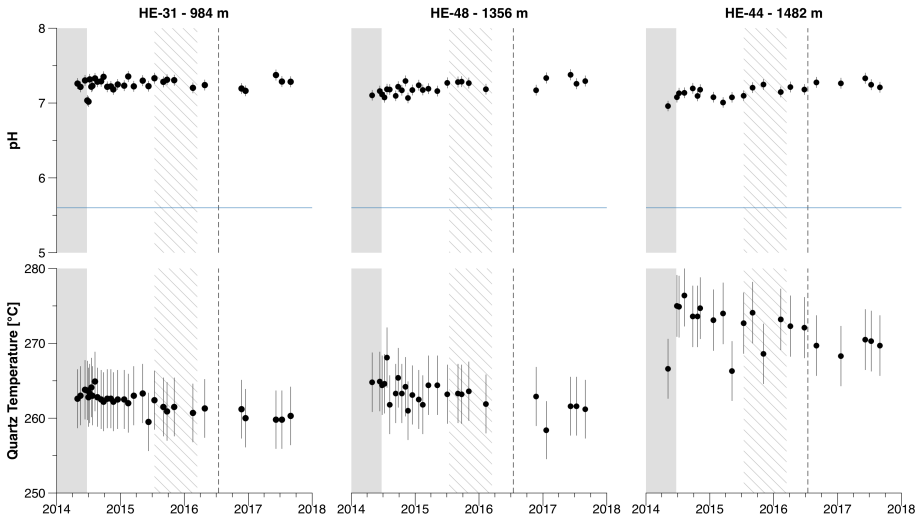

Figure 4.3. The in situ pH and the reservoir temperature based on quartz solubility in the HE-31, HE-48, and HE-44 monitoring wells located 984, 1356, and 1482 m, respectively, from the HN-16 injection well prior to and during the injection of CO_2 and H_2S charged waters. The symbols illustrate the measured fluid values, the gray shaded area indicates the time before the injection of gas-charged waters into well HN-16, the diagonal lines denote when well HN-14 was used for the injection of gas-charged waters, and the vertical dashed line signifies the time when the amount of CO_2 and H_2S injected was doubled. Note that the horizontal blue line plotted with pH represents neutral pH of 5.6 at 250 °C.

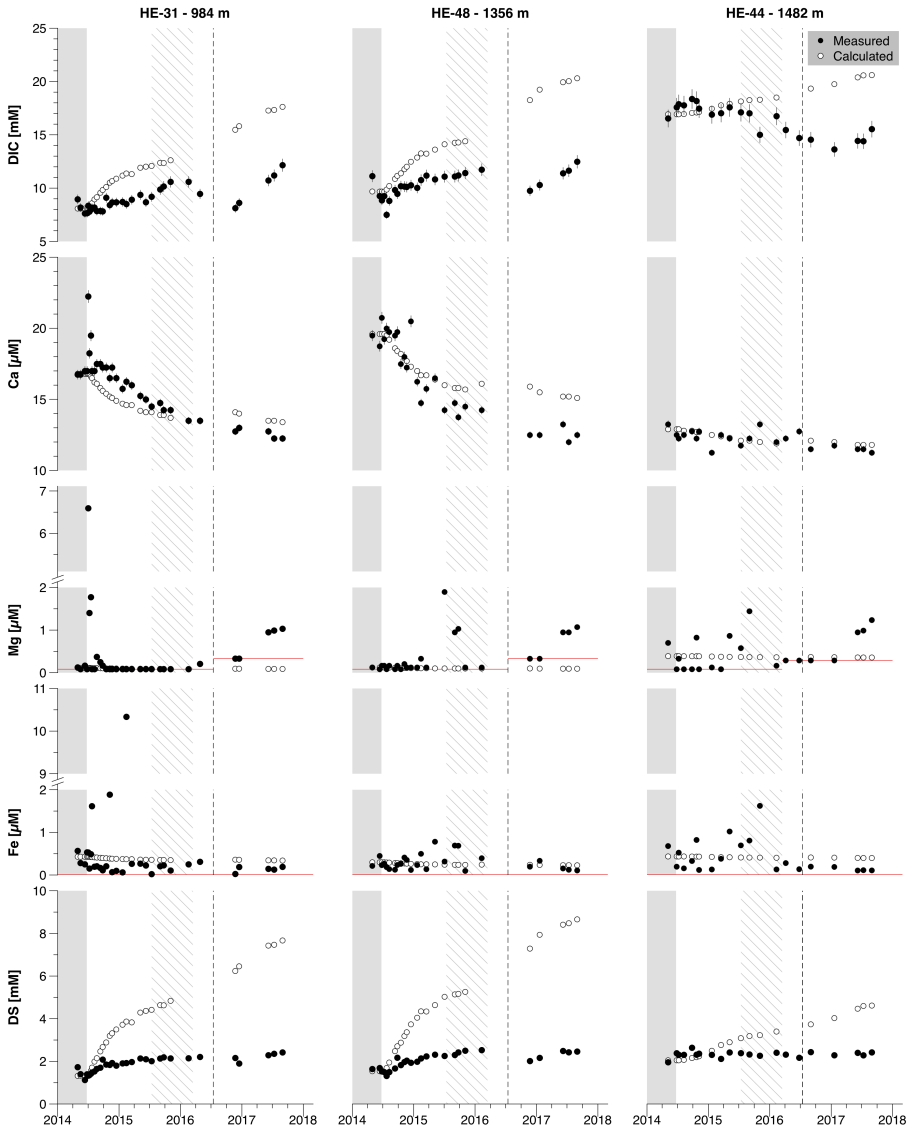

Figure 4.4. In situ concentrations of DIC, Ca, Mg, Fe, and DS in samples collected from the HE-31, HE-48, and HE-44 monitoring wells located 984, 1356, and 1482 m, respectively, from the HN-16 injection well prior to and during the injection of CO_2 and H_2S. The gray shaded area indicates the time before the injection of gas-charged waters into well HN-16, the diagonal lines denote when well HN-14 was used for the injection of gas-charged waters, and the dashed line signifies the time when the amount of CO_2 and H_2S injected was doubled. Black circles depict the measured concentrations, while the white circles correspond to concentrations calculated assuming non-reactive fluid mixing using Eqn. 4.2. The red lines are the limit of detection for Mg and Fe concentrations.

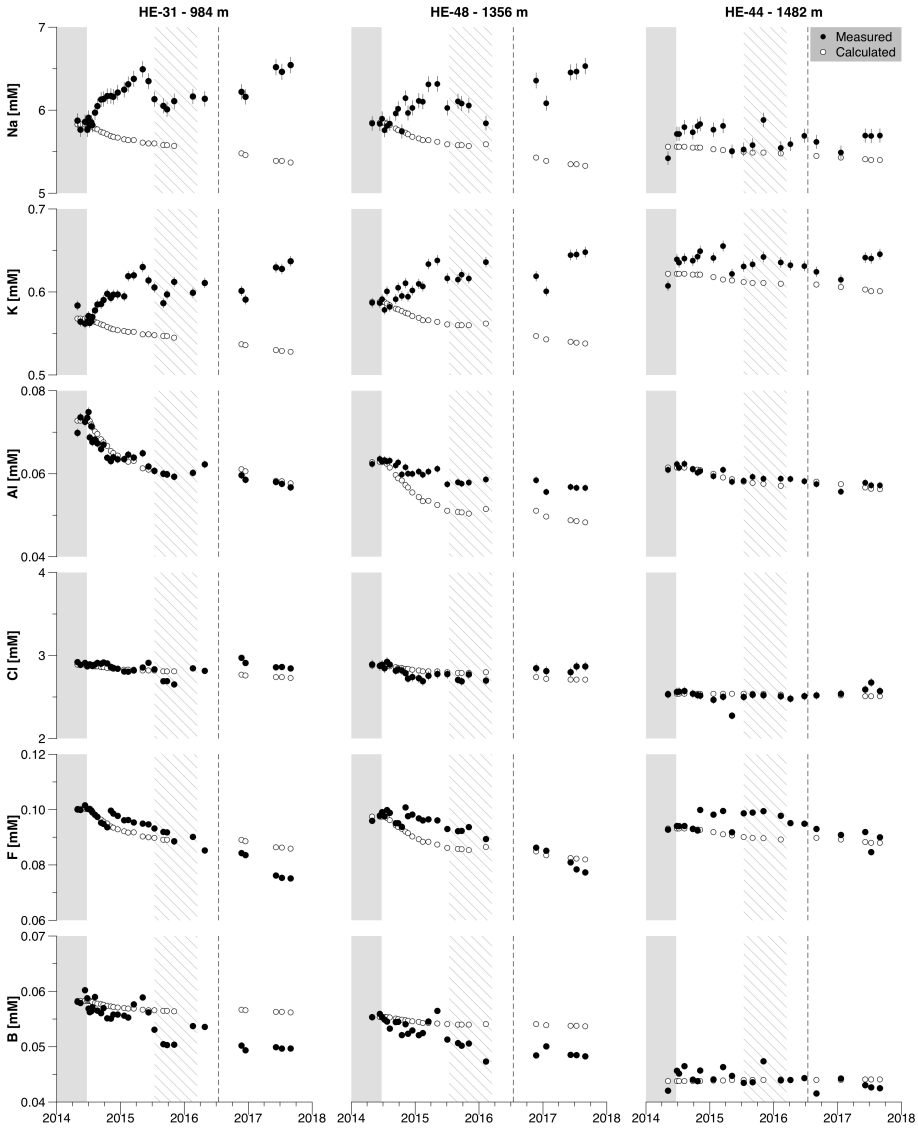

Figure 4.5. In situ concentrations of Na, K, Al, Cl, F, and B in samples collected from the HE-31, HE-48, and HE-44 monitoring wells located 984, 1356, and 1482 m, respectively, from the HN-16 injection well prior to and during the injection of CO_2 and H_2S. The gray shaded area indicates times before injection of gas-charged water into well HN-16, the diagonal lines denote when well HN-14 was used for the injection of gas-charged water, and the dashed line signifies the time when the amount of CO_2 and H_2S injected was doubled. Black circles depict the measured concentrations, while the white circles correspond to concentrations calculated assuming non-reactive fluid mixing using Eqn. 4.2.

March 2016 (a time period signified by diagonal lines in these figures), and the amount of dissolved gas injected into HN-16 was doubled on 15 July 2016, as denoted on these figures by vertical dashed lines. The gas-charged water injected into HN-14 was not observed in the monitoring wells.

The quartz temperature is reported in Fig. 4.3 along with the calculated *in situ* pH for all three wells. The pH exhibits no significant change throughout the injection, whereas the reservoir temperature shows a small decrease post-injection and compares well to previous downhole temperature measurements, for example with the temperature logs of HE-31 in Fig. C.1 in Appendix C.

Figures 4.4 and 4.5 compare the *in situ* major element concentrations as well as DIC and DS to those calculated assuming non-reactive fluid mixing using Eqn. 4.2. Of the three major divalent cations, Ca had the highest concentrations with Fe and Mg concentrations close to or at the detection limit (Fig. 4.4). Ca and Mg show a brief peak in concentration in monitoring well HE-31 upon the first arrival of the gas-charged injection water. There was a decrease in the fluid phase Ca concentrations observed in both HE-31 and HE-48 concurrent with a gradual increase in observed DIC and even a more gradual increase in DS over time. Results from HE-44 show minimal change in DS but a decrease in DIC post injection.

As seen in Fig. 4.5, both fluid Na and K concentrations increased until 2015, particularly in HE-31 and HE-48, but then these elements decreased, only increasing again when the gas injection was switched into well HN-14 and back again to HN-16. Aluminium concentrations show a similar pattern as Ca in that there was a brief peak in concentration in well HE-31 before gradually decreasing. The decline was less apparent in wells HE-48 and HE-44; these wells are further away from the injection well than HE-31. The concentration of the anions, Cl, F, and B, all changed in concentration over time, though to a much lesser extent compared to Ca and Al. The least variance between concentrations calculated from non-reactive mixing and observed concentrations was in well HE-44.

4.4.2 Saturation states of primary and secondary mineral

Saturation indices (SI) of the collected monitoring well fluids with respect to the primary minerals present in the basalt and of basaltic glass are shown in Fig. 4.6. Leached basaltic glass ($SiAl_{0.35}O_2(OH)_{1.05}$) was always undersaturated in the monitoring wells, and the doubling of the gas injection rate in 2016 had little effect on this saturation state. Magnetite, however, was supersaturated throughout the monitoring period. The plagioclase endmembers were close to saturation in the collected monitoring well fluids over the entire study period with high-albite right at saturation and anorthite just below. The injected water was undersaturated with respect to both of these plagioclase endmembers. The saturation state of monitoring well fluids with respect to clinopyroxene (augite) and orthopyroxene were mostly at saturation or supersaturated compared to their undersaturated state in the heated injected fluids. The saturation state of the olivine endmembers show the largest changes between the injection and monitoring well fluids

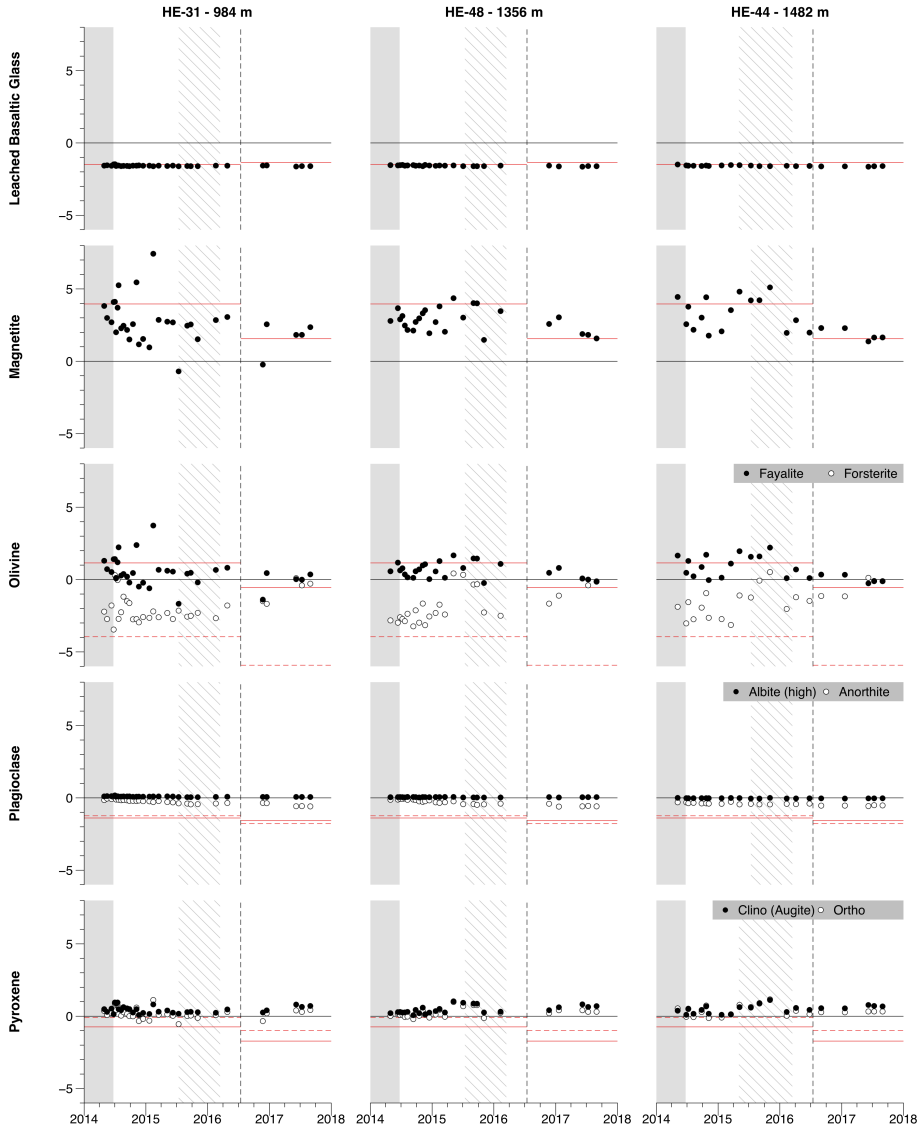

Figure 4.6. The in situ saturation indices (SI) of the fluids collected from the HE-31, HE-48, and HE-44 monitoring wells with respect to the primary minerals found in unaltered basalt at Hellisheiði – magnetite, olivine, plagioclase, and pyroxene, and leached basalt glass. The black and white symbols correspond to the saturation state of the collected fluids, the gray shaded area indicates the time prior to the injection of gas-charged waters into well HN-16, the diagonal lines denote when well HN-14 was used for the gas-charged water injection, and the vertical dashed line signifies the time when the amount of CO_2 and H_2S injected was doubled. The SI of minerals in the injected gas-charged waters, after mixing with geothermal effluent water and their heating to 260 °C, but prior to their interaction with the rock (Clark et al., 2018), are depicted as horizontal and dotted red lines. The minerals in black circles are represented by the horizontal red line and the minerals in white circles by the dotted red line.

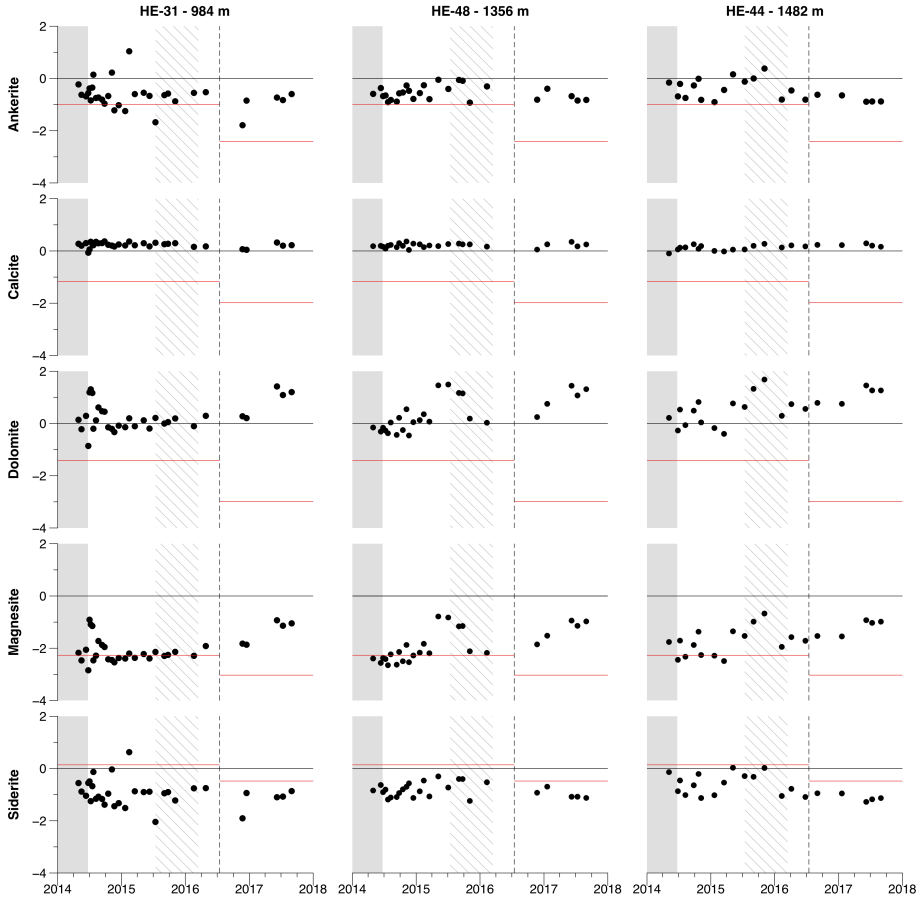

Figure 4.7. In situ saturation indices (SI) of the fluids collected from the HE-31, HE-48, and HE-44 monitoring wells with respect to the carbonate minerals – ankerite, calcite, dolomite, magnesite, and siderite. The black symbols corespond to calculated fluid saturation indexes, the gray shaded area indicates times before the injection of gas-charged water into well HN-16, the diagonal lines denote when well HN-14 was used for the injection of gas-charged waters, and the vertical dashed line signifies the time when the amount of CO_2 and H_2S injected into the subsurface was doubled. The SI of these mineral in the injected gas-charged waters, after mixing with geothermal effluent water and heating to 260 °C, but prior to their interaction with the rock (Clark et al., 2018), are depicted by horizontal red lines.

as well as the greatest variation, though fayalite was supersaturated with respect to the monitoring well fluids during the first two years of injection.

Figure 4.7 shows the saturation states of the collected monitoring well fluids with respect to various carbonate minerals – ankerite ($CaFe(CO_3)_2$), calcite ($CaCO_3$), dolomite ($CaMg(CO_3)_2$), magnesite ($MgCO_3$), and siderite ($FeCO_3$) – compared to that of the injected gas-charged fluid. Calcite was consistently at saturation or supersaturation in the monitoring well fluids. Dolomite was also at equilibrium (within uncertainty) in these fluids and then supersaturated during the second phase of gas injection. Magnesite was always undersaturated, whereas siderite and ankerite were undersaturated in these fluids with few exceptions.

The saturation indices of these fluids with respect to the iron sulfide phases, pyrite (FeS_2) and pyrrhotite (FeS), are presented in Fig. 4.8. Both minerals were supersaturated in the injection and monitoring wells fluids. They were, however, closer to saturation in the latter.

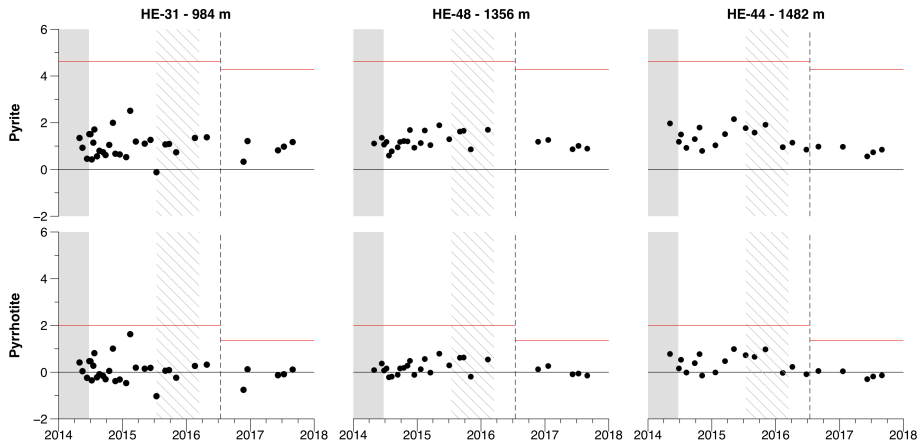

Figure 4.8. In situ saturation indices of the fluids collected from monitoring wells HE-31, HE-48, and HE-44 with respect to the sulfide minerals, pyrite and pyrrhotite. The symbols correspond to calculated saturation indexex, the gray shaded area indicates time prior to the injection of gas-charged water into well HN-16, the diagonal lines denote when when gas-charged waters were injected into well HN-14, and the vertical dashed line signifies the time when the amount of CO_2 and H_2S gas injected was doubled. The SI of these minerals in the injected gas-charged waters, after mixing with geothermal effluent water and its heating to 260 °C, but prior to their interaction with the rock (Clark et al., 2018), is depicted as horizontal red lines.

The saturation state of the subsurface fluids with respect to some of the secondary minerals commonly observed in high temperature Hellisheiði basalts are presented in Fig. 4.9. These minerals include chlorite ($(Mg/Fe)_5Al_2Si_3O_{10}(OH)_8$), epidote ($Ca_2FeAl_2Si_3O_{12}(OH)$), prehnite ($Ca_2Al_2Si_3O_{10}(OH)_2$), wairakite ($CaAl_2Si_4O_{10}(OH)_4$), wollastonite ($CaSiO_3$), and actinolite ($Ca_2(Fe/Mg)_5Si_8O_{22}(OH)_2$). Many of these min-

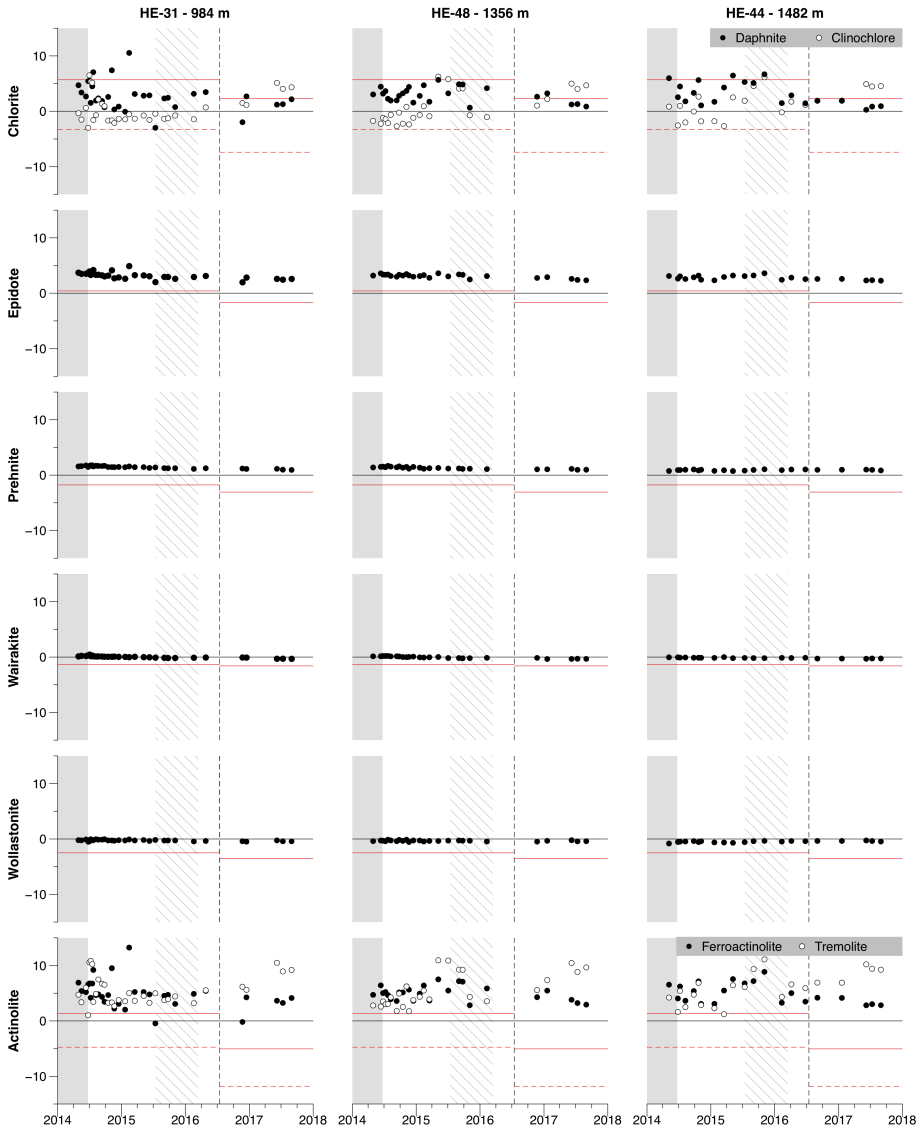

Figure 4.9. In situ saturation indices (SI) of the fluids collected from the HE-31, HE-48, and HE-44 monitoring wells with respect to secondary minerals observed in the higher temperature regions of the Hellisheiði geothermal reservoir (Snæbjörnsdóttir et al., 2018b). The gray shaded area indicates saturation states of the formation waters before injection into well HN-16, the diagonal lines denote when the HN-14 well was used for injection, and the vertical dashed line signifies the time when the amount of CO_2 and H_2S injected was doubled. The SI of minerals in the injected gas-charged waters, after mixing with geothermal effluent water and heated to 260 °C, but prior to their interaction with the rock (Clark et al., 2018), are depicted as horizontal and dotted red lines. The minerals in black circles are represented by the horizontal red line and the minerals in white circles by the dotted red line.

erals were found to be stable throughout the mixed gas injection, with epidote and prehnite supersaturated, wairakite at saturation, and wollastonite just undersaturated. The saturation states of the fluids with respect to actinolite and chlorite fluctuated with both actinolite endmembers above saturation and the Fe-chlorite endmember (daphnite) more stable. Mg-chlorite (clinochlore) became supersaturated in the subsurface fluids after doubling the gas injection.

4.4.3 Partial pressure of CO_2 and H_2S

The temporal evolution of *in situ* pCO_2 and pH_2S of the fluids collected from the monitoring wells is shown in Fig. 4.10, with red lines denoting the average pCO_2 and pH_2S in the gas-charged injection fluids before mixing and water-rock interaction in the reservoir. Both pCO_2 and pH_2S increased upon the arrival of the initial injection fluids to the first two monitoring wells. There was a noticeable drop, particularly in pCO_2, after well HN-14 was used for gas injection, before rising again after the amount of gas injected was doubled and again injected into HN-16. Results from HE-44 show minimal change in pH_2S and a small decrease in pCO_2, which was similar to the observed DIC and DS concentrations (Fig. 4.4).

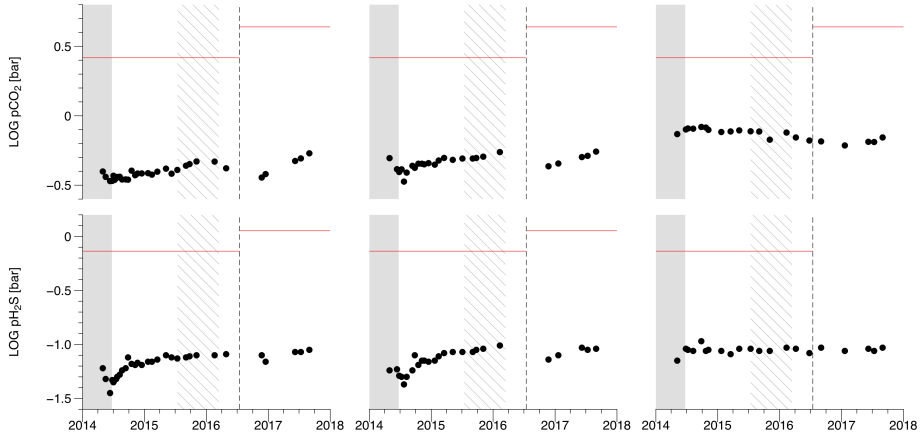

Figure 4.10. Logarithm of the in situ pCO_2 and pH_2S in the fluids collected from the HE-31, HE-48, and HE-44 monitoring wells. The gray shaded area indicates the time prior to the injection of gas-charged waters into well HN-16, the diagonal lines denote when well HN-14 was used for the gas-charged water injection, and the vertical dashed line signifies the time when the amount of CO_2 and H_2S injected was doubled. Horizontal red lines depict the logarithim of the pCO_2 and pH_2S of the injected gas-charged waters, after mixing with geothermal effluent water and heated to 260 °C, but prior to their interaction with the rock and mixing with formation waters.

4.5 Discussion

The pCO_2 and pH_2S in equilibrium with the minerals relevant for carbon and sulfur storage are plotted together with the composition of collected monitoring well samples in Fig. 4.11. Figure 4.11A confirms that the monitoring well temperatures are close to the upper stability limit of calcite at the current DIC levels. This is further supported by the mineral saturation states of the collected fluids. However, Fig. 4.11B shows that the composition of the collected monitoring well fluids are also close to the decomposition temperature of iron sulfide minerals. As pointed out by Stefánsson et al. (2011), the precipitation of pyrite and pyrrhotite is inhibited by epidote formation at temperatures above ∼260 °C, consequently requiring a larger amount of basalt dissolution for H_2S mineralization. The Eh-pH diagrams of the H_2S-H_2O-Fe system (Fig. 4.12) indicate that redox conditions in the monitoring well fluids are close to or at equilibrium with pyrite and magnetite.

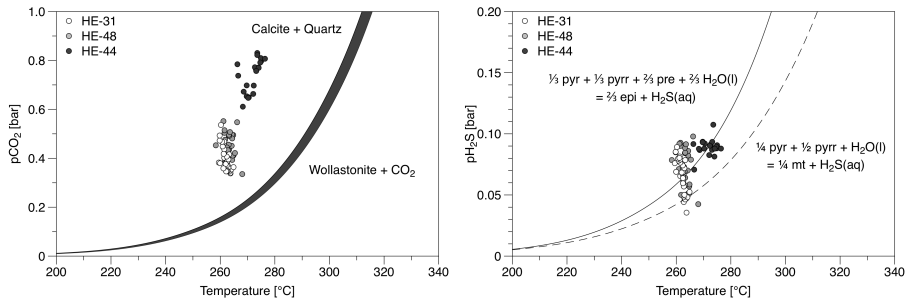

Figure 4.11. The in situ pCO_2 and pH_2S of the fluids collected from the HE-31, HE-48, and HE-44 monitoring wells plotted against the calculated reservoir temperature. Curves represent the partial pressures of the indicated gases in equilibrium as a function of temperature according to the following mineral-gas reactions: (A) the formation of wollastonite and CO_2 from calcite and quartz at fixed total pressures from 1 to 300 bars based on Skippen (1977); (B) the formation of epidote (epi) and H_2S from pyrite (pyr), pyrrhotite (pyrr), and prehnite (pre), represented by the solid curve, and the formation of magnetite (mt) and H_2S from pyrite, pyrrhotite, and H_2O, represented by the dashed curve, based on data reported by Sigfússon et al. (2007) and Stefánsson et al. (2011).

Calcium was the most abundant divalent cation in the fluid phase, but its concentration continuously decreased throughout the injection as DIC rose maintaining equilibrium with calcite. Magnesium and Fe were close to or at the detection limit, but Mg concentration increased after the injection rate was doubled (Fig. 4.4). This is similar to seawater-basalt experiments of Voigt et al. (2018b) (comparable to natural marine hydrothermal vent systems) where Ca was the most abundant cation in the fluid and any available Mg and Fe had been quickly removed and incorporated into clays. The brief peak in Ca concentration observed when the initial gas-charged water plume arrives at the monitoring well was also observed in the pure CO_2 injection at the original CarbFix site (Snæbjörnsdóttir et al., 2017) and during the arrival of the CO_2-charged waters of the column experiment mimicking this pure CO_2 injection (Clark et al., 2019). In both

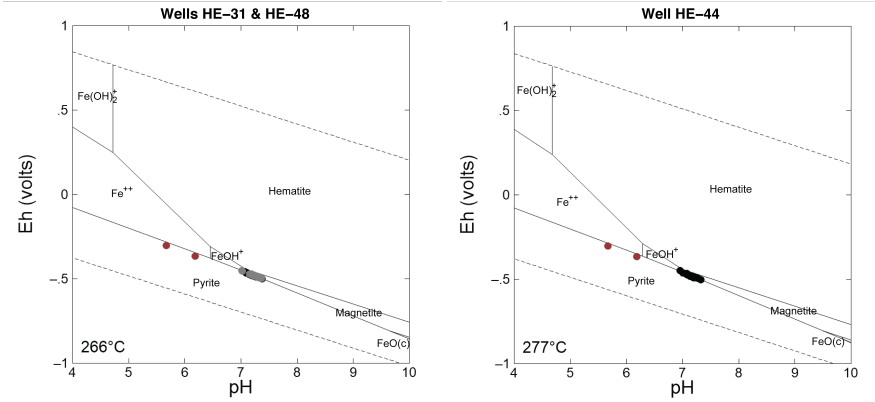

Figure 4.12. Pourbaix diagrams for the H_2S-H_2O-Fe system at (A) T = 266 °C, P = 200 bars, $a_{[H2O]}$ = 1, $a_{[Fe+2]} = 10^{-9.98}$, $a_{[SO4-2]} = 10^{-4.13}$ with the in situ compositions of fluids from the HE-31 and HE-48 monitoring wells represented by black and gray points, respectively, and (B) T = 277 °C, P = 200 bars, $a_{[H2O]}$ = 1, $a_{[Fe+2]} = 10^{-9.93}$, $a_{[SO4-2]} = 10^{-4.26}$ with the deep fluid from HE-44 represented by black points. The red points represent the gas injected waters mixed with geothermal brine within the well and heated to 260 °C (before any reaction in geothermal reservoir) and the dotted lines depict the stability limits of water. The temperature, $a_{[Fe+2]}$, and $a_{[SO4-2]}$ are based on the average temperature and fluid compositions from HE-31, HE-48, and HE-44; wells HE-31 and HE-48 were grouped together because of the similar fluid compositions and same average temperature.

field injections, this peak results in the formation of calcite as the dominant carbonate; its precipitation continues due to the constant availability of Ca. Note that the injected fluid contains three orders of magnitude more DIC than Ca (Fig. 4.4), thus the Ca required for calcite precipitation must come from the rocks. Although the decrease in measured Ca concentrations are similar to the corresponding non-reactive mixing concentrations especially during the first two years of injection, there is a steady decline in these Ca concentrations. This decline, and the fact that the dissolved Ca concentration are several orders of magnitude lower than those of DIC indicate that the release of this cation from the host rock to the fluid phase is the limiting factor for calcite precipitation. Figures 4.13 and 4.14 depict the relationship between the injection and monitoring well fluid compositions, and provide insight into the potential carbonate and other secondary minerals that form from these deep fluids. The mineral predominance diagrams of the carbonate system (Fig. 4.13) suggests that the increase in dissolved Mg concentrations and pCO_2 after the injection rate was doubled (see Figs. 4.4 and 4.10) favors dolomite precipitation. This suggestion is consistent with the greater supersaturation of these fluids with respect to dolomite after July 2016, as shown in Fig. 4.7. In contrast, thermodynamic calculations suggest that Fe will not be incorporated into siderite (Figs. 4.13C and 4.13D), which is consistent with its saturation indices (Fig. 4.7). In addition to sulphide minerals other secondary minerals, such as epidote and chlorite, likely consume the available Fe.

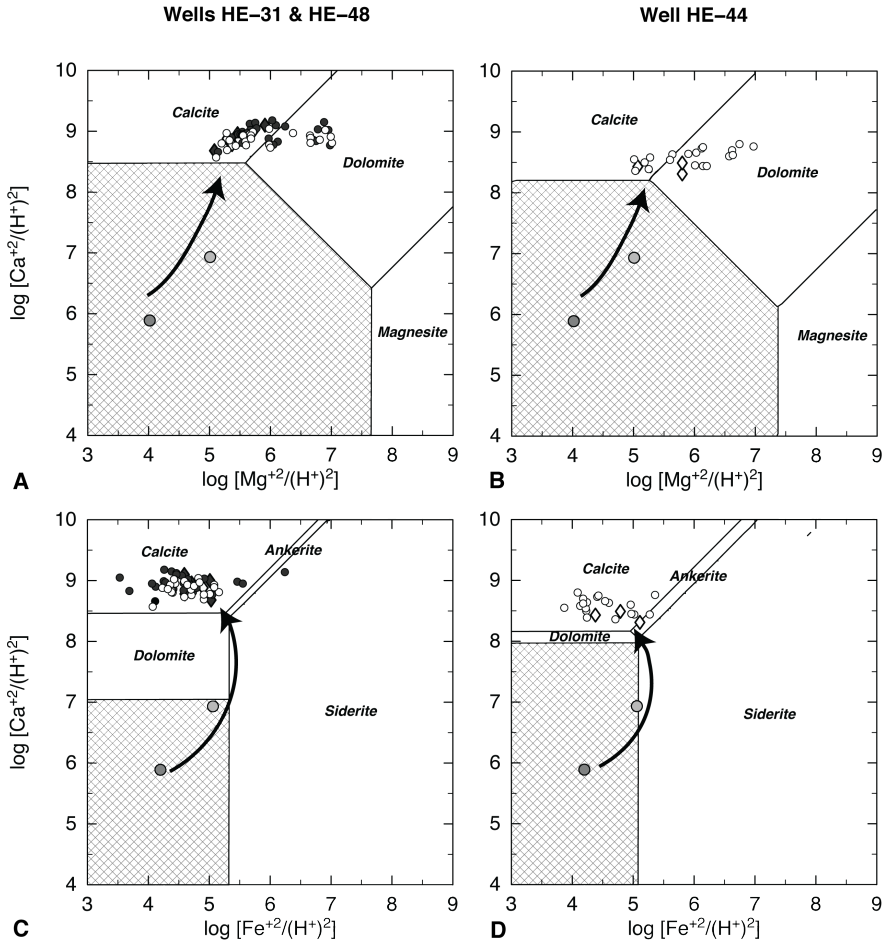

Figure 4.13. Mineral predominance diagrams among carbonate minerals in the CaO-MgO-FeO-CO_2 system for monitoring wells (A) HE-31 and HE-48 at T = 266 °C, [Fe] = 0.482 µmol/kg, and [CO_2] = 9.5 mmol/kg, and (B) HE-44 at T = 273 °C, [Fe] = 0.444 µmol/kg, and [CO_2] = 16.5 mmol/kg, and in the CaO-MgO-FeO-CO_2 system for monitoring wells (C) HE-31 and HE-48 at T = 266 °C, [Mg] = 0.489 µmol/kg, and [CO_2] = 9.5 mmol/kg, and (D) HE-44 at T = 273 °C, [Mg] = 0.522 µmol/kg, and [CO_2] = 16.5 mmol/kg. The black circles represent the in situ compositions of fluids collected from HE-31 and white circles the in situ compositions of fluids collected from HE-48 and HE-44 with the black and white diamonds depicting the in situ pre-injection fluid compositions for each well. The gray points represent the gas injected waters mixed with geothermal brine within the well and heated to 260 °C (before any further mixing and reaction in geothermal reservoir) with the light gray symbols signifying the first two years of injection and the dark gray symbols these fluids after doubling the amount of gas injected. The cross-hatched area represents fluid compositions where no stable carbonate minerals are present. The temperature, [Fe], [Mg], and [CO_2] adopted in the figure are based on the average temperature and fluid compositions from HE-31, HE-48, and HE-44; wells HE-31 and HE-48 were grouped together because of their similar fluid compositions and same average temperature.

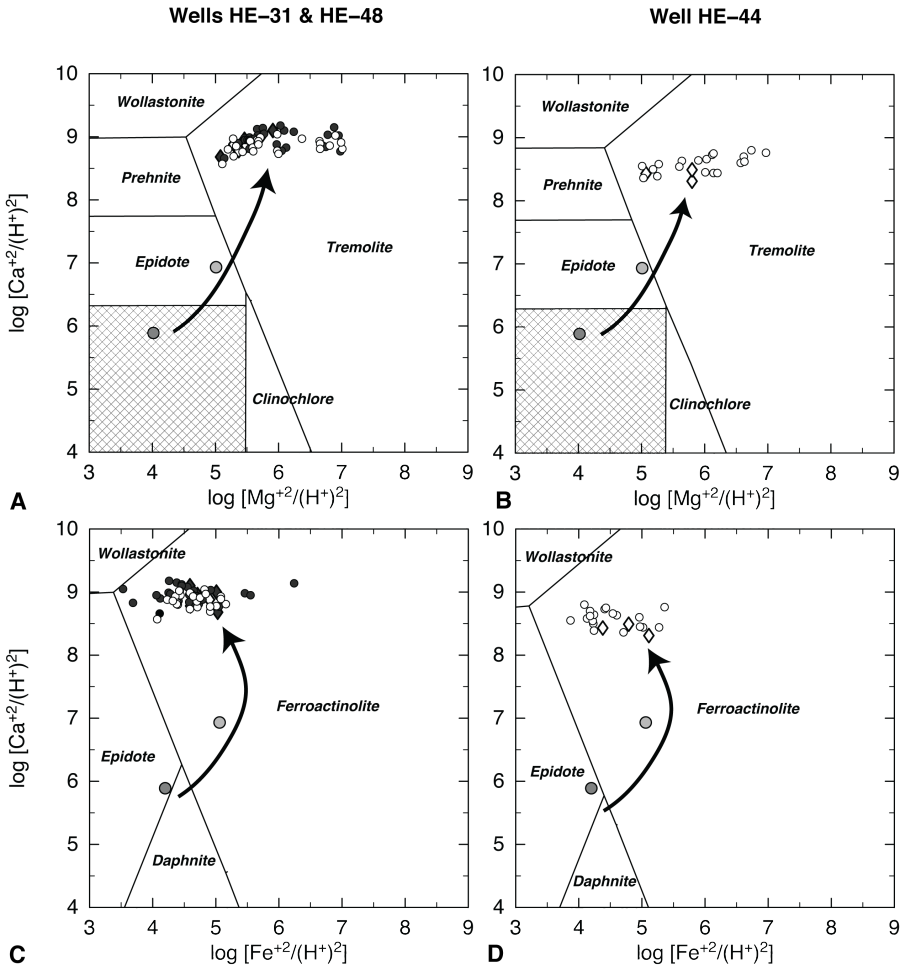

Figure 4.14. Predominance diagrams among some minerals in the CaO-MgO-FeO-Al_2O_2-SiO_2-H_2O system for monitoring wells (A) HE-31 and HE-48 at T = 266 °C, [Fe] = 0.482 µmol/kg, [Al] = 0.059 mmol/kg, and [Si] = 8.81 mmol/kg and (B) HE-44 at T = 277 °C, [Fe] = 0.444 µmol/kg, [Al] = 0.059 mmol/kg, and [Si] = 9.46 mmol/kg, and in the CaO-FeO-Al_2O_2-SiO_2-H_2O system for monitoring wells (C) HE-31 and HE-48 at T = 266 °C, [Al] = 0.064 mmol/kg, and [Si] = 8.81 mmol/kg and (D) HE-44 at T = 277 °C, [Al] = 0.059 mmol/kg, and [Si] = 9.46 mmol/kg. Black circles represent the in situ compositions of fluids collected from HE-31 and white circles the deep fluid from HE-48 and HE-44 with the black and white diamonds depicting the deep fluid pre-injection for each well. The gray points represent the gas injected waters mixed with geothermal brine and heated to 260 °C (before any reaction in geothermal reservoir) with light gray symbols signifying the first two years of injection and the dark gray symbols after doubling the amount of injected gas. The cross-hatched area represents fluid compositions where no stable minerals are present. The temperature, [Si], [Al], and [Fe] are based on the average temperature and fluid compositions from HE-31, HE-48, and HE-44; wells HE-31 and HE-48 were grouped together because of their similar fluid compositions and same average temperature.

Basalt at the CarbFix2 site before the injection was altered by high temperature fluids forming secondary minerals from the breakdown of primary minerals like basaltic glass, olivine, pyroxene, and plagioclase (Franzson et al., 2010; 2005; Snæbjörnsdóttir et al., 2018b). Olivine and basaltic glass likely alter to smectites, zeolites, chalcedony, and calcite, which was characteristic of the CarbFix pilot site (Alfredsson et al., 2013). As temperatures rise past about 200 °C, chalcedony is converted to quartz, smectites to mixed layer clays and eventually to chlorite. Since the reservoir temperatures around the main feed zones of the monitoring wells at this site are greater than 250 °C, the other primary minerals in basalt, notably plagioclase and pyroxene, are also altered. One clear sign of plagioclase alteration is the occurrence of albitization; Ca-rich plagioclase dissolves leading to albite formation (Snæbjörnsdóttir et al., 2018b), consistent with the mineral saturation indices in Fig. 4.6. Plagioclase was also altered to epidote and wairakite before the injection (Snæbjörnsdóttir et al., 2018b), as supported by their mineral saturation states reported before and after the injection in Fig. 4.9. These observations, in addition to the observed saturation of the fluids with respect to chlorite, is consistent with the fact that the monitoring wells are cased off to the transition temperatures between the mixed layer clay and the chlorite-epidote zones of alteration at 750 m depth, before the injection, with the epidote-actinolite zone below at higher temperature (Franzson et al., 2010; 2005; Snæbjörnsdóttir et al., 2018b). Additionally, the continuous net release of Na and K (Fig. 4.5) could be attributed to the dissolution of basaltic and altered basalt minerals like mixed layer clays and chlorites by their interaction with the acidic gas-charged injection waters. A similar mobility of Na and K was also observed in the original CarbFix site (Snæbjörnsdóttir et al., 2017).

Predominance diagrams of secondary minerals resulting from high temperature alteration, other than the carbonates and sulfides, are presented in Fig. 4.14. All the monitoring well samples are present in the ferroactinolite and tremolite (endmembers of actinolite) fields. The reaction path of the injected fluid likely passed through the Fe-chlorite (daphnite) and epidote fields before ending in the ferroactinolite and tremolite predominance fields during its flow from the injection well to the monitoring wells. Note that Figs. 4.14C and D represent the average temperature of the fluids as they enter the monitoring wells at 266 °C (wells HE-31 and HE-48) and 277 °C (HE-44).

Although Cl^-, F^-, and B might be expected to exhibit a conservative behavior, these anions steadily decreased in concentration from the start of injection (Fig. 4.5). While Cl^- and B only slightly deviate from their concentrations calculated assuming non-reactive fluid mixing using Eqn. 4.3, there was a larger variance in B accompanied by a small peak in concentrations, notably in HE-31 and HE-48. This peak is concurrent with an increase in Na, K, and Al, suggesting the dissolution of silicate minerals. Several studies describe the potential uptake of these anions by carbonate minerals, particularly calcite. According to Kitano et al. (1975), calcite can incorporate chloride and fluoride during precipitation, while the uptake of boron has been extensively studied in Ca and Mg carbonates (e.g. Hemming et al., 1995; Saldi et al., 2018). Experiments by Turner et al. (2005) also suggest fluoride adsorption onto the surfaces of calcite in addition to fluorite precipitation, though the reservoir fluids were undersaturated with respect to fluorite (data not shown). Moreover, as there are trace amounts of phosphorus in

basaltic glass (Oelkers and Gíslason, 2001) and Ca phosphate had been observed in CO_2-H_2S sequestration experiments by Marieni et al. (2018), phosphate minerals could also consume fluoride upon the dissolution of the basalt. Thus, the minor fluctuations in B, Cl^-, and F^- concentrations, could be attributed to dissolution of carbonate minerals already in the reservoir as the injected gas-charged water plume moves towards the monitoring wells. Subsequent carbonate precipitation could then incorporate trace amounts of these anions.

4.6 Implications

4.6.1 Timescale of carbon and sulfur mineralization

At the original CarbFix site, where temperatures ranged from 20 to 50 °C and the acidity of the injected gases drove mineral reactions, chemical equilibrium with most minerals was only attained after more than three months after CO_2 injection (Snæbjörnsdóttir et al., 2017). H_2S sequestration experiments from Přikryl et al. (2018) suggest that at higher temperatures (> 200 °C) H_2S-fluid-mineral equilibrium is attained relatively fast compared to temperatures of ∼100 °C. In this study, minerals such as calcite and iron sulfides attained equilibrium in the first two monitoring wells, HE-31 and HE-48, within one month of the start of injection in June 2014 in a > 250 °C geothermal reservoir, as indicated by their saturation indices in Figs. 4.7 and 4.8. Furthermore, the stability of these minerals, in addition to the high temperature alteration minerals, epidote and actinolite, was not perturbed when gas injection switched from well HN-16 to HN-14 in July 2015 and when the amount of gas injected was doubled in July 2016.

Gunnarsson et al. (2018) reported that over 50% of the injected CO_2 and 76% of the injected H_2S were mineralized within a few months of continuous flow between the injection well and the first monitoring well, up to November 2015. This was based on mass balance calculations. Using the same approach, when the amount of injected gas was doubled in July 2016, we calculate that over 60% of injected CO_2 and over 85% of injected H_2S were mineralized within four months after the gas-charged waters are continuously injected into the CarbFix2 site. This enhanced mineralization at CarbFix2, despite the decline in Ca concentrations, resulted from the increased acidity in the injected fluids and fewer secondary minerals reaching supersaturation within the injection well (Clark et al., 2018) along with the increased water-rock interaction nearer to the monitoring wells (Tables to). For comparison, mineralization of more than 95% of injected CO_2 at the Wallula Basalt pilot site occurred within two years of injection (Matter et al., 2016; McGrail et al., 2017a, 2017b; Snæbjörnsdóttir et al., 2017).

This study thus further demonstrates the mineral carbonation of carbon via the CarbFix method is significantly faster than other common geological carbon storage methods by orders of magnitude. In the latter, CO_2 is stored for long periods of time in deep geological formations, such as depleted oil and gas reservoirs, coal formations, and saline formations. Over time, the injected CO_2 becomes less mobile through multiple trapping mechanisms, going from structural and stratigraphic trapping to solubility and

mineral trapping (Benson and Cole, 2008). However, mineral trapping of the injected CO_2 in these sedimentary basins, if it occurs, can take tens of thousands of years, limited by the low reactivity of silicate minerals in sedimentary rocks and the lack of Ca-, Mg-, and Fe-bearing minerals for carbonation (Gilfillan et al., 2009; Gíslason and Oelkers, 2014).

4.6.2 Storage capacity

The total volume of mineral precipitation can be estimated by noting that one ton of CO_2 would create 0.84 m^3 of calcite and one ton of H_2S would create 0.70 m^3 of pyrite (Gunnarsson et al., 2018). If all the gas injected into the CarbFix2 site from June 2014 to December 2017 precipitated as calcite and pyrite, these minerals would have a total volume of about 29,000 m^3. As the target reservoir at Hellisheiði has a volume of 6 $\times$ 10^8 m^3, the precipitated calcite and pyrite would only consume 0.005 vol percent of the reservoir. If some of the available divalent cations were incorporated with the secondary minerals like epidote and actinolite instead of carbonates, these would still only take up less than 0.002 vol percent of the volume of the target basaltic reservoir (see Appendix C for further explanation). Overall, mineralization would constitute a relatively small volume compared to the reservoir size and thus likely negligibly affect its permeability. Note, however, that secondary mineral precipitation could still create new fractures, thereby maintaining or enhancing the permeability (Jamtveit et al, 2009; Ulven et al., 2014). It is also likely that the relatively cold injection fluids (62 °C) compared to reservoir temperature (> 250 °C), and the 9 bar overpressure at the well head, could result in thermal- and hydro-fracturing of the rock near the injection well. Such possibilities are consistent with induced seismic activity (Gunnarsson et al., 2015b) and the observations that the permeability of the target reservoir systems has remained close to constant over the 3.5 year injection period.

The Hellisheiði geothermal reservoir has a storage potential of up to 5,200 Mt CO_2 (Sigfússon et al., 2018) and 2.6 Mt H_2S (Prikryl et al., 2018). Considering Iceland emitted 7.1 Mt CO_2 in 2017, excluding agriculture, forestry, and other land use (Keller et al., 2019), and the country's geothermal energy sector emitted 19,000 tonnes H_2S in 2016 (Sigfússon et al., 2018), much less than 1% of the storage potential at Hellisheiði could be utilized each year for just the CO_2 and H_2S emissions from Iceland. Furthermore, taking ino account the distribution of natural carbon fixation in Iceland's geothermal systems, Snæbjörnsdóttir et al. (2014) estimated that 953–2,470 Gt CO_2 could be stored in basaltic rocks in the active rift zones of Iceland, many orders of magnitude larger than Iceland's annual emissions. When taking into account the world's mid-oceanic basalt ridges, the storage capacity is on the order of 100,000 to 250,000 Gt CO_2 (Snæbjörnsdóttir et al., 2014). This storage potential is thus notably even larger than the 18,500 Gt CO_2 that can be attributed to the burning of all fossil fuel carbon on Earth (Archer, 2005), thereby highlighting that even with the substantial storage capacity within Iceland, the largest potential for CO_2 storage is offshore.

4.6.3 Temperature limitations for carbon and sulfur mineralization in meteoric water

Reaction path modelling of the low temperature (20–50 °C) CO_2 injection at the original CarbFix site indicates that the initial carbon mineralization might have begun with siderite precipitation at pH ∼5, then mixtures of Fe-, Mg-, and Ca-carbonates may form with increasing pH and decreasing pCO_2, followed by calcite at the highest pH and lowest pCO_2 (Snæbjörnsdóttir et al., 2018a). As the pH of the fluids collected from the original CarbFix monitoring well was > 8, only calcite was observed in the well (Snæbjörnsdóttir et al., 2017). The rise in pCO_2 and Mg concentrations in the CarbFix2 monitoring well samples collected in the present study after doubling the gas injection rate in July 2016 forced the monitoring fluids into dolomite's stability field (Fig. 4.7), suggesting greater fluid-rock interaction closer to the monitoring wells, and as previously mentioned, enhanced mineralization.

The temperature of the CarbFix2 target basaltic reservoir is close to that of the upper temperature limit of ∼280 °C for CO_2-H_2S mineral sequestration has been reached in this CarbFix2 target basaltic reservoir. Although the reservoir temperatures are stable and current DIC levels indicate calcite formation in Fig. 4.11A, injection at temperatures at 280 °C or higher would result in the precipitation of wollastonite rather than the mineralization of CO_2. The same applies to sulfide precipitation as the fluids would favor epidote and magnetite precipitation at these temperatures (Fig. 4.11B). Nevertheless, the long-term success of the CarbFix2 subsurface mineralization testifies to the ability to store significant quantities of carbon and sulfur securely through mineral reactions from 20 °C up to ∼260 °C.

4.6.4 Alteration of basaltic crust

Based on this study, it is clear that the consumption of CO_2 by the dissolution of Ca-containing silicates in basaltic rocks coupled to calcite precipitation is rapid. Iceland is the largest part of the oceanic ridge system that is above sea level. From geological and surface water maps of Iceland, a relationship between the age of basalts and their permeability is evident. There is nearly no surface runoff within the rift zone. The number of streams and rivers noticeably increases outside of Iceland's rift zone, which contains basalt rocks younger than 0.8 million years; the basalts surrounding this zone are not older than 3.3 million years (Gíslason, 2008; Jóhannesson, 2014). Though this indicates a long timeframe for silicate weathering on the Earth's surface at ambient temperatures, it is an important sink for atmospheric CO_2 (Brady and Gíslason, 1997; Gíslason et al., 1996; 2009).

The low temperature (< 60 °C) alteration of the oceanic crust from hydrothermal circulation is another important sink for CO_2 (Alt and Teagle, 1999; Brady and Gíslason, 1997; Coogan and Gillis, 2018). Alteration of these basalts is considered to occur within 10–20 million years of its initial formation (Brady and Gíslason, 1997; Coogan et al., 2016; Muehlenbachs, 1977), although they are already pervasively altered by 3.2 million years (Muehlenbachs, 1977; Muehlenbachs and Hodges, 1978).

The rapid formation of carbonates and silicates within the young and fractured basalts at the CarbFix and CarbFix2 sites in Iceland suggests that such alteration reactions occur over timescales of months to years rather than millions of years, when the subsurface systems are perturbed by external forcing at 20 to ∼260 °C.

4.7 Conclusions

The results summarized above show that the carbon and sulphur mineralization at the CarbFix2 site in Hellisheiði, Iceland continue successfully and without slowing over the first 3.5 years of continued gas injection into this site. In fact, the efficiency of the mineralization has increased over time. During the first phase of injection, over 50% of injected carbon and 76% of sulfur mineralized within four to nine months according to mass balance calculations. These percentages increased, after the amount of gas injected was doubled; during the second phase of the injection over 60% of carbon and over 85% of sulfur were mineralized. The increased mineralization is likely due to the increased acidity of the injection fluid after the increase in gas concentration in the condensate water, resulting in enhanced dissolution in the vicinity of the injection well.

Notably, despite 3.5 years of injecting a CO_2-H_2S charged fluids for their mineralization into subsurface basaltic rock, there is no sign of a decrease in the permeability of the target reservoir. There are likely several reasons for this. First, the injection fluids are acidic and undersaturated with respect to the minerals present in the target reservoir. This will tend to open fluid pathways near the injection wells. Second, the volume of carbonate- sulfide- and other secondary minerals precipitating in the target aquifer was relatively small compared to the size of the reservoir (no more than a total of 0.025 volume percent of the target reservoir). Finally, new fractures may have formed as a result of pressure and temperature gradients close to the injection well induced by the injection of cooler gas-charged fluids.

Based on mineral saturation states and predominance diagrams, the principal carbonates precipitating in the subsurface were calcite and potentially dolomite. Siderite was at saturation after the injected fluid was heated to > 250 °C and therefore may be the first carbonate to reach saturation and potentially precipitate. Once the gas-charged injection fluids reached the monitoring wells, these fluids were saturated with respect to Ca-rich carbonates, typical for relatively low pCO_2 and high pH (Clark et al., 2019; Rogers et al., 2006; Snæbjörnsdóttir et al., 2018a). The significant decrease in Ca concentrations was observed over time as DIC increased consistent with calcite saturation. As Ca and Mg concentrations were orders of magnitude lower than DIC, the release of these metals to the fluid phase likely limits carbonation in this system.

Acknowledgements

This publication has been produced with support from the European Commission through the projects CarbFix (EC Project 283148), CO2-React (EC Project 317235), CarbFix2 (EC Project 764760), S4CE (EC Project 764810). Special thanks to Reykjavik Energy, particularly Þorsteinn A. Þorgeirsson for all the fun sampling trips as well as S.S. Sigurðardóttir, T. Kristinsson, H. Bergmann, V. Eiríksdóttir, C. Marieni, and F. Jónsdóttir. We would also like to acknowledge Jón Örn Bjarnason for his invaluable assistance in addition to Iwona Galeczka, Martin Voigt, Thomas Ratouis, Joaquín Muñoz-Cobo Belart, and the CarbFix group for their support.

4.8 References

Alfredsson, H.A., Oelkers, E.H., Harðarsson, B.S., Franzson, H., Gunnlaugsson, E. and Gíslason, S.R. (2013) The geology and water chemistry of the Hellisheidi, SW-Iceland carbon storage site. *International Journal of Greenhouse Gas Control* 12, 399–418.

Alt, J.C. and Teagle, D.A.H. (1999) The uptake of carbon during alteration of ocean crust. *Geochimica et Cosmochimica Acta* 63, 1527–1535.

Aradóttir, E.S.P., Gunnarsson, I., Sigfússon, B., Gíslason, S.R., Oelkers, E.H., Stute, M., Matter, J.M., Snæbjörnsdóttir, S.Ó., Mesfin, K., Alfredsson, H.A., Hall, J., Arnarson, M.T., Dideriksen, K., Júliusson, B.M., Broecker, W.S. and Gunnlaugsson, E. (2015) Towards Cleaner Geothermal Energy: Subsurface Sequestration of Sour Gas Emissions from Geothermal Power Plants, World Geothermal Congress 2015, Melbourne, Australia.

Archer, D. (2005) Fate of fossil fuel CO_2 in geologic time. *Journal of Geophysical Research* 110, C09S05.

Arnórsson, S., Bjarnason, J.O., Giroud, N., Gunnarsson, I. and Stefánsson, A. (2006) Sampling and analysis of geothermal fluids. *Geofluids* 6, 203–216.

Arnórsson, S., Sigurdsson, S. and Svavarsson, H. (1982) The chemistry of geothermal waters in Iceland. I. Calculation of aqueous speciation from 0°C to 370°C. *Geochimica et Cosmochimica Acta*46, 1513–1532.

Arnórsson, S., Stefánsson, A. and Bjarnason, J.O. (2007) Fluid-Fluid Interactions in Geothermal Systems. *Reviews in Mineralogy and Geochemistry* 65, 259–312.

Arnórsson, S., Axelsson, G. and Sæmundsson, K. (2008) Geothermal systems in Iceland. *Jökull* 58, 269–302.

Benson, S.M. and Cole, D.R. (2008) CO_2 sequestration in deep sedimentary formations. *Elements* 4, 325–331.

Benson, S.M. and Cook, P. (2005) Underground geological storage, IPCC Special Report on Carbon Dioxide Capture and Storage. Cambridge University Press, Cambridge, U.K.

Bjarnason, J.O. and Arnórsson, S. (2010) The chemical speciation program WATCH, 2.4 ed.

Brady, P.V. and Gíslason, S.R. (1997) Seafloor weathering controls on atmospheric CO_2 and global climate. *Geochimica et Cosmochimica Acta* 61, 965–973.

Clark, D.E., Galeczka, I., Dideriksen, K., Voigt, M., Wolff-Boenisch, D. and Gíslason, S.R. (2019) Experimental observations of CO_2-water-basaltic glass interaction in a large column reactor experiment at 50°C. *International Journal of Greenhouse Gas Control* 89, 9–19.

Clark, D.E., Gunnarsson, I., Aradóttir, E.S., Arnarson, M.Þ., Þorgeirsson, Þ.A., Sigurðardóttir, S.S., Sigfússon, B., Snæbjörnsdóttir, S.Ó., Oelkers, E.H. and Gíslason, S.R. (2018) The chemistry and potential reactivity of the CO_2-H_2S charged injected waters at the basaltic CarbFix2 site, Iceland. *Energy Procedia* 146, 121–128.

Coogan, L.A. and Gillis, K.M. (2018) Low-Temperature Alteration of the Seafloor: Impacts on Ocean Chemistry. *Annual Review of Earth and Planetary Sciences* 46, 21–45.

Coogan, L.A., Parrish, R.R. and Roberts, N.M.W. (2016) Early hydrothermal carbon uptake by the upper oceanic crust: Insight from in situ U-Pb dating. *Geology* 44, 147–150.

Fournier, R.O. and Potter, R.W. (1982) A revised and expanded silica (quartz) geothermometer. *Geothermal Resources Council Bulletin*, 3–9.

Franzson, H., Gunnlaugsson, E., Árnason, K., Sæmundsson, K., Steingrímsson, B. and Harðarsson, B.S. (2010) The Hengill Geothermal System, Conceptual Model and Thermal Evolution, World Geothermal Congress 2010, Bali, Indonesia.

Franzson, H., Kristjánsson, B.R., Gunnarsson, G., Björnsson, G., Hjartarson, A., Steingrímsson, B., Gunnlaugsson, E. and Gíslason, G. (2005) The Hengill-Hellisheiði Geothermal Field. Development of a Conceptual Geothermal Model, World Geothermal Congress 2005, Antalya, Turkey.

Gilfillan, S.M.V., Lollar, V.S., Holland, G., Blagburn, D., Stevens, S., Schoell, M., Cassidy, M., Ding, Z., Zhou, Z., Lacrampe-Couloume, G. and Ballentine, C.J. (2009) Solubility trapping in formation water as dominant CO_2 sink in natural gas fields. *Nature* 458, 614–618.

Gíslason, S.R. (2008) Weathering in Iceland. *Jökull* 58, 387–408.

Gíslason, S.R. and Oelkers, E.H. (2014) Carbon Storage in Basalt. *Science* 344, 373–374.

Gíslason, S.R., Arnórsson, S. and Ármannsson, H. (1996) Chemical weathering of basalt in southwest Iceland: effects of runoff, age of rocks and vegetative/glacial cover. *American Journal of Science* 296, 837–907.

Gíslason, S.R., Oelkers, E.H., Eiriksdóttir, E.S., Kardjilov, M.I., Gísladóttir, G., Sigfússon, B., Snorrason, A., Elefson, S., Harðardóttir, J., Torssander, P. and Óskarsson, N. (2009) Direct evidence of the feedback between climate and weathering. *Earth and Planetary Science Letters* 277, 213–222.

Goldberg, D., Aston, L., Bonneville, A., Demirkanli, I., Evans, C., Fisher, A., Garcia, H., Gerrard, M., Heesemann, M., Hnottavange-Telleen, K., Hsu, E., Malinverno, C. Moran, K., Park. A.-H., Scherwath, M., Slagle, A., Stute, M., Weathers, T., Webb, R., White, M., White, S. and the CarbonSAFE Cascadia Project Team. (2018) Geological storage of CO2 in sub-seafloor basalt: the CarbonSAFE pre-feasibility study offshore Washington State and British Columbia. *Energy Procedia* 146, 158–165.

Gunnarsson, I., Aradóttir, E.S., Oelkers, E.H., Clark, D.E., Arnarson, M.Þ., Sigfússon, B., Snæbjörnsdóttir, S.Ó., Matter, J.M., Stute, M., Júlíusson, B.M. and Gíslason, S.R. (2018) The rapid and cost-effective capture and subsurface mineral storage of carbon and sulfur at the CarbFix2 site. *International Journal of Greenhouse Gas Control* 79, 117–126.

Gunnarsson, I. and Arnórsson, S. (2000) Amorphous silica solubility and the thermodynamic propoerties of H_4SiO_4 in the range of 0 to 350°C at Pamt. *Geochimica et Cosmochimica Acta* 64, 2295–2307.

Gunnarsson, I., Júliusson, B.M., Aradóttir, E.S., Sigfússon, B. and Arnarson, M.Þ. (2015a) Pilot Scale Geothermal Gas Separation, Hellisheiði Power Plant, Iceland, World Geothermal Congress, Melbourne, Australia.

Gunnarsson, G., Kristjánsson, B.R., Gunnarsson, I. and Júlíusson, B.M. (2015b) Reinjection into a Fractured Reservoir – Induced seismicity and other challenges in operating reinjection wells in the Hellisheiði field, SW-Iceland, World Geothermal Congress 2015, Melbourne, Australia.

Hemming, N.G., Reeder, R.J. and Hanson, G.N. (1995) Mineral-fluid partitioning and isotopic fractionation of boron in snythetic calcium carbonate. *Geochimica et Cosmochimica Acta* 59, 371–379.

Jamtveit, B., Putnis, C.V. and Malthe-Sørenssen, A. (2009) Reaction induced fracturing during replacement processes. *Contributions to Mineralogy and Petrology* 157, 127–133.

Jóhannesson, H. (2014) Geological Map of Iceland – Bedrock Geology – 1:600 000. Icelandic Institute of Natural History.

Keller, N., Stefani, M., Einarsdóttir, S.R., Helgadóttir, Á.K., Guðmundsson, J., Snorrason, A., Þórsson, J. and Tinganelli, L. (2019) National Inventory Report. The Environment Agency of Iceland.

Kinniburgh, D. and Cooper, D. (2011) PhreePlot: Creating graphical output with PHREEQC.

Kitano, Y., Okumura, M. and Idogaki, M. (1975) Incorporation of sodium, chloride and sulfate with calcium carbonate. *Geochemical Journal* 9, 75–84.

Marieni, C., Přikryl, J., Aradóttir, E.S., Gunnarsson, I. and Stefánsson, A. (2018) Towards 'green' geothermal energy: Co-mineralization of carbon and sulfur in geothermal reservoirs. *International Journal of Greenhouse Gas Control* 77, 96–105.

Matter, J.M., Stute, M., Snæbjörnsdóttir, S.Ó., Oelkers, E.H., Gíslason, S.R., Aradóttir, E.S., Sigfússon, B., Gunnarsson, I., Sigurðardóttir, H., Gunnlaugsson, E., Axelsson, G., Alfredsson, H.A., Wolff-Boenisch, D., Mesfin, K., Fernandez de la Reguera Taya, D., Hall, J., Dideriksen, K. and Broecker, W.S. (2016) Rapid carbon mineralization for permanent disposal of anthropogenic carbon dioxide emissions. *Science* 352, 1312–1314.

McGrail, B.P., Schaef, H.T., Ho, A.M., Chien, Y.-J., Dooley, J.J. and Davidson, C.L. (2006) Potential for carbon dioxide sequestration in flood basalts. *Journal of Geophysical Research: Solid Earth* 111.

McGrail, B.P., Schaef, H.T., Spane, F.A., Cliff, J.B., Qafoku, O., Horner, J.A., Thompson, C.J., Owen, A.T. and Sullivan, C.E. (2017a) Field Validation of Supercritical CO2 Reactivity with Basalts. *Environmental Science & Technology Letters* 4,

6–10.
McGrail, B.P., Schaef, H.T., Spane, F.A., Horner, J.A., Owen, A.T., Cliff, J.B., Qafoku, O., Thompson, C.J. and Sullivan, E.C. (2017b) Wallula Basalt Pilot Demonstration Project: Post-injection Results and Conclusions. *Energy Procedia* 114, 5783–5790.
Muhlenbachs, K. (1977) Low temperature alteration oxygen isotope exchange between oceanic crust and seawater. Proceedings 2nd International Symposium Water-Rock Interaction, 317–326.
Muhlenbachs, K. and Hodges F.N. (1978) Oxygen isotope geochemistry of rocks from DSDP leg 46. In Initial Report of the Deep Sea Drilling Project (46) (ed. L. Dmitriev et al.) pp. 257–258. U.S. Gov't Print. Office.
Neveu, M., Desch, S.J. and Castillo-Rogez, J.C. (2017) Aqueous geochemistry in icy world interiors: Equilibrium fluid, rock, and gas compositions, and fate of antifreezes and radionuclides. *Geochimica et Cosmochimica Acta* 212, 324–371.
Oelkers, E.H., Butcher, R., Pogge von Strandmann, P.A.E., Schuessler, J.A., von Blanckenburg, F., Snæbjörnsdóttir, S.Ó., Mesfin, K., Aradóttir, E.S., Gunnarsson, I., Sigfússon, B., Gunnlaugsson, E., Matter, J.M., Stute, M. and Gíslason, S.R. (2019a) Using stable Mg isotope signatures to assess the fate of magnesium during the in situ mineralisation of CO_2 and H_2S at the CarbFix site in SW-Iceland. *Geochimica et Cosmochimica Acta* 245, 542–555.
Oelkers, E.H. and Gíslason, S.R. (2001) The mechanism, rates and consequences of basaltic glass dissolution: I. An experimental study of the dissolution rates of basaltic glass as a function of aqueous Al, Si and oxalic acid concentration at 25°C and pH = 3 and 11. *Geochimica et Cosmochimica Acta* 65, 3671–3681.
Oelkers, E.H., Pogge von Strandmann, P.A.E. and Mavromatis, V. (2019b) The rapid resetting of the Ca isotopic signatures of calcite at ambient temperature during its congruent dissolution, precipitation, and at equilibrium. *Chemical Geology* 512, 1–10.
Parkhurst, D.L. and Appelo, C.A.J. (2013) Description of Input and Examples for PHREEQC Version 3 - A Computer Program for Speciation, Batch-Reaction, One-Dimensional Transport, and Inverse Geochemical Calculations, in: Survey, U.S.G. (Ed.), Techniques and Methods, p. 497.
Pogge von Strandmann, P.A.E., Burton, K.W., Snæbjörnsdóttir, S.Ó., Sigfússon, B., Aradóttir, E.S., Gunnarsson, I., Alfredsson, H.A., Mesfin, K.G., Oelkers, E.H. and Gíslason, S.R. (2019) Rapid CO_2 mineralisation into calcite at the CarbFix storage site quantified using calcium isotopes. *Nature Communications* 10, 1983.
Power, I.M., Harrison, A.L., Dipple, G.M., Wilson, S.A., Kelemen, P.B., Hitch, M. and Southam, G. (2013) Carbon Mineralization: From Natural Analogues to Engineered Systems. *Reviews in Mineralogy and Geochemistry* 77, 305–360.
Přikryl, J., Marieni, C., Gudbrandsson, S., Aradóttir, E.S., Gunnarsson, I. and Stefánsson, A. (2018) H_2S sequestration process and sustainability in geothermal systems. *Geothermics* 71, 156–166.
Rogers, K.L., Neuhoff, P.S., Pedersen, A.K. and Bird, D.K. (2006) CO_2 metasomatism in a basalt-hosted petroleum reservoir, Nuussuaq, West Greenland. *Lithos* 92, 55–82.
Saldi, G.D., Noireaux, J., Louvat, P., Faure, L., Balan, E., Schott, J. and Gaillardet, J. (2018) Boron isotopic fractionation during adsorption by calcite – Implication for

the seawater pH proxy. *Geochimica et Cosmochimica Acta* 240, 255–273.

Sigfússon, B., Arnarson, M.Þ., Snæbjörnsdóttir, S.Ó., Karlsdóttir, M.R., Aradóttir, E.S. and Gunnarsson, I. (2018) Reducing emissions of carbon dioxide and hydrogen sulphide at Hellisheidi power plant in 2014–2017 and the role of CarbFix in achieving the 2040 Iceland climate goals. *Energy Procedia* 146, 135–145.

Sigfússon, B., Gíslason, S.R., Matter, J.M., Stute, M., Gunnlaugsson, E., Gunnarsson, I., Aradóttir, E.S., Sigurðardóttir, H., Mesfin, K., Alfredsson, H.A., Wolff-Boenisch, D., Arnarson, M.T. and Oelkers, E.H. (2015) Solving the carbon-dioxide buoyancy challenge: The design and field testing of a dissolved CO_2 injection system. *International Journal of Greenhouse Gas Control* 37, 213–219.

Skippen, G.B. (1977) Dehydration and decarbonation equlibria, in: Greenwood, H.J. (Ed.), Application of Thermodynamics to Petrology and Ore Deposits. Short Course (Vol. 2). Mineralogical Association of Canada. Evergreen Press Limited, Vancouver.

Snæbjörnsdóttir, S.Ó., Gíslason, S.R., Galeczka, I.M. and Oelkers, E.H. (2018a) Reaction path modelling of in-situ mineralisation of CO_2 at the CarbFix site at Hellisheidi, SW-Iceland. *Geochimica et Cosmochimica Acta* 220, 348–366.

Snæbjörnsdóttir, S.Ó., Oelkers, E.H., Mesfin, K., Aradóttir, E.S., Dideriksen, K., Gunnarsson, I., Gunnlaugsson, E., Matter, J.M., Stute, M. and Gíslason, S.R. (2017) The chemistry and saturation states of subsurface fluids during the in situ mineralisation of CO_2 and H_2S at the CarbFix site in SW-Iceland. *International Journal of Greenhouse Gas Control* 58, 87–102.

Snæbjörnsdóttir, S.Ó., Tómasdóttir, S., Sigfússon, B., Aradóttir, E.S., Gunnarsson, G., Niemi, A., Basirat, F., Dessirier, B., Gíslason, S.R., Oelkers, E.H. and Franzson, H. (2018b) The geology and hydrology of the CarbFix2 site, SW-Iceland. *Energy Procedia* 146, 146–157.

Snæbjörnsdóttir, S.Ó., Wiese, F. Fridriksson, T., Ármansson, H., Einarsson, G.M., and Gíslason, S.R. (2014). CO_2 storage potential of basaltic rocks in Iceland and the oceanic ridges. *Energy Procedia* 63, 4585–4600.

Stefánsson, A., Arnórsson, S., Gunnarsson, I., Kaasalainen, H. and Gunnlaugsson, E. (2011) The geochemistry and sequestration of H_2S into the geothermal system at Hellisheidi, Iceland. *Journal of Volcanology and Geothermal Research* 202, 179–188.

Tómasdóttir, S. (2018) Flow Paths in the Húsmúli Reinjection Zone, Iceland, Department of Earth Sciences. MSc Thesis, Uppsala University, Uppsala, Sweden.

Turner, B.D., Binning, P. and Stipp, S.L.S. (2005) Fluoride Removal by Calcite: Evidence for Fluorite Precipitation and Surface Adsorption. *Environmental Science & Technology* 39, 9561–9568.

Ulven, O.I., Jamveit, B. and Malthe-Sørenssen, A. (2014) Reaction-driven fracturing of porous rocks. *Journal of Geophysical Research: Solid Earth* 119, 7473–7485.

Voigt, M., Marieni, C., Clark, D.E., Gíslason, S.R. and Oelkers, E.H. (2018a) Evaluation and refinement of thermodynamic databases for mineral carbonation. *Energy Procedia* 146, 81–91.

Voigt, M., Pearce, C.R., Baldermann, A. and Oelkers, E.H. (2018b) Stable and radiogenic strontium isotope fractionation during hydrothermal seawater-basalt interaction. *Geochimica et Cosmochimica Acta* 240, 131–151.

Wolff-Boenisch, D. and Galeczka, I.M. (2018) Flow-through reactor experiments on basalt-(sea)water-CO_2 reactions at 90°C and neutral pH. What happens to the basalt pore space under post-injection conditions? *International Journal of Greenhouse Gas Control* 68, 176–190.

5 Paper IV

Mobility of trace metals following the injection of CO_2-H_2S gas mixture into basaltic rocks at 250°C

Deirdre E. Clark, Iwona M. Galeczka, Eric H. Oelkers, Bergur Sigfússon, Ingvi Gunnarsson, Sandra Ó. Snæbjörnsdóttir, Edda S. Aradóttir, and Sigurður R. Gíslason

To be submitted to Chemical Geology

Abstract

The trace element geochemistry of geothermal fluids from the CarbFix2 monitoring wells were assessed. Basaltic rock dissolution is known to release trace elements, and have been extensively studied in Icelandic geothermal systems. However, little is known on the potential mobility as a consequence of CO_2-H_2S gas injection into basaltic rocks. The results presented here suggest the mobilization and uptake of several trace elements, specifically Ba, Sr, Mn, As, Sb, and Mo in addition to transition metal elements (e.g. Cu, Cr, Ni). Carbonates and sulfides likely incorporated these elements in addition to secondary minerals such as epidote and actinolite. Moreover, though this fluid is not meant for consumption, the trace elements were generally not above WHO, EU, and Iceland drinking water standards with the main exception of As. However, while As was significantly elevated at the start of gas injection, concentrations have since been greatly reduced over time to levels at or below drinking water standards.

5.1 Introduction

A portion of the CO_2 and H_2S emissions from the Hellisheidi geothermal power plant in Iceland has been injected into geothermally altered basalts using the CarbFix method since June 2014 (Clark et al., submitted; Gunnarsson et al., 2018). This approach captures the geothermal gases in water in a scrubbing tower adjacent to the gas source before transportation to the injection site (Sigfússon et al., 2018). The injection of the acidic gas-charged water in basaltic rocks accelerates its dissolution, which release divalent cations, Ca^{2+}, Mg^{2+}, and Fe^{2+}, to the injected waters. Subsequent reactions with the dissolved CO_2 and H_2S form stable carbonate and sulfide minerals (Gíslason and Oelkers, 2014; Stefánsson et al., 2011).

Trace elements are known to be also released via basaltic rock dissolution, especially in the early stages of water-rock interaction while the pH is still low (Flaathen et al., 2009; Galeczka et al., 2013). Their distribution in liquid and vapor phases of geothermal fluids as well as the processes controlling their geochemistry have been extensively studied in Iceland (Arnórsson and Andrésdóttir, 1995; Arnórsson and Óskarsson, 2007; Kaasalainen and Stefánsson, 2012; Kaasalainen et al., 2015; Libbey and Williams-Jones, 2016; Markússon and Stefánsson, 2011; Olsen et al., 2010; Arnórsson and Arnórsson, 2005; Thomas et al., 2016), and elsewhere (Aiuppa et al., 2000a; 2000b; 2005; Christensen et al., 1983; Gurav et al., 2015; Karakaya et al., 2007; Migdisov and Bychkov, 1998). Natural analogues of trace metal mobility and scavenging during CO_2-rich fluid-basalt interaction were examined by Flaathen et al. (2009) and Olsson et al. (2014). Trace element concentrations from the Carbfix pilot project are also available in an appendix of Snæbjörnsdóttir (2017). In addition, Thomas et al. (2016) considers the potential implications for carbon mineralization in Icelandic geothermal reservoirs with regards to trace elements. The study suggests that CO_2-rich fluids promotes the dissolution of hydrothermal sulfide minerals (enriched in trace elements like As) and the transport of trace elements through the aqueous phase. Accordingly, the mobility of trace metals would be dependent on the amount of dissolved inorganic carbon in the fluid, the resulting pH, and the presence of secondary Fe-oxyhydroxides and clays.

By the end of 2017, 23,200 metric tons CO_2 and 11,800 metric tons of H_2S had been injected to a depth of 750 m. Results from the monitoring of the dissolved CO_2 and H_2S, major elements, and divalent cations in the wells downstream from the injection well have been reported by Gunnarsson et al. (2018) and Clark et al. (submitted). They state that the injection has remained stable throughout the 2014–2017 monitoring period, with mineralization rates accelerated by the high temperatures and enhanced carbon and sulfur mineralization after the doubling of gas injection rates in July 2016.

This study follows the geochemical monitoring data presented by Clark et al. (submitted), which assessed the magnitude of carbon and sulfur mineralization of the CarbFix2 project using major and minor element concentrations. Here the trace element concentrations are reported to investigate the potential mobility of trace elements following CO_2-H_2S injection in basalts at temperatures higher than 250 °C.

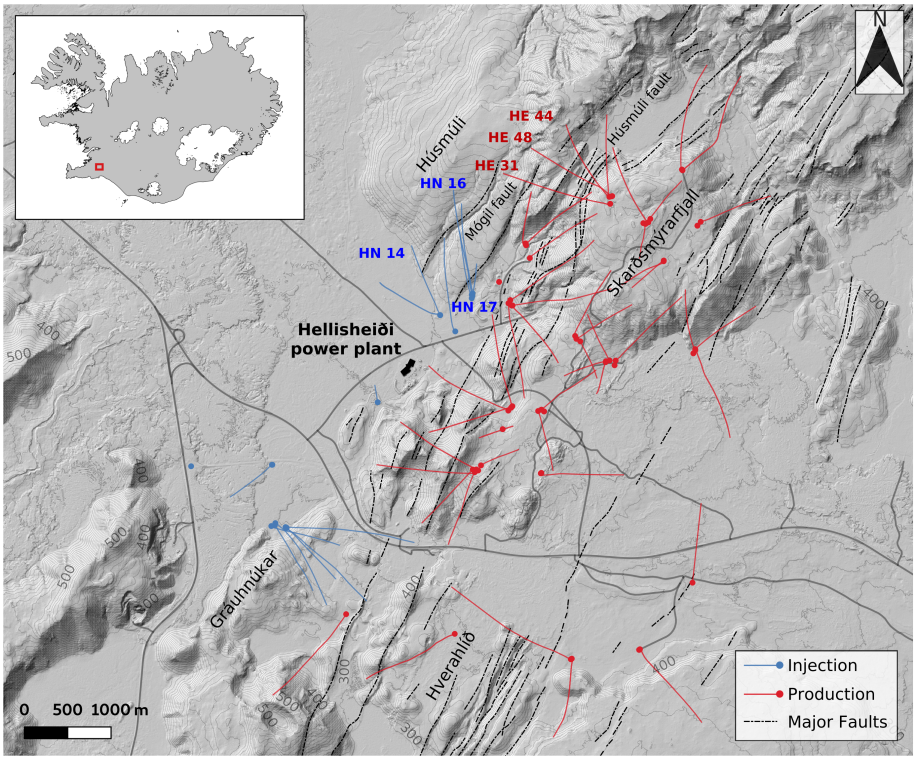

Figure 5.1. An overview of the CarbFix2 injection site. The gas separation plant is located at the Hellisheiði power in the center of the figure. A 1.5 km long, gas-charged water pipe connects the gas capture plant to the injection wells. Injection was into wells HN-16 and HN-14, which are directionally drilled as shown by the line from the surface location. The three monitoring wells (HE-31, HE-48, and HE-44), also directionally drilled, are located from one to two km down gradient from the injection well.

5.2 CarbFix2

The CarbFix2 project captured and injected 23,200 metric tons of CO_2 and 11,800 metric tons of H_2S from the Hellisheiði geothermal power plant into fractured, geothermally altered basalts. The injection site is located 1.5 km north of the power plant (Fig. 5.1), where the gas was injected to a depth of 750 m at temperatures higher than 250 °C. A description of the hydrology and the alteration of the rocks before the CarbFix2 injection is written by Snæbjörnsdóttir et al. (2018).

The gas injection is divided into two distinct phases, which is described by Clark et al. (submitted) and Sigfússon et al. (2018). From 23 June 2014 to 15 July 2016, approximately 25% of the exhaust gas from the power plant was dissolved into 20 °C condensate (condensed steam from the power plant). The CO_2 and H_2S charged condensate water was then transported to injection wells HN-16 or HN-14 (Fig. 5.1).

During the second phase of injection from 15 July 2016, the scrubbing tower gas capture capacity was doubled and injected only into well HN-16. The injection wells already inject power plant effluent water, thus the gas-charged condensate water was injected separately into a 4“ stainless steel pipe within the carbon steel pipe of the well (Clark et al., 2018). Flow rates of the injection wells are reported in Sigfússon et al. (2018) and the effluent and gas-charged condensate water composition in Clark et al. (2018). Clark et al. (submitted) notes that the gas mixture injected into HN-14 from 15 July 2014 to 14 March 2015 flowed outside the CarbFix2 site and was not observed in the monitoring wells. Three geothermal production wells, HE-31, HE-48, and HE-44 (Fig. 4.1), were used as monitoring wells, with the first geochemical results published by Gunnarsson et al. (2018) and expanded by Clark et al. (submitted).

5.3 Methods

5.3.1 Sampling and analysis

A total of 76 geothermal fluid samples were collected in 2014–2017 from three wet-steam wells at the Hellisheiði Geothermal Power Plant. The samples were collected and analyzed according to methods previously described in detail by Arnórsson et al. (2006) and Clark et al. (submitted), and are briefly described here. The vapor and liquid samples were separated using a stainless steel Webre separator. To prevent boiling of the water during the collection of the liquid samples, the separator was connected to a stainless steel cooling coil; this brings the temperature down well below 100 °C (Arnórsson et al., 2006).

Major element concentrations were analyzed in filtered and acidified (1.0 vol % concentrated suprapure HNO_3) water samples using Spectro Ciros Vision ICP-OES and a Thermo Scientific iCAPQc ICP-MS. Additional subsamples were taken to measure Cl^-, F^-, and $SO_4{}^{2-}$ using a Dionex ICS-2000 Chromatography system. Vapor samples were collected into evacuated gas-bulbs containing a 5–10 mL 50% aqueous KOH solution and measured using a HP-Molesieve column and Thermal Conductivity Detector. Dissolved inorganic carbon (DIC) and H_2S in both liquid and vapor phases were determined by titration; detailed sampling and analysis methods are in Arnórsson et al. (2006).

For the present study, water subsamples for trace element analysis were also collected and acidified with concentrated supra-pure HNO_3 (1.0 vol %) and measured by ICP-MS. Analytical uncertainties were on the order of $\leq 5\%$ and the detection limits listed in the Supplementary Material. These samples may be contaminated with the trace elements in steel (Co, Cr, Mn, Ni, V) and Fe. However, as sulphide phases deposit easily from geothermal fluids when boiling and cooling, a protective coating is created between the fluid and the steel in the casing, thus the leaching of the casing and wellhead equipment material is not considered significant (Arnórsson et al., 2006). Moreover, each monitoring well has its own cooling coil and approximately 4–5 liters of geothermal fluid was flushed through the Webre separater and cooling coil during the rinsing and collection

of other water samples before a subsample was collected for trace element analysis.

5.3.2 Geochemical calculations

The WATCH speciation program (Arnórsson et al., 1982; Bjarnason and Arnórsson, 2010) was used to re-calculate the major element concentrations of the downhole, or reservoir, fluids before phase segregation from the liquid and vapor phase samples collected at the surface (Clark et al., submitted). The reservoir temperature was calculated using a silica geothermometer equation (Gunnarsson and Arnórsson, 2000), and the pH from the sum of the concentrations of the anions of the weak acids and their complexes (a measure of alkalinity) of both the steam and liquid phases (Bjarnason and Arnórsson, 2010).

The three monitoring wells are liquid enthalpy wells (Gunnarsson et al., 2018), therefore the vapor fraction at the sample collection pressure was determined assuming adiabatic boiling from the reservoir temperature to the sampling pressure (Arnórsson et al., 2007). Trace element concentrations were then calculated with the following equation using the vapor fraction computed by the WATCH program:

$$C_{i,fluid} = C_{i,liquid} \cdot (1 - X) + C_{i,vapor} \cdot X \tag{5.1}$$

where C designates the concentration of the component emphi, and X stands for the vapor fraction at the sampling pressure. Boiling and phase segregation may lead to the partitioning of some trace elements such as B, As, Cu, Hg, Mo, and Sb (Giroud, 2008; Glover, 1988; Heinrich, 2007; Kaasalainen and Stefánsson, 2012; Neely et al., 2018), however negligible amounts of metals in the low density vapor would form upon low pressure boiling of geothermal fluids (Heinrich, 2007). Therefore the concentration of trace elements was assumed to be zero in the vapor phase.

5.4 Monitoring and mobility of trace elements

The aqueous trace element concentrations of geothermal fluid samples are reported for each monitoring well (HE-31, HE-48, and HE-44) in Tables D.1 to D.9. The evolution of selected trace elements from 2014–2017 are grouped together and shown in Figs. 5.2–5.5. Sampling of the geothermal reservoir fluid began on 29 April 2014, prior to the gas-charged water injection on 23 June; these pre-gas injection samples are highlighted in gray. Injection of gas-charged water occurred mainly into well HN-16, except from 15 July 2015 to 15 March 2016 (a time period signified by diagonal lines in these figures), and the amount of dissolved gas injected into HN-16 was doubled on 15 July 2016, as denoted on these figures by vertical dashed lines. The gas-charged water injected into HN-14 was not observed in the monitoring wells (Clark et al., submitted). The range of trace element concentrations from Hellisheiði geothermal well fluid samples collected in 2008 (Stefánsson et al., 2009) were also plotted in Figs. 5.2–5.5 as the blue shaded area and the average plotted as a vertical dark blue line. These samples serve as background concentrations for this study.

5.4.1 Alkali metal elements Li, Rb, and Cs

Lithium, Rb, Cs, and V concentrations, as shown in Fig. 5.2, were mostly within or near the range of 2008 background samples, with some outliers. There was a clear drop in Li in 2017 after the gas injection doubled. Overall, Rb displays a slight increase in concentration and Cs shows no significant change throughout the study period.

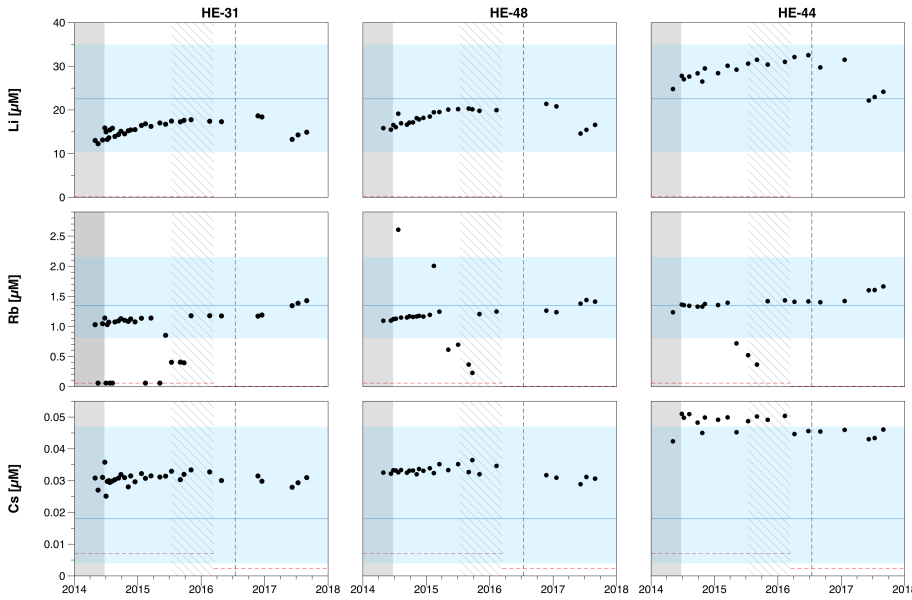

Figure 5.2. In situ concentrations of Li, Rb, and Cs collected from the HE-31, HE-48, and HE-44 monitoring wells located 984, 1356, and 1482 m, respectively, from the HN-16 injection well prior to and during the injection of CO_2 and H_2S. The gray shaded area indicates times before injection of gas-charged water into well HN-16, the diagonal lines denote when well HN-14 was used for the injection of gas-charged water, and the dashed line signifies the time when the amount of CO_2 and H_2S injected was doubled. The red horizontal dashed lines indicate the limit of detection. The blue shaded area represents the range of concentrations in 2008 Hellisheiði geothermal well samples reported by Stefánsson et al. (2009) with the average concentration depicted as a the blue vertical line.

Concentrations of Li, Rb, and Cs (alkali metals) increase with increasing temperature (Christensen et al., 1983; Kaasalainen et al., 2015), which is reflected by the difference in concentrations between HE-31 and HE-48 at average temperatures of 266 °C compared to HE-44 at an average temperature of 277 °C (Fig. 5.2). These trace alkali metals are the most mobile in geothermal reservoir fluids, although less mobile than B (Kaasalainen et al., 2015), leaching from silicates, such as olivines, pyroxenes, and feldspars (Berger et al., 1988; Ellis and Mahon, 1967). They can be scavenged by several common geothermal alteration minerals like feldspars, clays, and zeolites (Berger et al., 1988; Christensen et al., 1983; Goguel, 1983) as well as Li into quartz (Goguel, 1983). Kaasalainen et al. (2015) also highlights a systematic relationship with the major alkali

elements, Na and K, suggesting that the trace akalis follow Na and K evolution upon fluid-rock interaction.

5.4.2 Alkaline metal elements Ba and Sr

Barium concentrations were within the 2008 background levels with a slow decrease over time in the first two wells, HE-31 and HE-48 (Fig. 5.3). Strontrium was mostly higher than the 2008 background range in HE-31 and HE-48 and sharply rose in concentration in all three wells after the gas injection was doubled in Fig. 5.3; this matched the increase in Mg concentrations observed by Clark et al. (submitted).

Minor amounts of Sr have been measured in epidote, calcite, anhydrite, and zeolites like heulandite from Icelandic geothermal systems (Exley, 1982; Fridriksson et al., 2009; Marks et al., 2010); there is no current data available for Ba in secondary minerals from Iceland. Both elements are known to form sulfate and carbonate minerals, but can also be incorporated into carbonates and sulfates as well as substituting for Ca in major alteration minerals (Gurav et al., 2015; Kaasalainen and Stefánsson, 2012; Kaasalainen et al., 2015). Furthermore, Kaasalainen et al. (2015) and Gurav et al. (2015) observe a systematic relationship between Sr and Ca, with Sr following Ca upon fluid-rock interaction; a similar trend is possible between Ba and Ca, though the relationship is not well-defined.

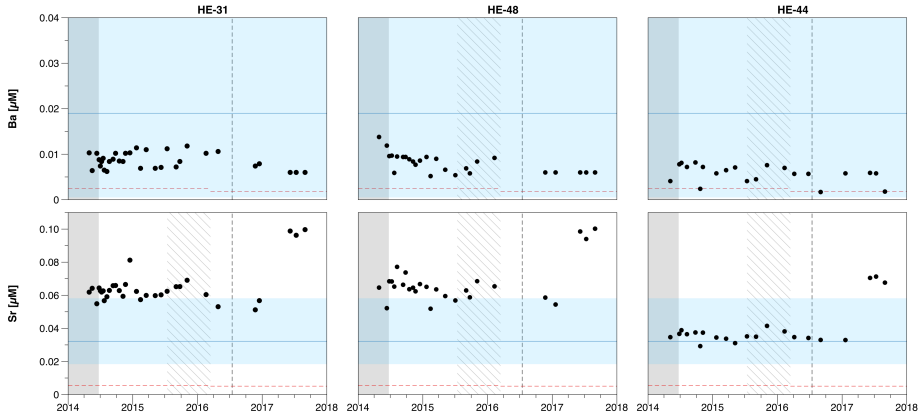

Figure 5.3. In situ concentrations of Ba and Sr collected from the HE-31, HE-48, and HE-44 monitoring wells located 984, 1356, and 1482 m, respectively, from the HN-16 injection well prior to and during the injection of CO_2 and H_2S. The gray shaded area indicates times before injection of gas-charged water into well HN-16, the diagonal lines denote when well HN-14 was used for the injection of gas-charged water, and the dashed line signifies the time when the amount of CO_2 and H_2S injected was doubled. The red horizontal dashed lines indicate the limit of detection. The blue shaded area represents the range of concentrations in 2008 Hellisheiði geothermal well samples reported by Stefánsson et al. (2009) with the average concentration depicted as a the blue vertical line.

5.4.3 Trace elements As, Sb, and Mo

All three trace elements, As, Sb, and Mo, show a significant drop in concentration after one year of gas injection in Fig. 5.4, with the majority of the subsequent samples close to at their respective detection limits (note there was also a significant change in Sb's detection limit in 2016 and 2017). Arsenic and Mo both had similar levels of concentrations in 2014 to the 2008 background samples, but from 2015 were below this range, and in the case of As at or below the World Health Organization (WHO) guideline value for safe drinking water (WHO, 2017). Antimony concentrations during the first phase of gas injection were well above the 2008 background levels, which are close to the detection limit of the second gas injection phase. After the hiatus of gas injection into HN-14 where the gas-charged injection fluid did not reach the monitoring wells (Clark et al., submitted), As briefly increased in concentrations in all three monitoring wells. The three elements displayed no change in concentration after the gas injection was doubled in July 2016, rather concentrations continued to stay near or at the detection limit.

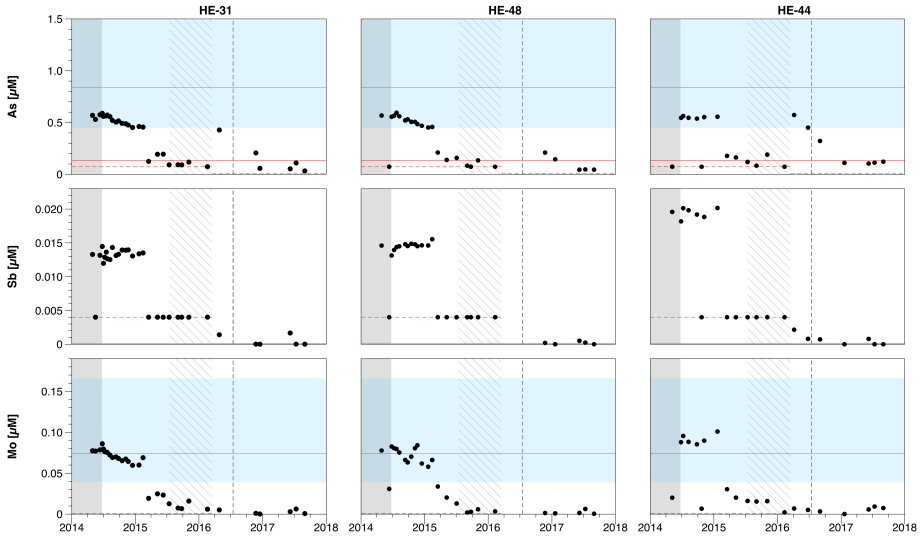

Figure 5.4. In situ concentrations of As, Sb, and Mo collected from the HE-31, HE-48, and HE-44 monitoring wells located 984, 1356, and 1482 m, respectively, from the HN-16 injection well prior to and during the injection of CO_2 and H_2S. The gray shaded area indicates times before injection of gas-charged water into well HN-16, the diagonal lines denote when well HN-14 was used for the injection of gas-charged water, and the dashed line signifies the time when the amount of CO_2 and H_2S injected was doubled. The red vertical line indicates the World Health Organization guideline value for safe drinking water (As) and red horizontal dashed lines the limit of detection. The blue shaded area represents the range of concentrations in 2008 Hellisheiði geothermal well samples reported by Stefánsson et al. (2009) with the average concentration depicted as a the blue vertical line.

Arsenic, Sb, and Mo are typically contained in primary Fe-Ti minerals (magnetite, ilmentite, titanomagnetite) of basalt (Arnórsson, 2003; Arnórsson and Óskarsson, 2007; Ellis and Mahon, 1964; Onishi and Sandell, 1955; Stefánsson and Arnórsson, 2005) and are highly mobile in geothermal reservoir fluids, increasing with temperature and progressive water-rock interaction (Arnórsson, 2003; Arnórsson and Óskarsson, 2007; Christensen et al., 1983; Stefánsson and Arnórsson, 2005). This mobility can be limited by their uptake into sulfide phases (Kaasalainen et al., 2015). Arsenic is known to be incorporated into pyrite (Abraitis et al., 2004; Ballantyne and Moore, 1988; Christensen et al., 1983; Libbey and Williams-Jones, 2016; O'Day, 2006) and can be mobilized during hydrothermal alteration and then sequestered within Fe-sulfide minerals (Thomas et al., 2016). Antimony behaves similarly to As, also co-precipitating with pyrite (Abraitis et al., 2004; Christensen et al., 1983; Libbey and Williams-Jones, 2016). Molybdenum is rapidly removed from solution in H_2S-rich waters and can be incorporated into clay minerals (i.e. illite, Fe-bearing kaolinite and montmorillonite) and sulfides like pyrite, pyrrhotite (Abraitis et al., 2004; Kendall et al., 2017; Libbey and Williams-Jones, 2016) and chalcopyrite (Neely et al., 2018).

5.4.4 Transition metal elements Mn, Cu, Ni, Cr, and V

The concentrations of the transition metals, Cu, Ni, and Cr, fluctuated throughout the study period, with the higher concentrations above the 2008 background range (Fig. 5.5). Small fluctuations in Mn concentrations were also observed in Fig. 5.5, though mostly within the range of background values. Copper shows a peak after gas injection, decreasing over time with concentrations close to or at the detection limit after the gas injection was doubled. There was no clear trend in Ni and Cr concentrations, although there was greater variation from 2015. Figure 5.5 shows V slowly decreased over time in HE-31, while constant in HE-48 and HE-44 at the lower background range.

Typically present in low concentrations in geothermal reservoir fluids, the low mobility of the transition elements suggest that they are largely scavenged into secondary minerals (Kaasalainen et al., 2015) and not present at concentrations high enough to form pure phases (Kaasalainen and Stefánsson, 2012). Manganese is a trace element in clinopyroxene in basalt rocks (Klein and Dutrow, 2008) and chlorite and epidote from Icelandic geothermal systems (Exley, 1982; Lonker et al., 1993), and can substitute for Ca and Mg in carbonates (Klein and Dutrow, 2008). Possible sources for Ni include pyrite, clinopyroxene (Thomas et al., 2016), and olivine (Galoisy et al., 1995), and Cu has been measured in sulfides like chalcopyrite (Hardardóttir et al., 2010). Copper as well as Ni can be co-precipitated in sulfides like pyrite (Abraitis et al., 2004; O'Day, 2006). Chromium may be present in Fe-containing primary minerals like titanomagnetite, and incorporated into Fe-containing minerals, such as ferrihydrite (Stefánsson et al., 2015). These elements as well as V (amongst other transition elements like Cd, Pb, Se, Zn) have been detected in pyrite samples from the Reykjanes geothermal system in Iceland (Libbey and Williams-Jones, 2016).

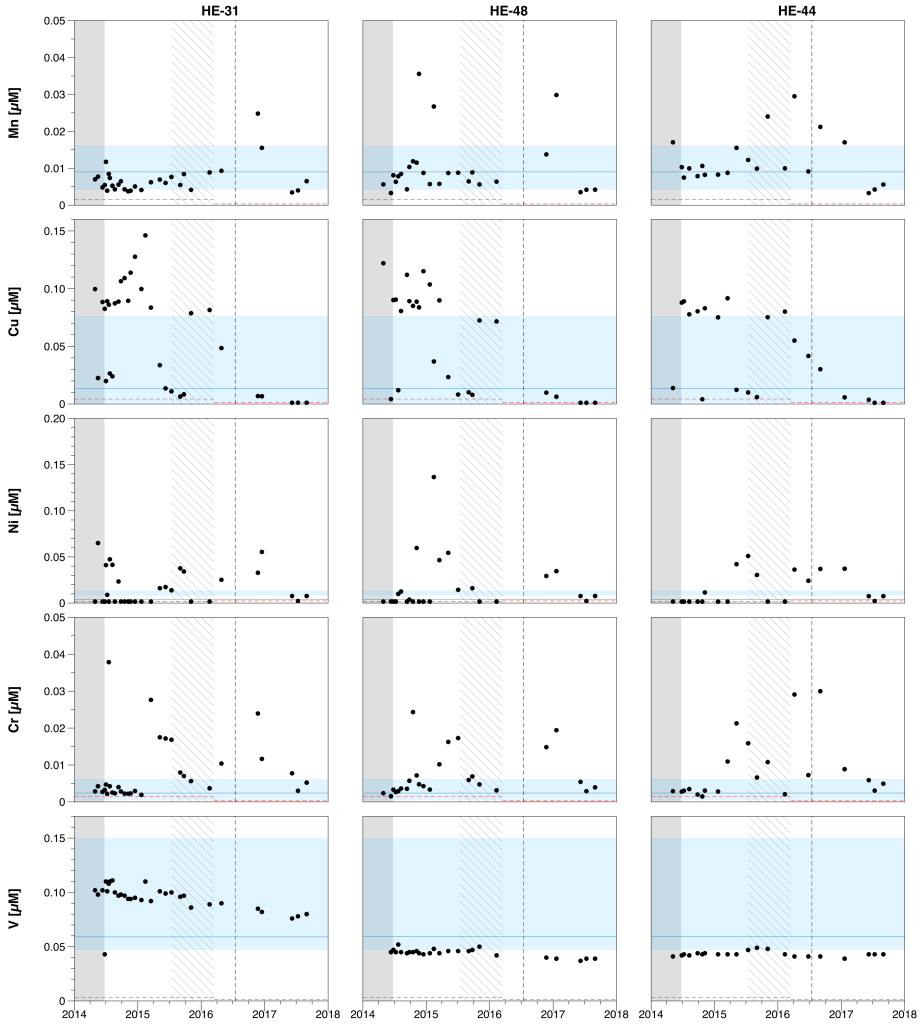

Figure 5.5. In situ concentrations of Mn, Cu, Ni, Cr, and V collected from the HE-31, HE-48, and HE-44 monitoring wells located 984, 1356, and 1482 m, respectively, from the HN-16 injection well prior to and during the injection of CO_2 and H_2S. The gray shaded area indicates times before injection of gas-charged water into well HN-16, the diagonal lines denote when well HN-14 was used for the injection of gas-charged water, and the dashed line signifies the time when the amount of CO_2 and H_2S injected was doubled. The red horizontal dashed lines indicate the limit of detection. The blue shaded area represents the range of concentrations in 2008 Hellisheiði geothermal well samples reported by Stefánsson et al. (2009) with the average concentration depicted as a the blue vertical line.

5.5 Implications for CO_2-H_2S gas injection

5.5.1 Chlorine and boron distribution

Chlorine and boron ratios were used to determine the extent of rock dissolution similar to the approach by Thomas et al. (2016) in Fig. 5.6. These elements are highly mobile and the sources well known, and therefore often used as proxies for rock dissolution with a positive correlation between water-rock interaction and basalt dissolution (Arnórsson and Andrésdóttir, 1995). They are easily dissolved from volcanic rocks (Ellis and Mahon, 1964; Ellis and Mahon, 1967), but not significantly incorporated into alteration minerals (Arnórsson and Andrésdóttir, 1995). Any Cl released would be from the crystal surfaces and in the microfissures of the rock as well as the hydrated glass (Ellis and Mahon, 1967). Relative Cl/B ratios of different sources were also plotted in Fig. 5.6: seawater with a ratio of 1330, alkali basalts from the Snaefellsnes area at 27.3, and the average ratio of 43.2 in tholeiitic basalts from the Mid Atlantic Ridge. The latter two were calculated by Thomas et al. (2016) from average Cl and B bulk rock concentrations (Arnórsson and Andrésdóttir, 1995). Geothermal reservoir fluids from Kaasalainen et al. (2015), depicted as blue triangles, along with the 2008 Hellisheiði samples (Stefánsson et al., 2009), represented by red diamonds, were plotted with this study's samples from the three monitoring wells (circles).

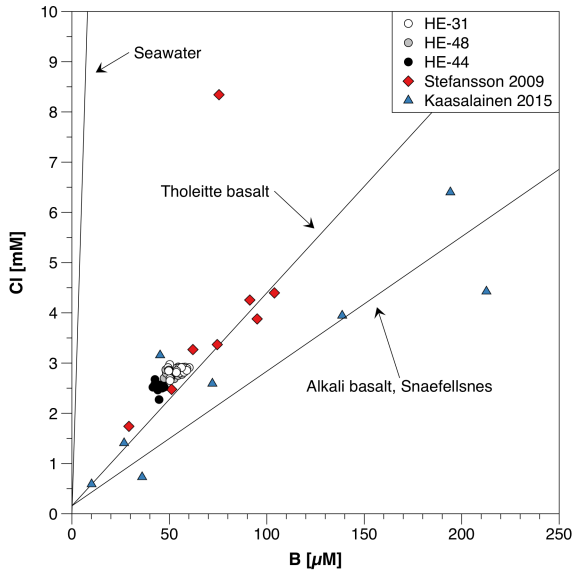

Figure 5.6. Chlorine and boron concentrations relative to the Cl/B ratio of different sources (Arnórsson and Andresdóttir, 1995). Circles represent 2014–2017 CarbFix2 samples from three Hellisheiði wells (HE-31, HE-48, HE-44), red diamonds for 2008 Hellisheiði geothermal well samples (Stefánsson et al., 2009), and the blue triangles for Icelandic geothermal fluids sampled by Kaasalainen et al. (2015).

The geothermal fluid samples from the HE-31, HE-48, and HE-44 monitoring wells all plot near the Tholeiitic basalt Cl/B ratio, HE-44 samples showing the lowest ratios. The 2008 samples similarly plot along this ratio, except the one outlier. The lower Cl/B of this study's samples in comparison indicate that there was fluid-rock interaction, but not above normal levels for the Hellisheiði geothermal field despite the gas injection. Approximately 30–60 g of basalt rock / kg water would have dissolved to obtain the Cl and B levels observed in the monitoring well fluids.

Table 5.1. World Health Organization guideline values for safe drinking water in addition to provisional (P), or health-based (H) values for drinking water (WHO, 2017), European Union Water Directive guidelines (EU, 2015), and the Icelandic drinking water regulations (Umhverfisráðuneyti, 2001).

Element	World Health Organization [μM]	European Union [μM]	Iceland [μM]
Aluminum	33.4	7.41	7.41
Antimony	0.164 [H]	0.041	0.041
Arsenic	0.133	0.133	0.133
Barium	5.10	-	-
Beryllium	1.33 [H]	-	-
Boron	222	222	92.5
Cadmium	0.027	0.044	0.044
Chloride	141 [1]	7050	7050
Chromium	0.960 [P]	0.960	0.960
Copper	31.5	31.5	71.4
Fluoride	79.0	79.0	79.0
Lead	0.048 [P]	0.048	0.048
Manganese	7.28 [H;2]	0.910	0.910
Mercury	0.030	0.005	0.005
Molybdenum	0.729	-	-
Nickel	1.19	0.340	0.340
Selenium	0.507 [P]	0.127	0.127
Zinc	45.9 [3]		

[1] As free chlorine.
[2] Not of health concern at levels normally causing acceptability problems in drinking water. However, there are circumstances where Mn may remain in solution at higher concentrations in some acidic or anaerobic waters, particularly groundwater.
[3] There is no guideline, the value shown is the maximum ideal tasting value for consumers.

5.5.2 Icelandic geothermal reservoir fluids

The trace elements, As, Mo, and Mn, in addition to Al (Clark et al., submitted) are plotted as a function of the dissolved sulfur (DS) and DIC in the fluids (Fig. 5.7), and the transition metals, Cr, Cu, Ni, and Zi as a function of DS (Fig. 5.8), along with published analyses of Icelandic geothermal fluid samples (Kaasalainen et al., 2015) and the 2008 geothermal well fluid samples from the Hellisheiði power plant (Stefánsson et al., 2009). This was to establish the potential influence of the gas-charged injection

on the geothermal reservoir as these metals (among others) can be toxic at elevated concentrations and the World Health Organization (2017), the European Union (2015), and Iceland's Ministry of Environment (Umhverfisráðuneyti, 2001) have established guidelines for safe drinking water (Table 5.1). It is necessary to point out though that these fluids are not meant for human consumption.

5.6 Results

There was a clear decrease in As and Mo concentrations after one year of injection (Fig. 5.4), which can only be attributed to the gas injection in the Hellisheiði geothermal field as the background samples from 2008 only match concentrations before and just after the start of the gas injection. Moreover, a portion of the Mo concentrations were even lower than that of the Icelandic geothermal reservoir fluids sampled by Kaasalainen et al. (2015). The uptake of As throughout the gas injection has led to reduced levels in the geothermal fluids that are now below the recommended WHO drinking water standards, with Mo below this standard throughout the entire period. Manganese and Al concentrations (except one outlier) were all within the expected levels for Icelandic geothermal fluids in addition to the Hellisheiði samples. This indicates the gas injection was not significantly affecting Mn or Al mobility near the monitoring wells. Although Mn was well below recommended WHO levels, Al concentrations were consistently above the health-based value, which is also characteristic of the Hellisheiði geothermal fluids. Of note is that all elements show lower DS levels than many of the 2008 fluids, although the latter were not sampled from the same geothermal wells.

Chromium, Cu, and Ni behaved similarly with regards to the variation of concentrations, some of which were within the background concentration range from the 2008 samples. There were, however, two outliers that plotted higher than the recommended WHO, EU, and Iceland guidelines for Cr and Ni, with the rest of the samples between guideline values and the background range. In comparison, Zn concentrations were all below the maximum ideal taste value for consumers, and actually lower than the majority of the 2008 background concentrations and closer to the geothermal fluid concentrations reported by Kaasalainen et al. (2015). The change in concentrations suggests that the gas injection mobilized all of the metals during this study period. Copper concentrations were reduced as gas injection progressed, similar to As and Mo in Fig. 5.7, though not to the same extent. However, no such pattern was determined from Cr, Ni, and Zn. Other potentially toxic metals likd Cd, Hg, Pb, and Se were all below the WHO, EU Water Directive, and Iceland guideline values.

5.6.1 Mineral precipitation

Kaasalainen et al. (2015) studied the mass transfer and mobility of trace elements from progressive fluid-rock interaction through geochemical modelling using the PHREEQC program (Parkhurst and Appelo, 1999). The results of modelling indicates the incorpo-

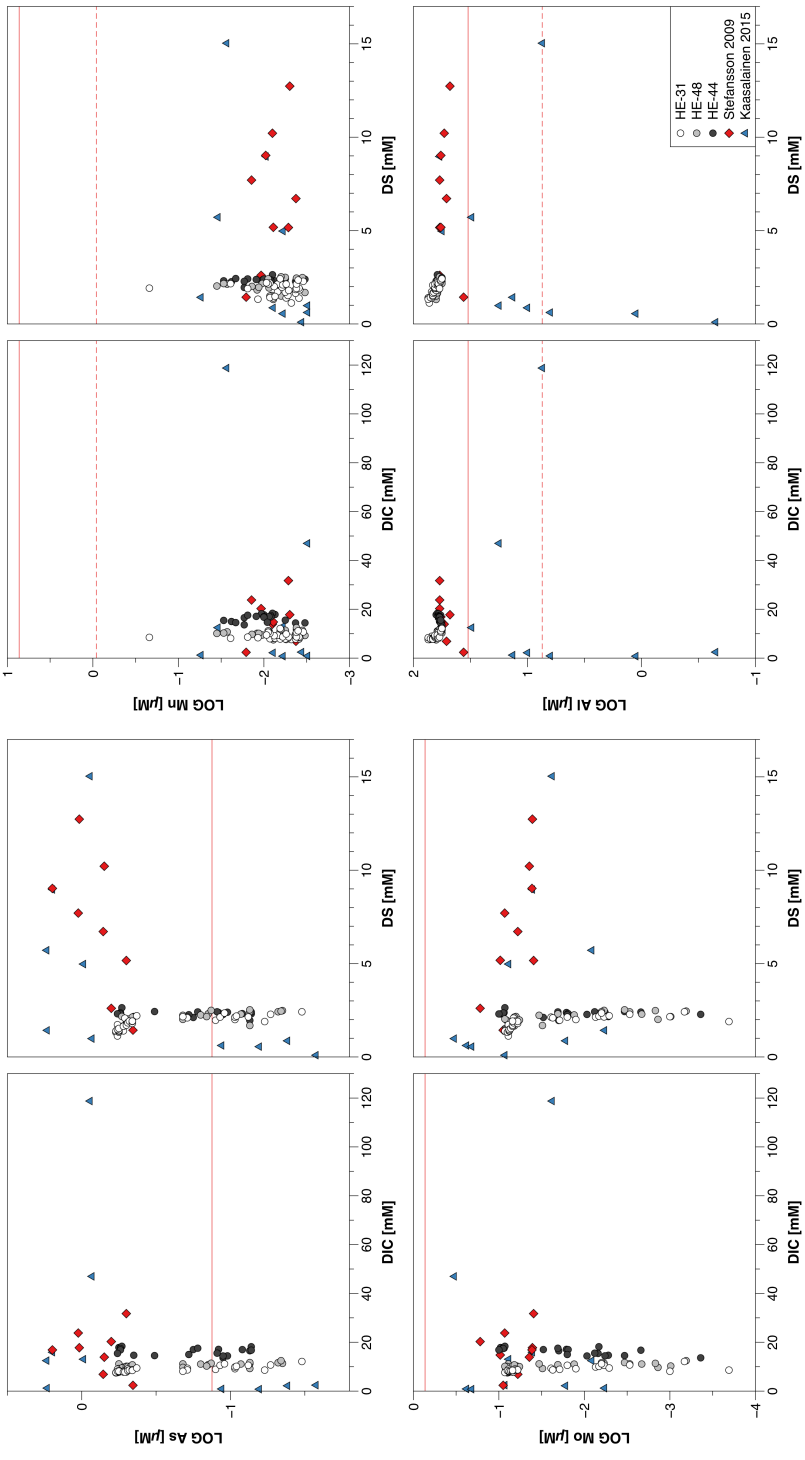

Figure 5.7. Concentration of As, Mo, Mn, and Al as a function of DIC and DS. The red vertical solid line indicates the World Health Organization guideline value for safe drinking water (As, Mo) or the health-based value for drinking water (Mn, Al). The red vertical dashed line indicates the European Union's Water Directive and Iceland's regulations value (Mn, Al); this value is the same as WHO's guideline for As. Circles represent 2014–2017 CarbFix2 samples from three Hellisheiði wells (HE-31, HE-48, HE-44), red diamonds for 2008 Hellisheiði geothermal well samples (Stefánsson et al., 2009), and the blue triangles for Icelandic geothermal fluids sampled by Kaasalainen et al. (2015).

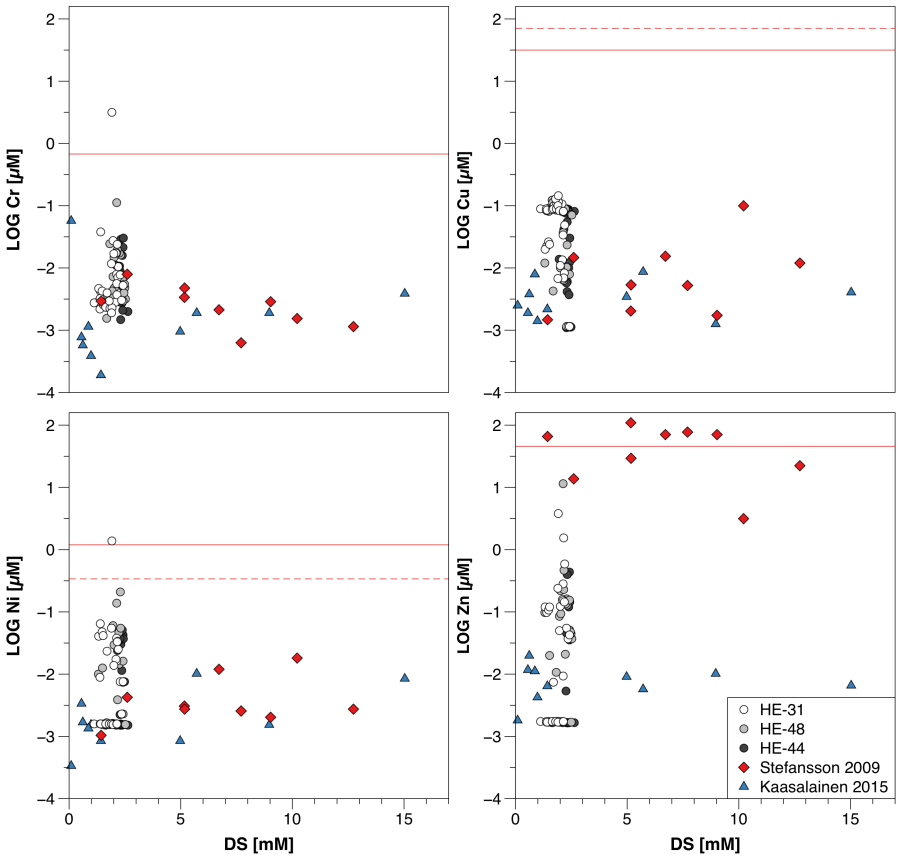

Figure 5.8. Concentration of Cr, Cu, Ni, and Zn as a function of DS. The red vertical line indicates the World Health Organization guideline value for safe drinking water (Cu, Ni) or a provisional guideline (Cr). Zinc does not have an official value, but there is a ideal maximum tasting value for consumers displayed. The red vertical dashed line indicates the European Union's Water Directive and Iceland's regulations guideline for Ni. The values are the same as WHO's gudelines for Cr. While WHO and EU have the same guideline for Cu, Iceland's value is depicted by a red vertical dashed line. Circles represent 2014–2017 CarbFix2 samples from three Hellisheiði wells (HE-31, HE-48, HE-44), red diamonds for 2008 Hellisheiði geothermal well samples (Stefánsson et al., 2009), and the blue triangles for Icelandic geothermal fluids sampled by Kaasalainen et al. (2015).

ration of Ba, Sr, and Mn in carbonates, while the geothermal fluids are undersaturated with respect to the pure mineral phases Ba, Sr-, and Mn-carbonates. For instance, the geothermal fluids approach saturation with respect to Sr-carbonate and Sr-sulfate when in solid solution with calcite and anhydrite, respectively. The results also suggest Mo could be incorporated into sulfides, although the reservoir fluids are undersaturated with As and Sb containing minerals. For transition metals like Ni and Cr, the exact secondary phases and concentrations in major alteration minerals are unknown. In general the modelling indicates that element concentrations are source-controlled, i.e. availability is limited by the concentration in the host rock (Kaasalainen et al., 2015).

From preliminary geochemical modelling of the fluid from the monitoring wells, the fluids were supersaturated with respect to transition metal containing-sulfides, such as Cu, Co, and Cr (results not shown). However, as Kaasalainen et al. (2015) also highlights, there is a lack of thermodynamic calculations and unknown stabilities at elevated temperatures. This leads to difficulties in assessing geochemical behavior and resolving aqueous speciation of trace elements. Keeping this and the modelling results of Kaasalainen et al. (2015) in mind, the trace elements were most likely incorporated into other minerals, rather than precipitating as a pure phase. With the saturation and supersaturation of the monitoring well fluids with respect to calcite and dolomite as well as pyrite and pyrrhotite (Clark et al., submitted), this study's results indicate the uptake of Ba, Sr, and Mn into carbonates and As, Sb, Mo, and the transition metals into sulfides. Conversely, other secondary minerals could also incorporate these metals; Ba, Sr, and Mn can substitute for Ca into epidote and actinolite, and Mo and Cr into clays.

5.7 Conclusions

Trace element concentrations are presented here after 3.5 years of CO_2 and H_2S injection into the Hellisheiði geothermal reservoir. The assessment of these trace elements indicates uptake and mobilization of As, Mo in addition to alkaline earth and several transition metals as a result of basaltic rock dissolution. Concentrations of As, Mo, Sb, and Cu decreased over time in all three monitoring wells, whereas Sr rose over time. Despite the lack of thermodynamic calculations at elevated temperatures, it is likely that Ba, Sr and Mn were incorporated into Ca- carbonates and secondary minerals (epidote, actinolite) rather than precipitating as a pure phase. Furthermore, As, Mo, Sb and transition metals such as Cu, Cr, and Ni would be taken up by sulfides such as pyrite. Many other transition metals and rare earth elements were not mobilized by the gas injection and were close to and/or at the detection limit.

Some of these trace elements can be toxic in high concentrations and were of interest in this study, particularly As as this element already had elevated concentrations above WHO, EU, and Iceland guidelines for safe drinking water since 2008. Yet as a direct result of the carbon and sulfur mineralization, As concentrations have been greatly reduced after one year of gas injection with some samples safely below drinking water guidelines. One sample each of Ni and Cr also had higher concentrations than

the recommended guidelines. Although this fluid is not meant for consumption, the trace elements here were generally not above WHO, EU, and Iceland drinking water standards with the main exception of As at the start of the gas injection.

Acknowledgements

This publication has been produced with support from the European Commission through the projects CarbFix (EC Project 283148), CO2-React (EC Project 317235), CarbFix2 (EC Project 764760), S4CE (EC Project 764810) and two University of Iceland Travel Grants. Special thanks to Reykjavik Energy, particularly Þorsteinn A. Þorgeirsson for all the fun sampling trips as well as S.S. Sigurðardóttir, T. Kristinsson, H. Bergmann, V. Eiríksdóttir, C. Marieni, and F. Jónsdóttir. We would also like to acknowledge Stephen Reid for the ICP-MS analysis and Jón Örn Bjarnason for his invaluable assistance in addition to the CarbFix group for their support.

5.8 References

Abraitis, P.K., Pattrick, R.A.D. and Vaughan, D.J. (2004) Variations in the compositional, textural and electrical properties of natural pyrite: a review. *International Journal of Mineral Processing* 74, 41–59.

Aiuppa, A., Allard, P., D'Alessandro, W., Michel, A., Parello, F., Treuil, M., Valenza, M. (2000a) Mobility and fluxes of major, minor and trace metals during basalt weathering and groundwater transport at Mt. Etna volcano (Sicily). *Geochimica et Cosmochimica Acta* 64, 1827–1841.

Aiuppa, A., Dongarra, G., Capasso, G. and Allard, P. (2000b) Trace elements in the thermal groundwaters of Vulcano Island (Sicily). *Journal of Volcanology and Geothermal Research* 98, 189–207.

Aiuppa, A., Federico, C., Allard, P., Gurrieri, S. and Valenza, M. (2005) Trace metal modeling of groundwater–gas–rock interactions in a volcanic aquifer: Mount Vesuvius, Southern Italy. *Chemical Geology* 216, 289–311.

Arnórsson, S. (2003) Arsenic in surface- and up to 90°C ground waters in a basalt area, N-Iceland: processes controlling its mobility. *Applied Geochemistry* 18, 1297–1312.

Arnórsson, S. and Andrésdóttir, A. (1995) Processes controlling the distribution of boron and chlorine in natural waters in Iceland. *Geochimica et Cosmochimica Acta* 59, 4125–4146.

Arnórsson, S., Bjarnason, J.O., Giroud, N., Gunnarsson, I. and Stefánsson, A. (2006) Sampling and analysis of geothermal fluids. *Geofluids* 6, 203–216.

Arnórsson, S. and Óskarsson, N. (2007) Molybdenum and tungsten in volcanic rocks and in surface and <100°C ground waters in Iceland. *Geochimica et Cosmochimica Acta* 71, 284–304.

Arnórsson, S., Sigurdsson, S. and Svavarsson, H. (1982) The chemistry of geothermal waters in Iceland. I. Calculation of aqueous speciation from 0C to 370C.

Geochimica et Cosmochimica Acta 46, 1513–1532.
Arnórsson, S., Stefánsson, A. and Bjarnason, J.O. (2007) Fluid-Fluid Interactions in Geothermal Systems. *Reviews in Mineralogy and Geochemistry* 65, 259–312.
Ballantyne, J.M. and Moore, J.N. (1988) Arsenic geochemistry in geothermal systems. *Geochimica et Cosmochimica Acta* 52, 475–483.
Berger, G., Schott, J. and Guy, C. (1988) Behavior of Li, Rb and Cs during basalt glass and olivine dissolution and chlorite, smectite and zeolite precipitation from seawater: Experimental investigations and modelization between 50° and 300°C. *Chemical Geology* 71, 297–312.
Bjarnason, J.O. and Arnórsson, S. (2010) The chemical speciation program WATCH.
Christensen, O.D., Capuano, R.A. and Moore, J.N. (1983) Trace-element distribution in an active hydrotherml system, Roosevelt hot springs thermal area, Utah. *Journal of Volcanology and Geothermal Research* 16, 99–129.
Clark, D.E., Gunnarsson, I., Aradóttir, E.S., Arnarson, M.Þ., Þorgeirsson, Þ.A., Sigurðardóttir, S.S., Sigfússon, B., Snæbjörnsdóttir, S.Ó., Oelkers, E.H., and Gíslason, S.R. (2018) The chemistry and potential reactivity of the CO_2-H_2S charged injected waters at the basaltic CarbFix2 site, Iceland. *Energy Procedia* 146, 121–128.
Clark, D.E., Oelkers, E.H., Gunnarsson, I., Sigfússon, B, Snæbjörnsdóttir, S.Ó., Aradóttir, ES. and Gíslason, S.R. (Submitted) An update on CO_2 and H_2S mineralization at the CarbFix2 injection site after 3.5 years of continuous injection into basaltic rocks at more than 250 °C. *Geochimica et Cosmochimica Acta*
Ellis, A.J. and Mahon, W.A.J. (1964) Natural hydrothermal systems and experimental hot-water/rock interactions. *Geochimica et Cosmochimica Acta* 28, 1323–1357.
Ellis, A.J. and Mahon, W.A.J. (1967) Natural hydrothermal systems and experimental hot water/rock interactions (Part II). *Geochimica et Cosmochimica Acta* 31, 519–538.
EU, 2015. Council Directive 98/83/EC of 3 November 1998 on the quality of water intended for human consumption, European Union.
Exley, R.A. (1982) Electron microprobe studies of Iceland Research Drilling Project high-temperature hydrothermal mineral geochemistry. *Journal of Geophysical Research: Solid Earth* 87, 6547–6557.
Flaathen, T.K., Gíslason, S.R., Oelkers, E.H. and Sveinbjörnsdóttir, Á.E. (2009) Chemical evolution of the Mt. Hekla, Iceland, groundwaters: A natural analogue for CO_2 sequestration in basaltic rocks. *Applied Geochemistry* 24, 463–474.
Fridriksson, T., Arnórsson, S. and Bird, D.K. (2009) Processes controlling Sr in surface and ground waters of Tertiary tholeiitic flood basalts in Northern Iceland. *Geochimica et Cosmochimica Acta* 73, 6727–6746.
Galeczka, I., Wolff-Boenisch, D. and Gíslason, S. (2013) Experimental Studies of Basalt-H_2O-CO_2 Interaction with a High Pressure Column Flow Reactor: the Mobility of Metals. *Energy Procedia* 37, 5823–5833.
Galoisy, L., Calada, G. and Brown Jr., G.E. (1995) Intracrystalline distribution of Ni in San Carlos olivine: An EXAFS study. *American Mineralogist* 80, 1089–1092.
Giroud, N. (2008) A chemical study of arsenic, boron and gases in high-temperature geothermal fluids in Iceland, University of Iceland, Reykjavik, 128 pp.
Gíslason, S.R. and Oelkers, E.H. (2014) Carbon Storage in Basalt. *Science* 344, 373–374.

Glover, R.B. (1988) Boron distribution between liquid and vapour in geothermal fluids, 10th New Zealand Geothermal Workshop, New Zealand.

Goguel, R. (1983) The rare alkalies in hydrothermal alteration at Wairakei and Broadlands, geothermal fields, N.Z. *Geochimica et Cosmochimica Acta* 47, 429–437.

Gunnarsson, I., Aradóttir, E.S., Oelkers, E.H., Clark, D.E., Arnarson, M.Þ., Sigfússon, B., Snæbjörnsdóttir, S.Ó., Matter, J.M., Stute, M., Júlíusson, B.M. and Gíslason, S.R. (2018) The rapid and cost-effective capture and subsurface mineral storage of carbon and sulfur at the CarbFix2 site. *International Journal of Greenhouse Gas Control* 79, 117–126.

Gunnarsson, I. and Arnórsson, S. (2000) Amorphous silica solubility and the thermodynamic propoerties of H_4SiO_4 in the range of 0 to 350°C at P_{amt}. *Geochimica et Cosmochimica Acta* 64, 2295–2307.

Gurav, T., Singh, H.K. and Chandrasekharam, D. (2015) Major and trace element concentrations in the geothermal springs along the west coast of Maharashtra, India. *Arabian Journal of Geosciences* 9.

Harðardóttir, V., Hannington, M., Hedenquist, J., Kjarsgaard, I. and Hoal, K. (2010) Cu-rich scales in the Reykjanes geothermal system, Iceland. *Economic Geology* 105, 1143–1155.

Heinrich, C.A. (2007) Fluid-Fluid Interactions in Magmatic-Hydrothermal Ore Formation. *Reviews in Mineralogy and Geochemistry* 65, 363–387.

Kaasalainen, H. and Stefánsson, A. (2012) The chemistry of trace elements in surface geothermal waters and steam, Iceland. *Chemical Geology* 330-331, 60–85.

Kaasalainen, H., Stefánsson, A., Giroud, N. and Arnórsson, S. (2015) The geochemistry of trace elements in geothermal fluids, Iceland. *Applied Geochemistry* 62, 207–223.

Karakaya, N., Karakaya, M.Ç., Nalbantçılar, M.T. and Yavuz, F. (2007) Relation between spring-water chemistry and hydrothermal alteration in the Şaplıca volcanic rocks, Şebinkarahisar (Giresun, Turkey). *Journal of Geochemical Exploration* 93, 35–46.

Kendall, B., Dahl, T.W. and Anbar, A.D. (2017) The Stable Isotope Geochemistry of Molybdenum. *Reviews in Mineralogy and Geochemistry* 82, 683–732.

Klein, C. and Dutrow, B. (2008) Manual of Mineral Science. John Wiley & Sons.

Libbey, R.B. and Williams-Jones, A.E. (2016) Relating sulfide mineral zonation and trace element chemistry to subsurface processes in the Reykjanes geothermal system, Iceland. *Journal of Volcanology and Geothermal Research* 310, 225–241.

Lonker, S.W., Franzson, H. and Kristmannsdóttir, H. (1993) Mineral-fluid interaction in the Reykjanes and Svartsengi geothermal systems, Iceland. *American Journal of Science* 293, 605–670.

Marks, N., Schiffman, P., Zierenberg, R., Elders, W.A., Friðleifsson, G.Ó. and Franzson, H. (2010) Isotopic evidence of hydrothermal exchange and seawater ingress from alteration minerals in the Reykjanes geothermal system: Results from the IDDP, World Geothermal Congress, Bali, Indonesia.

Markússon, S.H. and Stefánsson, A. (2011) Geothermal surface alteration of basalts, Krýsuvík Iceland—Alteration mineralogy, water chemistry and the effects of acid supply on the alteration process. *Journal of Volcanology and Geothermal Research* 206, 46–59.

Migdisov, A.A. and Bychkov, A.Y. (1998) The behaviour of metals and sulphur during the formation of hydrothermal mercury–antimony–arsenic mineralization, Uzon caldera, Kamchatka, Russia. *Journal of Volcanology and Geothermal Research* 84, 153-171.

Neely, R.A., Gíslason, S.R., Ólafsson, M., McCoy-West, A.J., Pearce, C.R. and Burton, K.W. (2018) Molybdenum isotope behaviour in groundwaters and terrestrial hydrothermal systems, Iceland. *Earth and Planetary Science Letters* 486, 108–118.

O'Day, P.A. (2006) Chemistry and Mineralogy of Arsenic. *Elements* 2, 77-83.

Olsen, N.J., Bird, D.K., Arnórsson, S., Fridriksson, Þ., Friðleifsson, G.Ó. and Elders, W.A. (2010) Iceland deep drilling project (IDDP): Arsenic distribution and mobility in active and fossil geothermal systems in Iceland, World Geothermal Congress, Bali, Indonesia.

Olsson, J., Stipp, S.L.S., Makovicky, E. and Gíslason, S.R. (2014) Metal scavenging by calcium carbonate at the Eyjafjallajökull volcano: A carbon capture and storage analogue. *Chemical Geology* 384, 135–148.

Onishi, H. and Sandell, E.B. (1955) Geochemistry of arsenic. *Geochimica et Cosmochimica Acta* 7, 1–33.

Parkhurst, D.L. and Appelo, C.A.J. (1999) User's Guide to PHREEQC (Version 2) - A Computer Program for Speciation, Batch-Reaction, One-Dimensional Transport, and Inverse Geochemical Calculations, U.S. Department of the Interior.

Sigfússon, B., Arnarson, M.Þ., Snæbjörnsdóttir, S.Ó., Karlsdóttir, M.R., Aradóttir, E.S. and Gunnarsson, I. (2018) Reducing emissions of carbon dioxide and hydrogen sulphide at Hellisheidi power plant in 2014-2017 and the role of CarbFix in achieving the 2040 Iceland climate goals. *Energy Procedia* 146, 135–145.

Snæbjörnsdóttir, S.Ó. (2017) Mineral storage of carbon in basaltic rocks, PhD Thesis. University of Iceland, Reykjavik, 158 pp.

Snæbjörnsdóttir, S.Ó., Tómasdóttir, S., Sigfússon, B., Aradóttir, E.S., Gunnarsson, G., Niemi, A., Basirat, F., Dessirier, B., Gíslason, S.R., Oelkers, E.H. and Franzon, H. (2018) The geology and hydrology of the CarbFix2 site, SW-Iceland. *Energy Procedia* 146, 146–157.

Stefánsson, A. and Arnórsson, S. (2005) The Geochemistry of As, Mo, Sb, and W in Natural Geothermal Waters, Iceland, Proceedings World Geothermal Congress, Antalya, Turkey.

Stefánsson, A., Arnórsson, S., Gunnarsson, I. and Kaasalainen, H. (2009) Förgun brennisteins frá Hellisheiðarvirkjun Jarðefnafræðileg athugun, Orkuveita Reykjavíkur (Reykjavik Energy).

Stefánsson, A., Arnórsson, S., Gunnarsson, I., Kaasalainen, H. and Gunnlaugsson, E. (2011) The geochemistry and sequestration of H_2S into the geothermal system at Hellisheidi, Iceland. *Journal of Volcanology and Geothermal Research* 202, 179–188.

Stefánsson, A., Gunnarsson, I., Kaasalainen, H. and Arnórsson, S. (2015) Chromium geochemistry and speciation in natural waters, Iceland. *Applied Geochemistry* 62, 200–206.

Thomas, D.L., Bird, D.K., Arnórsson, S. and Maher, K. (2016) Geochemistry of CO_2-rich waters in Iceland. *Chemical Geology* 444, 158–179.

Umhverfisráðuneyti, 2001. Reglugerð 536/2001 um neysluvatn. Stjórnarráð Íslands.

WHO, 2017. Guidelines for drinking-water quality: fourth edition incorporating the first addendum. World Health Organization.

A Appendix

Supplementary Material to Paper I

Material

The basaltic glass was first crushed in a jaw crusher and then in a steel ball mill. Afterwards it was sieved to 45–100 µm and washed in DI water by repeated gravitational settling to remove ultrafine particles. The resulting material was dried at 50 °C for two days. The cleaned glass was then mixed with DI water and poured into the column reactor. The total mass of glass measured inside the column was 6.74 kg. Taking into account that the empty column can fit 4.78 L of water, the void volume was calculated to be 2.54 L and the porosity 0.53 assuming a density of 3.05 g/cm^3 (Wolff-Boenisch et al., 2006).

Analysis

An expander-transducer setup (as described in Galeczka et al. 2013) was also connected to the experimental setup by a 5 mL sampling loop, which determines DIC *in situ*. During the course of the experiment, it became apparent that this method was unable to accurately determine the correct concentration as the pH of the fluid samples was > 5.5 and the H_2O/CO_2 pump flow ratio of 875 was at the method's upper limit of detection, which has an optimal recovery at pump flow ratios of 22–100 (Galeczka et al., 2013).

Fluid samples were filtered in line using a 0.2 µm cellulose acetate filter, and then acidified with concentrated supra-pure HNO_3 (1.0 vol.%) prior to analysis by Inductively Coupled Plasma Optical Emission Spectrometer (Spectro Ciros Vision ICP-OES). Analytical uncertainties of ICP-OES analyses, as estimated from repeat analyses, were on the order of $\leq 5\%$. Samples to determine Fe species (Fe^{II} and Fe^{III}) were captured directly into a 0.1 M HCl solution to avoid any contact with the atmosphere before acidification to slow down the Fe^{II} oxidation kinetics (Stumm and Morgan, 1996). Subsequently, samples were analyzed using ion chromatography (Dionex IC 3000). To note, the fluid flow in the column was stagnant for up to three days when either the inlet fluid in the 'mixing chamber' was sampled and/or when the CO_2(l) in the syringe pump was refilled from the cylinder. Chemical compositions of samples taken following such circumstances were similar to that of previous samples.

Upon completion of the experiment, the CO_2 syringe pump and heater were turned off and the pressure slowly released over the course of an hour. The column was next

flushed with N_2 and depressurized. Then each compartment was removed one at a time (while the other compartments were still flushed with N_2), frozen immediately with liquid N_2, and placed into a freezer. The solid material within each compartment was later transferred into clear polycarbonate tubing using a hydraulic press, frozen again, and shipped in frozen state to the University of Copenhagen. Upon arrival, the samples were transferred into a hard-walled anaerobic chamber (mBraun). After thawing, the first two cm of the material in the compartments were discarded. Approximately one gram of material was then scraped from the central two cm of the compartments and dried.

Material for scanning electron microscopy (SEM) was transferred to Al sample stubs covered with carbon tape. The sample stubs were then placed into an airtight container to minimize oxidation during transport to the sputter coater. The samples were quickly transferred to the coater that applied a $\sim$10 nm layer of gold to alleviate charging. Samples were analyzed on a FEI Quanta 3D FEG SEM using an accelerating voltage of 20 KeV and a current of 7.5 pA for SEM imaging of secondary electrons. During energy dispersive X-ray spectroscopy (EDXS), the current was increased to 0.25 nA and X-rays were detected using an Oxford instrument X-max 20 mm2 EDXS detector.

For X-ray diffraction (XRD), the material was crushed and placed on a low-background Si sample holder, which was capped with a plastic dome to minimize oxidation during measurement. Samples were analyzed on a Bruker D8 DISCOVER using Cu radiation. Data was acquired from 5-90° (2Θ) with a step size of 0.01° and a total measurement time of 12 hours.

Material for X-ray photoelectron spectroscopy (XPS) were placed on sample holders that transferred through a flange into an airtight transfer chamber. The transfer chamber was then mounted on a flange in the N_2 vented entry chamber allowing sample entry with minimal oxidation. Analysis was conducted using a Kratos Axis UltraDLD equipped with a monochromatic AlKα X-ray source operated at a power of 150 eV. For high-resolution scans, the pass energy was 20 eV. Binding energies were calibrated assuming an energy of 285 eV for the C1s peak of adventitious carbon.

Table A.1. The dissolution reactions for minerals and leached basaltic glass included in the reactive transport model.

Minerals	Reaction	log K (25 °C)
Leached basaltic glass [1*]	$SiAl_{0.35}O_2(OH)_{1.05} + 0.35\ OH^- = 0.35\ Al(OH)_4^- + SiO_2$	-2.36
Allophane, Al/Si = 2.02 [2*]	$Al_2O_3SiO_2 \cdot 2.53\ H_2O + 2.47\ H_2O = 2\ Al(OH)_4^- + 2\ H^+ + SiO_2$	-32.14
Ankerite [3]	$CaFe(CO_3)_2 = Ca^{+2} + Fe^{+2} + 2\ CO_3^{-2}$	-20.87
Calcite	$CaCO_3 + H^+ = Ca^{+2} + HCO_3^-$	1.85
Chabazite-Ca [4]	$CaAl_2Si_4O_{12} \cdot 6\ H_2O = 2\ Al(OH)_4^- + 2\ Ca^+ + 4\ SiO_2 + 2\ H_2O$	-30.95
Dolomite [4]	$CaMg(CO_3)_2 = Ca^{+2} + Mg^{+2} + 2\ CO_3^{-2}$	-17.58
Magnesite	$MgCO_3 + H^+ = Mg^{+2} + HCO_3^-$	2.29
Mesolite [4]	$Ca_{0.67}Na_{0.66}Al_2Si_3O_{10} \cdot 2.67\ H_2O + 1.33\ H_2O = 2\ Al(OH)_4^- + 0.67\ Ca^{+2} + 3\ SiO_2 + 0.66\ Na^+$	-28.59
Moganite [7*]	$SiO_2 = SiO_2$	-2.88
Saponite-Fe-Fe [8]	$Fe_{3.175}Al_{0.35}Si_{3.65}O_{10}(OH)_2 + 7.4\ H^+ = 0.35\ Al^{+3} + 3.175\ Fe^{+2} + 3.65\ SiO_2 + 4.7\ H_2O$	18.94
Saponite-Mg-Mg [8]	$Mg_{3.175}Al_{0.35}Si_{3.65}O_{10}(OH)_2 + 7.4\ H^+ = 0.35\ Al^{+3} + 3.175\ Mg^{+2} + 3.65\ SiO_2 + 4.7\ H_2O$	26.25
Saponite-Mg-K [8]	$K_{0.35}Mg_3Al_{0.35}Si_{3.65}O_{10}(OH)_2 + 7.4\ H^+ = 0.35\ K^+ + 0.35\ Al^{+3} + 3\ Mg^{+2} + 3.65\ SiO_2 + 4.7\ H_2O$	26.01
Siderite [9]	$FeCO_3 = Fe^{+2} + CO_3^{-2}$	-11.04

[*] Not included in *carbfix.dat* from Voigt et al. (2018).
[1] Calculated from a stoichiometric mixture of amorphous SiO_2 from Voigt et al. (2018) and amorphous $Al(OH)_3$ from Naumov et al. (1971).
[2] Dissolution reaction and solubility constants from Stefansson and Gislason (2001).
[3] Calculated from database in Holland and Powell (2011).
[4] Calculated from database in Neuhoff (2000).
[5] Dissolution reaction and solubility constants from Bénézeth et al. (2018).
[6] Dissolution reaction and solubility constants from Gysi and Stefánsson (2011).
[7] Dissolution reaction and solubility constants from Gislason et al. (1997).
[8] Calculated from database in Catalano (2013).
[9] Dissolution reaction and solubility constants from Bénézeth et al. (2009).

Table A.2. Chemical compositions of the liquid samples taken during the experiment. b.d. = below detection limit

Detection Limit	[mM]		0.0001	0.001	0.0003	0.001	0.0002	0.0001	0.0001	0.001	0.003	0.0007	0.001
Elapsed Time [Days]	pH *in situ*	Alkalinity [meq/L]	Al [mM]	Ca [mM]	Cl [mM]	F [mM]	Fe^{II} [mM]	Fe^{III} [mM]	Mg [mM]	Na [mM]	K [mM]	SO_4 [mM]	Si [mM]
0.04	9.89	-	0.035	0.44	0.003	0.006	b.d. *	b.d. *	0.0018	0.318	0.024	0.002	0.876
0.38	10.5	-	0.075	0.41	0.009	0.015	b.d. *	b.d. *	0.0003	0.505	0.031	0.005	0.968
0.50	9.18	-	0.004	2.30	0.019	0.005	0.658	0.068	0.412	2.82	0.096	0.010	1.15
0.65	6.45	-	0.004	2.31	0.006	0.001	0.511	0.038	1.05	1.81	0.103	0.008	1.64
0.75	6.01	-	0.003	2.15	0.003	0.003	0.065	0.010	0.581	0.630	0.066	0.002	1.53
0.88	6.36	-	0.002	2.28	0.002	0.002	0.041	0.007	1.06	0.450	0.080	0.001	1.64
1.01	6.34	-	0.002	2.27	0.003	0.001	0.033	0.011	1.59	0.362	0.091	0.001	1.82
1.13	6.24	-	0.003	2.25	0.002	0.003	0.013	0.004	1.55	0.280	0.084	0.001	1.75
1.42	6.70	-	0.004	1.10	0.001	0.006	0.002	0.002	0.581	0.153	0.041	0.001	1.54
1.63	7.06	-	0.006	0.66	0.001	0.011	b.d. *	0.001	0.281	0.119	0.029	0.001	1.44
1.89	7.37	-	0.008	0.52	0.001	0.009	b.d. *	b.d. *	0.186	0.155	0.025	0.001	1.42
2.14	7.25	-	0.002	2.27	0.002	0.001	0.013	0.004	1.51	0.410	0.061	0.002	1.76
2.38	6.15	-	0.002	2.21	0.002	0.002	0.010	0.006	1.01	0.212	0.038	0.001	1.77
2.73	6.33	-	0.002	2.28	0.002	b.d.	0.029	0.005	1.61	0.190	0.040	0.002	1.80
3.33	6.37	-	0.003	1.35	0.001	0.005	0.006	0.002	0.333	0.082	0.013	0.001	1.76
3.82	7.06	-	0.005	1.13	0.001	0.005	b.d. *	0.001	0.214	0.087	0.010	0.001	1.66
4.67	6.19	-	0.002	2.26	0.001	0.001	0.016	0.004	0.747	0.111	0.015	0.001	2.07
5.63	6.02	-	0.002	1.98	0.001	0.002	0.015	0.006	0.587	0.106	0.012	0.001	2.36
6.59	5.81	-	0.002	1.10	0.001	0.002	0.070	0.010	0.632	0.115	0.011	0.001	2.45
7.51	5.72	-	0.002	0.77	0.001	0.003	0.120	0.011	0.660	0.116	0.012	0.001	2.44
8.56	5.87	-	0.002	0.67	0.001	0.003	0.155	0.010	0.663	0.148	0.011	0.001	2.40
9.60	5.72	-	0.002	0.63	0.001	0.003	0.177	0.010	0.727	0.150	0.012	0.001	2.45
10.4	5.67	-	0.002	0.34	0.002	0.003	0.102	0.008	0.412	0.112	0.009	0.005	2.48
12.7	5.84	-	0.002	0.70	0.001	0.002	0.257	0.011	0.876	0.176	0.015	0.001	2.40
14.6	5.99	-	0.002	0.12	b.d.	b.d.	0.030	0.002	0.140	0.097	0.007	b.d.	2.33

15.6	6.32	-	0.003	0.19	0.003	0.006	0.037	0.005	0.212	0.464	0.012	0.004	2.05
17.5	6.15	-	0.004	0.07	0.001	0.007	0.006	0.002	0.0812	0.076	0.008	0.002	2.22
19.7	7.28	-	0.015	0.08	b.d.	b.d.	0.001	0.002	0.0842	0.398	0.008	b.d.	1.62
23.6	5.61	3.32	0.002	0.77	0.002	0.002	0.070	0.016	0.720	0.180	0.018	0.001	2.42
27.7	5.79	2.44	0.001	0.58	0.011	0.004	0.096	0.004	0.621	0.247	0.020	0.001	2.41
31.0	6.10	2.80	0.006	0.57	0.003	0.002	0.025	0.002	0.512	0.133	0.019	0.001	2.11
34.1	5.86	3.42	0.005	0.77	0.002	0.002	0.123	0.005	0.617	0.181	0.016	0.002	2.25
37.9	5.71	1.62	0.005	0.32	0.004	0.003	0.135	0.006	0.286	0.125	0.011	0.002	2.26
42.9	5.71	2.77	0.005	0.51	0.014	0.003	0.234	0.006	0.469	0.161	0.014	0.002	2.14
48.1	5.68	3.56	0.005	0.68	0.003	0.002	0.162	0.006	0.637	0.153	0.016	0.002	2.14
52.0	5.73	3.17	0.005	0.56	0.079	0.002	0.254	0.009	0.546	0.161	0.016	0.002	2.06
57.1	6.17	1.23	0.006	0.21	1.06	0.003	0.053	0.004	0.209	0.235	0.012	0.006	1.78
58.9	7.40	0.552	0.017	0.07	0.011	0.022	b.d. *	0.002	0.0610	0.165	0.010	0.006	1.43
61.1	8.59	0.550	0.032	0.06	0.106	0.021	b.d. *	b.d. *	0.0390	0.201	0.012	0.004	1.24
61.7	8.70	0.892	0.022	0.08	0.004	0.014	b.d. *	b.d. *	0.0473	0.427	0.018	0.004	1.27
61.8	8.26	1.27	0.018	0.15	0.137	0.010	b.d. *	b.d. *	0.0831	0.544	0.024	0.003	1.19
62.0	7.92	1.93	0.006	0.30	0.015	0.008	b.d. *	b.d. *	0.141	0.503	0.032	0.003	1.16
62.8	6.49	8.52	0.005	1.59	0.031	0.002	0.001	0.002	1.51	0.173	0.050	0.001	1.67
63.8	6.12	5.60	0.004	1.45	0.007	0.001	b.d. *	0.018	0.940	0.098	0.022	0.001	2.05
64.8	5.82	3.77	0.002	0.88	0.004	0.001	0.009	0.004	0.553	0.108	0.014	0.001	2.41
66.0 [1]	5.68	3.27	0.006	0.79	0.008	0.001	0.016	0.004	0.661	0.163	0.016	0.001	2.43
68.8	5.66	3.41	0.006	0.75	0.049	0.002	0.047	0.005	0.719	0.201	0.017	0.002	2.32
69.8	5.44	2.74	0.006	0.62	0.006	0.001	0.098	0.009	0.617	0.176	0.018	0.001	2.66
71.0	6.30	0.334	0.008	0.05	0.034	0.007	0.009	0.001	0.0491	0.165	0.006	0.006	2.02
71.8	6.67	0.347	0.015	0.02	0.080	0.018	0.002	0.001	0.0143	0.239	0.004	0.008	1.88
76.0	6.42	-	0.006	2.92	0.018	0.002	0.005	0.002	2.47	0.574	0.068	0.001	1.80
76.8	6.27	1.17	0.008	0.29	0.003	0.005	0.005	0.003	0.293	0.185	0.020	0.001	2.04
77.7	6.65	1.20	0.010	0.22	0.066	0.007	0.003	0.002	0.226	0.313	0.019	0.001	1.86
78.8	6.46	1.09	0.008	1.45	0.202	0.006	0.002	0.001	1.38	0.280	0.039	0.001	1.74
79.8	5.91	3.59	0.007	0.81	0.216	0.003	0.013	0.004	0.851	0.168	0.028	b.d.	2.34
83.7	5.26	0.943	0.005	0.22	0.003	0.002	0.028	0.003	0.213	0.124	0.012	0.002	2.81
85.0	5.92	0.379	0.007	0.05	0.207	0.005	0.010	0.003	0.0469	0.098	0.006	0.004	2.27

89.9	5.69	2.70	0.006	0.51	0.021	0.003	0.041	0.004	0.532	0.167	0.016	0.002	2.33
91.8	5.68	0.384	0.005	0.14	0.017	0.003	0.035	0.003	0.144	0.093	0.008	0.002	2.29
98.0	5.55	3.18	0.005	0.60	0.015	0.002	0.064	0.005	0.609	0.176	0.017	0.001	2.14
103.9	5.71	2.82	0.004	0.58	0.040	0.002	0.073	0.006	0.577	0.205	0.017	0.002	2.15

* Values set to 0.0001 mM for geochemical calculations with PHREEQC 3.4.0 geochemical code in order to obtain saturation states for Fe-bearing minerals.
[1] The last sample discussed in the paper.

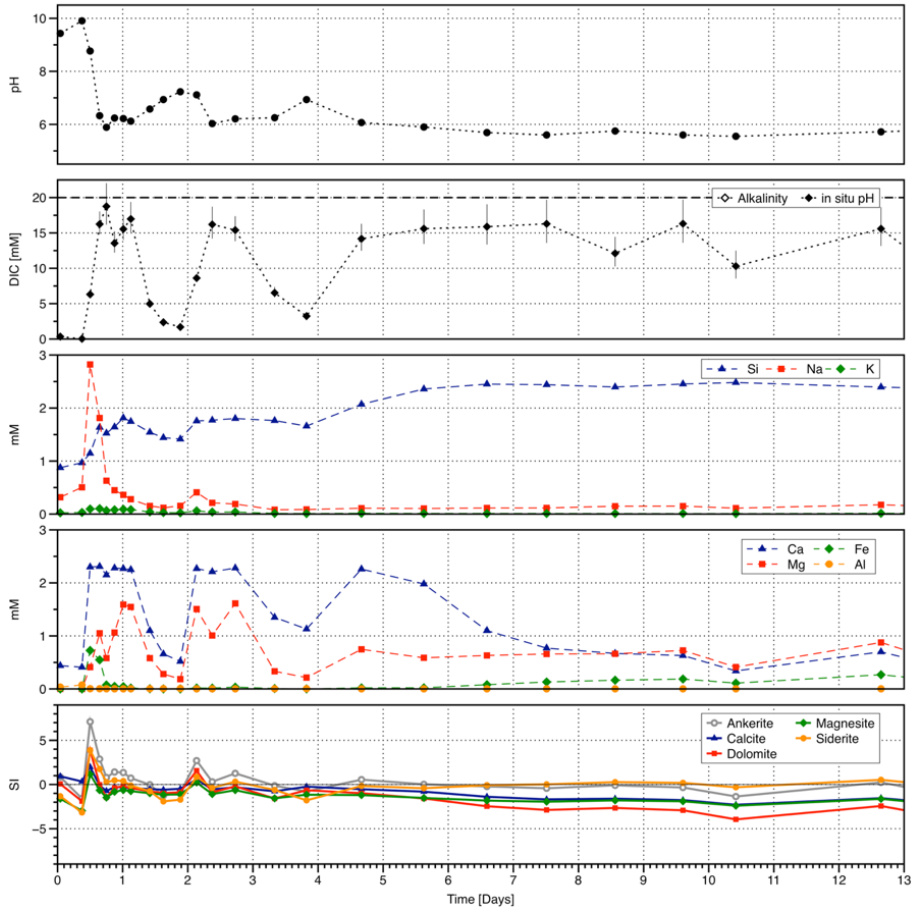

Figure A.1. Outlet pH, DIC, major element concentrations, and mineral saturation indices (SI) of carbonates during the first 13 days of the experiment. Error bars for DIC concentrations were calculated from only varying pH ± 0.10. The dotted line represents the input DIC.

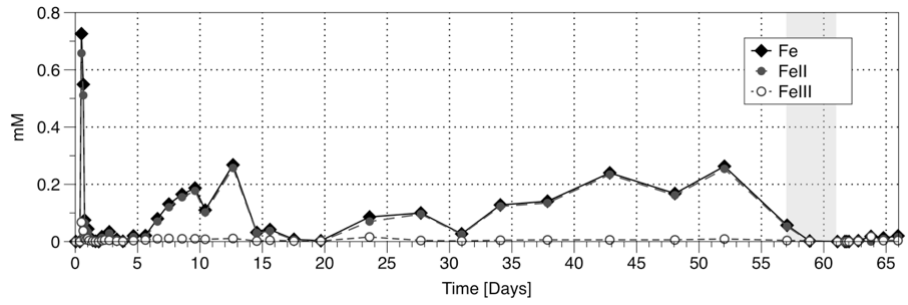

Figure A.2. Results of Fe^{II} and Fe^{III} as compared to total dissolved Fe. Concentrations of Fe^{III} were highest during the first stage – the arrival of the CO_2-charged water, though Fe^{II} remained the dominant species.

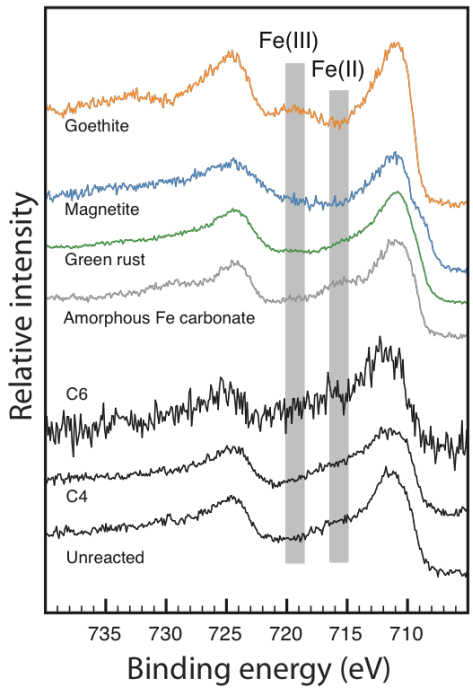

Figure A.3. Detailed scan for Fe2p of the unreacted material, the material after reaction in compartment 4 (C4) and compartment 6 (C6) and reference materials with known Fe^{II} molar fraction. Goethite: 0; magnetite: 1/3; green rust: 2/3; amorphous Fe carbonate: 1. Goethite and magnetite were synthesised using methods given in Schwertmann and Cornell (2003), green rust through oxidation of a 50 mM $FeSO_4$ solution at pH 7, and amorphous Fe carbonate based on methods in Dideriksen et al. (2015).

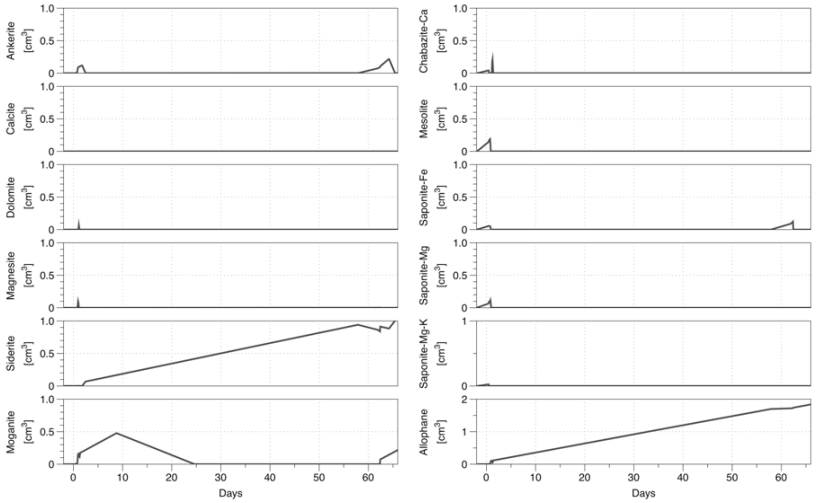

Figure A.4. Cumulative volume (cm^3) of selected minerals allowed to precipitate in the reactive transport model. Note that the scale for allophane is different from the rest.

References

Bénézeth, P., Berninger, U., Bovet, N., Schott, J. and Oelkers, E.H. (2018) Experimental determination of the solubility product of dolomite at 50-253 °C. *Geochimica et Cosmochimica Acta* 224, 262–275.

Bénézeth, P., Dandurand, J.L. and Harrichoury, J.C. (2009) Solubility product of siderite ($FeCO_3$) as a function of temperature (25-250 °C). *Chemical Geology* 265, 3–12.

Catalano, J.G. (2013) Thermodynamic and mass balance constraints on iron-bearing phyllosilicate formation and alteration pathways on early Mars. *Journal of Geophysical Research: Planets* 118, 2124–2136.

Dideriksen, K., Frandsen, C., Bovet, N., Wallace, A., Sel, O., Arbour, T., Navrotsky, A., De Yoreo, J.J. and Banfield, J.F. (2015) Formation and transformation of a short range ordered iron carbonate precursor. *Geochimica et Cosmochimica Acta* 164, 94–109.

Galeczka, I., Wolff-Boenisch, D., Jonsson, T., Sigfússon, B., Stefánsson, A. and Gíslason, S.R. (2013) A novel high pressure column flow reactor for experimental studies of CO_2 mineral storage. *Applied Geochemistry* 30, 91–104.

Gíslason, S.R., Heaney, P.J., Oelkers, E.H. and Schott, J. (1997) Kinetic and thermodynamic properties of moganite, a novel silica polymorph. *Geochimica et Cosmochimica Acta* 61, 1193–1204.

Gysi, A.P. and Stefánsson, A. (2011) CO_2–water–basalt interaction. Numerical simulation of low temperature CO_2 sequestration into basalts. *Geochimica et Cosmochimica Acta* 75, 4728–4751.

Holland, T.J.B. and Powell, R. (2011) An improved and extended internally consistent thermodynamic dataset for phases of petrological interest, involving a new equation of state for solids. *Journal of Metamorphic Geology* 29, 333–383.

Naumov, G.B., Ryshenko, B.N. and Khodakovsky, I.L. (1971) Handbook of thermodynamic data (translation of Russian report): United States Geological Service Report WRD-74-001, 328p.

Neuhoff, P.S. (2000) Thermodynamic Properties and Parageneses of Rock-Forming Zeolites. PhD Thesis. Stanford University.

Schwertmann, U. and Cornell, R.M. (2000) Iron Oxides in the Laboratory: Preparation and Characterization. Wiley-VCH Verlag GmbH, 204p.

Stefánsson, A. and Gíslason, S.R. (2001) Chemical Weathering of Basalts, Southwest Iceland: Effect of Rock Crystallinity and Secondary Minerals on Chemical Fluxes to the Ocean. *American Journal of Science* 501, 513–556.

Stumm, W. and Morgan, J.J. (1996) Aquatic chemistry: chemical equilibria and rates in natural waters, third ed. John Wiley & Sons, New York, 683p.

Voigt, M., Marieni, C., Clark, D.E., Gíslason, S.R. and Oelkers, E.H. (2018) Evaluation and refinement of thermodynamic databases for mineral carbonation. *Energy Procedia* 146, 81–91.

Wolff-Boenisch, D., Gíslason, S.R. and Oelkers, E.H. (2006) The effect of crystallinity on dissolution rates and CO_2 consumption capacity of silicates. *Geochimica et Cosmochimica Acta* 70, 858–870.

B Appendix

Column Experiment Trace Element Geochemical Data

	µg L-1											
	Li	Be	Mg	Ca	V	Cr	Mn	Fe	Co	Rb	Cs	Ti
Limit of Detection / µg L-1	0.24	0.05	9.51	1.41	0.07	0.02	0.02	0.38	0.02	0.63	0.40	0.056
Limit of Quantification / µg L-1	0.80	0.17	31.69	4.70	0.22	0.06	0.08	1.26	0.08	2.12	1.32	0.187
% Uncertainty	2.92	1.87	1.69	0.29	0.39	0.51	0.55	0.23	0.29	1.87	1.04	1.68
27/01/2017	8.16E-01	<LOD	8.98E+02	5.05E+02	7.33E+00	1.09E+00	2.47E+00	5.80E+01	7.77E-02	<LOD	<LOD	7.92E+00
03/02/2017	<LOQ	<LOD	7.94E+02	4.63E+02	4.65E+00	2.78E+00	1.50E+00	6.62E+01	<LOD	<LOD	<LOD	8.71E+00
10/02/2017	1.37E+00	<LOD	1.16E+02	3.67E+03	8.94E+01	6.06E-01	1.05E+00	5.59E+01	<LOD	4.98E+00	<LOD	2.78E+01
16/02/2017	1.33E+00	<LOD	8.70E+01	1.93E+04	5.75E+01	6.41E-01	1.60E+00	6.53E+01	<LOD	2.40E+00	<LOD	3.69E+01
27/02/2017 23:30	1.52E+00	<LOD	1.14E+02	2.02E+02	4.86E-01	2.85E+00	2.85E+00	1.15E+02	<LOQ	<LOD	<LOD	1.35E+01
23/03/2017 23:00	<LOQ	<LOD	2.28E+02	2.59E+02	<LOQ	9.64E-01	1.02E+01	1.30E+02	<LOD	<LOD	<LOD	1.97E+00
26/03/2017 23:00	<LOQ	<LOQ	7.77E+01	1.99E+02	2.47E-01	3.88E-01	1.82E+00	2.77E+01	1.19E-01	<LOD	<LOD	1.00E+00
12/05/2017 15:00	<LOD	<LOD	1.90E+02	2.93E+02	3.27E-01	3.13E+00	4.17E+00	4.20E+01	<LOD	<LOD	<LOD	1.64E+00
13/05/2017 10:00	<LOD	<LOD	5.69E+01	1.96E+02	<LOQ	5.83E-01	1.16E+00	1.98E+01	<LOD	<LOD	<LOD	1.15E+00
14/05/2017 12:00	<LOQ	<LOD	4.93E+01	2.26E+02	<LOD	5.68E-01	3.98E-01	1.12E+01	<LOD	<LOD	<LOD	9.82E-01
15/05/2017 10:15	<LOQ	<LOD	4.15E+01	1.92E+02	<LOD	5.57E-01	1.30E-01	1.53E+01	<LOD	<LOD	<LOD	1.09E+00
28/02/2017 01:00	2.40E+00	<LOD	4.92E+01	1.79E+04	6.29E+01	5.82E-01	4.01E-01	1.40E+01	<LOD	2.29E+00	<LOD	2.86E+01
28/02/2017 09:00	2.40E+00	<LOD	6.82E+01	1.67E+04	8.71E+01	5.62E-01	8.02E-01	3.83E+01	<LOD	2.79E+00	<LOD	2.98E+01
28/02/2017 12:00	3.54E+01	<LOD	1.31E+04	1.88E+05	2.74E+01	1.20E+00	4.40E+03	3.50E+04	1.57E+00	9.55E+00	<LOD	3.28E+02
28/02/2017 15:30	2.32E+01	<LOD	2.66E+04	1.70E+05	3.75E+00	2.28E+00	5.64E+03	3.62E+04	2.40E+00	9.40E+00	<LOD	2.95E+02
28/02/2017 18:00	1.07E+01	<LOD	1.47E+04	8.78E+04	2.24E+00	6.14E-01	1.64E+03	7.45E+03	7.11E-01	5.58E+00	<LOD	1.46E+02
28/02/2017 21:00	9.86E+00	<LOD	3.05E+04	1.38E+05	4.04E+00	8.85E-01	1.67E+03	4.41E+03	1.60E+00	7.08E+00	<LOD	2.38E+02
01/03/2017 00:15	9.18E+00	<LOD	4.44E+04	1.30E+05	4.46E+00	8.73E-01	1.97E+03	5.61E+03	2.59E+00	7.67E+00	<LOD	2.23E+02
01/03/2017 06:00	6.86E+00	<LOD	4.11E+04	1.09E+05	3.93E+00	4.99E-01	9.90E+02	1.75E+03	1.07E+00	6.75E+00	<LOD	1.81E+02
01/03/2017 13:00	3.15E+00	<LOD	1.50E+04	4.51E+04	2.97E+00	3.33E-01	2.56E+02	3.50E+02	2.43E-01	3.35E+00	<LOD	7.14E+01
01/03/2017 18:00	2.88E+00	<LOD	7.45E+03	2.74E+04	3.60E+00	2.25E-01	8.73E+01	9.79E+01	<LOQ	2.45E+00	<LOD	4.25E+01
02/03/2017 00:15	3.38E+00	<LOD	4.80E+03	2.18E+04	4.95E+00	6.16E-01	4.55E+01	4.47E+01	<LOD	2.24E+00	<LOD	3.48E+01
02/03/2017 06:15	9.16E+00	<LOD	4.37E+04	1.56E+05	3.79E+00	4.45E-01	8.16E+02	1.69E+03	1.50E+00	5.81E+00	<LOD	2.60E+02
02/03/2017 12:00	4.86E+00	<LOD	2.67E+04	1.00E+05	3.62E+00	3.25E-01	7.14E+02	1.76E+03	1.61E+00	3.77E+00	<LOD	1.64E+02
02/03/2017 20:30	5.46E+00	<LOD	4.47E+04	1.93E+05	2.71E+00	6.69E-01	1.41E+03	3.66E+03	3.15E+00	4.65E+00	<LOD	3.34E+02
03/03/2017 11:00	1.97E+00	<LOD	9.23E+03	6.01E+04	3.67E+00	2.58E-01	2.80E+02	6.92E+02	7.24E-01	<LOQ	<LOD	9.60E+01
03/03/2017 22:45	1.60E+00	<LOD	5.19E+03	4.55E+04	4.51E+00	2.20E+00	8.44E+01	1.15E+02	1.10E-01	<LOQ	<LOD	7.41E+01
04/03/2017 19:30	2.53E+00	<LOD	1.99E+04	1.34E+05	1.73E+00	2.42E-01	8.42E+02	2.22E+03	2.05E+00	2.40E+00	<LOD	2.24E+02
05/03/2017 18:30	1.98E+00	<LOD	1.59E+04	8.95E+04	1.62E+00	1.12E-01	1.10E+03	2.74E+03	2.41E+00	<LOQ	<LOD	1.48E+02
06/03/2017 17:45	1.73E+00	<LOD	1.67E+04	4.69E+04	1.70E+00	9.87E-02	1.92E+03	5.37E+03	3.83E+00	<LOQ	<LOD	7.67E+01
07/03/2017 15:45	1.63E+00	<LOD	1.73E+04	3.23E+04	1.76E+00	2.03E+01	2.43E+03	8.24E+03	4.95E+00	<LOQ	<LOD	5.15E+01
08/03/2017 17:00	1.43E+00	<LOD	1.69E+04	2.76E+04	1.61E+00	6.50E-02	2.63E+03	9.74E+03	4.74E+00	<LOQ	<LOD	4.49E+01
09/03/2017 18:00	1.30E+00	<LOD	1.90E+04	2.66E+04	2.00E+00	6.55E-01	2.38E+03	1.14E+04	5.11E+00	<LOQ	<LOD	4.35E+01
10/03/2017 13:30	1.00E+00	<LOD	1.09E+04	1.42E+04	2.66E+00	4.26E-01	1.15E+03	7.15E+03	2.94E+00	<LOQ	<LOD	2.30E+01
12/03/2017 19:00	1.55E+00	<LOD	2.24E+04	2.88E+04	2.21E+00	<LOQ	1.54E+03	1.60E+04	5.11E+00	<LOQ	<LOD	4.66E+01
14/03/2017 16:45	9.16E-01	<LOD	3.46E+03	4.64E+03	4.69E+00	<LOD	1.86E+02	2.40E+03	6.17E-01	<LOQ	<LOD	7.42E+00
15/03/2017 18:00	<LOQ	<LOD	6.22E+03	8.98E+03	5.79E+00	<LOQ	2.86E+02	2.56E+03	6.22E-01	<LOQ	<LOD	1.46E+01
17/03/2017 16:15	9.33E-01	<LOD	2.19E+03	3.11E+03	7.05E+00	2.46E-01	7.40E+01	6.59E+02	1.71E-01	<LOD	<LOD	4.81E+00
19/03/2017 20:00	<LOQ	<LOD	1.55E+03	2.37E+03	4.08E+01	3.83E+00	2.95E+01	2.41E+02	<LOQ	<LOD	<LOD	3.80E+00
20/03/2017 18:30	2.00E+00	<LOD	2.27E+04	3.89E+04	3.82E+00	3.79E+00	6.51E+02	5.21E+03	1.23E+00	2.20E+00	<LOD	6.23E+01
21/03/2017 09:50	1.77E+00	<LOD	1.85E+04	3.19E+04	3.83E+00	2.80E-01	9.27E+02	1.01E+04	1.71E+00	<LOQ	<LOD	5.11E+01
22/03/2017 10:00	1.90E+00	<LOD	2.40E+04	4.08E+04	3.56E+00	2.82E-01	1.19E+03	1.39E+04	2.34E+00	2.14E+00	<LOD	6.60E+01
23/03/2017 17:50	1.32E+00	<LOD	1.65E+04	2.51E+04	4.86E+00	1.91E-01	6.51E+02	6.81E+03	9.68E-01	<LOQ	<LOD	4.07E+01
27/03/2017 20:30	1.72E+00	<LOD	1.50E+04	2.40E+04	4.10E+00	7.91E-01	2.31E+02	1.67E+03	3.16E-01	<LOQ	<LOD	3.86E+01
31/03/2017 14:00	2.12E+00	<LOD	1.86E+04	3.28E+04	3.98E+00	7.89E-02	7.66E+02	7.95E+03	9.51E-01	<LOQ	<LOD	5.41E+01
03/04/2017 16:30	1.63E+00	<LOD	8.93E+03	1.49E+04	5.13E+00	6.59E-02	4.05E+02	9.38E+03	6.59E-01	<LOQ	<LOD	2.40E+01
07/04/2017 10:15	1.08E+00	<LOD	1.41E+04	2.28E+04	5.52E+00	9.60E-02	4.56E+02	1.42E+04	7.60E-01	<LOQ	<LOD	3.65E+01
12/04/2017 15:15	1.83E+00	<LOD	1.88E+04	3.17E+04	4.03E+00	<LOQ	6.68E+02	1.57E+04	8.65E-01	<LOQ	<LOD	5.05E+01
17/04/2017 15:15	1.20E+00	<LOD	1.59E+04	2.63E+04	6.97E+00	4.07E-01	5.41E+02	1.63E+04	7.93E-01	<LOQ	<LOD	4.32E+01
21/04/2017 14:30	9.66E-01	<LOD	5.88E+03	9.83E+03	1.72E+01	6.45E-02	1.36E+02	3.47E+03	8.05E-02	<LOQ	<LOD	1.52E+01
26/04/2017 15:00	<LOQ	<LOD	1.76E+03	3.25E+03	4.10E+01	<LOQ	1.25E+01	1.58E+02	<LOD	<LOQ	<LOD	5.05E+00
28/04/2017 10:30	<LOD	<LOD	1.10E+03	2.75E+03	9.98E+01	1.51E-01	2.54E+00	1.93E+01	<LOD	<LOQ	<LOD	4.34E+00
30/04/2017 16:00	<LOD	<LOD	1.40E+03	4.09E+03	8.40E+01	<LOQ	2.06E+00	7.26E+00	<LOD	<LOQ	<LOD	6.44E+00
01/05/2017 06:15	<LOD	<LOD	2.44E+03	7.64E+03	5.51E+01	<LOD	3.46E+00	8.62E+00	<LOD	<LOQ	<LOD	1.20E+01
01/05/2017 06:15	<LOD	<LOD	4.28E+03	1.53E+04	4.14E+01	<LOQ	5.87E+00	1.15E+01	<LOD	2.12E+00	<LOD	2.43E+01
01/05/2017 09:45	9.16E-01	<LOD	4.34E+04	7.66E+04	4.12E+00	<LOQ	1.61E+02	5.54E+02	<LOD	4.02E+00	<LOD	1.30E+02
01/05/2017 16:00	1.22E+00	<LOD	2.70E+04	7.04E+04	3.12E+00	<LOQ	1.77E+02	1.14E+03	1.52E-01	2.95E+00	<LOD	1.19E+02
02/03/2017 10:00	1.93E+00	<LOQ	1.58E+04	4.27E+04	2.36E+00	3.16E-01	2.00E+02	2.10E+03	4.31E-01	2.63E+00	<LOD	6.96E+01
03/05/2017 10:30	1.38E+00	<LOD	1.63E+04	3.28E+04	2.38E+00	<LOQ	2.79E+02	3.30E+03	3.53E-01	<LOQ	<LOD	5.33E+01
04/05/2017 10:30	1.93E+00	<LOD	1.76E+04	3.00E+04	2.97E+00	6.80E-02	7.19E+02	7.78E+03	5.32E-01	<LOQ	<LOD	4.81E+01
05/05/2017 14:30	1.88E+00	<LOD	1.52E+04	2.59E+04	1.83E+00	1.08E-01	9.76E+02	1.51E+04	9.03E-01	2.25E+00	<LOD	4.12E+01
08/05/2017 10:30	<LOQ	<LOD	1.05E+03	1.89E+03	1.22E+01	8.23E-01	5.23E+01	7.40E+02	<LOD	<LOD	<LOD	2.72E+00
09/05/2017 10:15	<LOD	<LOD	3.31E+02	5.42E+02	3.30E+01	2.15E+00	1.51E+01	1.98E+02	<LOD	<LOD	<LOD	1.14E+00
10/05/2017 14:30	<LOQ	<LOD	5.99E+04	1.14E+05	5.61E+00	5.99E+00	7.89E+02	2.27E+03	1.31E-01	4.28E+00	<LOD	1.94E+02
11/05/2017 11:30	<LOQ	<LOD	7.92E+03	1.29E+04	7.11E+00	1.15E+00	9.78E+01	5.51E+02	<LOD	<LOQ	<LOD	2.01E+01
15/05/2017 15:00	<LOQ	<LOD	5.46E+03	8.91E+03	1.11E+01	3.83E+00	5.73E+01	3.33E+02	7.65E-02	<LOQ	<LOD	1.38E+01
16/05/2017 10:00	<LOQ	<LOD	3.28E+04	5.74E+04	6.56E+00	7.79E-02	2.66E+02	7.88E+02	<LOD	2.89E+00	<LOD	9.73E+01
17/05/2017 09:15	9.66E-01	<LOD	2.04E+04	3.24E+04	3.25E+00	4.02E+00	3.08E+02	1.93E+03	1.34E-01	2.39E+00	<LOD	5.26E+01
18/05/2017 10:45	1.43E+00	<LOD	5.04E+03	8.81E+03	3.19E+00	4.15E-01	3.10E+02	4.29E+03	2.09E-01	<LOQ	<LOD	1.42E+01
19/05/2017 11:30	<LOQ	<LOD	1.16E+03	1.96E+03	1.18E+01	6.66E+00	6.28E+01	8.51E+02	<LOQ	<LOQ	<LOD	3.31E+00
23/05/2017 09:00	1.37E+00	<LOD	1.31E+04	2.16E+04	3.62E+00	3.56E+00	4.93E+02	5.83E+03	2.71E-01	<LOQ	<LOD	3.65E+01
24/05/2017 15:15	<LOQ	<LOD	3.41E+03	5.68E+03	6.55E+00	3.61E-01	1.52E+02	2.40E+03	<LOQ	<LOQ	<LOD	9.35E+00
29/05/2017 13:30	1.63E+00	<LOD	1.53E+04	2.56E+04	4.38E+00	4.72E+00	5.30E+02	9.17E+03	4.90E-01	<LOQ	<LOD	4.31E+01
31/05/2017 10:40	1.37E+00	<LOD	1.40E+04	2.35E+04	7.81E+00	2.26E-01	4.90E+02	1.25E+04	4.94E-01	<LOQ	<LOD	3.85E+01
06/06/2017 15:30	<LOQ	<LOD	1.33E+04	2.00E+04	8.32E-01	4.08E-01	5.47E+02	1.81E+04	1.02E+00	<LOD	<LOD	3.58E+01
12/06/2017 13:00	<LOD	<LOD	2.17E+03	3.34E+03	<LOQ	3.91E-01	9.53E+01	3.42E+03	1.87E-01	<LOD	<LOD	5.58E+00

	µg L-1										
	Ni	Cu	Zn	Ga	As	Se	Sr	Cd	Ba	Pb	Bi
Limit of Detection / µg L-1	1.66E-01	8.95E-02	6.90E-01	9.07E-01	8.99E-01	6.04E-01	5.64E-01	4.22E-01	3.07E-01	5.17E-01	9.68E-01
Limit of Quantification / µg L-1	5.54E-01	2.98E-01	2.30E+00	3.02E+00	3.00E+00	2.01E+00	1.88E+00	1.41E+00	1.02E+00	1.72E+00	3.23E+00
% Uncertainty	0.683	0.773	0.453	1.68	1.75	3.78	2.38	1.36	0.585	0.694	0.755
27/01/2017	3.09E+00	1.94E+00	4.55E+00	<LOD	<LOD	<LOD	5.69E+00	<LOD	<LOD	<LOD	<LOD
03/02/2017	1.31E+00	1.36E+00	3.97E+00	<LOD	<LOD	<LOD	5.60E+00	<LOD	<LOD	<LOD	<LOD
10/02/2017	8.08E-01	1.04E+00	5.12E+00	8.81E+00	<LOD	<LOD	2.80E+01	<LOD	<LOD	<LOD	<LOD
16/02/2017	8.30E-01	1.27E+00	5.54E+00	6.79E+00	<LOD	<LOD	3.49E+01	<LOD	<LOQ	<LOD	<LOD
27/02/2017 23:30	1.14E+01	2.36E+00	1.28E+01	<LOD	<LOD	<LOD	4.67E+00	<LOD	<LOD	<LOD	<LOD
23/03/2017 23:00	2.01E+00	2.49E+00	9.64E+00	<LOD	<LOD	<LOD	5.77E+00	<LOD	<LOQ	<LOD	<LOD
26/03/2017 23:00	8.19E-01	3.74E-01	3.62E+00	<LOD	<LOD	<LOD	4.22E+00	<LOD	<LOD	<LOD	<LOD
12/05/2017 15:00	5.22E+00	7.13E-01	4.53E+00	<LOD	<LOD	<LOD	5.55E+00	<LOD	<LOQ	<LOD	<LOD
13/05/2017 10:00	9.83E-01	1.11E+00	5.38E+00	<LOD	<LOD	<LOD	4.40E+00	<LOD	<LOQ	<LOD	<LOD
14/05/2017 12:00	6.41E-01	3.57E-01	7.60E+00	<LOD	<LOD	<LOD	4.29E+00	<LOD	<LOD	<LOD	<LOD
15/05/2017 10:15	<LOQ	9.42E-01	4.32E+00	<LOD	<LOD	<LOD	4.29E+00	<LOD	<LOD	<LOD	<LOD
28/02/2017 01:00	2.45E+00	1.91E+00	4.39E+00	<LOQ	<LOD	<LOD	3.26E+01	<LOD	<LOD	<LOD	<LOD
28/02/2017 09:00	9.03E-01	1.18E+00	4.79E+00	7.42E+00	<LOD	<LOD	3.25E+01	<LOD	<LOQ	<LOD	<LOD
28/02/2017 12:00	2.26E+00	1.07E+00	5.76E+01	<LOQ	<LOD	<LOD	3.94E+02	<LOD	1.30E+01	<LOD	<LOD
28/02/2017 15:30	4.04E+00	2.02E+00	1.97E+02	<LOD	<LOD	<LOD	3.92E+02	<LOD	1.61E+01	<LOD	<LOD
28/02/2017 18:00	1.44E+00	1.12E+00	5.46E+01	<LOD	<LOD	<LOD	1.90E+02	<LOD	6.94E+00	<LOD	<LOD
28/02/2017 21:00	3.41E+00	1.34E+00	5.17E+01	<LOD	<LOD	<LOD	2.99E+02	<LOD	1.12E+01	<LOD	<LOD
01/03/2017 00:15	6.14E+00	1.33E+00	7.27E+01	<LOD	<LOD	<LOD	2.89E+02	<LOD	1.23E+01	<LOD	<LOD
01/03/2017 06:00	3.64E+00	1.24E+00	2.73E+01	<LOD	<LOD	<LOD	2.39E+02	<LOD	9.99E+00	<LOD	<LOD
01/03/2017 13:00	1.89E+00	1.47E+00	9.32E+00	<LOD	<LOD	<LOD	9.37E+01	<LOD	3.39E+00	<LOD	<LOD
01/03/2017 18:00	8.70E-01	1.02E+00	4.85E+00	<LOD	<LOD	<LOD	5.69E+01	<LOD	1.86E+00	<LOD	<LOD
02/03/2017 00:15	1.14E+00	1.08E+00	3.25E+00	<LOQ	<LOD	<LOD	4.31E+01	<LOD	1.15E+00	<LOD	<LOD
02/03/2017 06:15	6.51E+00	9.47E-01	3.16E+01	<LOD	<LOD	<LOQ	3.37E+02	<LOD	1.32E+01	<LOD	<LOD
02/03/2017 12:00	6.07E+00	2.17E+00	2.37E+01	<LOD	<LOD	<LOD	2.05E+02	<LOD	7.86E+00	<LOD	<LOD
02/03/2017 20:30	8.77E+00	1.26E+00	3.75E+01	<LOD	<LOD	<LOD	4.04E+02	<LOD	1.48E+01	<LOD	<LOD
03/03/2017 11:00	2.57E+00	9.07E-01	7.32E+00	<LOD	<LOQ	<LOD	1.15E+02	<LOD	3.07E+00	<LOD	<LOD
03/03/2017 22:45	2.48E+00	2.14E+00	5.50E+00	<LOD	<LOQ	<LOD	8.70E+01	<LOD	1.78E+00	<LOD	<LOD
04/03/2017 19:30	7.87E+00	1.24E+00	1.44E+01	<LOD	<LOQ	<LOQ	2.64E+02	<LOD	6.68E+00	<LOD	<LOD
05/03/2017 18:30	8.61E+00	<LOD	1.30E+01	<LOD	<LOQ	<LOD	1.77E+02	<LOD	4.72E+00	<LOD	<LOD
06/03/2017 17:45	1.14E+01	<LOD	2.10E+01	<LOD	<LOQ	<LOD	9.37E+01	<LOD	3.34E+00	<LOD	<LOD
07/03/2017 15:45	1.96E+01	7.04E-01	3.02E+01	<LOD	<LOQ	<LOD	7.20E+01	<LOD	2.94E+00	<LOD	<LOD
08/03/2017 17:00	9.69E+00	<LOD	3.29E+01	<LOD	<LOQ	<LOD	6.78E+01	<LOD	2.81E+00	<LOD	<LOD
09/03/2017 18:00	1.03E+01	<LOD	3.92E+01	<LOD	<LOQ	<LOD	7.02E+01	<LOD	3.37E+00	<LOD	<LOD
10/03/2017 13:30	6.27E+00	<LOQ	2.76E+01	<LOD	<LOQ	<LOD	4.20E+01	<LOD	1.90E+00	<LOD	<LOD
12/03/2017 19:00	8.67E+00	<LOD	4.78E+01	<LOD	<LOQ	<LOD	1.07E+02	<LOD	4.67E+00	<LOD	<LOD
14/03/2017 16:45	1.47E+00	<LOD	7.11E+00	<LOD	<LOD	<LOD	1.83E+01	<LOD	<LOQ	<LOD	<LOD
15/03/2017 18:00	1.27E+00	<LOD	7.50E+00	<LOD	<LOD	<LOD	3.67E+01	<LOD	1.04E+00	<LOD	<LOD
17/03/2017 16:15	1.55E+00	7.86E-01	5.38E+00	<LOD	<LOD	<LOD	1.02E+01	<LOD	<LOD	<LOD	<LOD
19/03/2017 20:00	9.73E-01	<LOD	<LOQ	4.60E+00	<LOD	<LOD	6.63E+00	<LOD	<LOD	<LOD	<LOD
20/03/2017 18:30	5.99E+00	<LOQ	1.42E+01	<LOD	<LOD	<LOD	9.85E+01	<LOD	4.80E+00	<LOD	<LOD
21/03/2017 09:50	4.05E+00	<LOD	2.12E+01	<LOD	<LOD	<LOD	8.15E+01	<LOD	4.90E+00	<LOD	<LOD
22/03/2017 10:00	6.65E+00	<LOQ	3.47E+01	<LOD	<LOD	<LOD	1.05E+02	<LOD	5.68E+00	<LOD	<LOD
23/03/2017 17:50	2.91E+00	4.94E-01	1.77E+01	<LOD	<LOD	<LOD	6.48E+01	<LOD	4.00E+00	<LOD	<LOD
27/03/2017 20:30	1.64E+00	<LOQ	6.19E+00	<LOD	<LOD	<LOD	5.54E+01	<LOD	3.86E+00	<LOD	<LOD
31/03/2017 14:00	3.45E+00	5.62E-01	1.38E+01	<LOD	<LOD	<LOD	7.65E+01	<LOD	5.24E+00	<LOD	<LOD
03/04/2017 16:30	2.48E+00	<LOQ	1.11E+01	<LOD	<LOD	<LOD	4.13E+01	<LOD	3.10E+00	<LOD	<LOD
07/04/2017 10:15	2.51E+00	<LOQ	1.24E+01	<LOD	<LOD	<LOD	6.27E+01	<LOD	5.83E+00	<LOD	<LOD
12/04/2017 15:15	2.82E+00	<LOD	1.21E+01	<LOD	<LOD	<LOD	7.63E+01	<LOD	8.16E+00	<LOD	<LOD
17/04/2017 15:15	2.48E+00	<LOQ	1.22E+01	<LOD	<LOD	<LOD	6.83E+01	<LOD	8.69E+00	<LOD	<LOD
21/04/2017 14:30	7.22E-01	<LOD	3.97E+00	<LOD	<LOD	<LOD	2.26E+01	<LOD	2.72E+00	<LOD	<LOD
26/04/2017 15:00	<LOQ	<LOD	<LOQ	3.81E+00	<LOD	<LOD	6.25E+00	<LOD	<LOD	<LOD	<LOD
28/04/2017 10:30	<LOQ	<LOD	<LOQ	9.03E+00	<LOD	<LOD	4.46E+00	<LOD	<LOD	<LOD	<LOD
30/04/2017 16:00	<LOD	<LOQ	<LOD	8.22E+00	<LOD	<LOD	6.72E+00	<LOD	<LOD	<LOD	<LOD
01/05/2017 06:15	<LOQ	<LOQ	<LOQ	5.67E+00	<LOD	<LOD	1.25E+01	<LOD	<LOQ	<LOD	<LOD
01/05/2017 06:15	<LOQ	<LOQ	<LOQ	4.56E+00	<LOD	<LOD	2.59E+01	<LOD	1.36E+00	<LOD	<LOD
01/05/2017 09:45	9.47E+00	3.37E-01	<LOQ	<LOD	<LOD	<LOD	1.50E+02	<LOD	1.31E+01	<LOD	<LOD
01/05/2017 16:00	1.23E+00	6.83E-01	2.85E+00	<LOD	<LOD	<LOD	1.31E+02	<LOD	1.32E+01	<LOD	<LOD
02/03/2017 10:00	1.11E+00	<LOQ	2.95E+00	<LOD	<LOD	<LOD	7.65E+01	<LOD	9.19E+00	<LOD	<LOD
03/05/2017 10:30	8.68E+00	4.57E-01	4.91E+00	<LOD	<LOD	<LOD	6.19E+01	<LOD	8.32E+00	<LOD	<LOD
04/05/2017 10:30	2.28E+00	7.54E-01	7.28E+00	<LOD	<LOD	<LOD	6.77E+01	<LOD	1.00E+01	<LOD	<LOD
05/05/2017 14:30	3.27E+00	8.17E-01	1.43E+01	<LOD	<LOD	<LOD	7.42E+01	<LOD	1.26E+01	<LOD	<LOD
08/05/2017 10:30	1.54E+00	5.75E-01	2.39E+00	<LOD	<LOD	<LOD	4.56E+00	<LOD	<LOQ	<LOD	<LOD
09/05/2017 10:15	2.46E+00	3.30E-01	<LOQ	<LOQ	<LOD	<LOD	<LOQ	<LOD	<LOD	<LOD	<LOD
10/05/2017 14:30	4.82E+00	4.91E-01	7.48E+00	<LOD	<LOD	<LOD	2.72E+02	<LOD	2.82E+01	<LOD	<LOD
11/05/2017 11:30	1.28E+00	3.19E-01	4.41E+00	<LOD	<LOD	<LOD	2.99E+01	<LOD	3.32E+00	<LOD	<LOD
15/05/2017 15:00	6.10E+00	9.08E-01	2.63E+00	<LOQ	<LOD	<LOD	2.01E+01	<LOD	1.99E+00	<LOD	<LOD
16/05/2017 10:00	9.02E-01	3.06E-01	2.35E+00	<LOD	<LOD	<LOD	1.26E+02	<LOD	1.33E+01	<LOD	<LOD
17/05/2017 09:15	4.36E+00	9.20E-01	4.78E+00	<LOD	<LOD	<LOD	7.20E+01	<LOD	9.81E+00	<LOD	<LOD
18/05/2017 10:45	1.34E+00	<LOQ	5.27E+00	<LOD	<LOD	<LOD	2.32E+01	<LOD	5.20E+00	<LOD	<LOD
19/05/2017 11:30	4.69E+00	4.19E-01	5.35E+00	<LOD	<LOD	<LOD	5.89E+00	<LOD	<LOQ	<LOD	<LOD
23/05/2017 09:00	1.94E+00	3.03E-01	5.16E+00	<LOD	<LOD	<LOD	5.82E+01	<LOD	1.06E+01	<LOD	<LOD
24/05/2017 15:15	1.08E+01	4.72E-01	3.45E+00	<LOD	<LOD	<LOD	1.56E+01	<LOD	3.30E+00	<LOD	<LOD
29/05/2017 13:30	6.92E+00	5.99E-01	7.69E+00	<LOD	<LOD	<LOD	6.53E+01	<LOD	1.34E+01	<LOD	<LOD
31/05/2017 10:40	1.63E+00	<LOD	6.48E+00	<LOD	<LOD	<LOD	6.07E+01	<LOD	1.46E+01	<LOD	<LOD
06/06/2017 15:30	3.76E+00	6.73E-01	1.09E+01	<LOD	<LOD	<LOD	3.63E+01	<LOD	5.09E+00	<LOD	<LOD
12/06/2017 13:00	1.05E+00	3.37E-01	3.72E+00	<LOD	<LOD	<LOD	6.25E+00	<LOD	<LOQ	<LOD	<LOD

	µg L-1											
	Sc	Zr	Mo	Nb	In	Sn	Sb	La	Ce	Pr	Nd	Sm
Limit of Detection / µg L-1	1.40E-01	7.65E-02	2.90E-03	1.10E-02	4.94E-01	3.03E-02	1.18E-03	7.47E-04	1.06E-03	8.22E-05	2.92E-04	1.06E-04
Limit of Quantification / µg L-1	4.68E-01	2.55E-01	9.68E-03	3.66E-02	1.65E+00	1.01E-01	3.93E-03	2.49E-03	3.55E-03	2.74E-04	9.75E-04	3.54E-04
% Uncertainty	2.58	1.23	0.64	1.00	2.37	1.48	1.28	1.80	0.99	2.07	0.86	1.38
27/01/2017	<LOQ	4.64E-01	6.39E-01	<LOD	<LOD	<LOQ	<LOD	7.74E-02	1.51E-01	<LOD	4.13E-02	<LOD
03/02/2017	<LOQ	<LOQ	4.74E-01	<LOD	<LOD	1.04E-01	<LOD	8.53E-02	1.47E-01	<LOD	4.28E-02	<LOD
10/02/2017	<LOQ	<LOD	4.98E-01	<LOD	<LOD	<LOD	2.14E-02	8.73E-02	1.54E-01	<LOD	4.23E-02	<LOD
16/02/2017	<LOD	<LOQ	2.32E-01	<LOD	<LOD	<LOD	<LOD	1.05E-01	1.69E-01	6.50E-04	4.23E-02	<LOD
27/02/2017 23:30	<LOD	<LOQ	5.98E-01	<LOQ	<LOD	<LOQ	1.25E-02	1.26E-01	2.27E-01	1.60E-03	7.59E-02	7.00E-04
23/03/2017 23:00	<LOD	<LOD	1.30E-01	<LOD	<LOQ	<LOD	<LOD	6.83E-02	1.40E-01	<LOD	3.26E-02	<LOD
26/03/2017 23:00	<LOD	<LOD	2.04E-01	<LOD	<LOD	<LOD	<LOD	8.08E-02	1.33E-01	<LOD	3.40E-02	<LOD
12/05/2017 15:00	<LOD	<LOD	1.92E-01	<LOD	<LOD	<LOD	<LOD	7.64E-02	1.45E-01	<LOD	3.03E-02	<LOD
13/05/2017 10:00	<LOD	<LOD	9.02E-02	<LOD	<LOD	<LOD	<LOD	6.95E-02	1.26E-01	<LOD	3.13E-02	<LOD
14/05/2017 12:00	<LOD	<LOD	3.25E-02	<LOD	<LOD	<LOD	<LOD	8.19E-02	1.43E-01	<LOD	3.90E-02	<LOD
15/05/2017 10:15	<LOD	<LOD	1.02E-02	<LOD	<LOD	<LOD	<LOD	8.95E-02	1.55E-01	<LOD	8.25E-02	<LOD
28/02/2017 01:00	<LOD	<LOD	3.48E+00	<LOD	<LOD	<LOD	<LOD	6.84E-02	1.34E-01	<LOD	3.27E-02	<LOD
28/02/2017 09:00	<LOD	<LOD	2.28E+00	<LOD	<LOD	<LOD	<LOD	8.45E-02	1.53E-01	<LOD	4.33E-02	<LOD
28/02/2017 12:00	1.48E+00	<LOQ	1.55E+00	2.12E-01	<LOD	1.91E-01	<LOD	8.32E-02	1.57E-01	<LOD	4.64E-02	<LOD
28/02/2017 15:30	1.53E+00	<LOD	1.79E+00	8.89E-02	<LOD	1.82E-01	2.12E-02	1.04E-01	1.70E-01	<LOD	5.33E-02	<LOD
28/02/2017 18:00	<LOQ	<LOD	8.67E+00	<LOD	<LOD	<LOQ	<LOQ	8.06E-02	1.41E-01	<LOD	4.25E-02	<LOD
28/02/2017 21:00	9.27E-01	<LOD	6.91E+00	<LOQ	<LOD	<LOD	1.22E-02	9.01E-02	1.42E-01	<LOD	4.84E-02	<LOD
01/03/2017 00:15	8.88E-01	<LOD	4.56E+00	<LOQ	<LOD	<LOD	2.82E-02	9.17E-02	1.51E-01	<LOD	5.00E-02	<LOD
01/03/2017 06:00	4.73E-01	<LOD	4.86E+00	<LOD	<LOD	<LOD	3.95E-02	8.67E-02	1.46E-01	<LOD	4.27E-02	<LOD
01/03/2017 13:00	<LOD	<LOD	5.98E+00	<LOD	<LOD	<LOD	5.26E-02	7.04E-02	1.34E-01	<LOD	3.58E-02	<LOD
01/03/2017 18:00	<LOD	<LOD	4.68E+00	<LOD	<LOD	<LOD	8.00E-02	7.57E-02	1.34E-01	<LOD	3.60E-02	<LOD
02/03/2017 00:15	<LOD	<LOD	4.02E+00	<LOD	<LOD	<LOD	1.29E-01	<LOD	<LOD	1.40E-03	<LOD	1.70E-03
02/03/2017 06:15	<LOQ	<LOQ	2.68E+00	9.04E-02	<LOD	<LOD	6.69E-02	8.40E-03	1.21E-02	<LOD	2.80E-03	6.50E-04
02/03/2017 12:00	<LOD	<LOD	4.05E+00	<LOQ	<LOD	<LOD	9.54E-02	<LOQ	<LOD	<LOD	<LOD	<LOD
02/03/2017 20:30	7.31E-01	<LOQ	2.92E+00	1.22E-01	<LOD	<LOD	5.68E-02	1.72E-02	2.87E-02	2.10E-03	9.30E-03	1.00E-03
03/03/2017 11:00	<LOD	<LOD	5.26E+00	<LOD	<LOD	<LOD	1.19E-01	<LOD	<LOD	<LOD	<LOD	5.50E-04
03/03/2017 22:45	<LOD	<LOD	3.41E+00	<LOD	<LOD	<LOD	1.89E-01	<LOQ	<LOD	<LOD	<LOD	<LOD
04/03/2017 19:30	<LOQ	<LOD	2.72E+00	<LOQ	<LOD	<LOD	1.00E-01	8.65E-03	4.50E-03	<LOD	3.75E-03	2.20E-03
05/03/2017 18:30	<LOD	<LOD	2.77E+00	<LOQ	<LOD	<LOD	1.32E-01	<LOD	<LOD	<LOD	<LOD	<LOD
06/03/2017 17:45	<LOD	<LOD	2.16E+00	<LOD	<LOD	<LOD	1.20E-01	<LOD	<LOD	<LOD	<LOD	<LOD
07/03/2017 15:45	<LOD	<LOD	1.86E+00	<LOD	<LOD	<LOD	1.29E-01	<LOQ	<LOD	<LOD	<LOD	<LOD
08/03/2017 17:00	<LOD	<LOD	1.49E+00	<LOD	<LOD	<LOD	1.25E-01	<LOD	<LOD	<LOD	7.20E-03	<LOD
09/03/2017 18:00	<LOD	<LOD	1.28E+00	<LOD	<LOD	<LOD	1.64E-01	<LOQ	<LOD	<LOD	1.55E-03	7.00E-04
10/03/2017 13:30	<LOD	<LOD	1.78E+00	<LOD	<LOD	<LOD	1.78E-01	<LOQ	<LOD	1.15E-03	<LOD	<LOD
12/03/2017 19:00	<LOD	<LOD	9.80E-01	<LOD	<LOD	<LOD	1.84E-01	2.65E-03	<LOD	<LOD	<LOD	5.00E-04
14/03/2017 16:45	<LOD	<LOD	2.04E+00	<LOD	<LOD	<LOD	2.19E-01	<LOD	<LOD	<LOD	<LOD	<LOD
15/03/2017 18:00	<LOD	<LOD	1.38E+00	<LOD	<LOD	<LOD	1.98E-01	<LOD	<LOD	<LOD	<LOD	<LOD
17/03/2017 16:15	<LOD	<LOD	8.45E-01	<LOD	<LOD	<LOD	1.75E-01	<LOD	<LOD	<LOD	3.35E-03	8.50E-04
19/03/2017 20:00	<LOD	<LOD	7.50E-01	<LOD	<LOD	<LOD	1.72E-01	<LOQ	<LOD	<LOD	2.90E-03	<LOD
20/03/2017 18:30	<LOD	<LOD	3.01E-01	<LOD	<LOD	<LOD	1.48E-01	<LOD	<LOD	<LOQ	<LOQ	3.85E-03
21/03/2017 09:50	<LOD	<LOD	3.01E-01	<LOD	<LOD	<LOD	1.01E-01	4.70E-03	<LOD	<LOD	<LOQ	6.50E-04
22/03/2017 10:00	<LOD	<LOD	9.55E-01	<LOQ	<LOD	<LOD	8.44E-02	<LOQ	6.75E-03	9.00E-04	2.70E-03	<LOD
23/03/2017 17:50	<LOD	<LOD	8.73E-01	<LOD	<LOD	<LOD	1.09E-01	3.45E-03	<LOQ	<LOD	4.35E-03	<LOQ
27/03/2017 20:30	<LOD	<LOD	3.26E-01	<LOD	<LOD	<LOD	5.74E-02	4.88E-02	6.63E-02	5.45E-03	3.49E-02	4.45E-03
31/03/2017 14:00	<LOD	<LOD	2.84E-01	<LOD	<LOD	<LOD	5.60E-02	2.04E-02	2.00E-02	7.00E-04	6.45E-03	<LOQ
03/04/2017 16:30	<LOD	<LOD	4.58E-01	<LOD	<LOD	<LOD	5.63E-02	4.25E-03	<LOD	<LOD	2.65E-03	<LOD
07/04/2017 10:15	<LOD	<LOD	3.29E-01	<LOD	<LOD	<LOD	4.11E-02	1.31E-02	7.45E-03	<LOD	3.00E-03	1.20E-03
12/04/2017 15:15	<LOD	<LOD	2.35E-01	<LOD	<LOD	<LOD	2.08E-02	1.23E-02	1.84E-02	4.00E-04	5.05E-03	1.50E-03
17/04/2017 15:15	<LOD	<LOD	2.73E-01	<LOD	<LOD	<LOD	2.23E-02	1.12E-02	8.05E-03	1.20E-03	6.75E-03	2.45E-03
21/04/2017 14:30	<LOD	<LOD	3.60E-01	<LOD	<LOD	<LOD	2.15E-02	<LOD	<LOD	<LOD	<LOD	1.55E-03
26/04/2017 15:00	<LOD	<LOD	5.31E-01	<LOD	<LOD	<LOD	2.79E-02	<LOD	<LOD	<LOD	<LOD	2.55E-03
28/04/2017 10:30	<LOD	<LOD	3.84E-01	<LOD	<LOD	<LOD	3.67E-02	<LOD	<LOD	<LOD	<LOD	<LOD
30/04/2017 16:00	<LOD	<LOD	3.58E-01	<LOD	<LOD	<LOD	3.45E-02	<LOD	<LOD	<LOD	<LOD	6.50E-04
01/05/2017 06:15	<LOD	<LOD	3.25E-01	<LOD	<LOD	<LOD	8.60E-03	<LOD	<LOD	<LOD	<LOD	<LOD
01/05/2017 06:15	<LOD	<LOD	2.64E-01	<LOD	<LOD	<LOD	1.23E-02	<LOD	<LOD	<LOD	<LOD	<LOD
01/05/2017 09:45	<LOD	<LOD	1.02E-01	<LOD	<LOD	<LOD	<LOQ	<LOD	<LOD	<LOD	<LOD	<LOD
01/05/2017 16:00	<LOD	<LOD	7.33E-02	<LOD	<LOD	<LOD	<LOQ	<LOQ	<LOD	<LOD	<LOD	<LOD
02/03/2017 10:00	<LOD	<LOD	9.45E-02	<LOQ	<LOD	<LOQ	1.55E-02	1.28E-02	8.00E-03	6.60E-03	6.05E-03	6.85E-03
03/05/2017 10:30	<LOD	<LOD	7.89E-02	<LOD	<LOD	<LOD	<LOQ	<LOD	<LOD	<LOD	<LOD	<LOD
04/05/2017 10:30	<LOD	<LOD	1.23E-01	<LOD	<LOD	<LOD	2.50E-02	<LOD	<LOD	<LOD	<LOD	<LOD
05/05/2017 14:30	<LOD	<LOD	1.23E-01	<LOD	<LOD	<LOD	<LOD	1.06E-02	4.35E-03	<LOD	<LOD	<LOD
08/05/2017 10:30	<LOD	<LOD	2.39E-01	<LOD	<LOD	<LOD	7.30E-03	<LOD	<LOD	<LOD	<LOD	<LOD
09/05/2017 10:15	<LOD	<LOD	5.21E-01	<LOD	<LOD	<LOD	1.45E-02	<LOD	<LOD	<LOD	<LOD	<LOD
10/05/2017 14:30	<LOD	<LOD	5.35E-01	<LOD	<LOD	<LOD	4.35E-03	7.51E-02	1.00E-01	<LOD	4.43E-02	<LOD
11/05/2017 11:30	<LOD	<LOD	2.19E-01	<LOD	<LOD	<LOD	<LOD	<LOD	<LOD	<LOD	<LOD	<LOD
15/05/2017 15:00	<LOD	<LOD	1.99E-01	<LOD	<LOD	<LOD	1.02E-02	<LOD	<LOD	<LOD	<LOD	<LOD
16/05/2017 10:00	<LOD	<LOD	1.14E-01	<LOD	<LOD	<LOD	<LOQ	1.30E-02	<LOD	<LOD	1.35E-03	<LOD
17/05/2017 09:15	<LOD	<LOD	1.24E-01	<LOD	<LOD	<LOD	<LOD	<LOD	<LOD	<LOD	<LOD	<LOD
18/05/2017 10:45	<LOD	<LOD	1.60E-01	<LOD	<LOD	<LOD	<LOD	<LOD	<LOD	<LOD	<LOD	<LOD
19/05/2017 11:30	<LOD	<LOD	2.40E-01	<LOD	<LOD	<LOD	<LOD	<LOD	<LOD	<LOD	<LOD	<LOD
23/05/2017 09:00	<LOD	<LOD	1.34E-01	<LOD	<LOD	<LOD	<LOD	1.32E-02	1.34E-02	<LOD	2.35E-03	<LOD
24/05/2017 15:15	<LOD	<LOD	1.61E-01	<LOD	<LOD	<LOD	<LOD	3.51E-02	3.84E-02	<LOD	<LOQ	<LOD
29/05/2017 13:30	<LOD	<LOD	1.11E-01	<LOD	<LOD	<LOD	<LOD	7.09E-02	1.15E-01	<LOD	4.01E-02	<LOD
31/05/2017 10:40	<LOD	<LOD	1.07E-01	<LOD	<LOD	<LOD	1.59E-01	3.23E-02	2.92E-02	<LOD	1.01E-02	<LOD
06/06/2017 15:30	<LOD	<LOD	2.78E-02	<LOD	<LOD	<LOD	<LOD	3.85E-02	2.91E-02	<LOD	<LOQ	<LOD
12/06/2017 13:00	<LOD	<LOD	3.77E-02	<LOD	<LOD	<LOD	<LOD	<LOD	<LOD	<LOD	<LOD	<LOD

	µg L-1										
	Eu	Gd	Tb	Dy	Ho	Er	Tm	Yb	Lu	Hf	Ta
Limit of Detection / µg L-1	8.22E-05	2.92E-04	8.22E-05	1.25E-04	1.96E-04	1.71E-04	1.06E-04	8.22E-05	8.22E-05	1.05E-03	3.09E-03
Limit of Quantification / µg L-1	2.74E-04	9.75E-04	2.74E-04	4.18E-04	6.52E-04	5.70E-04	3.54E-04	2.74E-04	2.74E-04	3.49E-03	1.03E-02
% Uncertainty	1.05	1.28	0.98	0.83	0.49	0.53	0.25	0.68	1.21	0.79	0.86
27/01/2017	<LOD	<LOD	<LOD	<LOD	<LOD	<LOD	<LOD	<LOD	<LOD	<LOD	<LOD
03/02/2017	<LOD	<LOD	<LOD	<LOD	<LOD	<LOD	<LOD	<LOD	<LOD	<LOD	<LOD
10/02/2017	<LOD	<LOD	<LOD	<LOD	<LOD	<LOD	<LOD	<LOD	<LOD	<LOD	<LOD
16/02/2017	<LOD	<LOD	<LOD	<LOD	<LOD	<LOD	<LOD	<LOD	<LOD	<LOD	<LOD
27/02/2017 23:30	<LOD	<LOD	<LOD	<LOD	<LOD	<LOD	<LOD	<LOD	<LOD	<LOD	<LOD
23/03/2017 23:00	<LOD	<LOD	<LOD	<LOD	<LOD	<LOD	<LOD	<LOD	<LOD	<LOD	<LOD
26/03/2017 23:00	<LOD	<LOD	<LOD	<LOD	<LOD	<LOD	<LOD	<LOD	<LOD	<LOD	<LOD
12/05/2017 15:00	<LOD	<LOD	<LOD	<LOD	<LOD	<LOD	<LOD	<LOD	<LOD	<LOD	<LOD
13/05/2017 10:00	<LOD	<LOD	<LOD	<LOD	<LOD	<LOD	<LOD	<LOD	<LOD	<LOD	<LOD
14/05/2017 12:00	<LOD	<LOD	<LOD	<LOD	<LOD	<LOD	<LOD	<LOD	<LOD	<LOD	<LOD
15/05/2017 10:15	<LOD	<LOD	<LOD	<LOD	<LOD	<LOD	<LOD	<LOD	<LOD	<LOD	<LOD
28/02/2017 01:00	<LOD	<LOD	<LOD	<LOD	<LOD	<LOD	<LOD	<LOD	<LOD	<LOD	<LOD
28/02/2017 09:00	<LOD	<LOD	<LOD	<LOD	<LOD	<LOD	<LOD	<LOD	<LOD	<LOD	<LOD
28/02/2017 12:00	<LOD	<LOD	<LOD	<LOD	<LOD	<LOD	<LOD	<LOD	<LOD	<LOD	<LOD
28/02/2017 15:30	<LOD	<LOD	<LOD	<LOD	<LOD	<LOD	<LOD	<LOD	<LOD	<LOD	<LOD
28/02/2017 18:00	<LOD	<LOD	<LOD	<LOD	<LOD	<LOD	<LOD	<LOD	<LOD	<LOD	<LOD
28/02/2017 21:00	<LOD	<LOD	<LOD	<LOD	<LOD	<LOD	<LOD	<LOD	<LOD	<LOD	<LOD
01/03/2017 00:15	<LOD	<LOD	<LOD	<LOD	<LOD	<LOD	<LOD	<LOD	<LOD	<LOD	<LOD
01/03/2017 06:00	<LOD	<LOD	<LOD	<LOD	<LOD	<LOD	<LOD	<LOD	<LOD	<LOD	<LOD
01/03/2017 13:00	<LOD	<LOD	<LOD	<LOD	<LOD	<LOD	<LOD	<LOD	<LOD	<LOD	<LOD
01/03/2017 18:00	<LOD	<LOD	<LOD	<LOD	<LOD	<LOD	<LOD	<LOD	<LOD	<LOD	<LOD
02/03/2017 00:15	<LOD	<LOD	<LOD	<LOD	<LOD	<LOD	<LOD	1.50E-03	<LOD	<LOD	<LOD
02/03/2017 06:15	9.50E-04	3.25E-03	<LOD	8.50E-04	<LOD	<LOQ	<LOD	4.50E-04	<LOD	<LOD	<LOD
02/03/2017 12:00	4.00E-04	<LOD	<LOD	<LOD	<LOD	<LOD	<LOD	1.65E-03	<LOD	<LOD	<LOD
02/03/2017 20:30	2.05E-03	1.30E-03	<LOD	4.50E-04	<LOD	1.45E-03	<LOD	2.30E-03	<LOQ	<LOD	<LOD
03/03/2017 11:00	<LOD	<LOD	<LOD	<LOQ	<LOD	<LOD	<LOD	<LOD	<LOD	<LOD	<LOD
03/03/2017 22:45	<LOD	<LOD	<LOD	<LOD	<LOD	<LOD	<LOD	4.50E-04	<LOD	<LOD	<LOD
04/03/2017 19:30	6.00E-04	1.65E-03	<LOD	<LOD	<LOD	1.30E-03	<LOD	1.90E-03	<LOD	<LOD	<LOD
05/03/2017 18:30	<LOD	<LOD	<LOD	<LOD	<LOD	<LOD	<LOQ	1.90E-03	<LOD	<LOD	<LOD
06/03/2017 17:45	4.50E-04	<LOD	<LOD	1.40E-03	<LOD	1.75E-03	<LOD	<LOD	<LOD	<LOD	<LOD
07/03/2017 15:45	3.00E-04	<LOQ	<LOD	<LOD	<LOD	<LOD	<LOD	7.50E-04	<LOD	<LOD	<LOD
08/03/2017 17:00	<LOD	<LOD	<LOD	<LOD	<LOD	<LOQ	<LOD	<LOQ	<LOD	<LOD	<LOD
09/03/2017 18:00	<LOD	<LOD	<LOD	4.50E-04	<LOD	8.50E-04	<LOD	<LOQ	<LOD	<LOD	<LOD
10/03/2017 13:30	4.50E-04	<LOD	<LOD	<LOD	<LOD	<LOD	<LOD	<LOD	<LOD	<LOD	<LOD
12/03/2017 19:00	<LOD	<LOD	<LOD	<LOD	<LOD	<LOQ	<LOD	6.00E-04	<LOD	<LOD	<LOD
14/03/2017 16:45	<LOD	<LOD	<LOD	<LOD	<LOD	<LOD	<LOD	<LOQ	<LOD	<LOD	<LOD
15/03/2017 18:00	1.50E-03	<LOQ	<LOD	<LOD	<LOD	1.00E-03	<LOD	3.00E-04	<LOD	<LOD	<LOD
17/03/2017 16:15	<LOQ	<LOD	<LOD	2.80E-03	<LOD	1.05E-03	<LOQ	<LOD	9.50E-04	<LOD	<LOD
19/03/2017 20:00	8.50E-04	<LOD	<LOD	<LOD	<LOD	<LOD	<LOD	<LOQ	<LOD	<LOD	<LOD
20/03/2017 18:30	8.00E-04	2.05E-03	<LOD	1.15E-03	<LOD	<LOD	<LOD	1.20E-03	<LOD	<LOD	<LOD
21/03/2017 09:50	6.50E-04	2.30E-03	<LOD	<LOD	<LOD	<LOQ	<LOD	1.30E-03	6.00E-04	<LOD	<LOD
22/03/2017 10:00	<LOQ	2.90E-03	<LOD	<LOQ	<LOD	9.00E-04	<LOD	2.40E-03	8.00E-04	<LOD	<LOD
23/03/2017 17:50	5.50E-04	<LOD	<LOD	5.00E-04	<LOQ	2.95E-03	<LOD	1.70E-03	<LOD	<LOD	<LOD
27/03/2017 20:30	1.90E-03	3.60E-03	<LOD	2.95E-03	<LOD	1.25E-03	<LOD	1.45E-03	<LOD	<LOD	<LOD
31/03/2017 14:00	1.45E-03	<LOD	<LOD	1.65E-03	<LOD	<LOD	<LOD	<LOQ	<LOD	<LOD	<LOD
03/04/2017 16:30	7.50E-04	1.05E-03	<LOD	<LOD	<LOD	1.10E-03	<LOD	5.00E-04	4.50E-04	<LOD	<LOD
07/04/2017 10:15	1.65E-03	2.05E-03	<LOD	<LOD	<LOD	<LOD	<LOD	2.55E-03	<LOD	<LOD	<LOD
12/04/2017 15:15	<LOD	1.10E-03	<LOD	1.05E-03	<LOD	1.15E-03	<LOD	6.00E-04	<LOD	<LOD	<LOD
17/04/2017 15:15	2.55E-03	2.55E-03	<LOD	<LOD	<LOD	3.40E-03	<LOD	2.50E-03	<LOQ	<LOD	<LOD
21/04/2017 14:30	<LOD	<LOD	<LOD	<LOD	<LOD	<LOD	<LOD	<LOD	<LOD	<LOD	<LOD
26/04/2017 15:00	<LOD	<LOD	<LOD	<LOD	<LOD	<LOD	<LOD	<LOD	<LOD	<LOD	<LOD
28/04/2017 10:30	<LOQ	<LOD	<LOD	9.50E-04	<LOD	<LOD	<LOD	<LOD	<LOQ	<LOD	<LOD
30/04/2017 16:00	5.50E-04	<LOD	<LOD	<LOD	<LOD	6.00E-04	<LOD	<LOD	<LOQ	<LOD	<LOD
01/05/2017 06:15	<LOD	<LOD	<LOD	<LOD	<LOD	<LOD	<LOD	<LOD	<LOD	<LOD	<LOD
01/05/2017 06:15	<LOD	<LOD	<LOD	<LOD	<LOD	<LOD	<LOD	<LOD	<LOD	<LOD	<LOD
01/05/2017 09:45	<LOD	<LOD	<LOD	<LOD	<LOD	<LOD	<LOD	<LOD	<LOD	<LOD	<LOD
01/05/2017 16:00	<LOD	<LOD	<LOD	<LOD	<LOD	<LOD	<LOD	<LOD	<LOD	<LOD	<LOD
02/03/2017 10:00	5.35E-03	5.85E-03	3.55E-03	3.60E-03	2.00E-03	3.15E-03	9.30E-03	3.22E-02	4.21E-02	4.24E-02	4.58E-02
03/05/2017 10:30	<LOD	<LOD	<LOD	<LOD	<LOD	<LOD	<LOD	<LOD	<LOD	<LOD	<LOD
04/05/2017 10:30	<LOD	<LOD	<LOD	<LOD	<LOD	<LOD	<LOD	<LOD	<LOD	<LOD	<LOD
05/05/2017 14:30	<LOD	<LOD	<LOD	<LOD	<LOD	<LOD	<LOD	<LOD	<LOD	<LOD	<LOD
08/05/2017 10:30	<LOD	<LOD	<LOD	<LOD	<LOD	<LOD	<LOD	<LOD	<LOD	<LOD	<LOD
09/05/2017 10:15	<LOD	<LOD	<LOD	<LOD	<LOD	<LOD	<LOD	<LOD	<LOD	<LOD	<LOD
10/05/2017 14:30	<LOD	<LOD	<LOD	<LOD	<LOD	<LOD	<LOD	<LOD	<LOD	<LOD	<LOD
11/05/2017 11:30	<LOD	<LOD	<LOD	<LOD	<LOD	<LOD	<LOD	<LOD	<LOD	<LOD	<LOD
15/05/2017 15:00	<LOD	<LOD	<LOD	<LOD	<LOD	<LOD	<LOD	<LOD	<LOD	<LOD	<LOD
16/05/2017 10:00	<LOD	<LOD	<LOD	<LOD	<LOD	<LOD	<LOD	<LOD	<LOD	<LOD	<LOD
17/05/2017 09:15	<LOD	<LOD	<LOD	<LOD	<LOD	<LOD	<LOD	<LOD	<LOD	<LOD	<LOD
18/05/2017 10:45	<LOD	<LOD	<LOD	<LOD	<LOD	<LOD	<LOD	<LOD	<LOD	<LOD	<LOD
19/05/2017 11:30	<LOD	<LOD	<LOD	<LOD	<LOD	<LOD	<LOD	<LOD	<LOD	<LOD	<LOD
23/05/2017 09:00	<LOD	<LOD	<LOD	<LOD	<LOD	<LOD	<LOD	<LOD	<LOD	<LOD	<LOD
24/05/2017 15:15	<LOD	<LOD	<LOD	<LOD	<LOD	<LOD	<LOD	<LOD	<LOD	<LOD	<LOD
29/05/2017 13:30	<LOD	<LOD	<LOD	<LOD	<LOD	<LOD	<LOD	<LOD	<LOD	<LOD	<LOD
31/05/2017 10:40	<LOD	<LOD	<LOD	<LOD	<LOD	<LOD	<LOD	<LOD	<LOD	<LOD	<LOD
06/06/2017 15:30	<LOD	<LOD	<LOD	<LOD	<LOD	<LOD	<LOD	<LOD	<LOD	<LOD	<LOD
12/06/2017 13:00	<LOD	<LOD	<LOD	<LOD	<LOD	<LOD	<LOD	<LOD	<LOD	<LOD	<LOD

C Appendix

Supplementary Material to Paper III

Mass Balance Calculation

The concentration of the *i*th chemical component $C_{i,predicted}$ in a monitoring well sample due to mixing but in the absence of any chemical reaction can be determined from mass balance constraints. Taking account of the concentration of the ith component in the injection fluid $C_{i,injected}$ and that in the ambient groundwater $C_{i,background}$ it follows that

$$C_{i,predicted} = X \cdot C_{i,injected} + (1 - X) \cdot C_{i,background} \tag{C.1}$$

where X is the fraction of injected fluid (gas-charged condensate plus effluent water) in the monitoring well samples. The values of the fraction of injected solution in the monitoring well samples can be determined from the concentration of the non-reactive tracers using

$$X = \frac{C_{1-ns} - C_{1-ns,background}}{C_{1-ns,injected} - C_{1-ns,background}} \tag{C.2}$$

where $C_{i,injected}$ refers to the concentration of the inert tracer in the injected solution and $C_{i,background}$ the average background concentration of this inert tracer in each monitoring well prior to the injection. If the molar ratio, A, from Eqn. 4.3, is defined as

$$A = \frac{C_{i,injected}}{C_{1-ns,injected}} \tag{C.3}$$

The molar ratios calculated for each phase of gas injection are listed in Table C.2. Note that the molar ratio for Phase II was determined from the total amount of the chemical component injected $C_{i,injected}$ during both phases of the gas injection because the original tracer injected during Phase I was still present during Phase II. Therefore, the total amount of tracer injected $C_{1\text{-}ns,injected}$ was the measured 1-ns tracer (from Phase I) plus the 1-ns tracer calculated from the polynomial curve (see Figs. C.2 to C.4).

Combining Eqns. C.1 to C.3 results in

$$C_{i,predicted} = \frac{C_{i,background} \cdot (C_{1-ns,injected} - C_{1-ns}) + A \cdot C_{1-ns,injected} \cdot (C_{1-ns} - C_{1-ns,background})}{C_{1-ns,injected} - C_{1-ns,background}} \tag{C.4}$$

Table C.1. Dissolution reactions of primary and secondary minerals.

Minerals		Dissolution reaction
Primary	Leached basaltic glass [1*]	$SiAl_{0.35}O_2(OH)_{1.05} + 1.05\ H^+ = 0.35\ Al^{+3} + SiO_2 + 1.05\ H_2O$
	Albite	$NaAlSi_3O_8 + 4\ H^+ = Al^{+3} + Na^+ + 3\ SiO_2 + 2\ H_2O$
	Anorthite	$CaAl_2Si_2O_8 + 8\ H^+ = Ca^{+2} + 2\ Al^{+3} + 2\ SiO_2 + 4\ H_2O$
	Clinopyroxene / Augite [2*]	$Ca_{0.35}Mg_{0.42}Fe_{0.23}SiO_3 + 2\ H^+ = 0.35\ Ca^{+2} + 0.42\ Mg^{+2} + 0.23\ Fe^{+2} + SiO_2 + H_2O$
	Fayalite	$Fe_2SiO_4 + 4\ H^+ = 2\ Fe^{+2} + SiO_2 + 2\ H_2O$
	Forsterite	$Mg_2SiO_4 + 4\ H^+ = 2\ Mg^{+2} + SiO_2 + H_2O$
	Magnetite	$Fe_3O_4 + 8\ H^+ = Fe^{+2} + 2\ Fe^{+3} + 4\ H_2O$
	Orthopyroxene [2*]	$Mg_{0.38}Fe_{0.62}SiO_3 + 2\ H^+ = 0.38\ Mg^{+2} + 0.62\ Fe^{+2} + SiO_2 + H_2O$
Secondary	Ankerite	$CaFe(CO_3)_2 = Ca^{+2} + Fe^{+2} + 2\ CO_3^{-2}$
	Calcite	$CaCO_3 + H^+ = Ca^{+2+} + HCO_3^-$
	Clinochlore	$Mg_5Al_2Si_3O_{10}(OH)_8 + 16\ H^+ = 5\ Mg^{+2} + 2\ Al^{+3} + 3\ SiO_2 + 12\ H_2O$
	Daphnite	$Fe_5Al_2Si_3O_{10}(OH)_8 + 16\ H^+ = 5\ Fe^{+2} + 2\ Al^{+3} + 3\ SiO_2 + 12\ H_2O$
	Dolomite	$CaMg(CO_3)_2 = Ca^{+2} + Mg^{+2} + 2\ CO_3^{-2}$
	Epidote	$Ca_2FeAl_2Si_3O_{12}(OH) + 13\ H^+ = 2\ Ca^{+2} + Fe^{+2} + 2\ Al^{+3} + 3\ SiO_2 + 7\ H_2O$
	Ferroactinolite	$Ca_2Fe_5Si_8O_{22}(OH)_2 + 14\ H^+ = 2\ Ca^{+2} + 5\ Fe^{+2} + 8\ SiO_2 + 8\ H_2O$
	Magnesite	$MgCO_3 + H^+ = Mg^{+2} + HCO_3^-$
	Prehnite	$Ca_2Al_2Si_3O_{10}(OH)_2 + 10\ H^+ = Ca^{+2} + 2Al^{+3} + 3\ SiO_2 + 6\ H_2O$
	Pyrite	$FeS_2 + H_2O = Fe^{+2} + 0.25\ H^+ + 0.25\ SO_4^{-2} + 1.75\ HS^-$
	Pyrrhotite	$FeS + H^+ = Fe^{+2} + HS^-$
	Siderite	$FeCO_3 = Fe^{+2} + CO_3^{-2}$
	Tremolite	$Ca_2Mg_5Si_8O_{22}(OH)_2 + 14\ H^+ = 2\ Ca^{+2} + 5\ Mg^{+2} + 8\ SiO_2 + 8\ H_2O$
	Wairakite	$CaAl_2Si_4O_{10}(OH)_4 + 8\ H^+ = Ca^{+2} + 2\ Al^{+3} + 4\ SiO_2 + 6\ H_2O$
	Wollastonite	$CaSiO_3 + 2\ H^+ = Ca^{+2} + SiO_2 + H_2O$

[*] Not included in *carbfix.dat* from Voigt et al. (2018).
[1] Calculated from a stoichiometric mixture of amorphous SiO_2 from Voigt et al. (2018) and amorphous $Al(OH)_3$ from Naumov et al. (1971).
[2] Dissolution reaction and solubility constants from Stefansson (2001).

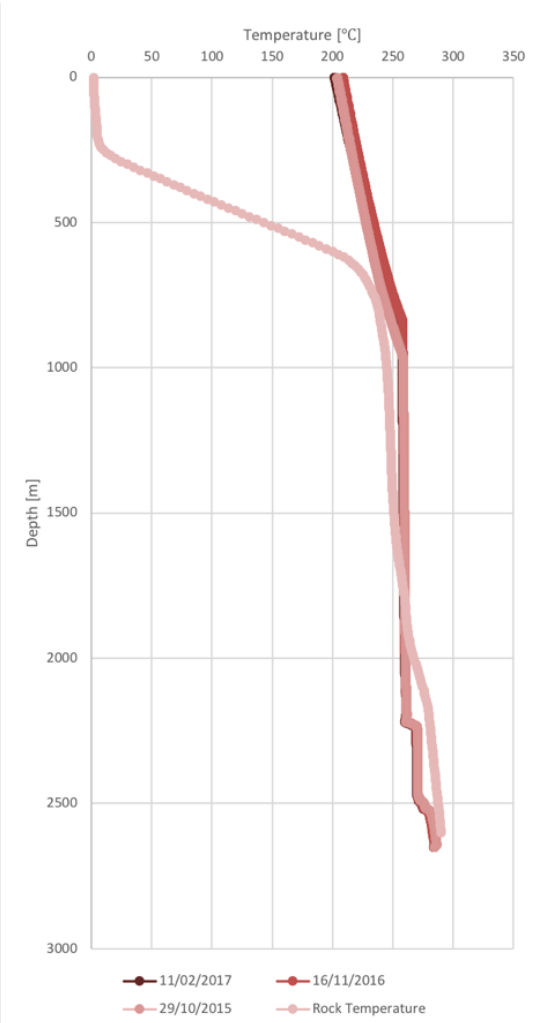

Figure C.1. Temperature logs measured in well HE-31 during discharge.

*Table C.2. Molar ratios (A) for mass balance calculations (Eqn. 4.3) for Phase I and II of the mixed gas injections determined from average fluid compositions (Clark et al., 2018) and injected water flow rates (Sigfússon et al., 2018). Note that the molar ratio of Phase II was calculated from the total amount of component injected during both phases of gas injection. *Molar ratios of CO_2 and H_2S were determined using only the gas-charged condensate water composition and flow rate.*

Component	Molar Ratio Phase I	Molar Ratio Phase II
CO_2*	79573	210770
H_2S*	57404	129378
SO_4	533	164
Al	98.3	59.2
B	144	99.2
Cl	7265	5468
F	110	73.2
Na	13244	8441
K	1332	896
Ca	31.0	15.1
Fe	3.09	7.47
Mg	4.32	4.48

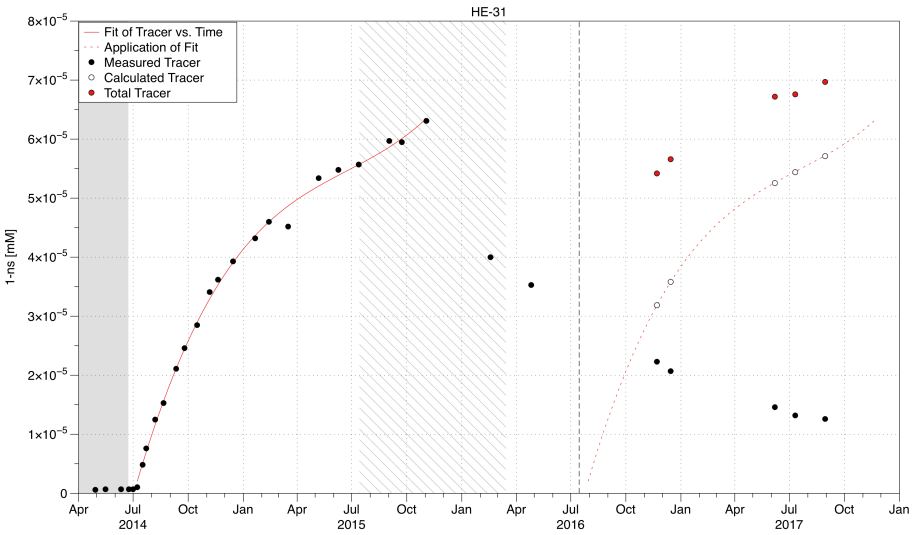

Figure C.2. 1-ns tracer concentrations in monitoring well HE-31 fit with a third degree polynomial curve (red solid line) from the first appearance of the tracer (08/07/2014). The polynomial curve is then applied from when the gas injection was doubled (15/07/2016), depicted as a red dotted line. The gray shaded area indicates times before the injection of gas-charged water into well HN-16, the diagonal lines denote times when well HN-14 was used for the injection of gas-charged waters, and the vertical dashed line signifies the time when the amount of CO_2 and H_2S injected into the subsurface was doubled.

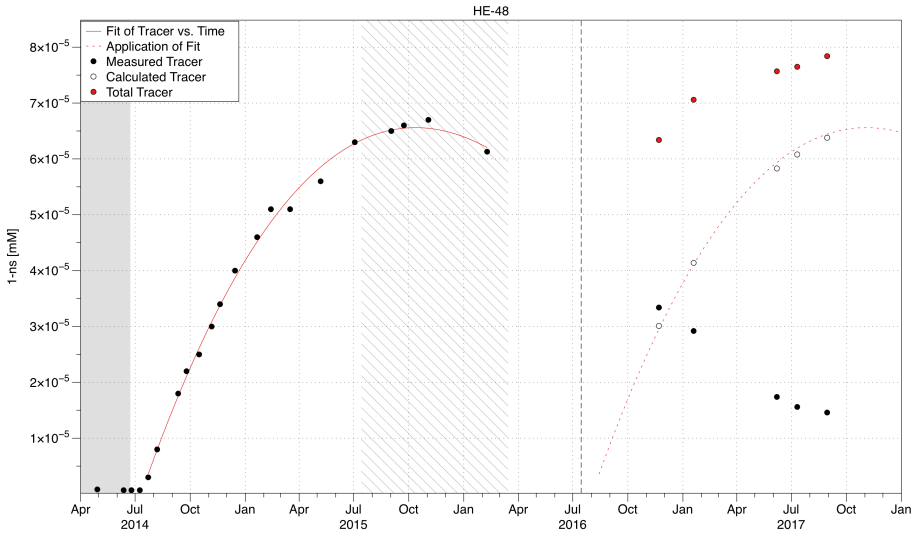

Figure C.3. 1-ns tracer concentrations in monitoring well HE-48 fit with a third degree polynomial curve (red solid line) from the first appearance of the tracer (23/07/2014). The polynomial curve is then applied from when the gas injection was doubled (15/07/2016), depicted as a red dotted line. The gray shaded area indicates times before the injection of gas-charged water into well HN-16, the diagonal lines denote times when well HN-14 was used for the injection of gas-charged waters, and the vertical dashed line signifies the time when the amount of CO_2 and H_2S injected into the subsurface was doubled.

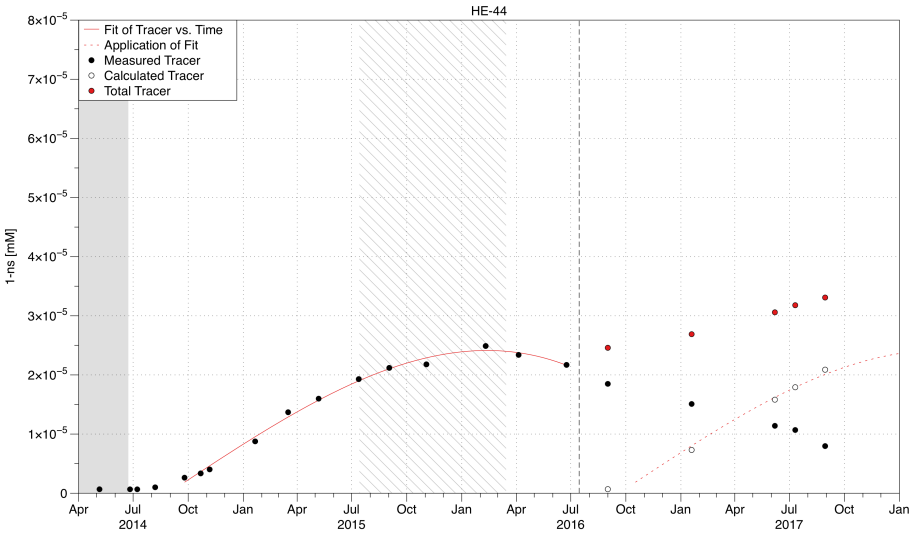

Figure C.4. 1-ns tracer concentrations in monitoring well HE-44 fit with a third degree polynomial curve (red solid line) from the first appearance of the tracer (25/09/2014). The polynomial curve is then applied from when the gas injection was doubled (15/07/2016), depicted as a red dotted line. The gray shaded area indicates times before the injection of gas-charged water into well HN-16, the diagonal lines denote times when well HN-14 was used for the injection of gas-charged waters, and the vertical dashed line signifies the time when the amount of CO_2 and H_2S injected into the subsurface was doubled.

*Table C.3. Chemical compositions of Well HE-31 liquid-phase samples. Italicized samples are used for background concentrations in the initial reservoir fluid (Eqn. 4.2). *Limit of detection for samples analysed in 2017.*

Detection Limit					0.0007	0.0001	0.001	0.0003	0.001	0.001	0.003	0.001	1.0	0.010 0.007 *	0.09 0.39 *
Sample no	Date	P_s [bar-g]	CO_2 [mM]	H_2S [mM]	SO_4 [mM]	Al [mM]	B [mM]	Cl [mM]	F [mM]	Na [mM]	K [mM]	Si [mM]	Ca [µM]	Fe [µM]	Mg [µM]
14-5109	29/04/2014	7.8	0.689	0.955	0.341	0.0873	0.0727	3.65	0.125	7.35	0.730	11.0	21.1	0.705	0.151
14-5119	16/05/2014	8.0	0.696	0.531	0.331	0.0919	0.0723	3.61	0.125	7.20	0.705	11.0	20.9	0.349	b.d.
14.5161	11/06/2014	9.0	0.728	0.267	0.341	0.0899	0.0746	3.61	0.126	7.26	0.696	11.1	21.0	0.310	0.184
14-5183	24/06/2014	8.5	0.344	0.506	0.337	0.0915	0.0731	3.57	0.125	7.18	0.703	11.0	21.2	0.661	0.114
14-5205	01/07/2014	9.0	0.720	0.393	0.336	0.0925	0.0703	3.57	0.124	7.30	0.706	10.9	27.6	0.652	8.13
14-5210	08/07/2014	8.5	0.675	0.496	0.342	0.0855	0.0700	3.60	0.125	7.24	0.700	11.1	22.8	0.185	1.30
14-5236	17/07/2014	8.5	0.685	0.499	0.337	0.0890	0.0706	3.60	0.124	7.30	0.704	11.1	24.1	0.608	1.91
14-5243	23/07/2014	8.5	0.729	0.535	0.348	0.0840	0.0710	3.57	0.123	7.23	0.708	11.0	21.2	2.01	b.d.
14-5251	07/08/2014	9.0	0.767	0.564	0.344	0.0849	0.0734	3.60	0.122	7.43	0.719	11.2	21.0	0.240	b.d.
14-5288	21/08/2014	9.0	0.733	0.664	0.351	0.0832	0.0698	3.60	0.120	7.48	0.723	10.9	21.7	0.253	0.436
14-5306	11/09/2014	9.0	0.760	0.682	0.342	0.0814	0.0692	3.58	0.118	7.57	0.723	10.9	21.7	0.204	0.285
14-5330	25/09/2014	9.0	0.776	1.10	0.349	0.0826	0.0703	3.60	0.117	7.57	0.728	10.9	21.4	0.133	0.198
14-5364	16/10/2014	9.0	0.895	0.691	0.345	0.0786	0.0679	3.57	0.115	7.59	0.736	10.8	21.4	0.251	0.100
14-5387	06/11/2014	9.0	0.835	0.706	0.349	0.0778	0.0680	3.54	0.123	7.62	0.732	10.9	20.5	2.33	0.115
14-5402	20/11/2014	9.0	0.812	0.745	0.373	0.0789	0.0688	3.52	0.122	7.60	0.736	10.8	21.2	0.083	b.d.
14-5429	15/12/2014	8.5	0.889	0.638	0.336	0.0787	0.0692	3.52	0.121	7.71	0.740	10.9	20.5	0.255	b.d.
15-5041	21/01/2015	7.9	0.841	0.698	0.335	0.0793	0.0694	3.50	0.120	7.80	0.743	11.0	19.7	0.075	b.d.
15-5132	13/02/2015	8.5	0.890	0.683	0.350	0.0800	0.0685	3.47	0.119	7.82	0.767	10.9	20.1	12.8	b.d.
15-5200	17/03/2015	8.0	0.960	0.781	0.313	0.0798	0.0720	3.52	0.119	7.97	0.774	11.0	19.9	0.327	b.d.
15-5260	07/05/2015	9.0	0.901	0.859	0.320	0.0804	0.0729	3.53	0.117	8.04	0.780	11.0	18.8	0.249	b.d.
15-5322	09/06/2015	8.0	0.904	0.865	0.335	0.0763	0.0694	3.60	0.117	7.85	0.759	10.6	18.5	0.276	0.136
15-5344	13/07/2015	9.0	1.03	0.808	0.290	0.0749	0.0655	3.50	0.115	7.57	0.747	10.9	18.0	0.233	b.d.
15-5402	02/09/2015	8.6	1.03	0.863	0.370	0.0741	0.0623	3.32	0.114	7.48	0.725	10.8	18.3	0.252	b.d.
15-5418	23/09/2015	9.0	1.05	0.889	0.391	0.0742	0.0625	3.34	0.114	7.46	0.741	10.8	17.5	0.281	b.d.
15-5453	03/11/2015	8.0	1.12	0.872	0.304	0.0737	0.0626	3.30	0.110	7.60	0.761	10.9	17.6	0.129	b.d.

16-5096	18/02/2016	9.0	0.975	0.851	0.283	0.0739	0.0660	3.49	0.111	7.57	0.735	10.6	16.7	0.305	b.d.
16-5142	26/04/2016	7.7	0.990	0.899	0.314	0.0776	0.0667	3.51	0.106	7.65	0.760	10.9	16.7	0.386	0.256
16-5362	22/11/2016	8.6	0.494	1.21	0.287	0.0736	0.0620	3.67	0.104	7.68	0.742	10.7	15.6	0.291	b.d. *
16-5377	15/12/2016	8.2	1.05	0.798	0.297	0.0723	0.0609	3.59	0.103	7.61	0.730	10.6	16.0	0.231	b.d. *
17-5214	07/06/2017	8.2	1.17	0.968	0.302	0.0716	0.0616	3.53	0.094	8.05	0.777	10.7	15.8	0.177	1.15
17-5250	11/07/2017	8.3	1.25	1.01	0.376	0.0710	0.0613	3.53	0.093	7.97	0.774	10.7	15.1	0.156	1.24
17-5282	30/08/2017	8.6	1.34	0.992	0.340	0.0698	0.0611	3.50	0.092	8.05	0.784	10.7	15.1	0.235	1.27

Table C.4. Calculated and measured tracer (1-ns) concentrations of Well HE-31 liquid-phase samples and chemical compositions of Well HE-31 steam-phase samples. "l_{gas}/kg_{gas}" indicates the liters of gas analysed per kg of condensate in the gas bulb. Italicized samples are used for background concentrations in the initial reservoir fluid (Eqn. 4.2).

Sample No	Date	1-ns [mM] Meas.	1-ns [mM] Calc.	l_{gas} / kg_{gas}	CO_2 [mM]	H_2S [mM]	H_2 [%]	O_2 [%]	N_2 [%]	CH_4 [%]
14-5109	29/04/2014	5.96E-07		0.0899	41.4	2.99	5.70	1.33	84.59	3.24
14-5119	16/05/2014	6.88E-07		0.0897	37.7	3.19	5.96	0.42	88.14	3.47
14.5161	11/06/2014	6.97E-07		0.0889	35.9	3.00	5.63	0.72	80.68	3.49
14-5183	24/06/2014	6.92E-07		0.0910	37.0	3.27	6.06	0.33	81.83	3.81
14-5205	01/07/2014	6.95E-07		0.0959	40.2	3.52	5.33	1.55	83.21	3.87
14-5210	08/07/2014	1.04E-07		0.0961	36.5	3.26	5.27	1.03	82.60	3.83
14-5236	17/07/2014	4.84E-06		0.0872	37.1	3.41	5.07	0.00	73.23	3.63
14-5243	23/07/2014	7.61E-06		0.0873	38.3	3.54	5.25	0.40	81.61	3.79
14-5251	07/08/2014	1.25E-05		0.0914	38.1	3.67	5.56	0.56	91.11	3.97
14-5288	21/08/2014	1.53E-05		0.1080	37.5	3.86	5.00	0.17	84.66	3.80
14-5306	11/09/2014	2.11E-05		0.0839	37.6	4.12	5.51	0.00	86.44	4.06
14-5330	25/09/2014	2.46E-05		0.0925	37.6	4.19	5.80	0.00	84.32	2.60
14-5364	16/10/2014	2.85E-05		0.1048	44.0	4.84	6.15	0.48	86.19	3.91
14-5387	06/11/2014	3.41E-05		0.0851	40.2	4.62	6.13	0.77	87.55	2.97
14-5402	20/11/2014	3.62E-05		0.1002	41.8	4.83	5.27	0.00	90.80	2.97
14-5429	15/12/2014	3.93E-05		0.1139	40.5	4.72	4.63	1.86	88.09	2.41
15-5041	21/01/2015	4.32E-05		0.0788	39.8	4.88	5.80	0.23	87.12	3.67
15-5132	13/02/2015	4.60E-05		0.0820	39.9	5.09	6.69	0.15	85.50	3.72
15-5200	17/03/2015	4.52E-05		0.0858	40.3	4.93	5.50	0.00	83.53	3.52
15-5260	07/05/2015	5.34E-05		0.0881	44.5	5.53	5.84	0.15	85.15	3.41
15-5322	09/06/2015	5.48E-05		0.0723	41.1	5.30	6.30	1.25	82.28	3.42
15-5344	13/07/2015	5.57E-05		0.0875	43.5	5.31	5.98	1.44	82.00	3.47
15-5402	02/09/2015	5.97E-05		0.0936	46.8	5.33	4.77	0.00	77.70	3.71
15-5418	23/09/2015	5.95E-05		0.0914	47.3	5.34	4.74	0.87	80.82	4.21
15-5453	03/11/2015	6.31E-05		0.1010	48.8	5.47	5.77	2.50	82.71	3.54
16-5096	18/02/2016	4.00E-05		0.1107	52.1	5.92	5.94	0.65	71.30	4.05
16-5142	26/04/2016	3.53E-05		0.0653	43.3	5.60	8.13	0.12	81.93	4.25
16-5362	22/11/2016	2.23E-05	3.19E-05	0.0752	40.1	4.34	7.23	3.24	78.40	4.17
16-5377	15/12/2016	2.07E-05	3.58E-05	0.0736	40.3	4.76	7.28	2.04	79.37	4.45
17-5214	07/06/2017	1.46E-05	5.26E-05	0.0801	50.8	5.94	8.25	2.17	73.77	5.61
17-5250	11/07/2017	1.32E-05	5.44E-05	0.0825	53.1	5.81	9.30	0.00	81.60	6.26
17-5282	30/08/2017	1.26E-05	5.71E-05	0.0870	58.2	6.39	10.03	1.31	63.71	4.98

*Table C.5. Chemical compositions of Well HE-48 liquid-phase samples. Italicized samples are used for background concentrations in the initial reservoir fluid (Eqn. 4.2). *Limit of detection for samples analysed in 2017.*

Detection Limit					0.0007	0.0001	0.001	0.0003	0.001	0.001	0.003	0.001	1.0	0.010 0.007 *	0.09 0.39 *
Sample no	Date	P_s [bar-g]	CO_2 [mM]	H_2S [mM]	SO_4 [mM]	Al [mM]	B [mM]	Cl [mM]	F [mM]	Na [mM]	K [mM]	Si [mM]	Ca [µM]	Fe [µM]	Mg [µM]
14-5110	29/04/2014	5.7	0.641	0.698	0.362	0.0805	0.0714	3.73	0.124	7.54	0.758	11.5	26.2	0.276	0.175
14-5164	12/06/2014	9.0	0.696	0.740	0.361	0.0791	0.0695	3.57	0.122	7.26	0.730	11.1	23.4	0.557	b.d. *
14-5187	25/06/2014	8.5	0.338	0.529	0.383	0.0785	0.0690	3.60	0.124	7.36	0.738	11.1	25.9	0.292	0.197
14-5213	09/07/2014	8.5	0.767	0.529	0.361	0.790	0.0686	3.55	0.122	7.19	0.723	11.1	24.2	0.333	0.040
14-5244	23/07/2014	8.7	0.679	0.415	0.388	0.0794	0.0688	3.68	0.126	7.32	0.757	11.6	25.1	0.234	0.013
14-5252	08/08/2014	9.0	0.822	0.523	0.364	0.0778	0.0656	3.56	0.122	7.19	0.717	10.8	24.4	0.173	0.185
14-5308	11/09/2014	8.0	0.830	0.653	0.355	0.0775	0.0681	3.52	0.119	7.45	0.739	11.0	24.4	0.157	0.118
14-5331	25/09/2014	9.0	0.861	1.11	0.365	0.0781	0.0679	3.53	0.118	7.49	0.754	11.2	24.7	0.295	0.224
14-5365	16/10/2014	8.0	0.781	0.658	0.366	0.0762	0.0697	3.52	0.117	7.39	0.747	10.8	21.8	0.328	b.d.
14-5388	06/11/2014	9.0	0.914	0.739	0.369	0.0764	0.0671	3.46	0.125	7.63	0.758	11.1	22.4	0.510	0.276
14-5403	20/11/2014	8.0	1.05	0.751	0.402	0.0745	0.0650	3.38	0.121	7.41	0.738	10.8	21.3	0.441	0.137
14-5430	15/12/2014	8.5	0.989	0.695	0.344	0.0746	0.0658	3.41	0.122	7.49	0.748	11.0	21.2	0.150	0.172
14-5040	21/01/2015	8.0	0.946	0.664	0.348	0.0755	0.0650	3.40	0.121	7.62	0.761	11.0	20.4	0.293	0.164
15-5131	13/02/2015	7.5	1.02	0.716	0.355	0.0748	0.0656	3.37	0.120	7.64	0.759	10.9	18.5	0.623	b.d. *
15-5198	17/03/2015	8.5	1.13	0.798	0.337	0.0755	0.0681	3.44	0.120	7.88	0.791	11.2	21.8	0.171	0.140
15-5258	07/05/2015	9.0	0.983	0.943	0.324	0.0760	0.0701	3.45	0.119	7.84	0.792	11.1	20.4	1.93	2.23
15-5336	03/07/2015	8.0	1.04	0.872	0.301	0.0718	0.0641	3.47	0.116	7.53	0.770	11.1	17.7	1.03	0.91
15-5400	02/09/2015	8.5	1.06	0.904	0.344	0.0721	0.0630	3.37	0.115	7.60	0.765	11.1	18.3	0.861	1.17
15-5417	23/09/2015	8.0	1.10	0.981	0.377	0.720	0.0627	3.36	0.115	7.60	0.776	11.1	17.1	0.860	1.27
15-5455	03/11/2015	8.0	1.10	1.04	0.393	0.0724	0.0632	3.47	0.117	7.58	0.771	11.1	18.2	0.121	0.135
16-5075	09/02/2016	7.0	1.10	0.954	0.333	0.0738	0.0596	3.40	0.113	7.36	0.800	11.6	16.4	0.500	0.170
16-5363	22/11/2016	9.0	0.972	0.857	0.334	0.0722	0.0598	3.52	0.107	7.86	0.765	10.9	15.3	0.243	b.d. *
17-5058	19/01/2017	7.0	1.11	0.910	0.333	0.0693	0.0623	3.50	0.106	7.58	0.748	10.7	15.7	0.417	b.d. *
17-5215	07/06/2017	8.5	1.21	1.11	0.327	0.0703	0.0600	3.46	0.100	7.99	0.797	10.9	16.4	0.191	1.16
17-5248	11/07/2017	8.7	1.35	1.02	0.326	0.0699	0.0598	3.54	0.097	7.98	0.797	10.8	14.7	0.153	1.19
17-5283	30/08/2017	8.9	1.40	1.03	0.312	0.0696	0.0594	3.53	0.095	8.04	0.798	10.8	15.4	0.132	1.34

Table C.6. Calculated and measured tracer (1-ns) concentrations of Well HE-48 liquid-phase samples and chemical compositions of Well HE-48 steam-phase samples. "l_{gas}/kg_{gas}" indicates the liters of gas analysed per kg of condensate in the gas bulb. Italicized samples are used for background concentrations in the initial reservoir fluid (Eqn. 4.2).

Sample no	Date	1-ns [mM] Meas.	1-ns [mM] Calc.	l_{gas} / kg_{gas}	CO_2 [mM]	H_2S [mM]	H_2 [%]	O_2 [%]	N_2 [%]	CH_4 [%]
14-5110	29/04/2014	8.41E-07		0.1190	46.6	3.24	3.90	3.83	80.08	2.94
14-5164	12/06/2014	6.95E-07		0.1026	43.8	3.63	6.87	0.34	81.32	3.56
14-5187	25/06/2014	6.92E-07		0.0985	42.6	3.62	6.33	0.43	70.86	3.71
14-5213	09/07/2014	6.92E-07		0.1057	42.7	3.55	6.85	0.42	84.19	4.14
14-5244	23/07/2014	3.47E-06		0.0814	34.7	3.58	5.80	0.00	76.15	3.65
14-5252	08/08/2014	8.00E-06		0.0781	42.7	3.72	7.49	0.14	91.19	4.19
14-5308	11/09/2014	1.75E-05		0.1337	45.2	3.87	4.27	0.00	92.72	2.63
14-5331	25/09/2014	2.16E-05		0.0978	44.0	4.40	7.65	0.00	83.19	3.60
14-5365	16/10/2014	2.47E-05		0.0994	47.1	4.53	7.66	0.00	83.28	4.42
14-5388	06/11/2014	3.02E-05		0.0894	47.9	4.99	8.08	0.00	85.17	3.57
14-5403	20/11/2014	3.35E-05		0.0972	47.0	5.11	7.41	0.00	86.89	3.32
14-5430	15/12/2014	4.01E-05		0.1019	47.8	5.07	7.35	0.23	88.08	3.06
14-5040	21/01/2015	4.56E-05		0.0842	46.2	5.35	7.92	0.50	83.63	3.75
15-5131	13/02/2015	5.10E-05		0.0807	48.9	5.79	8.64	0.00	82.00	4.02
15-5198	17/03/2015	5.08E-05		0.0982	51.0	6.02	7.73	0.95	84.79	3.97
15-5258	07/05/2015	5.61E-05		0.0978	50.9	5.96	7.12	0.66	84.00	3.42
15-5336	03/07/2015	6.31E-05		0.1053	50.7	5.93	7.32	0.00	83.91	3.05
15-5400	02/09/2015	6.51E-05		0.0855	51.5	5.94	6.00	2.50	72.70	4.08
15-5417	23/09/2015	6.55E-05		0.0787	50.9	5.99	6.80	1.00	79.47	4.64
15-5455	03/11/2015	6.71E-05		0.0858	51.8	6.04	8.30	0.73	80.02	4.23
16-5075	09/02/2016	6.13E-05		0.0858	52.1	6.61	7.86	0.34	72.80	4.43
16-5363	22/11/2016	3.34E-05	3.01E-05	0.0848	46.4	4.92	8.58	2.62	75.60	3.33
17-5058	19/01/2017	2.92E-05	4.14E-05	0.0704	47.1	5.29	11.04	3.01	72.54	4.06
17-5215	07/06/2017	1.74E-05	5.83E-05	0.0762	53.6	6.18	10.39	1.69	70.35	4.85
17-5248	11/07/2017	1.56E-05	6.08E-05	0.0858	54.7	6.27	10.96	0.00	80.67	5.66
17-5283	30/08/2017	1.46E-05	6.38E-05	0.0751	59.7	6.54	12.29	0.42	68.40	4.99

*Table C.7. Chemical compositions of Well HE-44 liquid-phase samples. Italicized samples are used for background concentrations in the initial reservoir fluid (Eqn. 4.2). *Limit of detection for samples analysed in 2017.*

Detection Limit					0.0007	0.0001	0.001	0.0003	0.001	0.001	0.003	0.001	1.0	0.010 0.007 *	0.09 0.39 *
Sample no	Date	P_s [bar-g]	CO_2 [mM]	H_2S [mM]	SO_4 [mM]	Al [mM]	B [mM]	Cl [mM]	F [mM]	Na [mM]	K [mM]	Si [mM]	Ca [µM]	Fe [µM]	Mg [µM]
14-5113	06/05/2014	9.2	1.21	0.502	0.346	0.0760	0.0524	3.16	0.116	6.76	0.758	11.3	15.5	0.847	0.889
14-5188	26/06/2014	8.7	1.41	0.779	0.333	0.0803	0.0588	3.30	0.121	7.36	0.823	12.4	16.1	0.253	b.d.
14-5212	08/07/2014	8.5	1.27	0.756	0.315	0.0793	0.0582	3.31	0.121	7.37	0.820	12.5	15.9	0.679	0.447
14-5253	08/08/2014	9.0	1.28	0.752	0.327	0.0805	0.0600	3.32	0.121	7.48	0.826	12.6	16.1	0.205	b.d.
14-5332	25/09/2014	8.0	1.55	1.24	0.339	0.0788	0.0569	3.28	0.120	7.41	0.824	12.4	16.4	0.426	0.117
14-5371	22/10/2014	8.0	1.69	0.725	0.319	0.0778	0.0565	3.26	0.119	7.50	0.830	12.4	15.7	1.06	1.08
14-5389	06/11/2014	9.0	1.67	0.753	0.339	0.0778	0.0586	3.23	0.128	7.48	0.833	12.4	16.3	0.155	b.d.
15-5039	21/01/2015	8.5	1.29	0.699	0.339	0.0762	0.0565	3.16	0.126	7.39	0.822	12.2	14.3	0.168	0.156
15-5199	17/03/2015	8.5	0.960	0.781	0.268	0.0784	0.0596	3.22	0.128	7.48	0.843	12.3	17.0	0.490	b.d.
15-5259	07/05/2015	9.0	1.24	0.810	0.298	0.0725	0.0558	2.84	0.115	6.87	0.776	11.3	15.1	1.28	1.07
15-5346	13/07/2015	8.0	1.44	0.788	0.304	0.0751	0.0559	3.22	0.127	7.12	0.812	12.2	15.1	0.895	0.728
15-5401	02/09/2015	9.0	1.22	0.795	0.337	0.0759	0.0558	3.23	0.127	7.14	0.811	12.3	15.8	1.04	1.83
15-5454	03/11/2015	9.0	1.30	0.868	0.264	0.0740	0.0596	3.17	0.125	7.40	0.808	11.6	16.5	2.05	2.58
16-5080	10/02/2016	9.0	1.20	0.818	0.271	0.0751	0.0560	3.20	0.125	7.08	0.811	12.2	15.5	0.170	0.218
16-5146	05/04/2016	7.5	1.84	0.817	0.251	0.0760	0.0569	3.21	0.123	7.23	0.818	12.3	15.9	0.366	b.d. *
16-5194	24/06/2016	7.4	1.16	0.629	0.292	0.0776	0.0667	3.25	0.123	7.65	0.761	10.9	16.7	0.180	b.d. *
17-5059	19/01/2017	6.9	1.21	0.860	0.267	0.0716	0.0569	3.26	0.117	7.06	0.790	11.9	15.1	0.245	b.d. *
17-5216	07/06/2017	9.0	1.26	0.459	0.286	0.0730	0.0543	3.27	0.116	7.18	0.809	11.9	14.6	0.134	1.18
17-5284	30/08/2017	9.3	1.44	0.993	0.280	0.0720	0.0535	3.23	0.113	7.17	0.812	11.7	14.2	0.137	1.57

Table C.8. Calculated and measured tracer (1-ns) concentrations of Well HE-44 liquid-phase samples and chemical compositions of Well HE-44 steam-phase samples. "l_{gas}/kg_{gas}" indicates the liters of gas analysed per kg of condensate in the gas bulb. Italicized samples are used for background concentrations in the initial reservoir fluid (Eqn. 4.2).

Sample no	Date	1-ns [mM] Meas.	1-ns* [mM] Calc.	l_{gas} / kg_{gas}	CO_2 [mM]	H_2S [mM]	H_2 [%]	O_2 [%]	N_2 [%]	CH_4 [%]
14-5113	06/05/2014	6.72E-07		0.1642	77.4	5.89	17.97	0.45	73.11	4.48
14-5188	26/06/2014	6.69E-07		0.1455	72.7	6.17	18.04	0.12	71.87	4.39
14-5212	08/07/2014	6.68E-07		0.1592	74.1	5.97	14.98	0.21	73.64	4.25
14-5253	08/08/2014	1.01E-07		0.1466	73.6	5.94	18.46	0.20	73.13	4.41
14-5332	25/09/2014	2.64E-06		0.1637	75.0	6.21	15.43	0.08	72.34	3.30
14-5371	22/10/2014	3.36E-06		0.1336	73.8	6.07	22.23	0.00	73.88	3.65
14-5389	06/11/2014	4.03E-06		0.01346	72.3	6.22	21.50	0.32	75.08	3.69
15-5039	21/01/2015	8.77E-06		0.1230	71.2	6.18	20.78	0.26	73.20	4.04
15-5199	17/03/2015	1.37E-05		0.2605	72.2	5.29	10.65	1.74	82.68	2.02
15-5259	07/05/2015	1.60E-05		0.1620	82.1	6.97	18.81	0.59	69.42	3.73
15-5346	13/07/2015	1.93E-05		0.1232	70.7	6.26	16.11	0.00	75.60	4.42
15-5401	02/09/2015	2.12E-05		0.1679	72.4	5.96	10.29	2.16	75.50	3.60
15-5454	03/11/2015	2.18E-05		0.1282	67.3	6.00	13.70	1.45	76.74	4.09
16-5080	10/02/2016	2.49E-05		0.1203	72.0	6.51	18.03	0.34	68.60	4.46
16-5146	05/04/2016	2.34E-05		0.0994	61.1	5.96	15.41	0.12	74.71	4.33
16-5194	24/06/2016	2.17E-05		0.1062	60.0	5.85	11.47	0.20	75.80	4.08
17-5059	19/01/2017	1.51E-05	7.32E-06	0.0866	56.4	5.74	14.64	2.25	70.21	3.76
17-5216	07/06/2017	1.14E-05	1.58E-05	0.1030	63.3	6.00	15.08	1.56	67.51	4.19
17-5284	30/08/2017	7.98E-06	2.09E-05	0.1059	69.2	6.17	15.69	0.99	67.32	4.25

*Table C.9. The fraction of $CO_2$and H_2S mineralized during the transport of injected gas charged fluids to the HE-31 monitoring well. Italicized samples are used for background concentrations in the initial reservoir fluid. *First appearance of the 1-ns tracer.*

Gas Injection	Sample No	Date	DIC [%]	DS [%]
Phase I	*14-5109*	29/04/2014	-	-
	14-5119	16/05/2014	-	-
	14.5161	11/06/2014	-	-
	14-5183	24/06/2014	-	-
	14-5205	01/07/2014	-	-
*	14-5210	08/07/2014	-	-
	14-5236	17/07/2014	-	-
	14-5243	23/07/2014	96	80
	14-5251	07/08/2014	97	81
	14-5288	21/08/2014	129	71
	14-5306	11/09/2014	120	75
	14-5330	25/09/2014	119	52
	14-5364	16/10/2014	53	73
	14-5387	06/11/2014	89	78
	14-5402	20/11/2014	80	75
	14-5429	15/12/2014	81	83
	15-5041	21/01/2015	82	80
	15-5132	13/02/2015	89	81
	15-5200	17/03/2015	76	79
	15-5260	07/05/2015	68	77
	15-5322	09/06/2015	86	78
	15-5344	13/07/2015	74	81
	15-5402	02/09/2015	60	79
	15-5418	23/09/2015	53	77
	15-5453	03/11/2015	47	80
	16-5096	18/02/2016	-	-
	16-5142	26/04/2016	-	-
Phase II	16-5362	22/11/2016	100	82
	16-5377	15/12/2016	93	90
	17-5214	07/06/2017	76	87
	17-5250	11/07/2017	72	87
	17-5282	30/08/2017	65	87

*Table C.10. The fraction of CO_2 and H_2S mineralized during the transport of injected gas charged fluids to the HE-48 monitoring well. Italicized samples are used for background concentrations in the initial reservoir fluid. *First appearance of the 1-ns tracer.*

Gas Injection	Sample no	Date	DIC [%]	DS [%]
Phase I	*14-5110*	29/04/2014	-	-
	14-5164	12/06/2014	-	-
	14-5187	25/06/2014	-	-
	14-5213	09/07/2014	-	-
*	14-5244	23/07/2014	-	-
	14-5252	08/08/2014	-	-
	14-5308	11/09/2014	93	95
	14-5331	25/09/2014	119	56
	14-5365	16/10/2014	75	86
	14-5388	06/11/2014	81	80
	14-5403	20/11/2014	84	79
	14-5430	15/12/2014	81	87
	14-5040	21/01/2015	91	86
	15-5131	13/02/2015	72	83
	15-5198	17/03/2015	60	79
	15-5258	07/05/2015	73	79
	15-5336	03/07/2015	70	83
	15-5400	02/09/2015	71	82
	15-5417	23/09/2015	69	79
	15-5455	03/11/2015	65	78
	16-5075	09/02/2016	61	79
Phase II	16-5363	22/11/2016	100	90
	17-5058	19/01/2017	93	90
	17-5215	07/06/2017	86	89
	17-5248	11/07/2017	85	90
	17-5283	30/08/2017	79	87

*Table C.11. The fraction of CO_2 and H_2S mineralized during the transport of injected gas charged fluids to the HE-44 monitoring well. Italicized samples are used for background concentrations in the initial reservoir fluid. *First appearance of the 1-ns tracer.*

Gas Injection	Sample no	Date	DIC [%]	DS [%]
Phase I	*14-5113*	06/05/2014	-	-
	14-5188	26/06/2014	-	-
	14-5212	08/07/2014	-	-
	14-5253	08/08/2014	-	-
*	14-5332	25/09/2014	-	-
	14-5371	22/10/2014	-	-
	14-5389	06/11/2014	-	-
	15-5039	21/01/2015	128	72
	15-5199	17/03/2015	102	107
	15-5259	07/05/2015	47	73
	15-5346	13/07/2015	95	81
	15-5401	02/09/2015	103	87
	15-5454	03/11/2015	248	93
	16-5080	10/02/2016	114	88
	16-5146	05/04/2016	-	-
	16-5194	24/06/2016	-	-
Phase II	17-5059	19/01/2017	360	87
	17-5216	07/06/2017	187	89
	17-5284	30/08/2017	138	91

*Table C.12. Volume of mineral precipitation within the reservoir. *Pyrite values calculated using H_2S.*

Mineral	Molar Volume [cm³/mol]	CO_2 : Mineral Ratio	Volume from 1 ton CO_2 [m³]	Total volume of mineral [m³]	Vol percent in reservoir [vol %]
Calcite	36.934	1	0.84	19,500	0.0032
Epidote	139.2	8	0.40	9,170	0.0015
Ferroactionlite	284.2	40	0.16	3,750	0.0006
Termolite	272.92	22	0.28	6,540	0.0011
Clinochlore	207.11	22	0.21	4,960	0.0008
Daphnite	213.42	40	0.17	3,630	0.0006
Pyrite*	23.94	1	0.70	8,280	0.0014

Volume of Mineral Precipitation

By using the molar volume of the minerals and the ratio of gas needed for precipitation, one can calculate the potential volume of the minerals for every ton of gas (Table C.12). A 1:1 ratio was assumed between the gas and target minerals, calcite and pyrite. For the secondary minerals (epidote, actinolite, and chlorite), this ratio was determined by the amount of basalt rock needed to obtain the necessary amount of divalent cations for precipitation. Molar volumes were from the carbfix database (Voigt et al., 2018), and the following crystalline Stapafell basalt composition was used: $SiAl_{0.35}K_{0.005}Mg_{0.234}Na_{0.083}Ca_{0.264}Fe_{0.144}O_2(OH)_{1.05}$. Then by knowing the reservoir size (6×10^8 m^3) and the amount of gas injected, 23,200 metric tons of CO_2 and 11,800 H_2S, the total volume and the vol percent of mineral precipitation in the reservoir was determined. Note that the amount of secondary mineral precipitation was calculated using the injected amount of CO_2 rather than H_2S as little secondary mineral precipitation was assumed to compete with the sulfide minerals.

References

Naumov, G.B., Ryshenko, B.N. and Khodakovsky, I.L. (1971) Handbook of thermodynamic data (translation of Russian report): United States Geological Service Report WRD-74-001, 328p.

Stefánsson, A. and Gíslason, S.R. (2001) Chemical Weathering of Basalts, Southwest Iceland: Effect of Rock Crystallinity and Secondary Minerals on Chemical Fluxes to the Ocean. *American Journal of Science* 501, 513–556.

Voigt, M., Marieni, C., Clark, D.E., Gíslason, S.R. and Oelkers, E.H. (2018) Evaluation and refinement of thermodynamic databases for mineral carbonation. *Energy Procedia* 146, 81–91.

D Appendix

Supplementary Material to Paper IV

Table D.1. Trace element concentrations in µM from Well HE-31 liquid-phase samples.

Detection Limit			0.0928	0.0072	0.0022	0.0009	0.0054	0.0067	0.915	0.0020	0.0750	0.0043	0.0180	0.0067	0.0104	0.0040	0.0021
[µM]			0.0120*	0.0056*	0.0004*	0.0030*	0.0014*	0.0130*	0.0347*	0.0028*	0.0074*	0.0031*	0.0076*	0.0064*	0.0004*	0.0013*	0.0106*
Quantification Limit			0.0400*	0.0187*	0.0013*	0.0100*	0.0047*	0.0434*	0.116*	0.0094*	0.0248*	0.0104*	0.0255*	0.0215*	0.0013*	0.0044*	0.0352*
Uncertainty at 95% C.I. [%]			5.1	1.9	0.55	1.2	2.8	0.68	1.1	2.2	0.7	2.0	2.7	1.2	1.1	1.2	0.91
			1.8*	1.9*	0.29*	1.0*	0.77*	1.7*	0.29*	0.68*	1.9*	2.6*	3.8*	2.4*	1.7*	0.39*	0.45*
Sample no	**Date**	**Vapor fraction**	**As [µM]**	**Be [µM]**	**Co [µM]**	**Cs [µM]**	**Cu [µM]**	**Ga [µM]**	**Li [µM]**	**Ni [µM]**	**Rb [µM]**	**Sc [µM]**	**Se [µM]**	**Sr [µM]**	**Ti [µM]**	**V [µM]**	**Zn [µM]**
14-5109	29/04/2014	0.2014	0.713	0.0248	LOD	0.0386	0.125	0.124	16.3	LOD	1.29	0.121	LOD	0.0775	0.0524	0.127	LOD
14-5119	16/05/2014	0.2006	0.663	0.0136	LOD	0.0338	0.0282	0.112	15.3	0.0814	LOD	0.0219	LOD	0.0642	0.0435	0.122	0.122
14.5161	11/06/2014	0.1943	0.714	0.0198	LOD	0.0385	0.110	0.126	16.3	LOD	1.30	0.124	LOD	0.0681	0.0484	0.127	LOD
14-5183	24/06/2014	0.1980	0.734	0.0155	LOD	0.0446	0.103	0.117	19.8	LOD	1.42	0.121	LOD	0.0803	0.0532	0.0533	LOD
14-5205	01/07/2014	0.1918	0.691	0.0188	LOD	0.0311	0.0247	0.121	18.5	0.0509	LOD	0.0360	LOD	0.0776	0.0937	0.136	0.147
14-5210	08/07/2014	0.1971	0.701	0.0185	LOD	0.0370	0.111	0.125	16.5	0.0111	1.28	0.122	LOD	0.0772	0.0481	0.126	LOD
14-5236	17/07/2014	0.1990	0.705	0.0170	LOD	0.0374	0.107	0.130	17.0	LOD	1.34	0.122	LOD	0.0782	0.0617	0.135	LOD
14-5243	23/07/2014	0.1963	0.712	0.0100	LOD	0.0366	0.0330	0.128	19.2	0.0590	LOD	0.0386	LOD	0.0706	0.0604	0.137	0.132
14-5251	07/08/2014	0.1971	0.694	0.0136	LOD	0.0372	0.0299	0.129	19.7	0.0517	LOD	0.0400	LOD	0.0736	0.0446	0.138	0.149
14-5288	21/08/2014	0.1917	0.644	0.0196	LOD	0.0375	0.108	0.124	17.2	LOD	1.33	0.125	LOD	0.0779	0.0590	0.124	LOD
14-5306	11/09/2014	0.1909	0.624	0.0170	LOD	0.0381	0.110	0.122	17.8	0.0289	1.35	0.126	0.0182	0.0813	0.0551	0.120	0.0092
14-5330	25/09/2014	0.1902	0.638	0.0232	LOD	0.0394	0.131	0.124	18.7	LOD	1.39	0.137	LOD	0.0814	0.0774	0.121	LOD
14-5364	16/10/2014	0.1886	0.606	0.0152	LOD	0.0381	0.135	0.120	17.9	LOD	1.36	0.132	LOD	0.0774	0.0549	0.120	LOD
14-5387	06/11/2014	0.1912	0.603	0.0269	LOD	0.0346	0.111	0.123	18.8	LOD	1.34	0.141	LOD	0.0734	0.0585	0.116	LOD
14-5402	20/11/2014	0.1902	0.588	0.0099	LOD	0.0389	0.141	0.124	19.0	LOD	1.39	0.133	LOD	0.0822	0.0605	0.116	LOD
14-5429	15/12/2014	0.1950	0.562	0.0154	LOD	0.0368	0.159	0.117	19.2	LOD	1.34	0.144	LOD	0101	0.0642	0.118	LOD
15-5041	21/01/2015	0.2003	0.577	0.0267	LOD	0.0403	0.125	0.125	20.6	LOD	1.42	0.142	LOD	0.0780	0.0537	0.116	LOD
15-5132	13/02/2015	0.1939	0.566	0.0123	0.0130	0.0381	0.181	0.124	20.9	1.70	LOD	0.0406	LOD	0.0712	0.0419	0.137	4.67
15-5200	17/03/2015	0.2005	0.156	0.0151	LOD	0.0394	0.105	0.123	20.3	LOD	1.42	0.145	LOD	0.0749	0.0511	0.115	0.0622
15-5260	07/05/2015	0.1930	0.240	0.0233	LOD	0.0386	0.0417	0.122	21.1	0.0200	LOD	0.0411	LOD	0.0741	0.0378	0.125	0.347

15-5322	09/06/2015	0.1920	0.241	0.0304	LOD	0.0389	0.0168	0.118	20.7	0.0215	1.06	0.0398	LOD	0.0746	0.0409	0.122	0.198
15-5344	13/07/2015	0.1907	0.114	0.0252	LOD	0.0407	0.0136	0.121	21.6	0.0171	0.500	0.0409	LOD	0.0771	0.0464	0.124	0.153
15-5402	02/09/2015	0.1918	0.115	0.0211	LOD	0.0375	0.0081	0.117	21.4	0.0466	0.505	0.0388	LOD	0.0807	0.0365	0.119	0.186
15-5418	23/09/2015	0.1955	0.113	0.0161	LOD	0.0397	0.0104	0.118	21.9	0.0425	0.493	0.0396	LOD	0.0811	0.0464	0.120	0.179
15-5453	03/11/2015	0.1970	0.147	0.0211	LOD	0.0415	0.0980	0.119	22.1	LOD	1.47	0.152	LOD	0.0860	0.0570	0.107	0.0117
16-5096	18/02/2016	0.1865	LOD	0.0139	LOD	0.0402	0.100	0.119	21.4	LOD	1.45	0.144	LOD	0.0743	0.0549	0.109	LOD
16-5142	26/04/2016	0.1989	0.534	0.0222	LOQ*	0.0375	0.0605	0.120	21.6	0.0315	1.47	LOQ*	LOD	0.0663	0.0032	0.112	0.743
16-5362	22/11/2016	0.1910	0.256	0.0211	LOQ*	0.0389	0.0086	0.105	23.1	0.0406	1.45	LOD*	LOD	0.0633	0.0028	0.106	1.91
16-5377	15/12/2016	0.1915	0.0721	LOQ*	LOD*	0.0369	0.0083	0.115	22.7	0.0686	1.47	LOQ*	LOD	0.0702	0.0026	0.102	0.296
17-5214	07/06/2017	0.1910	0.0659	LOQ*	LOD*	0.0345	LOD*	0.108	16.4	LOQ*	1.66	0.0439	LOD	0.122	0.0437	0.0945	0.0687
17-5250	11/07/2017	0.1902	0.135	LOD*	LOD*	0.0362	LOD*	0.0848	17.6	LOD*	1.71	0.0492	LOD	0.119	0.0424	0.0967	0.0455
17-5282	30/08/2017	0.1887	0.0405	LOD*	LOD*	0.0381	LOD*	0.104	18.4	LOQ*	1.76	0.0493	LOD	0.0123	0.0458	0.0984	0.0532

*Limit of detection (LOD) and limit of quantification (LOQ) for samples analysed in 2017.

Table D.2. Trace element concentrations in nM from Well HE-31 liquid-phase samples.

Detection Limit	3.13	0.191	0.0890	1.83	10.7	2.00	1.41	0.215	1.45	1.13	0.807	5.59	0.505	0.055
[nM]	2.23*	4.63*	3.76*	0.333*	0.0524*	0.410*	0.0303*	0.118*	2.49*	0.0171*	-	0.0097*	0.255*	0.838*
Quantification Limit	7.44*	15.4*	12.5*	1.11*	0.175*	1.37*	0.101*	0.394*	8.31*	0.0570*	-	0.0323*	0.851*	2.79*
Uncertainty at 95% C.I. [%]	1.4	2.0	1.1	1.0	0.83	0.78	0.80	0.61	1.3	0.86	1.1	1.2	0.60	0.60
	0.60*	0.76*	1.4*	0.51*	0.79*	0.55*	0.64*	0.42*	0.69*	0.86*	-	1.3*	1.5*	1.2*
Sample no	**Ba [nM]**	**Bi [nM]**	**Cd [nM]**	**Cr [nM]**	**Hf [nM]**	**Mn [nM]**	**Mo [nM]**	**Nb [nM]**	**Pb [nM]**	**Ta [nM]**	**Tl [nM]**	**Sb [nM]**	**Sn [nM]**	**Zr [nM]**
14-5109	12.9	0.340	0.289	3.58	LOD	8.76	96.9	29.5	1.64	11.8	LOD	16.6	1.84	1.69
14-5119	7.98	0.251	0.143	5.33	LOD	9.69	96.5	LOD	LOD	LOD	LOD	LOD	LOD	2.17
14.5161	12.7	0.267	0.149	3.39	LOD	5.98	97.4	6.88	1.56	5.13	LOD	16.3	1.41	1.28
14-5183	11.0	0.304	0.137	4.04	LOD	6.83	107	9.29	LOD	5.51	LOD	18.0	1.42	1.35
14-5205	9.15	0.257	0.114	5.84	LOD	14.5	98.4	4.17	LOD	1.63	LOD	14.8	2.24	1.06
14-5210	10.5	0.303	0.231	2.75	LOD	4.90	95.0	4.21	1.47	3.67	LOD	16.0	1.52	1.32
14-5236	11.3	0.284	0.166	47.3	LOD	10.6	94.8	2.49	1.46	2.84	LOD	17.0	1.41	1.45
14-5243	8.09	0.295	0.121	5.28	LOD	9.17	93.7	2.41	LOD	LOD	LOD	15.7	2.07	0.913
14-5251	7.70	LOD	0.128	3.18	LOD	6.57	90.0	1.39	LOD	LOD	LOD	15.6	1.94	0.789
14-5288	10.4	0.268	0.246	2.87	LOD	5.31	85.6	0.897	LOD	1.90	LOD	17.7	1.49	1.24
14-5306	11.0	0.253	0.170	4.96	LOD	6.88	86.5	11.0	LOD	4.91	LOD	16.2	1.43	1.42
14-5330	12.6	0.301	0.169	3.50	LOD	8.01	84.0	0.737	1.50	1.14	LOD	16.4	1.40	1.34
14-5364	10.5	0.287	0.167	2.78	LOD	5.29	80.5	1.95	1.58	1.68	LOD	17.2	1.38	1.90
14-5387	10.4	0.251	0.207	2.76	LOD	4.65	83.2	0.447	LOD	LOD	LOD	17.2	1.20	1.44
14-5402	12.6	0.286	0.178	2.84	LOD	4.85	79.6	1.12	1.86	1.42	LOD	17.2	1.62	1.58
14-5429	12.8	0.298	0.269	3.69	LOD	6.30	74.0	0.336	2.46	LOD	LOD	16.2	1.60	1.64
15-5041	14.3	0.278	0.346	2.41	LOD	5.16	75.1	1.13	1.70	LOD	LOD	16.7	1.23	0.905
15-5132	8.62	LOD	0.103	3970	LOD	270	85.7	1.68	LOD	LOD	LOD	16.8	2.57	0.633
15-5200	13.8	0.292	LOD	34.6	LOD	7.78	24.2	0.462	LOD	LOD	LOD	LOD	1.21	1.13
15-5260	8.53	0.342	LOD	21.7	LOD	8.60	30.8	0.356	LOD	LOD	LOD	LOD	1.68	0.632
15-5322	8.77	0.307	LOD	21.3	LOD	7.47	28.8	0.298	LOD	LOD	LOD	LOD	1.82	0.639
15-5344	13.8	0.768	0.998	20.8	LOD	9.44	15.7	8.10	LOD	1.91	LOD	LOD	3.06	0.905

15-5402	8.95	0.453	0.110	9.86	LOD	6.78	9.18	1.61	LOD	LOD	LOD	LOD	1.82	0.759
15-5418	10.4	0.266	LOD	8.73	LOD	10.5	8.32	0.498	LOD	LOD	LOD	LOD	1.81	0.609
15-5453	14.7	0.240	0.129	7.04	LOD	5.18	19.8	0.421	LOD	LOD	LOD	LOD	1.15	33.1
16-5096	12.6	0.244	0.104	4.54	LOD	10.9	7.31	0.264	LOD	LOD	LOD	LOD	1.34	1.40
16-5142	13.3	LOD*	LOD*	13.0	LOD*	11.6	6.40	LOD*	LOD*	LOQ*	-	1.75	LOD*	LOD*
16-5362	9.11	LOD*	LOD*	26.6	LOD*	30.7	1.24	LOD*	LOD*	LOD*	-	0.0920	LOD*	LOD*
16-5377	9.72	LOD*	LOD*	14.4	LOD*	19.2	0.252	LOD*	LOD*	LOD*	-	0.0608	LOD*	LOD*
17-5214	LOQ*	LOD*	LOD*	9.59	LOD*	4.27	3.67		LOD*	LOD*	-	2.05	LOD*	LOD*
17-5250	LOQ*	LOD*	LOD*	3.73	LOD*	4.94	7.77		LOD*	LOD*	-	LOD*	LOD*	LOD*
17-5282	LOQ*	LOD*	LOD*	6.45	LOD*	8.01	0.843		LOD*	LOD*	-	LOD*	LOD*	LOD*

*Limit of detection (LOD) and limit of quantification (LOQ) for samples analysed in 2017.

Table D.3. Rare earth element concentrations in nM from Well HE-31 liquid-phase samples.

Detection Limit	0.107	1.38	0.0329	0.615	0.0636	10.6	0.174	0.0720	1.77	0.0347	0.0710	0.0333	0.220	1.81	1.28	1.91
[nM]	0.0076*	0.0010*	0.0005*	0.0008*	0.0019*	0.0115*	4.30*	0.0054*	0.0005*	0.0020*	0.0006*	0.0007*	0.0005*	0.0006*	3.74*	0.0005*
Quantification Limit	0.0253*	0.0034*	0.0018*	0.0026*	0.0062*	0.0383*	14.34*	0.0179*	0.0016*	0.0068*	0.0019*	0.0024*	0.0017*	0.0021*	12.5*	0.0016*
Uncertainty at 95% C.I. [%]	1.0	1.0	0.86	1.1	0.75	1.0	0.81	0.86	1.0	1.0	1.0	0.70	0.92	1.1	0.92	1.1
	1.0*	0.53*	1.1*	0.83*	1.3*	0.49*	2.4*	1.8*	1.2*	0.86*	2.1*	1.4*	098*	0.25*	0.88*	0.68*
Sample	**Ce**	**Er**	**Eu**	**Dy**	**Gd**	**Ho**	**In**	**La**	**Lu**	**Nd**	**Pr**	**Sm**	**Tb**	**Tm**	**U**	**Yb**
no	**[nM]**	**[nM]**	**[nM]**	**[nM]**	**[nM]**	**[nM]**	**[nM]**	**[nM]**	**[nM]**	**[nM]**	**[nM]**	**[nM]**	**[nM]**	**[nM]**	**[nM]**	**[nM]**
14-5109	0.509	LOD	0.351	LOD	0.316	LOD	0.207	0.497	LOD	0.458	0.349	0.319	0.347	LOD	LOD	LOD
14-5119	LOD	LOD	LOD	LOD	LOD	LOD	LOD	LOD	LOD	LOD	LOD	LOD	LOD	LOD	LOD	LOD
14.5161	0.464	LOD	0.286	LOD	0.279	LOD	LOD	0.464	LOD	0.376	0.310	0.324	0.291	LOD	LOD	LOD
14-5183	0.495	LOD	0.282	LOD	0.313	LOD	LOD	0.496	LOD	0.372	0.379	0.277	0.293	LOD	LOD	LOD
14-5205	0.142	LOD	0.0388	LOD	0.0510	LOD	LOD	0.0954	LOD	0.0631	LOD	0.0270	LOD	LOD	LOD	LOD
14-5210	0.479	LOD	0.304	LOD	0.291	LOD	LOD	0.446	LOD	0.309	0.332	0.313	0.296	LOD	LOD	LOD
14-5236	0.487	LOD	0.272	LOD	0.310	LOD	LOD	0.0430	LOD	0.362	0.346	0.315	0.291	LOD	LOD	LOD
14-5243	LOD	LOD	LOD	LOD	0.0510	LOD	LOD	LOD	LOD	0.0662	LOD	0.0270	LOD	LOD	LOD	LOD
14-5251	0.213	LOD	0.0678	LOD	0.0510	LOD	LOD	0.108	LOD	0.0863	0.0759	0.0270	LOD	LOD	LOD	LOD
14-5288	0.236	LOD	0.0888	LOD	0.0738	LOD	LOD	0.204	LOD	0.116	0.102	0.0752	LOD	LOD	LOD	LOD
14-5306	0.278	LOD	0.103	LOD	0.0839	LOD	LOD	0.241	LOD	0.116	0.112	0.107	LOD	LOD	LOD	LOD
14-5330	0.293	LOD	0.0902	LOD	0.0916	LOD	LOD	0.261	LOD	0.132	0.110	0.105	LOD	LOD	LOD	LOD
14-5364	0.341	LOD	0.0737	LOD	0.0801	LOD	LOD	0.392	LOD	0.126	0.110	0.0944	LOD	LOD	LOD	LOD
14-5387	0.221	LOD	0.0809	LOD	0.0833	LOD	LOD	0.177	LOD	0.111	0.0880	0.0758	LOD	LOD	LOD	LOD
14-5402	0.267	LOD	0.0875	LOD	0.0655	LOD	LOD	0.265	LOD	0.131	0.0908	0.105	LOD	LOD	LOD	LOD
14-5429	0.316	LOD	0.0757	LOD	0.0725	LOD	LOD	0.317	LOD	0.138	0.0944	0.0891	LOD	LOD	LOD	LOD
15-5041	0.225	LOD	0.0836	LOD	0.0890	LOD	LOD	0.176	LOD	0.122	0.0951	0.0685	LOD	LOD	LOD	LOD
15-5132	LOD	LOD	LOD	LOD	0.0510	LOD	LOD	LOD	LOD	LOD	LOD	0.0270	LOD	LOD	LOD	LOD
15-5200	0.212	LOD	0.0750	LOD	0.0700	LOD	LOD	0.198	LOD	0.119	0.0937	0.0652	LOD	LOD	LOD	LOD
15-5260	LOD	LOD	LOD	LOD	LOD	LOD	LOD	LOD	LOD	LOD	LOD	LOD	LOD	LOD	LOD	LOD
15-5322	LOD	LOD	LOD	LOD	LOD	LOD	LOD	LOD	LOD	LOD	LOD	LOD	LOD	LOD	LOD	LOD
15-5344	0.121	LOD	0.0619	LOD	LOD	LOD	LOD	0.114	LOD	0.0704	0.0816	0.0785	LOD	LOD	LOD	LOD

15-5402	LOD	LOD	LOD	LOD	LOD	LOD	1.20	LOD	LOD	LOD	LOD	LOD	LOD	LOD	LOD	LOD
15-5418	LOD	LOD	LOD	LOD	LOD	LOD	LOD	LOD	LOD	LOD	LOD	LOD	LOD	LOD	LOD	LOD
15-5453	0.236	LOD	0.0724	LOD	0.0941	LOD	LOD	0.181	LOD	0.149	0.0837	0.0851	LOD	LOD	LOD	LOD
16-5096	0.308	LOD	0.0994	LOD	0.0757	LOD	LOD	0.271	LOD	0.119	0.0986	0.0865	LOD	LOD	LOD	LOD
16-5142	LOQ*	LOD*	LOQ*	LOD*	LOD*	LOD*	LOD*	LOQ*	LOD*	LOQ*	LOQ*	LOQ*	LOD*	LOD*	LOD*	LOD*
16-5362	LOQ*	LOD*	LOQ*	LOD*	LOD*	LOD*	LOD*	LOQ*	LOD*	LOQ*	LOQ*	LOQ*	LOD*	LOD*	LOD*	LOQ*
16-5377	LOD*	LOD*	LOD*	LOD*	LOD*	LOD*	LOD*	LOQ*	LOD*	LOQ*	LOQ*	LOQ*	LOD*	LOD*	LOD*	LOD*
17-5214	1.10	LOD*	LOD*	LOD*	LOD*	LOD*	LOD*	0.531	LOD*	0.206	LOD*	LOD*		LOD*	-	LOD*
17-5250	0.970	LOD*	LOD*	LOD*	LOD*	LOD*	LOD*	0.558	LOD*	0.190	LOD*	LOD*		LOD*	-	LOD*
17-5282	0.979	LOD*	LOD*	LOD*	LOD*	LOD*	LOD*	0.541	LOD*	0.255	LOD*	LOD*		LOD*	-	LOD*

*Limit of detection (LOD) and limit of quantification (LOQ) for samples analysed in 2017.

Table D.4. Trace element concentrations in µM from Well HE-48 liquid-phase samples.

Detection Limit			0.0928	0.0072	0.0022	0.0009	0.0054	0.0067	0.915	0.0020	0.0750	0.0043	0.0180	0.0067	0.0104	0.0040	0.0021
[µM]			0.0120*	0.0056*	0.0004*	0.0030*	0.0026*	0.0130*	0.0347*	0.0028*	0.0074*	0.0031*	0.0076*	0.0064*	0.0004*	0.0013*	0.0106*
Quantification Limit			0.0400*	0.0187*	0.0013*	0.0100*	0.0087*	0.0434*	0.116*	0.0094*	0.0248*	0.0104*	0.0255*	0.0215*	0.0013*	0.0044*	0.0352*
Uncertainty at 95% CI [%]			5.1	1.9	0.55	1.2	2.8	0.68	1.1	2.2	0.7	2.0	2.7	1.2	1.1	1.2	0.91
			1.8*	1.9*	0.29*	1.0*	0.77*	1.7*	0.29*	0.68*	1.9*	2.6*	3.8*	2.4*	1.7*	0.39*	0.45*
Sample no	**Date**	**Vapor fraction**	**As [µM]**	**Be [µM]**	**Co [µM]**	**Cs [µM]**	**Cu [µM]**	**Ga [µM]**	**Li [µM]**	**Ni [µM]**	**Rb [µM]**	**Sc [µM]**	**Se [µM]**	**Sr [µM]**	**Ti [µM]**	**V [µM]**	**Zn [µM]**
14-5110	29/04/2014	0.2266	0.734	0.0198	LOD	0.0421	0.158	0.119	20.5	LOD	1.42	0.112	LOD	0.0836	0.0655	0.0575	LOD
14-5164	12/06/2014	0.1969	LOD	0.0150	LOD	0.0401	LOD	0.0957	19.3	LOD	1.37	0.0164	LOD	0.0651	0.0238	0.0558	LOD
14-5187	25/06/2014	0.1997	0.694	0.0140	LOD	0.0416	0.113	0.121	20.7	LOD	1.40	0.126	0.0226	0.0856	0.0571	0.0581	0.0247
14-5213	09/07/2014	0.2004	0.709	0.0143	LOD	0.0415	0.113	0.118	20.1	LOD	1.41	0.123	LOD	0.0855	0.0566	0.0559	LOD
14-5244	23/07/2014	0.2075	0.750	0.0159	LOD	0.0412	0.0151	0.123	24.2	0.0125	3.29	0.0408	LOD	0.0823	0.0626	0.0661	0.123
14-5252	08/08/2014	0.1893	0.692	0.0171	LOD	0.0411	0.0995	0.118	20.9	0.0155	1.42	0.125	LOD	0.0952	0.0551	0.0557	LOD
14-5308	11/09/2014	0.2012	0.652	0.0167	LOD	0.0407	0.140	0.115	20.8	LOD	1.44	0.132	0.0221	0.0831	0.0567	0.0554	LOD
14-5331	25/09/2014	0.1981	0.663	0.0173	LOD	0.0413	0.111	0.119	21.3	0.0048	1.46	0.141	0.0194	0.0920	0.0630	0.0558	0.579
14-5365	16/10/2014	0.2012	0.634	0.0125	LOD	0.0415	0.107	0.117	21.5	LOD	1.45	0.131	LOD	0.0797	0.0524	0.0564	0.0133
14-5388	06/11/2014	0.1952	0.629	0.0154	LOD	0.0398	0.110	0.115	22.5	0.0741	1.45	0.143	LOD	0.0803	0.0726	0.0570	0.015
14-5403	20/11/2014	0.1957	0.603	0.0169	LOD	0.0419	0.104	0.118	22.2	LOD	1.46	0.133	0.0182	0.0776	0.0539	0.0548	0.115
14-5430	15/12/2014	0.1966	0.584	0.0198	LOD	0.0412	0.143	0.117	22.7	LOD	1.45	0.143	LOD	0.0831	0.0593	0.0535	LOD
14-5040	21/01/2015	0.1993	0.565	0.0182	LOD	0.0423	0.129	0.117	23.1	LOD	1.49	0.144	LOD	0.0813	0.0650	0.0555	LOD
15-5131	13/02/2015	0.2020	0.574	0.0224	0.0072	0.0406	0.0463	0.114	24.4	0.171	2.51	0.0398	LOD	0.0650	0.0390	0.0600	14.5
15-5198	17/03/2015	0.1999	0.264	0.0211	LOD	0.0440	0.112	0.122	24.4	0.0582	1.56	0.148	LOD	0.0795	0.0518	0.0553	0.0259
15-5258	07/05/2015	0.1957	0.175	0.0133	LOD	0.0414	0.0291	0.115	25.0	0.0678	0.765	0.0409	LOD	0.0740	0.0381	0.0577	0.161
15-5336	03/07/2015	0.2010	0.200	0.0243	LOD	0.0440	0.0103	0.114	25.3	0.0180	0.873	0.0439	LOD	0.0712	0.0437	0.0582	0.168
15-5400	02/09/2015	0.1972	0.105	0.0263	LOD	0.0407	0.0127	0.117	25.3	0.262	0.459	0.0396	LOD	0.0784	0.0382	0.0569	0.201
15-5417	23/09/2015	0.2010	LOD	0.0099	LOD	0.0456	0.0100	0.115	25.2	0.0202	0.288	0.0405	LOD	0.0736	0.0398	0.0585	0.193
15-5455	03/11/2015	0.2019	0.170	0.0182	LOD	0.0401	0.0908	0.116	24.8	LOD	1.51	0.149	LOD	0.0859	0.0563	0.0623	LOD
16-5075	09/02/2016	0.2069	LOD	0.0083	LOQ*	0.0437	0.0903	0.114	25.2	LOD	1.57	0.145	LOD	0.0825	0.0587	0.0535	0.0469
16-5363	22/11/2016	0.1919	0.260	LOQ*	LOQ*	0.0392	0.0123	0.110	26.5	0.0364	1.56	LOQ*	LOD*	0.0726	0.0028	0.0498	0.269

17-5058	19/01/2017	0.1982	0.182	LOQ*	LOD*	0.0386	0.0079	0.109	26.0	0.0432	1.54	LOQ*	LOD*	0.0679	0.0034	0.0483	0.284
17-5215	07/06/2017	0.1929	0.557	LOD*	LOD*	0.0358	LOD*	0.104	18.1	LOQ*	1.71	0.0443	LOD*	0.122	0.0470	0.0462	0.0549
17-5248	11/07/2017	0.1912	0.588	LOD*	LOD*	0.0385	LOD*	0.0920	19.1	LOD*	1.78	0.0443	LOD*	0.116	0.0426	0.0486	0.0627
17-5283	30/08/2017	0.1886	0.563	LOD*	LOD*	0.0378	LOD*	0.0909	20.5	LOQ*	1.74	0.0468	LOD*	0.124	0.0439	0.0482	0.0586

*Limit of detection (LOD) and limit of quantification (LOQ) for samples analysed in 2017.

Table D.5. Trace element concentrations in nM from Well HE-48 liquid-phase samples.

Detection Limit	3.13	0.191	0.0890	1.83	10.7	2.00	1.41	0.215	1.45	1.13	0.807	5.59	0.505	0.055
[nM]	2.23*	4.63*	3.76*	0.333*	0.0524*	0.410*	0.0303*	0.118*	2.49*	0.0171*	-	0.0097*	0.255*	0.838*
Quantification Limit	7.44*	15.4*	12.5*	1.11*	0.175*	1.37*	0.101*	0.394*	8.31*	0.0570*	-	0.0323*	0.851*	2.79*
Uncertainty at 95% C.I. [%]	1.4	2.0	1.1	1.0	0.83	0.78	0.80	0.61	1.3	0.86	1.1	1.2	0.60	0.60
	0.60*	0.76*	1.4*	0.51*	0.79*	0.55*	0.64*	0.42*	0.69*	0.86*	-	1.3*	1.5*	1.2*
Sample	**Ba**	**Bi**	**Cd**	**Cr**	**Hf**	**Mn**	**Mo**	**Nb**	**Pb**	**Ta**	**Tl**	**Sb**	**Sn**	**Zr**
no	**[nM]**	**[nM]**	**[nM]**	**[nM]**	**[nM]**	**[nM]**	**[nM]**	**[nM]**	**[nM]**	**[nM]**	**[nM]**	**[nM]**	**[nM]**	**[nM]**
14-5110	17.8	0.335	0.354	3.06	LOD	7.30	101	12.8	2.09	6.60	LOD	18.9	1.68	2.18
14-5164	14.9	LOD	LOD	LOD	LOD	4.11	38.5	0.481	LOD	LOD	LOD	LOD	LOD	LOD
14-5187	12.0	0.278	0.123	4.16	LOD	10.1	104	1.85	1.71	2.50	LOD	16.4	1.40	1.38
14-5213	12.2	0.282	0.203	3.34	LOD	7.92	101	2.93	1.63	2.73	LOD	17.5	1.79	1.43
14-5244	7.41	LOD	LOD	3.67	LOD	9.88	101	1.74	LOD	LOD	LOD	18.1	2.05	0.780
14-5252	11.7	0.247	0.189	4.51	LOD	10.4	93.0	1.12	LOD	1.88	LOD	17.9	1.48	1.52
14-5308	11.8	0.261	0.0996	4.46	LOD	5.38	83.0	3.04	1.71	1.90	LOD	18.5	1.36	1.40
14-5331	11.7	0.254	0.133	7.14	LOD	12.9	78.9	0.653	1.60	LOD	LOD	18.1	1.44	1.19
14-5365	11.2	0.282	0.140	30.5	LOD	14.9	88.0	1.40	LOD	1.35	LOD	18.6	1.57	1.26
14-5388	10.5	0.227	0.129	8.93	LOD	14.3	100	0.435	LOD	LOD	LOD	18.4	1.46	7.63
14-5403	9.56	0.234	0.206	5.95	LOD	44.2	105	0.855	LOD	1.26	LOD	18.1	1.42	1.18
14-5430	10.7	0.234	0.165	5.32	LOD	10.9	77.0	0.330	1.56	LOD	LOD	18.2	1.56	2.50
14-5040	11.8	0.263	0.281	4.18	LOD	7.14	72.5	1.87	1.84	1.54	LOD	18.3	1.38	1.77
15-5131	6.55	0.233	0.118	142	LOD	33.5	83.0	0.706	LOD	LOD	LOD	19.5	1.76	0.638
15-5198	11.3	0.235	0.154	12.7	LOD	7.21	42.2	0.758	LOD	LOD	LOD	LOD	1.31	1.89
15-5258	8.23	LOD	0.101	20.2	LOD	10.9	25.2	0.372	LOD	LOD	LOD	LOD	1.68	0.617
15-5336	6.73	0.254	0.244	21.6	LOD	11.0	16.3	6.05	LOD	1.58	LOD	LOD	2.67	1.58
15-5400	8.54	0.301	0.133	7.40	LOD	8.04	2.63	4.17	LOD	LOD	LOD	LOD	2.08	0.928
15-5417	7.28	0.226	0.0965	8.66	LOD	11.1	3.70	0.646	LOD	LOD	LOD	LOD	1.95	0.610
15-5455	10.5	0.298	LOD	5.95	LOD	7.06	7.45	0.335	LOD	LOD	LOD	LOD	1.25	1.02
16-5075	11.7	0.239	LOD	3.98	LOD	8.04	4.26	0.300	LOD	LOD	LOD	LOD	1.76	0.937
16-5363	LOQ*	LOD*	LOD*	18.4	LOD*	17.0	1.71	LOD*	LOD*	LOD*	LOD	0.243	LOD*	LOD*

17-5058	LOQ*	LOD*	LOD*	24.2	LOD*	37.2	1.23	LOD*	LOD*	LOD*	LOD	0.0579	LOD*	LOD*
17-5215	LOQ*	LOD*	LOD*	6.74	LOD*	4.39	1.85	LOD*	LOD*	LOD*	-	0.639	LOD*	LOD*
17-5248	LOQ*	LOD*	LOD*	3.62	0.792	5.16	7.86	LOD*	LOD*	0.120	-	0.0306	LOD*	LOD*
17-5283	LOQ*	LOD*	LOD*	4.89	LOD*	5.19	0.797	LOD*	LOD*	LOD*	-	LOD*	LOD*	LOD*

*Limit of detection (LOD) and limit of quantification (LOQ) for samples analysed in 2017.

Table D.6. Rare earth element concentrations in nM from Well HE-48 liquid-phase samples.

Detection Limit	0.107	1.38	0.0329	0.615	0.0636	10.6	0.174	0.0720	1.77	0.0347	0.0710	0.0333	0.220	1.81	1.28	1.91
[nM]	0.0076*	0.0010*	0.0005*	0.0008*	0.0019*	0.0115*	4.30*	0.0054*	0.0005*	0.0020*	0.0006*	0.0007*	0.0005*	0.0006*	3.74*	0.0005*
Quantification Limit	0.0253*	0.0034*	0.0018*	0.0026*	0.0062*	0.0383*	14.34*	0.0179*	0.0016*	0.0068*	0.0019*	0.0024*	0.0017*	0.0021*	12.5*	0.0016*
Uncertainty at 95% C.I. [%]	1.0	1.0	0.86	1.1	0.75	1.0	1.0	0.81	0.86	1.0	1.0	0.70	0.92	1.1	0.92	1.1
	1.0*	0.53*	1.1*	0.83*	1.3*	1.2*	0.49*	2.4*	1.8*	0.86*	2.1*	1.4*	098*	0.25*	0.88*	0.68*
Sample	**Ce**	**Er**	**Eu**	**Dy**	**Gd**	**Ho**	**In**	**La**	**Lu**	**Nd**	**Pr**	**Sm**	**Tb**	**Tm**	**U**	**Yb**
no	**[nM]**	**[nM]**	**[nM]**	**[nM]**	**[nM]**	**[nM]**	**[nM]**	**[nM]**	**[nM]**	**[nM]**	**[nM]**	**[nM]**	**[nM]**	**[nM]**	**[nM]**	**[nM]**
14-5110	0.911	LOD	0.307	LOD	0.284	LOD	LOD	1.13	LOD	0.359	0.319	0.293	0.297	LOD	LOD	LOD
14-5164	LOD	LOD	LOD	LOD	LOD	LOD	LOD	LOD	LOD	LOD	LOD	LOD	LOD	LOD	LOD	LOD
14-5187	0.517	LOD	0.290	LOD	0.280	LOD	LOD	0.508	LOD	0.387	0.303	0.280	0.295	LOD	LOD	LOD
14-5213	0.482	LOD	0.297	LOD	0.281	LOD	LOD	0.474	LOD	0.324	0.324	0.318	0.261	LOD	LOD	LOD
14-5244	LOD	LOD	LOD	LOD	LOD	LOD	LOD	LOD	LOD	0.0419	LOD	0.0392	LOD	LOD	LOD	LOD
14-5252	0.270	LOD	0.0836	LOD	0.0820	LOD	LOD	0.219	LOD	0.121	0.102	0.0971	LOD	LOD	LOD	LOD
14-5308	0.309	LOD	0.0941	LOD	0.0909	LOD	LOD	0.276	LOD	0.130	0.0887	0.108	LOD	LOD	LOD	LOD
14-5331	0.238	LOD	0.0842	LOD	0.104	LOD	LOD	0.217	LOD	0.116	0.104	0.0984	LOD	LOD	LOD	LOD
14-5365	0.211	LOD	0.0836	LOD	0.0674	LOD	LOD	0.222	LOD	0.101	0.0972	0.0745	LOD	LOD	LOD	LOD
14-5388	0.248	LOD	0.0823	LOD	0.0814	LOD	LOD	0.200	LOD	0.0929	0.101	0.0865	LOD	LOD	LOD	LOD
14-5403	0.238	LOD	0.0803	LOD	0.0859	LOD	LOD	0.184	LOD	0.100	0.0915	0.0685	LOD	LOD	LOD	LOD
14-5430	0.265	LOD	0.0796	LOD	0.0954	LOD	LOD	0.230	LOD	0.126	0.114	0.0838	LOD	LOD	LOD	LOD
14-5040	0.301	LOD	0.0730	LOD	0.0808	LOD	LOD	0.228	LOD	0.118	0.0958	0.0439	LOD	LOD	LOD	LOD
15-5131	LOD	LOD	LOD	LOD	LOD	LOD	LOD	LOD	LOD	LOD	LOD	LOD	LOD	LOD	LOD	LOD
15-5198	0.236	LOD	0.0776	LOD	0.0897	LOD	LOD	0.214	LOD	0.101	0.0951	0.0771	LOD	LOD	LOD	LOD
15-5258	LOD	LOD	LOD	LOD	LOD	LOD	LOD	LOD	LOD	LOD	LOD	LOD	LOD	LOD	LOD	LOD
15-5336	0.269	LOD	0.223	LOD	0.210	LOD	0.195	0.260	LOD	0.251	0.231	0.256	LOD	LOD	LOD	LOD
15-5400	LOD	LOD	0.0651	LOD	0.0636	LOD	LOD	0.100	LOD	0.0790	LOD	0.0635	LOD	LOD	LOD	LOD
15-5417	LOD	LOD	LOD	LOD	LOD	LOD	LOD	LOD	LOD	LOD	LOD	LOD	LOD	LOD	LOD	LOD
15-5455	0.224	LOD	0.0836	LOD	0.0782	LOD	LOD	0.180	LOD	0.112	0.0930	0.0665	LOD	LOD	LOD	LOD
16-5075	0.237	LOD	0.0809	LOD	0.0967	LOD	LOD	0.203	LOD	0.112	0.0937	0.0891	LOD	LOD	LOD	LOD
16-5363	LOD*	LOQ*	0.0043	0.0034	LOQ*	LOQ*	LOD*	LOQ*	0.0017	0.0083	0.0064	0.0053	0.0031	LOQ*	LOD*	0.0023

17-5058	LOD*	LOD*	LOD*	LOQ*	LOD*	LOD*	LOD*	LOQ*	LOD*	LOQ*	LOQ*	LOQ*	LOD*	LOD*	LOD*	LOD*
17-5215	1.02	LOD*	LOD*	LOD*	LOD*	LOD*	LOD*	0.573	LOD*	0.220	LOD*	LOD*	LOD*	LOD*	-	LOD*
17-5248	1.01	LOD*	0.0063	0.0098	0.0232	LOD*	LOD*	0.617	0.0809	0.240	0.0355	0.0346	LOD*	LOD*	-	0.0451
17-5283	0.912	LOD*	LOD*	LOD*	LOD*	LOD*	LOD*	0.501	LOD*	0.243	LOD*	LOD*	LOD*	LOD*	-	LOD*

*Limit of detection (LOD) and limit of quantification (LOQ) for samples analysed in 2017.

Table D.7. Trace element concentrations in µM from Well HE-44 liquid-phase samples.

Detection Limit			0.0928	0.0072	0.0022	0.0009	0.0054	0.0067	0.915	0.0020	0.0750	0.0043	0.0180	0.0067	0.0104	0.0040	0.0021
[µM]			0.0120*	0.0056*	0.0004*	0.0030*	0.0026*	0.0130*	0.0347*	0.0028*	0.0074*	0.0031*	0.0076*	0.0064*	0.0004*	0.0013*	0.0106*
Quantification Limit			0.0400*	0.0187*	0.0013*	0.0100*	0.0087*	0.0434*	0.116*	0.0094*	0.0248*	0.0104*	0.0255*	0.0215*	0.0013*	0.0044*	0.0352*
Uncertainty at 95% C.I. [%]			5.1	1.9	0.55	1.2	2.8	0.68	1.1	2.2	0.7	2.0	2.7	1.2	1.1	1.2	0.91
			1.8*	1.9*	0.29*	1.0*	0.77*	1.7*	0.29*	0.68*	1.9*	2.6*	3.8*	2.4*	1.7*	0.39*	0.45*
Sample no	**Date**	**Vapor fraction**	**As [µM]**	**Be [µM]**	**Co [µM]**	**Cs [µM]**	**Cu [µM]**	**Ga [µM]**	**Li [µM]**	**Ni [µM]**	**Rb [µM]**	**Sc [µM]**	**Se [µM]**	**Sr [µM]**	**Ti [µM]**	**V [µM]**	**Zn [µM]**
14-5113	06/05/2014	0.1996	LOD	0.0225	LOD	0.0530	0.0173	0.0813	31.0	LOD	1.54	0.0171	0.0185	0.0434	0.140	0.0512	LOD
14-5188	26/06/2014	0.2250	0.705	0.0157	LOD	0.0658	0.113	0.119	35.9	LOD	1.76	0.128	0.0263	0.0474	0.0460	0.0537	LOD
14-5212	08/07/2014	0.2262	0.728	0.0158	LOD	0.0644	0.115	0.116	34.9	LOD	1.75	0.129	0.0200	0.0503	0.0650	0.0552	LOD
14-5253	08/08/2014	0.2260	0.705	0.0156	LOD	0.0658	0.100	0.113	35.7	LOD	1.74	0.133	LOD	0.0472	0.0400	0.0545	LOD
14-5332	25/09/2014	0.2271	0.696	0.0154	LOD	0.0624	0.104	0.111	36.7	LOD	1.72	0.146	0.0201	0.0486	0.0511	0.0572	LOD
14-5371	22/10/2014	0.2269	LOD	0.0111	LOD	0.0582	LOD	0.0901	34.3	LOD	1.72	0.0194	LOD	0.0379	0.0168	0.0556	LOD
14-5389	06/11/2014	0.2218	0.709	0.0228	LOD	0.0641	0.107	0.116	37.9	0.0148	1.77	0.146	LOD	0.0481	0.0530	0.0570	LOD
15-5039	21/01/2015	0.2216	0.714	0.0139	LOD	0.0632	0.0965	0.113	36.5	LOD	1.74	0.145	0.0194	0.0443	0.0469	0.0552	LOD
15-5199	17/03/2015	0.2239	0.230	0.0179	LOD	0.0643	0.118	0.120	38.8	LOD	1.80	0.160	LOD	0.0435	0.0456	0.0559	LOD
15-5259	07/05/2015	0.2005	0.205	0.0231	LOD	0.0566	0.0153	0.107	36.6	0.0528	0.900	0.0409	LOD	0.0389	0.0479	0.0542	0.548
15-5346	13/07/2015	0.2247	0.154	0.0149	LOD	0.0628	0.0130	0.120	39.5	0.0658	0.676	0.0443	LOD	0.0454	0.0511	0.0604	0.154
15-5401	02/09/2015	0.2202	0.108	0.0152	LOD	0.0644	0.0077	0.124	40.4	0.0391	0.472	0.0472	LOD	0.0449	0.0412	0.0623	0.173
15-5454	03/11/2015	0.2062	0.241	0.0195	LOD	0.0619	0.0948	0.118	38.3	LOD	1.79	0.154	LOD	0.0523	0.215	0.0601	0.0068
16-5080	10/02/2016	0.2179	LOD	0.0098	LOD	0.0644	0.102	0.118	39.7	LOD	1.83	0.160	LOD	0.0488	0.0578	0.0544	LOD
16-5146	05/04/2016	0.2281	0.742	0.0205	LOQ*	0.0579	0.0713	0.122	41.6	0.0470	1.83	LOQ*	0.0255	0.0450	0.0028	0.0537	0.514
16-5194	24/06/2016	0.2284	0.585	0.0216	LOD*	0.0591	0.0541	0.122	42.2	0.0313	1.84	LOQ*	LOD*	0.0443	0.0028	0.0530	0.198
17-5059	19/01/2017	0.2234	0.144	0.0189	LOQ*	0.0592	0.0075	0.115	40.6	0.0480	1.83	LOQ*	LOD*	0.0425	0.0024	0.0499	0.205
17-5216	07/06/2017	0.2086	0.133	LOD*	LOD*	0.0544	0.0047	0.109	28.0	0.0094	2.02	0.0505	LOD*	0.0891	0.0424	0.0544	0.0602
17-5284	30/08/2017	0.2066	0.153	LOD*	LOD*	0.0581	LOD*	0.0709	30.5	0.0094	2.10	0.0528	LOD*	0.0853	0.0428	0.0543	0.0451

*Limit of detection (LOD) and limit of quantification (LOQ) for samples analysed in 2017.

Table D.8. Trace element concentrations in nM from Well HE-44 liquid-phase samples.

Detection Limit	3.13	0.191	0.0890	1.83	10.7	2.00	1.41	0.215	1.45	1.13	0.807	5.59	0.505	0.055
[nM]	2.23*	4.63*	3.76*	0.333*	0.0524*	0.410*	0.0303*	0.118*	2.49*	0.0171*	-	0.0097*	0.255*	0.838*
Quantification Limit	7.44*	15.4*	12.5*	1.11*	0.175*	1.37*	0.101*	0.394*	8.31*	0.0570*	-	0.0323*	0.851*	2.79*
Uncertainty at 95% C.I. [%]	1.4	2.0	1.1	1.0	0.83	0.78	0.80	0.61	1.3	0.86	1.1	1.2	0.60	0.60
	0.60*	0.76*	1.4*	0.51*	0.79*	0.55*	0.64*	0.42*	0.69*	0.86*	-	1.3*	1.5*	1.2*
Sample	**Ba**	**Bi**	**Cd**	**Cr**	**Hf**	**Mn**	**Mo**	**Nb**	**Pb**	**Ta**	**Tl**	**Sb**	**Sn**	**Zr**
no	**[nM]**	**[nM]**	**[nM]**	**[nM]**	**[nM]**	**[nM]**	**[nM]**	**[nM]**	**[nM]**	**[nM]**	**[nM]**	**[nM]**	**[nM]**	**[nM]**
14-5113	5.11	LOD	LOD	3.64	LOD	21.3	25.1	0.607	LOD	LOD	LOD	24.5	LOD	0.362
14-5188	10.1	0.272	0.245	3.59	LOD	13.3	114	2.16	1.78	3.06	LOD	23.5	1.43	1.23
14-5212	10.5	0.298	0.235	3.94	LOD	9.66	124	3.55	1.70	3.34	LOD	26.0	1.39	1.57
14-5253	9.32	0.231	0.155	4.50	LOD	12.9	114	1.07	LOD	1.66	0.883	25.6	1.15	0.994
14-5332	10.6	0.250	0.105	2.60	LOD	10.2	110	0.509	LOD	LOD	LOD	24.8	1.18	1.37
14-5371	LOD	LOD	LOD	LOD	LOD	13.7	8.68	LOD	LOD	LOD	LOD	LOD	LOD	LOD
14-5389	9.25	0.238	0.125	3.96	LOD	10.6	116	0.403	LOD	LOD	LOD	24.2	1.22	1.10
15-5039	7.51	0.239	0.140	3.63	LOD	10.6	130	5.74	LOD	6.30	LOD	25.9	1.62	1.62
15-5199	8.32	0.260	0.0916	14.1	LOD	11.3	39.3	0.583	LOD	LOD	LOD	LOD	1.07	1.26
15-5259	8.84	0.293	LOD	26.6	LOD	19.4	25.3	0.328	LOD	LOD	LOD	LOD	2.10	0.827
15-5346	5.35	0.191	LOD	20.5	LOD	15.8	20.8	0.971	LOD	LOD	LOD	LOD	1.83	0.708
15-5401	5.79	0.300	0.299	8.48	LOD	12.7	19.9	3.39	LOD	2.29	LOD	LOD	2.44	0.898
15-5454	9.55	0.246	0.105	13.6	LOD	30.3	20.0	0.409	1.70	LOD	LOD	LOD	1.12	2.42
16-5080	8.89	0.249	LOD	2.67	LOD	12.8	2.77	0.238	LOD	LOD	LOD	LOD	1.13	1.13
16-5146	LOQ*	LOD*	LOD*	37.7	0.195	38.2	8.95	0.394	LOD*	LOQ*	LOD	2.80	LOD*	LOD*
16-5194	LOQ*	LOD*	LOD*	9.42	LOQ*	11.8	6.78	0.394	LOD*	LOQ*	LOD	1.05	LOD*	LOD*
17-5059	LOQ*	LOD*	LOD*	11.4	LOD*	21.9	0.561	LOD*	LOD*	LOD*	LOD	0.0323	LOD*	LOD*
17-5216	LOQ*	LOD*	LOD*	7.43	LOD*	4.14	7.35	LOD*	LOD*	LOD*	-	1.01	LOD*	LOD*
17-5284	LOD*	LOD*	LOD*	6.23	LOD*	7.06	9.48	LOD*	LOD*	LOD*	-	LOD*	LOD*	LOD*

*Limit of detection (LOD) and limit of quantification (LOQ) for samples analysed in 2017.

Table D.9. Rare earth element concentrations in nM from Well HE-44 liquid-phase samples.

Detection Limit	0.107	1.38	0.0329	0.615	0.0636	10.6	0.174	0.0720	1.77	0.0347	0.0710	0.0333	0.220	1.81	1.28	1.91
[nM]	0.0076*	0.0010*	0.0005*	0.0008*	0.0019*	0.0115*	4.30*	0.0054*	0.0005*	0.0020*	0.0006*	0.0007*	0.0005*	0.0006*	3.74*	0.0005*
Quantification Limit	0.0253*	0.0034*	0.0018*	0.0026*	0.0062*	0.0383*	14.34*	0.0179*	0.0016*	0.0068*	0.0019*	0.0024*	0.0017*	0.0021*	12.5*	0.0016*
Uncertainty at 95% C.I. [%]	1.0	1.0	0.86	1.1	0.75	1.0	0.81	0.86	1.0	1.0	1.0	0.70	0.92	1.1	0.92	1.1
	1.0*	0.53*	1.1*	0.83*	1.3*	0.49*	2.4*	1.8*	1.2*	0.86*	2.1*	1.4*	098*	0.25*	0.88*	0.68*
Sample no	**Ce [nM]**	**Er [nM]**	**Eu [nM]**	**Dy [nM]**	**Gd [nM]**	**Ho [nM]**	**In [nM]**	**La [nM]**	**Lu [nM]**	**Nd [nM]**	**Pr [nM]**	**Sm [nM]**	**Tb [nM]**	**Tm [nM]**	**U [nM]**	**Yb [nM]**
14-5113	0.0985	LOD	LOD	LOD	LOD	LOD	LOD	LOD	LOD	0.0639	LOD	LOD	LOD	LOD	LOD	LOD
14-5188	0.512	LOD	0.315	LOD	0.317	LOD	LOD	0.451	LOD	0.313	0.326	0.303	0.300	LOD	LOD	LOD
14-5212	0.562	LOD	0.302	LOD	0.261	LOD	LOD	0.480	LOD	0.384	0.330	0.277	0.289	LOD	LOD	LOD
14-5253	0.255	LOD	0.0757	LOD	0.0960	LOD	LOD	0.211	LOD	0.0984	0.100	0.114	LOD	LOD	LOD	LOD
14-5332	0.252	LOD	0.0809	LOD	0.0897	LOD	LOD	0.198	LOD	0.0714	0.0915	0.102	LOD	LOD	LOD	LOD
14-5371	LOD	LOD	LOD	LOD	LOD	LOD	LOD	LOD	LOD	LOD	LOD	LOD	LOD	LOD	LOD	LOD
14-5389	0.238	LOD	0.0783	LOD	0.0642	LOD	LOD	0.207	LOD	0.116	0.908	0.0911	LOD	LOD	LOD	LOD
15-5039	0.238	LOD	0.0750	LOD	0.0757	LOD	LOD	0.225	LOD	0.149	0.101	0.0971	LOD	LOD	LOD	LOD
15-5199	0.227	LOD	0.0954	LOD	0.0655	LOD	LOD	0.206	LOD	0.126	0.0937	0.0898	LOD	LOD	LOD	LOD
15-5259	0.138	LOD	LOD	LOD	LOD	LOD	LOD	0.456	LOD	0.0395	LOD	LOD	LOD	LOD	LOD	LOD
15-5346	LOD	LOD	LOD	LOD	LOD	LOD	LOD	LOD	LOD	LOD	LOD	LOD	LOD	LOD	LOD	LOD
15-5401	0.110	LOD	0.0510	LOD	LOD	LOD	0.412	0.101	LOD	0.0742	0.0795	0.0486	LOD	LOD	LOD	LOD
15-5454	0.428	LOD	0.0888	LOD	0.0871	LOD	LOD	0.288	LOD	0.205	0.108	0.0951	LOD	LOD	LOD	LOD
16-5080	0.233	LOD	0.0836	LOD	0.0897	LOD	LOD	0.212	LOD	0.145	0.0994	0101	LOD	LOD	LOD	LOD
16-5146	LOD*	LOQ*	0.0039	0.0040	LOQ*	LOQ*	LOD*	LOQ*	0.0017	LOQ*	0.0046	0.0047	0.0031	LOQ*	LOD*	LOQ*
16-5194	LOD*	LOD*	LOQ*	LOD*	LOD*	LOD*	LOD*	LOQ*	LOD*	LOQ*	0.0025	LOD*	LOD*	LOD*	LOD*	LOD*
17-5059	LOD*	LOQ*	0.0043	0.0034	LOQ*	LOQ*	LOD*	LOQ*	0.0017	LOQ*	0.0050	0.0030	0.0031	LOQ*	LOD*	LOQ*
17-5216	0.992	LOD*	LOD*	LOD*	LOD*	LOD*	LOD*	0.576	LOD*	0.219	LOD*	LOD*	LOD*	LOD*	-	LOD*
17-5284	0.946	LOD*	LOD*	LOD*	LOD*	LOD*	LOD*	0.543	LOD*	0.202	LOD*	LOD*	LOD*	LOD*	-	LOD*

*Limit of detection (LOD) and limit of quantification (LOQ) for samples analysed in 2017.

E Appendix

Evaluation and refinement of thermodynamic databases for mineral carbonation

Martin Voigt, Chiara Marieni, Deirdre E. Clark, Sigurður R. Gíslason, and Eric H. Oelkers

Energy Procedia 146, 81–91, 2018.
doi.org/10.1016/j.egypro.2018.07.012

Available online at www.sciencedirect.com

ScienceDirect

Energy Procedia 146 (2018) 81–91

Energy Procedia

www.elsevier.com/locate/procedia

International Carbon Conference 2018, ICC 2018, 10–14 September 2018, Reykjavik, Iceland

Evaluation and refinement of thermodynamic databases for mineral carbonation

Martin Voigt[a,*], Chiara Marieni[b], Deirdre E. Clark[a], Sigurður R. Gíslason[a], Eric H. Oelkers[a,b,c]

[a]*Institute of Earth Sciences, University of Iceland, Sturlugötu 7, 101 Reykjavík, Iceland*
[b]*Géosciences Environnement Toulouse (GET) - CNRS, 14 Avenue Édouard Belin, 31400 Toulouse, France*
[c]*Earth Sciences, UCL, Gower Street, London, United Kingdom*

Abstract

Thermodynamic models are often used to quantify fluid-rock interactions. The validity of such models critically depends on the accuracy of the thermodynamic database used. This study evaluated the quality of existing PHREEQC databases (*phreeqc.dat*, *llnl.dat*, and *core10.dat*) through the analysis of mineral saturation states for various carbonates, sulfur-containing minerals, silicates, and hydroxides. The comparison between data from available equilibrated dissolution-precipitation experiments and predicted saturation states reveals: i) systematic deviations when using *phreeqc.dat* at temperatures higher than ~ 90 °C; ii) a lack of direct solubility measurements of numerous sulfide and silicate minerals; iii) systematic solubility underestimates for kaolinite and brucite. To address these issues the *carbfix.dat* database was created based on the *core10.dat* database, revising several mineral solubilities and aqueous species stabilities to improve our ability to model fluid-rock interactions during basalt-hosted mineral carbonation efforts.

Selection and peer-review under responsibility of the publication committee of the International Carbon Conference 2018.

Keywords: Geochemistry; Thermodynamics; Solubility; Speciation; Databases; Carbon sequestration

1. Introduction

Geochemical modelling is widely used to quantify chemical reactions occurring between fluids and solid phases over a wide range of temperatures and pressures in the Earth. For example, carbon storage efforts in basalt rely on

* Corresponding author. Tel.: +354 525 4274.
E-mail address: martinvoigt@hi.is

1876-6102
Selection and peer-review under responsibility of the publication committee of the International Carbon Conference 2018.
10.1016/j.egypro.2018.07.012

CO_2-water-basalt interactions to fix CO_2 as stable carbonate minerals [1,2]. To better understand such processes thermodynamic models are often used, however the quality of model results depends critically on the quality of the chosen thermodynamic database [3]. Over the past decades a number of thermodynamic databases have been created and compiled for different geochemical modelling codes such as EQ3/6 [4], WATCH [5], SUPCRT92 [6], PHREEQC [7], Geochemist's Workbench [8], Visual MINTEQ [9], TOUGHREACT [10,11], CHNOSZ [12], and GEMS [13,14]. This has enabled predictions of mineral solubility and aqueous solute speciation in an assortment of geochemical systems. Nevertheless, it is an essential step to evaluate the databases as new and/or improved thermodynamic data are continuously published. Given this, Gysi and Stefansson [15] and Aradóttir et al. [16] evaluated and compiled thermodynamic datasets of pertinent minerals for CO_2 mineral sequestration in basalts. Aradóttir et al. [16] created a new database in the TOUGHREACT format based on the EQ3/6 database and SUPCRT92, while Gysi and Stefansson [15] based their work on the *phreeqc.dat* database in PHREEQC.

In this study, this effort is revisited by focusing on mineral saturation states. Mineral saturation states are key parameters in geochemical studies and indicate how far a solution is from thermodynamic equilibrium with respect to a certain mineral. The saturation state is defined as $\Omega \equiv Q/K_{SP}$, where K_{SP} is the equilibrium constant of the mineral dissolution reaction, and Q is the corresponding reaction quotient of this reaction, calculated from the activities of all species involved in the dissolution reaction. At equilibrium, $Q = K_{SP}$ so that $\Omega = 1$. The saturation index, defined as $SI \equiv \log_{10} \Omega$, is used in many cases instead of Ω (e.g. in PHREEQC), so that at equilibrium $SI = 0$. A saturation index greater than zero indicates that an aqueous solution is supersaturated with a specific mineral, and $SI < 0$ indicates that the aqueous solution is undersaturated with respect to the mineral. The interpretation of saturation states and indices can be complicated by various factors; for example, a positive SI does not necessarily imply that the mineral will precipitate from the solution, as the slow precipitation kinetics may inhibit the precipitation, or favor precipitation of another mineral. Nevertheless, these parameters have proven to be useful indicators of equilibrium or disequilibrium in natural environments.

To evaluate the quality of predicted mineral saturation states, we calculated the saturation indices for sets of laboratory experiments in which thermodynamic equilibration between aqueous solutions and one or more minerals was likely achieved, and analyzed the accuracy, precision, as well as systematic deviations of predicted SI from zero. The PHREEQC software package, version 3 [7], was used together with different popular databases to carry out these thermodynamic calculations. Furthermore, a new database, *carbfix.dat*, was created, modifying and extending existing databases.

2. Thermodynamic databases used for evaluations

Several thermodynamic databases are available for PHREEQC, for which the standard state for solid phases and H_2O is the pure phase, while a hypothetical 1 mol/kg aqueous solution referenced to infinite dilution is chosen for unit activity of aqueous species, both at the temperature and pressure of interest.

The default PHREEQC database *phreeqc.dat* is derived from PHREEQE [17] and contains thermodynamic data for aqueous species and minerals relevant to natural fluid-rock interactions. Most equilibrium constants (K or $\log K$) in this database are extrapolated to temperatures other than 25 °C assuming that the enthalpy of reaction ($\Delta_r H$) does not vary with temperature (i.e. using the Van 't Hoff equation). Changes in $\Delta_r H$ are negligible for small temperature changes, but not so for larger temperature changes, so that calculations using *phreeqc.dat* become less reliable with increasing temperature.

The *llnl.dat* database for PHREEQC contains the vast amount of thermodynamic data compiled at the Lawrence Livermore National Laboratory for the *thermo.com.V8.R6.230* database of Geochemist's Workbench [7]. Many of the equilibrium constants in this database were calculated from thermodynamic properties of minerals and aqueous species using the SUPCRT92 software package [6]. For aqueous species, revised Helgeson-Kirkham-Flowers (HKF) equations [18,19] are used together with parameters regressed by a number of authors [e.g. 18,20–22] using a large set of experimental data that was available at that time. Similarly, mineral data are described by equations given in [23] and regressed data based on numerous experimental data. The resulting equilibrium constants are parameterized as a function of temperature in the *llnl.dat* database, allowing calculations over a larger temperature range compared to *phreeqc.dat*.

The *core10.dat* database is based on *llnl.dat*, but contains several modifications and improvements [24]. This database was developed with the application to icy world interiors in mind, but is applicable to other geochemical settings as well due to its similarity to *llnl.dat*. Importantly, it corrects several erroneous data, only contains data for which analytical expressions for equilibrium constants were available (as opposed to assumptions of constant $\Delta_r H°$ or constant K), and only contains phases and species for which molar volumes were available, allowing PHREEQC to estimate the pressure dependence of equilibrium constants.

2.1. The CarbFix database for PHREEQC

In this study, a new thermodynamic database for PHREEQC, *carbfix.dat*, was created based on the existing *core10.dat* database [24]. Compared to *core10.dat*, it contains additional mineral solubilites and aqueous species stability constants. Furthermore, selected mineral solubilites were revised based on the results of the evaluations presented below, and a typographical error was corrected in the former database (the second parameter of the analytical expression for the solubility product of saponite-Fe-Fe should read '-1.630e-1' instead of '-1.630-1').

Minerals added into *carbfix.dat* include 18 zeolite group minerals, whose thermodynamic properties were taken from Neuhoff [25]. The equilibrium constants for the dissolution reactions of these minerals were calculated using thermodynamic data for aqueous species taken from the OBIGT and SUPCRTBL thermodynamic databases together with the CHNOSZ package for the software R [12,26]. As these databases and the software package are based on SUPCRT92, these newly added mineral solubilites are expected to be internally consistent with the other data in *core10.dat*. The equilibrium constants calculated by CHNOSZ were fit to the analytical expression form of PHREEQC using the standard non-linear regression techniques in Wolfram Mathematica, and molar volumes were taken directly from Neuhoff [25]. Furthermore, the thermodynamic properties of ferro-actinolite and ankerite were taken from Holland and Powell [27] and integrated into the database using the same procedure. The solubilites of dolomite and siderite were re-calibrated using experimental data as explained in section 3.

Several metal-carbonate aqueous complexes were added to or revised in *carbfix.dat*. The parameters used to calculate the specific volumes of these species with a Redlich-type equation were taken from the OBIGT and SUPCRTBL databases. The equilibrium constant for formation of $CaHCO_3^+$ was taken from *llnl.dat*, for $NaCO_3^-$ and $NaHCO_3$ from Stefánsson et al. [28], for $MgCO_3$ and $MgHCO_3^+$ from Stefánsson et al. [29], and for $NaSO_4^-$ from McCollum and Shock [30] using CHNOSZ. Furthermore, the equilibrium constant for the formation of $Al(OH)_2^+$ was added from *llnl.dat* and the stability of the $AlH_3SiO_4^{2+}$ complex was parameterized using data of Pokrovski et al. [31]. Using CHNOSZ, stabilities and specific volumes of $AlSO_4^+$ and $NaAl(OH)_4$ [32], $Fe(OH)_2^+$, $Fe(OH)_3$, $Fe(OH)_4^-$, $Fe(OH)_2$, $Fe(OH)_3^-$, HClO, $HClO_2$, HS_2O_3, and KOH [33] were added to the database as well.

The resulting latest version of the *carbfix.dat* database is available at GitHub at the address https://github.com/CarbFix/carbfix.dat where the version described in this article can be accessed from release v1.0.0, or alternatively at http://carbfix.com.

3. Evaluation of predicted saturation indices

Mineral saturation indices (SI) were calculated using the databases described above for aqueous solutions used in laboratory experiments during which equilibration between the fluid and one or more minerals was approached. Calculations were carried out using the originally reported fluid compositions (such as pH, total aqueous concentrations of elements or species, temperature, etc.) to avoid dependence of the results on other thermodynamic data.

All experimental studies used for these evaluations were originally performed to determine mineral solubilites. However, as the achievement of thermodynamic equilibrium cannot be proven for these experimental studies, disequilibrium would lead to deviations of calculated SI from zero. Most studies aimed to achieve equilibrium from under- as well as supersaturation by carrying out both dissolution and precipitation experiments. This approach limits systematic errors in calculated solubilites and helps to estimate the uncertainties in experimentally determined parameters. If equilibration is attained only from one direction, the distance from equilibrium is difficult to estimate, as mineral-fluid reactions might proceed at rates significantly slower than changes observable over reasonable timespans and experimental and analytical uncertainties. Errors in the thermodynamic data or models represent further

potential uncertainties. Errors in solubilities (K_{SP}) directly affect calculated SI and thus represent a prime source for errors, but many calculations also depend on other equilibrium constants (e.g., of reactions between different aqueous species). Oversimplifications in the thermodynamic model, such as the approximation of activity coefficients or the assumption of a temperature-invariant $\Delta_r H$ (like in the case of many reactions in *phreeqc.dat*) may also lead to significant systematic errors, as illustrated below. Finally, experimental and analytical uncertainties lead to (mostly random) variability in calculated SI.

Except for disequilibrium, all potential reasons mentioned above for deviations of SI from zero equally apply when SI are calculated in geochemical studies. If errors due to disequilibrium in the employed experimental studies are small compared to the other sources of errors (i.e. errors in the thermodynamic database or model, and analytical uncertainties), the deviation from zero and the variability of the calculated SI for these experimental studies indicate the magnitude the uncertainty in calculated SI. Therefore, we calculated the mean saturation index ($\overline{SI}$) and the standard deviation (σ) for all experimental datasets as measures for the accuracy and precision of calculated SI, respectively. It should be noted however that some of the experimental datasets used for the evaluations only cover a limited range of temperature, outside of which larger uncertainties may occur as thermodynamic data is often less well constrained at increasing temperatures. Furthermore, most natural systems are chemically more complex than laboratory experiments, which likely leads to larger uncertainties when predicting SI for such systems. Therefore, the uncertainties estimated here should be regarded as minimum estimates of the uncertainties that must be anticipated for modelled SI.

3.1. Carbonate minerals

Due to the importance of carbonate minerals for carbon mineral storage, the quality of SI calculated for the minerals calcite, aragonite, dolomite, magnesite, siderite, and dawsonite was evaluated. From the results (Table 1, Fig. 1), it can be seen that $\overline{SI}_{Calcite}$ deviate by less than 0.097 from zero for all databases at < 90 °C, indicating a high level of accuracy of calculated SI. Standard deviations are equally low (≤ 0.061) in all cases, suggesting that $SI_{Calcite}$ can be predicted with a high level of accuracy and precision in simple, low-temperature fluids. Similarly, the mean SI calculated for aragonite solubility experiments of temperatures up to 90 °C are small (≤ 0.075). Note however, that these aragonite solubility experiments [34,35] were conducted in pure water, so that larger uncertainties are likely for more complex solutions. SI calculated for the high temperature calcite solubility experiments of [36] show larger deviations from zero, but standard deviations remain below 0.169 except for *phreeqc.dat*, for which SI are systematically negative. Similarly, deviations of $SI_{Dolomite}$ and $SI_{Siderite}$ from zero are largest using *phreeqc.dat*, where SI are close to zero at up to 90 °C but become increasingly negative with higher temperatures as shown with siderite in Fig. 2. This behavior can be explained by use of the assumption of constant $\Delta_r H$ for many reactions in *phreeqc.dat*, as explained in section 2. SI calculated using *lllnl.dat* and *core10.dat* for these two minerals, as well as for magnesite and dawsonite, are much closer to zero (Table 1, Fig. 1). However, $\overline{SI}$ for siderite is approximately -0.5, indicating a systematic deviation from zero, and σ for dolomite is relatively large (0.67). Therefore, the parameters for the analytical expressions of the solubilities as a function of temperature were re-calibrated for these two minerals in *carbfix.dat* using the same experimental datasets used for the evaluations [37,38]. The log K_{SP} were fit to the same form of expressions used in these original studies, resulting in

$$\log K_{SP}^{Dolomite} = 29.3854 - \frac{6474.23}{T} - 0.08464\ T \tag{1}$$

$$\log K_{SP}^{Siderite} = 349.432 - \frac{13573.8}{T} - 0.0362811\ T - 131.651 \log_{10} T \tag{2}$$

where T is temperature in Kelvin for the dissolution reactions

$$CaMg(CO_3)_2 \rightleftharpoons Ca^{2+} + Mg^{2+} + 2\ CO_3^{2-} \tag{R1}$$

$$FeCO_3 \rightleftharpoons Fe^{2+} + CO_3^{2-} \tag{R2}$$

respectively. It can be seen from Table 1 and Fig. 1 that the SI predicted for these two minerals using *carbfix.dat* are an improvement over the other databases, which can be largely attributed to these re-calibrated solubility expressions. While the SI for dawsonite and magnesite also slightly deviate from zero using *core10.dat*, no re-calibration was necessary as several aqueous species were added to *carbfix.dat* (see section 2.1), improving the SI predicted using the latter database for these two minerals.

Table 1. Experimental studies of mineral solubilities used to in the present study to assess the quality of thermodynamic saturation index calculations using PHREEQC and different databases. The type refers to dissolution (D) and precipitation (P) experiments and N is the number of equilibrated aqueous solutions available in each study. $\overline{SI}$ and σ refer to the sample mean and standard deviation of the saturation indices calculated for the experimental solutions using the different databases, respectively.

Mineral	Formula	Ref.	N	Type	T / °C	pH	phreeqc.dat		llnl.dat		core10.dat		carbfix.dat	
							$\overline{SI}$	σ	$\overline{SI}$	σ	$\overline{SI}$	σ	$\overline{SI}$	σ
Carbonates														
Calcite	$CaCO_3$	[34]	40	D/P	5-50	~ 6	-0.007	0.017	0.020	0.023	0.064	0.017	0.020	0.022
		[35]	141	D/P	0.1-90	~ 6	-0.003	0.045	0.017	0.061	0.097	0.051	0.019	0.061
		[36]	46	D	120-290	5-6	-0.411	0.605	0.170[a]	0.169[a]	0.277	0.179	-0.122	0.118
Aragonite	$CaCO_3$	[35]	205	D/P	0.7-90	6-8	0.001	0.001	0.022	0.029	0.075	0.040	0.023	0.029
Dolomite	$CaMg(CO_3)_2$	[37]	28	D/P	50-250	5-7	-3.337	2.359	-0.047	0.660	-0.030	0.666	-0.004	0.317
Magnesite	$MgCO_3$	[39]	25	D/P	50-200	5-8	-	-	0.078	0.298	0.112	0.310	0.074	0.305
Siderite	$FeCO_3$	[38]	21	D/P	50-250	5-6	-1.469	1.450	-0.484	0.332	-0.512	0.343	-0.005	0.310
Dawsonite	$NaAlCO_3(OH)_2$	[40]	30	D/P	50-200	4-10	-	-	0.238	0.484	0.350	0.441	-0.025	0.431
Sulfur-bearing minerals														
Anhydrite	$CaSO_4$	[41]	103	D	70-300	~ 7	0.100	0.268	0.541	0.399	0.388	0.372	0.377	0.357
		[42]	54	D	100-260	~ 7	-0.034	0.089	0.414	0.273	0.116	0.104	0.116	0.104
		[43]	11	D	65	~ 7	-0.190	0.090	-0.355	0.160	0.080	0.103	-0.383	0.161
Pyrrhotite	FeS	[44]	1	D	25-60	4	-	-	-1.215	-	-1.220	-	-1.220	-
Mackinawite	FeS	[44]	6	D/P	25	3-4	-0.058	0.459	-	-	-	-	-	-
FeS	FeS	[44]	4	P	25	3-4	0.383	0.173	-	-	-	-	-	-
Silicates														
Quartz	SiO_2	[45]	6	D	136-240	7	-0.009	0.016	0.068	0.049	0.066	0.047	0.066	0.047
		[46]	10	D	21-96	7	0.149	0.066	0.128	0.108	0.128	0.108	0.128	0.108
Am. SiO_2	SiO_2	[47]	20	D/P	8-300	7	-0.015	0.041	0.002	0.061	-0.002	0.062	-0.002	0.062
Kaolinite	$Al_2Si_2O_5(OH)_4$	[48]	16	D/P	25	~ 4	0.190	0.100	0.889	0.101	0.900	0.101	0.881	0.100
		[49]	7	D/P	80	~ 3	0.515	0.226	1.443	0.217	1.451	0.216	1.301	0.208
Analcime	$NaAlSi_2O_6 \cdot H_2O$	[50]	60	D/P	25-300	7-10	-	-	0.173	0.416	0.165	0.425	0.017	0.489
Hydroxides														
Gibbsite	$Al(OH)_3$	[51]	10	D/P	25	4-6	0.050	0.079	0.510	0.114	0.599	0.166	0.510	0.114
		[52]	180	D	50	3-9	-0.643	0.260	0.020	0.207	0.044	0.167	-0.017	0.209
Boehmite	AlOOH	[53]	496	D/P	100-290	2-10	-	-	-0.261	0.978	-0.324	1.181	-0.356	1.215
Brucite	$Mg(OH)_2$	[54]	13	D	22	9-11	-	-	0.693	0.058	0.693	0.058	0.693	0.058

[a]Aqueous solution densities necessary for the calculation of SI for the experimental data were calculated using *core10.dat*, as *llnl.dat* does not allow the calculation of densities.

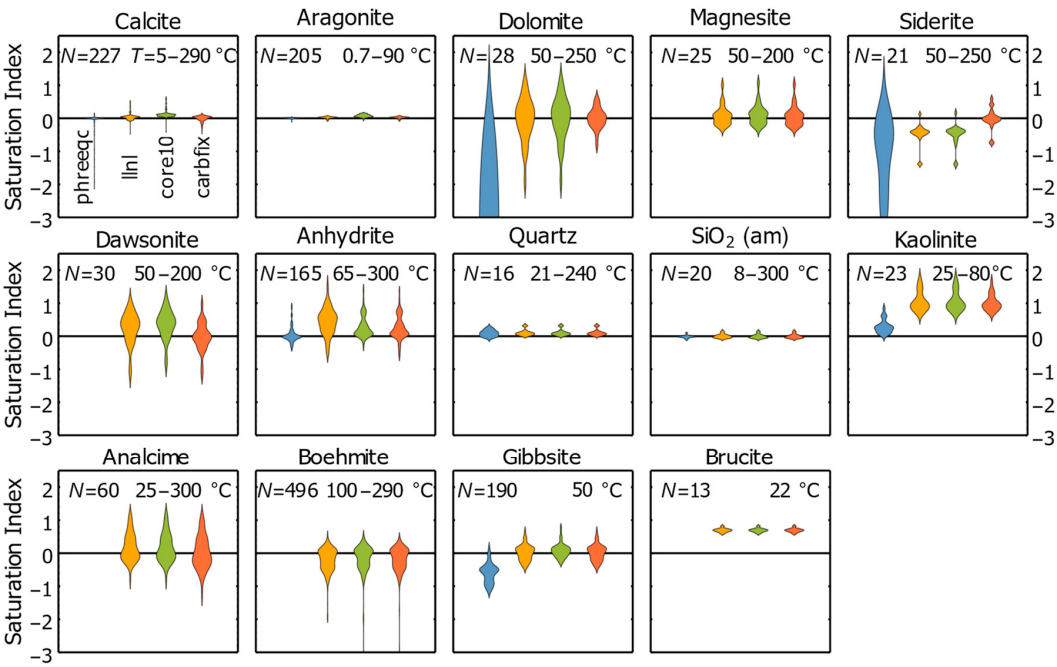

Fig. 1. Plot of the distributions of saturation indices (SI) calculated for aqueous solutions of studies that experimentally determined mineral solubilities. Thermodynamic SI calculations were carried out with PHREEQC using different databases shown in different colors as defined in the upper left-hand plot. The plotted distributions correspond to smoothed histograms, i.e. kernel density estimations of the probability density function.

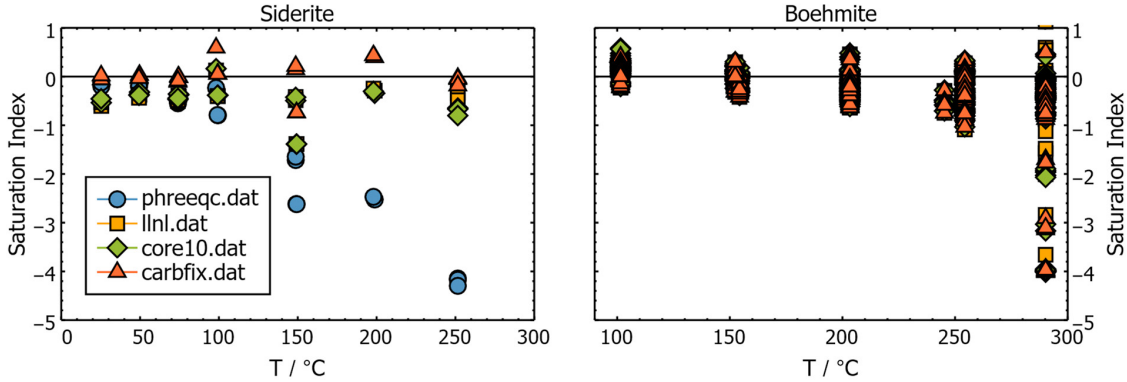

Fig. 2. Plots of saturation indices (SI) calculated for aqueous solutions of experimentally determined the solubilites of siderite (*left*) and boehmite (*right*) as a function of temperature. Thermodynamic SI calculations were carried out with PHREEQC using different databases shown in different colors as defined in the left-hand plot.

3.2. Sulfur-bearing minerals

A large number of experimental solubility experiments are available for the Ca-sulfate anhydrite (see Table 1). Mean SI calculated for data from the three experimental studies deviate from zero by less than 0.38, and standard deviations are smaller than 0.4, suggesting a reasonable accuracy and precision of the calculations over the temperature range 65-300 °C for simple aqueous solutions. Among the four tested databases, *phreeqc.dat* gives the best results and *llnl.dat* shows the largest variability.

On the other hand, the sulfide minerals are severely under-represented within the PHREEQC suite of databases due to the difficulties associated with the direct measurement of their solubility because of: i) their sluggish dissolution kinetics, which often prevents attainment of equilibrium at low temperatures; ii) the requirement of low redox potentials, which poses challenges to experimental and analytical techniques; iii) the potential release of toxic H_2S gas, which requires special experimental facilities; and iv) the electron configuration of some iron sulfide minerals such as pyrite which prevents solubility measurements at ambient temperatures [55]. Nevertheless, we calculated SI for pyrrhotite, mackinawite, and ferrous sulfide using experimental data of Berner [44] (Table 1). The single pyrrhotite experiment suggests an overestimation of its solubility in all three databases containing data for this mineral (*llnl.dat, core10.dat, carbfix.dat*), whereas data in *phreeqc.dat* for mackinawite and ferrous sulfide are in good agreement with the experimental data. However, no conclusive statement can be made about the accuracy and precision of the mineral solubilities of the sulfide minerals in any of these databases due to the lack of direct solubility measurements. These equilibrium constants are ultimately derived from indirect measurements (e.g., calorimetric measurements of the mineral properties).

3.3. Silicate minerals

Saturation states calculated for solubility experiments of quartz and amorphous SiO_2 are close to zero for all databases even at high temperatures (Table 1, Fig. 1), indicating a high degree of reliability of these SI, which can be explained by the relatively simple aqueous speciation of Si. The temperature dependence of the solubilities of these two minerals are widely used as geothermometers to calculate equilibration temperatures of natural fluids [45–47]. Thus, differences between such calculated equilibrium temperatures and measured experimental temperatures indicate minimum uncertainties that are to be expected from geothermometric calculations of natural fluids (assuming similar speciation and analytical uncertainties). Using *carbfix.dat*, we calculated the best-fit equilibrium temperatures (i.e. assuming SI=0) from the measured experimental SiO_2 concentrations within the temperature range of 8-300 °C; on average, they deviate from the measured experimental temperatures by 3 °C, with a standard deviation of 11 °C.

Direct solubility measurements of more complex silicate minerals are very limited, which is mainly due to 1) the sluggish dissolution/precipitation kinetics of many silicate minerals at low temperatures and 2) complications caused by synthesis and solid-solution formation, especially for sheet silicates like clays. Nevertheless, some experimental solubility measurements are available for kaolinite and analcime. For the former mineral, SI calculated from the experimental data of May et al. [48] and Nagy et al. [49] are close to zero for *phreeqc.dat* (Table 1, Fig. 1), whereas calculations with the other three databases are offset from zero by ~ 0.9 on average. However, it is unclear whether this difference is due to an incorrect solubility product (K_{SP}) or due to erroneous stability constants for aqueous alumina species, so that this solubility constant was not changed in *carbfix.dat*. It should be noted that all experiments were carried out at 25 to 80 °C, and that *phreeqc.dat* only contains a constant $\Delta_r H$ for the kaolinite dissolution reaction, so that calculated saturation indices are likely to show systematic errors at higher temperatures. Measured solubilities of analcime [50] at temperatures of up to 300 °C are reproduced relatively accurately by the three databases containing data for this mineral, as signified by the $\overline{\overline{SI}}$ close to zero (≤ 0.173, Table 1). However, the standard deviations are higher (~ 0.4), indicating that care must be taken when interpreting such saturation indices.

3.4. Hydroxide minerals

In general, aluminum hydroxide minerals are of great interest as Al is a major component in many natural rocks that interact with fluids, such as in geothermal reservoirs. Direct solubility measurements have been carried out for gibbsite and boehmite [51–53], and $\overline{SI}$ calculated for these data range from ~ 0.1 to 0.6 (Table 1, Fig. 1), while standard

deviations are of similar magnitude (gibbsite) or slightly larger (boehmite). For the latter mineral, the errors of calculated SI significantly increase above 250 °C as shown in Fig. 2, which is likely caused by the increased errors in extrapolated aqueous speciation constants in thermodynamic databases.

The solubility of brucite is of importance because of its similarity to more complex clay minerals for which direct measurements are complicated by the complex chemistry and solid solutions [56], in addition to its use as backfill material in nuclear waste storage sites [54]. Brucite solubilites measured at room temperature [54] are systematically higher (~ 0.7 in SI) than indicated by *llnl.dat, core10.dat,* and *carbfix.dat* (all containing the same constant), but show a lower standard deviation. This implies, similar to silicate minerals, that uncertainties in saturation state calculations for these minerals must be considered. No correction of solubility products was attempted for these phases, as it is unclear whether errors are caused by aqueous complex stability constants or the solubility products themselves.

4. Conclusions

Saturation indices were calculated for aqueous solutions that directly determined the solubility of various minerals. Calculations were carried out with PHREEQC using its different thermodynamic databases to assess the quality of such predictions. The results reveal varying degrees of deviation of the predicted saturation indices from zero, which may be caused by errors in the thermodynamic database or model, analytical and experimental uncertainties, or departures from equilibrium in the experiments. While the *phreeqc.dat* database reproduces low-temperature data relatively well, systematic errors appear at higher temperatures for many minerals due to the assumption of a constant enthalpy of reaction ($\Delta_r H$). For carbonate minerals, the fit is best for calcite and aragonite, while dolomite, magnesite, siderite and dawsonite SI deviate from zero by approximately up to 1 to 2. A similar degree of variability can be seen for anhydrite, analcime, and the alumina hydroxide minerals gibbsite and boehmite. Experimentally determined quartz and amorphous silica solubilities are reproduced well by all databases, and geothermometric (equilibrium) temperatures calculated from the same data deviate from measured experimental temperatures by 3 °C on average, with a standard deviation of 11 °C. Systematic underestimation of solubilities by approximately one SI are seen for kaolinite and brucite. A new database for PHREEQC, *carbfix.dat*, was created based on the *core10.dat* database of Neveu et al. [24], adding several additional mineral solubilites and aqueous species stabilities relevant for fluid-rock interactions in basalt-hosted carbon sequestration efforts, as well as improving several equilibrium constants based on available data.

In general, the variability of calculated SI and their deviance from zero indicate that care must be taken when interpreting thermodynamically calculated SI for natural fluids. The variability shown in this study should be regarded as a minimum estimate of uncertainty, as fluid compositions are commonly much more complex in natural systems, so that errors in the stabilities of aqueous species stabilities are amplified. Furthermore, the experimental data used for our quality assessments do not span the full range of temperature and pressure that occur in natural systems. Therefore, larger errors likely prevail under such conditions since many thermodynamic constants are extrapolated over a wide range of conditions [3]. Moreover, for many of the more complex minerals (especially sheet silicates such as clays, and zeolites), no direct solubility measurements are available; consequently, solubilites in thermodynamic databases are calculated indirectly from thermodynamic properties of the minerals and aqueous species, potentially introducing large errors that are difficult to estimate. This highlights the need for further experimental studies directly measuring the solubilites of such minerals over a wide range of conditions (temperature, pressure, composition) along with the evaluation of solid solution properties. Finally, the creation of a fully internally consistent thermodynamic database for a large set of minerals and aqueous species, including uncertainties of parameters evaluated using statistical methods during the regression process, is yet to be achieved. Although such a database is available for petrological purposes [27], its applicability to low- to medium-temperature fluids of complex composition is currently limited due to the lack of many aqueous species in the database.

Acknowledgements

This research has been carried out within the CarbFix2 project that has received funding from the European Union's Horizon 2020 research and innovation program under grant agreement No 764760.

References

[1] Matter J.M., M. Stute, S.Ó. Snæbjörnsdottir, E.H. Oelkers, S.R. Gislason, E.S. Aradottir, B. Sigfusson, I. Gunnarsson, H. Sigurdardottir, E. Gunnlaugsson, G. Axelsson, H.A. Alfredsson, D. Wolff-Boenisch, K. Mesfin, D.F. de la R. Taya, J. Hall, K. Dideriksen, and W.S. Broecker. "Rapid carbon mineralization for permanent disposal of anthropogenic carbon dioxide emissions" *Science* 352 (2016): 1312–4, doi:10.1126/science.aad8132.

[2] Oelkers E.H., S.R. Gislason, and J. Matter. "Mineral Carbonation of CO_2" *Elements* 4 (2008): 333–7, doi:10.2113/gselements.4.5.333.

[3] Oelkers E.H., P. Bénézeth, and G.S. Pokrovski. "Thermodynamic Databases for Water-Rock Interaction" *Reviews in Mineralogy and Geochemistry* 70 (2009): 1–46, doi:10.2138/rmg.2009.70.1.

[4] Daveler S.A., and T.J. Wolery. "EQPT, a data file preprocessor for the EQ3/6 software package: User's guide and related documentation (version 7.0)" Livermore, California, Lawrence Livermore National Laboratory (1992).

[5] Arnórsson S., S. Sigurdsson, and H. Svavarsson. "The chemistry of geothermal waters in Iceland. I. Calculation of aqueous speciation from 0° to 370 °C" *Geochimica et Cosmochimica Acta* 46 (1982): 1513–32, doi:10.1016/0016-7037(82)90311-8.

[6] Johnson J.W., E.H. Oelkers, and H.C. Helgeson. "SUPCRT92: A software package for calculating the standard molal thermodynamic properties of minerals, gases, aqueous species, and reactions from 1 to 5000 bar and 0 to 1000 °C" *Computers & Geosciences* 18 (1992): 899–947, doi:10.1016/0098-3004(92)90029-Q.

[7] Parkhurst D.L., and C.A.J. Appelo. "Description of input and examples for PHREEQC version 3 - A computer program for speciation, batch-reaction, one-dimensional transport, and inverse geochemical calculations" in *U.S. Geological Survey techniques and methods, modeling techniques, groundwater*, Denver, Colorado, U.S. Geological Survey (2013).

[8] Bethke C.M., B. Farrell, and S. Yeakel. "The Geochemist's Workbench® Release 12 - GWB Essentials Guide" (2018).

[9] Gustafsson J.P. "Visual MINTEQ version 3.1" (2018), https://vminteq.lwr.kth.se/download/.

[10] Xu T., E. Sonnenthal, N. Spycher, and K. Pruess. "TOUGHREACT—A simulation program for non-isothermal multiphase reactive geochemical transport in variably saturated geologic media: Applications to geothermal injectivity and CO_2 geological sequestration" *Computers & Geosciences* 32 (2006): 145–65, doi:10.1016/j.cageo.2005.06.014.

[11] Xu T., N. Spycher, E. Sonnenthal, G. Zhang, L. Zheng, and K. Pruess. "TOUGHREACT Version 2.0: A simulator for subsurface reactive transport under non-isothermal multiphase flow conditions" *Computers & Geosciences* 37 (2011): 763–74, doi:10.1016/j.cageo.2010.10.007.

[12] Dick J.M. "Calculation of the relative metastabilities of proteins using the CHNOSZ software package" *Geochemical Transactions* 9 (2008): 10, doi:10.1186/1467-4866-9-10.

[13] Kulik D.A., T. Wagner, S.V. Dmytrieva, G. Kosakowski, F.F. Hingerl, K.V. Chudnenko, and U.R. Berner. "GEM-Selektor geochemical modeling package: revised algorithm and GEMS3K numerical kernel for coupled simulation codes" *Computational Geosciences* 17 (2013): 1–24, doi:10.1007/s10596-012-9310-6.

[14] Wagner T., D.A. Kulik, F.F. Hingerl, and S.V. Dmytrieva. "GEM-Selektor geochemical modeling package: TSolMod library and data interface for multicomponent phase models" *The Canadian Mineralogist* 50 (2012): 1173–1195.

[15] Gysi A.P., and A. Stefánsson. "CO_2–water–basalt interaction. Numerical simulation of low temperature CO_2 sequestration into basalts" *Geochimica et Cosmochimica Acta* 75 (2011): 4728–51, doi:10.1016/j.gca.2011.05.037.

[16] Aradóttir E.S.P., E.L. Sonnenthal, and H. Jónsson. "Development and evaluation of a thermodynamic dataset for phases of interest in CO_2 mineral sequestration in basaltic rocks" *Chemical Geology* 304–305 (2012): 26–38, doi:10.1016/j.chemgeo.2012.01.031.

[17] Parkhurst D.L., D.C. Thorstenson, and L.N. Plummer. "PHREEQE—A computer program for geochemical calculations" Denver, Colorado, U.S. Geological Survey (1980).

[18] Tanger J.C., and H.C. Helgeson. "Calculation of the thermodynamic and transport properties of aqueous species at high pressures and temperatures; revised equations of state for the standard partial molal properties of ions and electrolytes" *American Journal of Science* 288 (1988): 19–98, doi:10.2475/ajs.288.1.19.

[19] Shock E.L., E.H. Oelkers, J.W. Johnson, D.A. Sverjensky, and H.C. Helgeson. "Calculation of the thermodynamic properties of aqueous species at high pressures and temperatures. Effective electrostatic radii, dissociation constants and standard partial molal properties to 1000 °C and 5 kbar" *Journal of the Chemical Society, Faraday Transactions* 88 (1992): 803–26, doi:10.1039/FT9928800803.

[20] Shock E.L., and H.C. Helgeson. "Calculation of the thermodynamic and transport properties of aqueous species at high pressures and temperatures: Correlation algorithms for ionic species and equation of state predictions to 5 kb and 1000 °C" *Geochimica et Cosmochimica Acta* 52 (1988): 2009–36, doi:10.1016/0016-7037(88)90181-0.

[21] Shock E.L., H.C. Helgeson, and D.A. Sverjensky. "Calculation of the thermodynamic and transport properties of aqueous species at high pressures and temperatures: Standard partial molal properties of inorganic neutral species" *Geochimica et Cosmochimica Acta* 53 (1989): 2157–83, doi:10.1016/0016-7037(89)90341-4.

[22] Shock E.L., and H.C. Helgeson. "Calculation of the thermodynamic and transport properties of aqueous species at high pressures and temperatures: Standard partial molal properties of organic species" *Geochimica et Cosmochimica Acta* 54 (1990): 915–45, doi:10.1016/0016-7037(90)90429-O.

[23] Helgeson H.C., J.M. Delany, H.W. Nesbitt, and D.K. Bird. "Summary and critique of the thermodynamic properties of rock-forming minerals" *American Journal of Science* 278-A (1978).

[24] Neveu M., S.J. Desch, and J.C. Castillo-Rogez. "Aqueous geochemistry in icy world interiors: Equilibrium fluid, rock, and gas compositions, and fate of antifreezes and radionuclides" *Geochimica et Cosmochimica Acta* 212 (2017): 324–71, doi:10.1016/j.gca.2017.06.023.

[25] Neuhoff P.S. "Thermodynamic Properties and Parageneses of Rock-Forming Zeolites" PhD Thesis Stanford University (2000).

[26] Zimmer K., Y. Zhang, P. Lu, Y. Chen, G. Zhang, M. Dalkilic, and C. Zhu. "SUPCRTBL: A revised and extended thermodynamic dataset and software package of SUPCRT92" *Computers & Geosciences* 90 (2016): 97–111, doi:10.1016/j.cageo.2016.02.013.
[27] Holland T.J.B., and R. Powell. "An improved and extended internally consistent thermodynamic dataset for phases of petrological interest, involving a new equation of state for solids" *Journal of Metamorphic Geology* 29 (2011): 333–83, doi:10.1111/j.1525-1314.2010.00923.x.
[28] Stefánsson A., P. Bénézeth, and J. Schott. "Carbonic acid ionization and the stability of sodium bicarbonate and carbonate ion pairs to 200 °C – A potentiometric and spectrophotometric study" *Geochimica et Cosmochimica Acta* 120 (2013): 600–11, doi:10.1016/j.gca.2013.04.023.
[29] Stefánsson A., P. Bénézeth, and J. Schott. "Potentiometric and spectrophotometric study of the stability of magnesium carbonate and bicarbonate ion pairs to 150 °C and aqueous inorganic carbon speciation and magnesite solubility" *Geochimica et Cosmochimica Acta* 138 (2014): 21–31, doi:10.1016/j.gca.2014.04.008.
[30] McCollom T.M., and E.L. Shock. "Geochemical constraints on chemolithoautotrophic metabolism by microorganisms in seafloor hydrothermal systems" *Geochimica et Cosmochimica Acta* 61 (1997): 4375–91, doi:10.1016/S0016-7037(97)00241-X.
[31] Pokrovski G.S., J. Schott, J.-C. Harrichoury, and A.S. Sergeyev. "The stability of aluminum silicate complexes in acidic solutions from 25 to 150 °C" *Geochimica et Cosmochimica Acta* 60 (1996): 2495–501, doi:10.1016/0016-7037(96)00123-8.
[32] Tagirov B., and J. Schott. "Aluminum speciation in crustal fluids revisited" *Geochimica et Cosmochimica Acta* 65 (2001): 3965–92, doi:10.1016/S0016-7037(01)00705-0.
[33] Shock E.L., D.C. Sassani, M. Willis, and D.A. Sverjensky. "Inorganic species in geologic fluids: Correlations among standard molal thermodynamic properties of aqueous ions and hydroxide complexes" *Geochimica et Cosmochimica Acta* 61 (1997): 907–50, doi:10.1016/S0016-7037(96)00339-0.
[34] Jacobson R.L., and D. Langmuir. "Dissociation constants of calcite and $CaHCO_3^+$ from 0 to 50 °C" *Geochimica et Cosmochimica Acta* 38 (1974): 301–18, doi:10.1016/0016-7037(74)90112-4.
[35] Plummer L.N., and E. Busenberg. "The solubilities of calcite, aragonite and vaterite in CO_2-H_2O solutions between 0 and 90 °C, and an evaluation of the aqueous model for the system $CaCO_3$-CO_2-H_2O" *Geochimica et Cosmochimica Acta* 46 (1982): 1011–40, doi:10.1016/0016-7037(82)90056-4.
[36] Ellis A.J. "The solubility of calcite in sodium chloride solutions at high temperatures" *American Journal of Science* 261 (1963): 259–67, doi:10.2475/ajs.261.3.259.
[37] Bénézeth P., U.-N. Berninger, N. Bovet, J. Schott, and E.H. Oelkers. "Experimental determination of the solubility product of dolomite at 50–253 °C" *Geochimica et Cosmochimica Acta* 224 (2018): 262–75, doi:10.1016/j.gca.2018.01.016.
[38] Bénézeth P., J.L. Dandurand, and J.C. Harrichoury. "Solubility product of siderite ($FeCO_3$) as a function of temperature (25–250 °C)" *Chemical Geology* 265 (2009): 3–12, doi:10.1016/j.chemgeo.2009.03.015.
[39] Bénézeth P., G.D. Saldi, J.-L. Dandurand, and J. Schott. "Experimental determination of the solubility product of magnesite at 50 to 200 °C" *Chemical Geology* 286 (2011): 21–31, doi:10.1016/j.chemgeo.2011.04.016.
[40] Bénézeth P., D.A. Palmer, L.M. Anovitz, and J. Horita. "Dawsonite synthesis and reevaluation of its thermodynamic properties from solubility measurements: Implications for mineral trapping of CO_2" *Geochimica et Cosmochimica Acta* 71 (2007): 4438–55, doi:10.1016/j.gca.2007.07.003.
[41] Blounot C.W., and F.W. Dickson. "The solubility of anhydrite ($CaSO_4$) in NaCl-H_2O from 100 to 450 °C and 1 to 1000 bars" *Geochimica et Cosmochimica Acta* 33 (1969): 227–45, doi:10.1016/0016-7037(69)90140-9.
[42] Dickson F.W., C.W. Blount, and G. Tunell. "Use of hydrothermal solution equipment to determine the solubility of anhydrite in water from 100 °C to 275 °C and from 1 bar to 1000 bars pressure" *American Journal of Science* 261 (1963): 61–78, doi:10.2475/ajs.261.1.61.
[43] Glew D.N., and D.A. Hames. "Gypsum, disodium pentacalcium sulfate, and anhydrite solubilities in concentrated sodium chloride solutions" *Canadian Journal of Chemistry* 48 (1970): 3733–8, doi:10.1139/v70-623.
[44] Berner R.A. "Thermodynamic stability of sedimentary iron sulfides" *American Journal of Science* 265 (1967): 773–85, doi:10.2475/ajs.265.9.773.
[45] Morey G.W., R.O. Fournier, and J.J. Rowe. "The solubility of quartz in water in the temperature interval from 25° to 300° C" *Geochimica et Cosmochimica Acta* 26 (1962): 1029–43, doi:10.1016/0016-7037(62)90027-3.
[46] Rimstidt J.D. "Quartz solubility at low temperatures" *Geochimica et Cosmochimica Acta* 61 (1997): 2553–8, doi:10.1016/S0016-7037(97)00103-8.
[47] Gunnarsson I., and S. Arnórsson. "Amorphous silica solubility and the thermodynamic properties of H_4SiO_4° in the range of 0 ° to 350 °C at P_{sat}" *Geochimica et Cosmochimica Acta* 64 (2000): 2295–307, doi:10.1016/S0016-7037(99)00426-3.
[48] May H.M., D.G. Kinniburgh, P.A. Helmke, and M.L. Jackson. "Aqueous dissolution, solubilities and thermodynamic stabilities of common aluminosilicate clay minerals: Kaolinite and smectites" *Geochimica et Cosmochimica Acta* 50 (1986): 1667–77, doi:10.1016/0016-7037(86)90129-8.
[49] Nagy K.L., A.E. Blum, and A.C. Lasaga. "Dissolution and precipitation kinetics of kaolinite at 80 °C and pH 3: the dependence on solution saturation state" *American Journal of Science* 291 (1991): 649–86.
[50] Wilkin R.T., and H.L. Barnes. "Solubility and stability of zeolites in aqueous solution: I. Analcime, Na-, and K-clinoptilolite" *American Mineralogist* 83 (2015): 746–761, doi:10.2138/am-1998-7-807.
[51] May H.M., P.A. Helmke, and M.L. Jackson. "Gibbsite solubility and thermodynamic properties of hydroxy-aluminum ions in aqueous solution at 25°C" *Geochimica et Cosmochimica Acta* 43 (1979): 861–8, doi:10.1016/0016-7037(79)90224-2.
[52] Wesolowski D.J., and D.A. Palmer. "Aluminum speciation and equilibria in aqueous solution: V. Gibbsite solubility at 50 °C and pH 3–9 in 0.1 molal NaCl solutions (a general model for aluminum speciation; analytical methods)" *Geochimica et Cosmochimica Acta* 58 (1994): 2947–69, doi:10.1016/0016-7037(94)90171-6.

[53] Bénézeth P., D.A. Palmer, and D.J. Wesolowski. “Aqueous high-temperature solubility studies. II. The solubility of boehmite at 0.03 m ionic strength as a function of temperature and pH as determined by in situ measurements” *Geochimica et Cosmochimica Acta* 65 (2001): 2097–111, doi:10.1016/S0016-7037(01)00585-3.
[54] Altmaier M., V. Metz, V. Neck, R. Müller, and T. Fanghänel. “Solid-liquid equilibria of $Mg(OH)_2$(cr) and $Mg_2(OH)_3Cl{\cdot}4H_2O$(cr) in the system Mg-Na-H-OH-Cl-H_2O at 25 °C” *Geochimica et Cosmochimica Acta* 67 (2003): 3595–601, doi:10.1016/S0016-7037(03)00165-0.
[55] Rickard D., and G.W. Luther. “Chemistry of Iron Sulfides” *Chemical Reviews* 107 (2007): 514–62, doi:10.1021/cr0503658.
[56] Wimpenny J., C.A. Colla, Q.-Z. Yin, J.R. Rustad, and W.H. Casey. “Investigating the behaviour of Mg isotopes during the formation of clay minerals” *Geochimica et Cosmochimica Acta* 128 (2014): 178–94, doi:10.1016/j.gca.2013.12.012.

F Appendix

The rapid and cost-effective capture and subsurface mineral storage of carbon and sulfur at the CarbFix2 site

Ingvi Gunnarsson, Edda S. Aradóttir, Eric H. Oelkers, Deirdre E. Clark, Magnús Þór Arnarson, Bergur Sigfússon, Sandra Ó. Snæbjörnsdóttir, Juerg M. Matter, Martin Stute, Bjarni M. Júlíusson, and Sigurður R. Gíslason

International Journal of Greenhouse Control 79, 117–126, 2018.
doi.org/10.1016/j.ijggc/2018.08.014

International Journal of Greenhouse Gas Control 79 (2018) 117–126

Contents lists available at ScienceDirect

International Journal of Greenhouse Gas Control

journal homepage: www.elsevier.com/locate/ijggc

The rapid and cost-effective capture and subsurface mineral storage of carbon and sulfur at the CarbFix2 site

Ingvi Gunnarsson[a,*], Edda S. Aradóttir[a], Eric H. Oelkers[b,c], Deirdre E. Clark[c], Magnús Þór Arnarson[d,e], Bergur Sigfússon[a], Sandra Ó. Snæbjörnsdóttir[a], Juerg M. Matter[f,g], Martin Stute[g], Bjarni M. Júlíusson[d], Sigurður R. Gíslason[c]

[a] Reykjavík Energy, Reykjavík, Iceland
[b] GET, CNRS/UMR5563, Toulouse, France
[c] Institute of Earth Sciences, University of Iceland, Reykjavík, Iceland
[d] ON Power, Reykjavík, Iceland
[e] Mannvit Engineering, Reykjavík, Iceland
[f] Ocean and Earth Science, University of Southamton, Southamton, UK
[g] Lamont Doherty Earth Observatory, Columbia University, Palisades, USA

ARTICLE INFO

Keywords:
CCS
CO_2
H_2S
Basalt
Mineralization
Hellisheiði

ABSTRACT

One of the main challenges of worldwide carbon capture and storage (CCS) efforts is its cost. As much as 90% of this cost stems from the capture of pure or nearly pure CO_2 from exhaust streams. This cost can be lowered by capturing gas mixtures rather than pure CO_2. Here we present a novel integrated carbon capture and storage technology, installed at the CarbFix2 storage site at Hellisheiði, Iceland that lowers considerably the cost and energy required at this site. The CarbFix2 site, located in deeper and hotter rocks than the original CarbFix site, permits the continuous injection of larger quantities of CO_2 and H_2S than the original site. The integrated process consists of soluble gas mixture capture in water followed by the direct injection of the resulting CO_2-H_2S-charged water into basaltic rock, where much of the dissolved carbon and sulfur are mineralized within months. This integrated method provides the safe, long-term storage of carbon dioxide and other acid gases at a cost of US $25/ton of the gas mixture at the CarbFix2 site and might provide the technology for lower CCS cost at other sites.

1. Introduction

The “Achilles heel” of carbon capture and storage (CCS) is its cost. Cost estimates range from US $38 to US $143/ton CO_2 (Global CCS Institute, 2011; Rubin et al., 2015). Here we describe an integrated method that substantially lowers this cost at the CarbFix2 storage site. This technology is based on the success of the rapid and safe subsurface mineralization of carbon and sulfur into basaltic rocks as a dissolved aqueous phase at the original CarbFix site (Matter et al., 2016; Snæbjörnsdóttir et al., 2017). Moreover, the cost of this CCS method in the present study is offset by the cost of sulfur fixation, which can exceed US $300/ton (U.S. Department of Energy, 2013). As such, this integrated method may provide the financial incentive for the general application of capturing and injecting gas mixtures into reactive rocks at other locations.

The present study builds on the original CarbFix project (Matter et al., 2016). The CarbFix approach is to accelerate the mineralization of injected acid gases into subsurface basaltic reservoirs. Carbon mineralization is the safest way of storing carbon in the subsurface (Benson et al., 2005; Gislason and Oelkers, 2014; Snæbjörnsdóttir et al., 2017). Basalt offers numerous advantages for the mineralization of CO_2 and other acid gases, as it is relatively reactive compared to most rocks, and its dissolution both liberates divalent metal cations such as Ca, Mg, and Fe, and helps neutralize acidic waters (Wolff-Boenisch et al., 2004, 2006; McGrail et al., 2006; Oelkers et al., 2008; Gislason et al., 2010; Gysi and Stefansson, 2012; Pham et al., 2012; Rosenbauer et al., 2012; Takazo et al., 2013; Schaef et al., 2013, 2014; Maskell et al., 2015; Gysi, 2017; Kanakiya et al., 2017; Luhmann, et al., 2017; Xiong et al., 2017; Snæbjörnsdóttir et al., 2018a). The original CarbFix project injected 175 tons of pure CO_2 into subsurface porous basalts from January to March 2012, then 73 tons of a gas mixture from the Hellisheiði power plant consisting of 75 mol% CO_2, 24 mol% H_2S, and 1 mol% H_2 from

* Corresponding author.
E-mail address: ingvi.gunnarsson@or.is (I. Gunnarsson).

https://doi.org/10.1016/j.ijggc.2018.08.014
Received 31 October 2017; Received in revised form 15 July 2018; Accepted 29 August 2018

June to August 2012 (Alfredsson et al., 2013; Matter et al., 2016; Snæbjörnsdóttir et al., 2017). In each case, the gases were dissolved into formation water during their injection (Gislason et al., 2010; Kervevan et al., 2014, 2017; Tao and Bryant, 2014; Sigfusson et al., 2015; Blount, et al., 2017). A combination of chemical and tracer analyses, geochemical calculations, and physical evidence demonstrated that the injected CO_2 and H_2S were fixed in minerals, notably calcite and iron sulfide minerals within two years of injection at 20–50 °C (Matter et al., 2016; Snæbjörnsdóttir et al., 2017). The present study was motivated to upscale this process toward the economically viable capture and storage of all the acid gases emitted from the Hellisheiði geothermal power plant. The purpose of the present communication is to report the results of our efforts to upscale the mineralization of CO_2 and H_2S in basaltic rocks at Hellisheiði and to explore the possibility of adopting a similar approach at other potential CCS sites.

2. Materials and methods

2.1. Capture and injection into the subsurface of the CO_2/H_2S charged fluid

Efforts in this study were based at the CarbFix2 injection site located approximately 1.5 km north of the Hellisheiði geothermal power plant (Fig. 1). The Hellisheiði geothermal field is equipped with over 100 vertical and diverted wells to varying depths ranging from 100 to 3300 m in depth, allowing for the detailed monitoring of the fate of fluids injected into the subsurface (Gunnlaugsson, 2012). The HN-16 CarbFix2 injection well, as well as the HE-31, HE-48, and HE-44 monitoring wells used in this study are directionally drilled to depths of 2204 m, 2703 m, 2248 m, and 2606 m, respectively, such that they intersect high permeability fractures at depths below 800 m.

The Hellisheiði field is located at the southern part of the Hengill volcanic system, which was formed by several volcanic cycles during

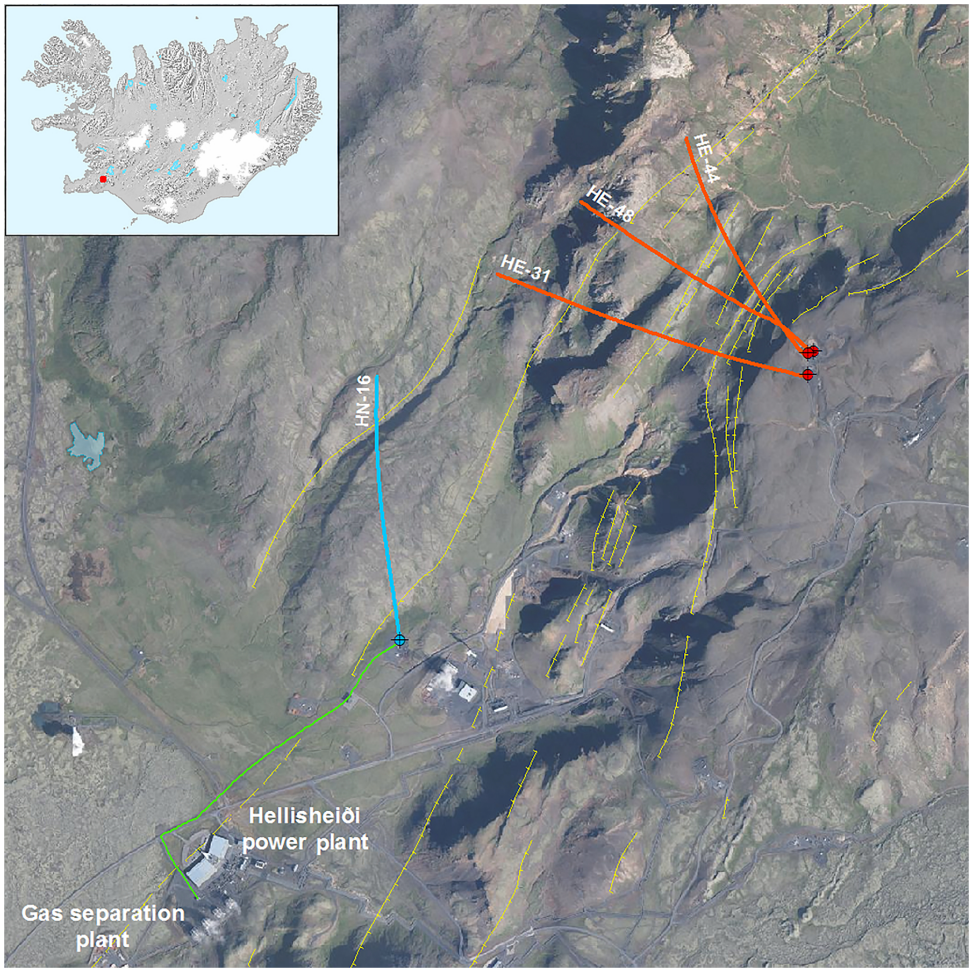

Fig. 1. Overview of the CarbFix2 injection site. The Hellisheiði power plant and the gas separation plant are in the lower left of the figure. The 1.5 km long, gas charged water pipe (shown in green) connects the separation plant to the injection well. Injection was into well HN-16 (shown in blue). The three monitoring wells (HE-31, HE-48, and HE-44, each shown in red) are located within 2 km down gradient from the injection well. Major faults and their relative movements are shown in yellow as well as the location of wells at the surface (blue and red dots). (For interpretation of the references to colour in this figure legend, the reader is referred to the web version of this article.)

spreading episodes in the rift zone. The Hengill central volcano occupies the central part of a 60–100 km long and 3–5 km wide volcanic NE-SW trending fissure swarm with a graben structure. The CarbFix2 site is located at the western side of the graben structure, with large normal faults having a total throw of more than 300 m (Franzson et al., 2005, 2010, Fig. 1). These faults contribute significantly to the permeability in the area (Kristjánsson et al., 2016).

The subsurface rocks at the CarbFix2 injection site consist of olivine tholeiitic basalts. The top 1000 m are dominated by hyaloclastites that erupted sub-glacially. The hyaloclastites are heterogeneous and can range from crystalline rocks with minor amounts of volcanic glass to almost solely volcanic glass. In the less mountainous parts of the system the stratigraphy consists of alternating successions of hyaloclastite formations and lava sequences. The most prominent originate from large lava shields, which erupted in the highlands and flowed to the surrounding lowlands (e.g. Franzson et al., 2005, 2010). Olivine tholeiitic lavas are usually rich in volcanic glass, especially on rapidly chilled surfaces of lava flows. Intrusive rocks dissect these hyaloclastite/lava successions below about 800 m depth and become dominant below 1700 m. These intrusive rocks contribute substantially to the subsurface permeability and the fracture networks created by their emplacement is a major control on aquifer permeability below 500 m (e.g. Franzson, 1988). The temperature at ~2000 m depth of the target acid gas storage reservoir ranges from 220 to 260 °C. At this depth chlorite, epidote, and calcite are the most common secondary minerals, together with prehnite, sulphides, wollastonite, and actinolite (Snæbjörnsdóttir, 2011; Snæbjörnsdóttir et al., 2018b).

Note the temperature of the target aquifer of the CarbFix2 injection is substantially higher than that of the original CarbFix injection. This higher temperature offers advantages and disadvantages compared to the lower temperature injection. First, the higher temperature of the CarbFix2 target aquifer limits the risk of subsurface biotic activity that might influence the injection well and aquifer injectivity (Trias et al., 2017). Second, the rates of basalt dissolution and of mineral carbonation reactions increase with increasing temperature (Gislason and Oelkers, 2003; Gudbrandsson et al., 2011). This effect will be offset somewhat by the decreasing thermodynamic drive for carbonate mineral formation with increasing temperature. For example, calcite and quartz decompose into wollasonite, liberating CO_2 at temperatures exceeding 325 °C (Skippen, 1980; Snæbjörnsdóttir et al., 2014). Due to these competing effects, some have suggested that the optimal temperature for subsurface mineral carbonation occurs at approximately 185 °C (e.g. Gerdemann et al., 2002; Keleman and Matter, 2008).

The acid gases injected into the CarbFix2 system originated from the Hellisheiði power plant. The power plant is located in SW Iceland, 25 km east of Reykjavík, the Icelandic capital (Fig. 1). This power plant annually emits 50,000 tons of a geothermal gas mixture with a composition of 63 vol% CO_2, 21 vol% H_2S, 14 vol% H_2, and 2 vol% of other gases, predominantly N_2, Ar, and CH_4. A CO_2 and H_2S dominated gas mixture was captured from this power plant exhaust gas stream by its dissolution into pure water in a scrubbing tower (Aradottir et al., 2015; Fig. 2, Tables 1 and 2). In total, 30 to 36 kg/s of pure water is sprayed into the top of the scrubbing tower, operated at an absolute pressure of 6 bars at 20 °C. This water interacts with a 0.336 m^3/s exhaust gas stream dissolving the water-soluble gases. The non-dissolved gases are vented into the atmosphere. The average composition of the water leaving the scrubbing tower contained 102 *mM* dissolved inorganic carbon (DIC) and 72.9 *mM* dissolved sulfur (Table 2), and it had a pH ranging between 3.5 and 4. The scrubbing tower is currently optimized to recover 56% of the CO_2 and 97% of the H_2S from the exhaust stream. The percentage CO_2 recovered could be increased by increasing the water to exhaust gas ratio, and/or the pressure in the scrubbing tower. A thermally stable inert tracer, 1-naftalenesulfonic acid (1-ns), was added to the gas-charged water using a dosing pump to monitor the fate of the dissolved gases after their injection. Prior to its transport from the capture plant, the resulting gas-charged water was pressurized to 9 bars.

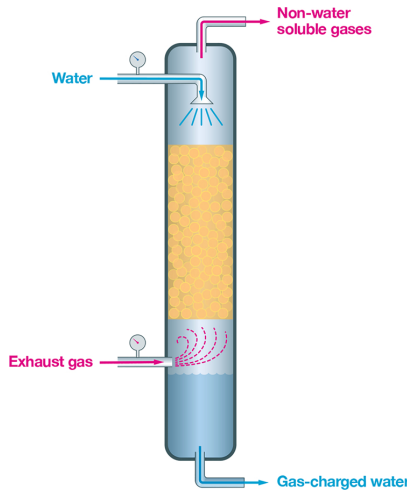

Fig. 2. Schematic illustration of the scrubbing tower in the gas capture plant. The scrubbing tower is 12.5 m high and 1 m wide and is used to capture CO^2 and other water-soluble gases. Nearly pure condensate water is injected into the top of the scrubber at 6 bars pressure and 20 °C. This water flows downwards and interacts with up flowing exhaust gas at this pressure while passing through a tortuous path around the filling material (total internal volume = 4.7 m^3) within the scrubber. Remaining non-dissolved gases are vented at the top of the unit and gas-charged water leaves the scrubbing tower from the bottom.

The pressurized gas-charged water was transported via a 1.5 km long and 279 mm inner diameter high density polyethylene pipe to the HN-16 injection well, where it was injected into the subsurface. The injection rate was 30 to 36 kg/s, such that a total of 14.5 tons CO_2 and 7.9 tons H_2S were injected each day (Figs. 2 and 3). This injection well was directionally drilled, 2206 m long and 0.311 m wide. The top 660 m is cased with carbon steel. As the gas-charged water is acidic and corrosive to the carbon steel, this water is piped to a depth of 750 m through a 4″ stainless steel pipe. This prevents any contact between the carbon steel and the gas-charged water. Effluent water was injected into the well between the inner stainless steel pipe and the casing (Fig. 3). The effluent water had a temperature ranging from 55 to 140 °C, had an average pH of 9.13 (Table 3), and was injected at a rate of 15 to 130 kg/s (Fig. 4). The two fluids, gas-charged condensate water and effluent water, mix at the exit of the stainless steel pipe at 750 m. The pH of the gas charged-effluent water mixture was calculated, using PHREEQC version 3 (Parkhurst and Appello, 2013) together with the core10 database (Neveu et al., 2017) to be ~5 at a temperature of 65 °C increasing to ~6 as its temperature increased to 250 °C. The main aquifer receiving the water mixture is located at a depth between 1900 and 2200 m. The formation temperature at the depth of this aquifer prior to injection was estimated to be 240–250 °C, based on measurements from adjacent wells. Although the mildly acidic injection water could liberate potentially toxic metals to the fluid phase, we observed negligible changes to the concentrations of such metals in our sampled monitoring fluids.

The gas injection began during June 2014 and was terminated 15th July 2015. In total, 4526 tons of water dissolved CO_2 and 2536 tons of water dissolved H_2S had been injected. The fluid mass in the geothermal system does not build up over time as fluid is continuously removed from this system to provide water and steam for the powerplant. The injected gas-charged water will tend to sink once it arrives in the reservoir because 1) the injected fluid is relatively cool and 2) it is gas-rich. Both factors increase the density of the injected fluid relative to that of the hot dilute formation water (e.g. Patel and Eubank, 1988; Teng et al., 2007; Hebach et al., 2004; Burton and Bryant, 2009; Pool et al., 2013).

Table 1
Average composition and flow of gases before and after the scrubbing tower and percentage dissolved in the scrubbing unit.[a]

Gas composition						
	CO_2 (vol%)	H_2S (vol%)	H_2 (vol%)	N_2 (vol%)	O_2 (vol%)	CH_4 (vol%)
Before scrubbing tower	54.5	22.7	15.9	5.44	1.14	0.40
After scrubbing tower	52.7	1.71	34.4	8.72	1.64	0.83

Gas flow[b]	CO_2 (m^3/s)	H_2S (m^3/s)	H_2 (m^3/s)	N_2 (m^3/s)	O_2 (m^3/s)	CH_4 (m^3/s)	Total flow (m^3/s)
Before scrubbing tower	0.183	0.0764	0.0535	0.0183	0.00383	0.00135	0.336[c]
After scrubbing tower[d]	0.0811	0.0026	0.0530	0.0134	0.00252	0.00128	0.154

	CO_2	H_2S	H_2	N_2	O_2	CH_4
Percentage dissolved	55.8%	96.6%	1.0%	26.7%	34.2%	5.1%

[a] Compositions and fluxes reflect conditions in the scrubber tower before the up-scale in June 2016.
[b] At 1.013 bar-a and 40 °C.
[c] According to gas compressor specification.
[d] Calculated assuming 1% loss of H_2 in the scrubbing water which is in good agreement with scrubbing tower design.

Table 2
Composition of gas-charged injection water.

Date	DIC (*mM*)	DS[a] (*mM*)
08-07-2014	117	71.8
11-07-2014	99.1	67.1
25-09-2014	107	74.0
16-10-2014	101	75.3
21-10-2014	93.7	70.3
04-12-2014	96.4	73.2
19-12-2014	97.9	78.3
16-01-2015	94.6	82.8
18-03-2015	81.3	71.4
13-04-2015	102	55.5
15-04-2015	102	76.4
13-05-2015	102	75.3
01-06-2015	108	67.8
30-07-2015	119	70.4
04-11-2015	107	83.4
Average	102	72.9

[a] Dissolved sulfur in the form of H_2S.

Notably, taking into account the fluid temperature and salinity, and using equations reported by Duan et al. (2008), the injected aqueous fluid has a density of 0.95–0.99 g/cm^3 whereas the formation fluid has a density ranging from 0.78 to 0.84 g/cm^3. This density difference, however decreases to less than 1% as the temperature of the injected fluid increases to that of the target basaltic reservoir.

2.2. Sampling and analysis

The fate of the injected gas mixture was monitored by the regular sampling of three monitoring wells, located 984 m (HE-31), 1356 m (HE-48), and 1482 m (HE-44) downstream from the injection well at the depths of the main aquifers, of about 1900–2200 m depth (Figs. 1 and 3). At these depths, the reservoir fluid is a single-phase aqueous fluid with a temperature of 266 to 277 °C, as the hydrostatic pressure is greater than the liquid-vapor saturation pressure of water (see supplementary material). As the fluid rises up the monitoring wells, it boils as the pressure decreases. Consequently, steam and water are sampled separately at 5.7 to 9.3 bars at the top of each monitoring well. Samples for the determination of dissolved inorganic carbon (DIC), hydrogen sulfide (H_2S), sulfate (SO_4), and the 1-ns (1-naphthalenesulfonate) tracer in the liquid

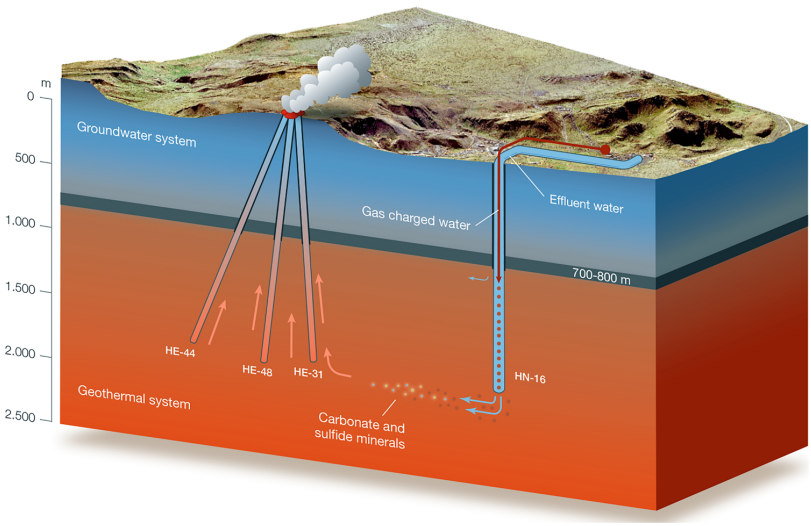

Fig. 3. Schematic cross section of the CarbFix2 injection site. Gas-charged and effluent water are injected separately to a depth of 750 m into well HN-16, then allowed to mix until they enter the aquifer at a depth of 1900–2200 m. This combined fluid flows down a hydraulic pressure gradient to monitoring wells HE-31, HE-48, and HE-44 located 984, 1356, and 1482 m from the injection well at the reservoir depth.

Table 3
Chemical composition of effluent water from Hellisheiði power plant.

Sample no	Date	pH/T (°C)	Si (*mM*)	Na (*mM*)	K (*mM*)	Ca (*mM*)	Mg (*mM*)	Fe (*mM*)	Al (*mM*)	Cl (*mM*)	F (*mM*)	DIC (*mM*)	H_2S (*mM*)	SO_4 (*mM*)
2014–5198	23-06-2014	9.65/23.3	8.19	6.37	0.637	0.0157	< 0.002	0.004	0.049	3.37	0.057	0.398	0.432	0.358
2014–5240	21-07-2014	9.23/23.7	8.01	6.07	0.604	0.0164	< 0.002	< 0.001	0.046	3.15	0.049	0.332	0.281	0.302
2014–5359	01-10-2014	9.12/23.3	7.99	5.98	0.604	0.0134	< 0.002	< 0.001	0.046	3.30	0.051	0.453	0.367	0.261
2014–5376	27-10-2014	9.05/23.3	8.22	6.03	0.609	0.0132	< 0.002	< 0.001	0.046	3.36	0.049	0.646	0.500	0.235
2014–5384	03-11-2014	8.99/25.0	8.44	6.35	0.637	0.0135	< 0.002	< 0.001	0.049	3.58	0.051	0.351	0.487	0.239
2014–5398	17-11-2014	8.80/25.2	8.14	6.03	0.611	0.0124	< 0.002	< 0.001	0.046	3.29	0.048	0.452	0.480	0.209
2015–5181	04-03-2015	9.10/16.9	8.20	6.05	0.611	0.0157	< 0.002	< 0.001	0.047	3.47	0.051	0.339	0.550	0.121

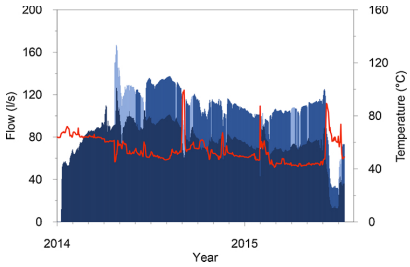

Fig. 4. Temporal evolution of the effluent water flow (dark blue area), gas-charged water flow (blue area), condensate water without gas (light blue area) and temperature of the combined fluids (red curve) in the HN-16 injection well. (For interpretation of the references to colour in this figure legend, the reader is referred to the web version of this article.)

phase, and CO_2, methane (CH_4), and H_2S in the vapor phase were collected using a Webre separator. The sampling procedure for these samples is described in detail by Arnórsson et al. (2006).

Distinct methods were used to measure the concentrations of the dissolved gases in the sampled fluids. The procedure used for the analysis of CO_2 and H_2S in the vapor phase as well as DIC and sulfide in the liquid phase is described in Arnórsson et al. (2006). The H_2S in the vapor phase, after its dissolution into a KOH rich aqueous solution, was analyzed by titration with silver nitrate and silver electrode endpoint detection (Metrohm 905 Titrando). The CH_4 in the vapor phase together, with other major geothermal gases, were analyzed using an Agilent Technologies 7890 A gas chromatography system using a HP-Molesieve (19095P-MSO) column and Thermal Conductivity Detector. Subsamples collected for aqueous sulfate concentration determination, previously treated at the sampling site with Zn acetate to precipitate sulfide as zinc sulfide preventing H_2S oxidation to SO_4 upon storage, were filtered through 0.2 µm cellulose acetate filters in the laboratory and subsequently analyzed using a Dionex ICS-2000 chromatography system. Samples for 1-ns tracer measurements were filtered through 0.2 µm cellulose acetate filters into 60 ml amber glass bottles and analyzed using a Thermo Ultimate 3000 HPLC with a BetaBasic C-18 column and fluorimetric detection. The analytical method adopted for these analyses was based on that described by Rose et al. (2002), but with a 100 mm column and a gradually increasing MeOH concentration in the eluent. The detection limit for 1-ns is 5×10^{-7} *mM*. Measured concentrations for DIC, H_2S, and SO_4^{2-} in liquid phase samples and for CO_2, H_2S, and CH_4 in vapor phase samples are orders of magnitudes higher than the detection limits of the analytical methods.

2.3. Calculation of reservoir fluid compositions and fraction mineralized

Concentrations of DIC, CH_4, H_2S, SO_4, and 1-ns in the sampled reservoir fluids before phase separation were calculated using the WATCH speciation program (Arnórsson et al., 1982; Bjarnason, 2010) from the analyzed concentration in the liquid and vapor phase, and the vapor fraction at collection pressure using:

$$m_i^{f,t} = m_i^{d,l}(1 - X^{d,v}) + m_i^{d,v}X^{d,v} \quad (1)$$

where m_i designates concentration of the component i, d stands for discharge, t for total, f for fluid, l and v for liquid and vapor. The $X^{d,v}$ stands for the vapor fraction at the sampling pressure. The concentration of 1-ns and SO_4 was assumed to be zero in the vapor phase and the concentration of CH_4 was assumed to be zero in the liquid phase. The pH at the reservoir temperature was calculated from measured pH value of the water phase at ambient temperature and the major element composition of the water and steam phase using the WATCH speciation program (Arnórsson et al., 1982; Bjarnason, 2010).

The HE-31, HE-48, and HE-44 monitoring wells are liquid enthalpy wells meaning that their discharge enthalpy corresponds closely to the enthalpy of the single-phase reservoir fluid at the reservoir temperature. The vapor fraction at the sample collection pressure was therefore calculated assuming adiabatic boiling from the reservoir temperature to the sampling pressure (c.f. Arnórsson et al., 2007). The reservoir temperature was calculated assuming equilibrium with quartz (Gunnarsson and Arnórsson, 2000) to be 266 °C for wells HE-31 and HE-48 and at 277 °C for well HE-44. These temperatures agree well with the measured temperature at the depth of the aquifers in the wells.

The concentrations of dissolved sulfur (DS) in the reservoir fluid ($m_{DS}^{f,t}$) were calculated from the concentration of H_2S ($m_{H_2S}^{f,t}$) and SO_4^{2-} ($m_{SO_4}^{f,t}$) in the reservoir fluid using:

$$m_{DS}^{f,t} = m_{H_2S}^{f,t} + m_{SO_4}^{f,t} \quad (2)$$

The total amount of gas injected during this study was a mixture of 4526 tons CO_2 and 2536 tons H_2S. This amount was calculated based on the flow of gas-charged water into the injection well and the concentration these gases in the water. A total of 291 kg of the 1-ns tracer were injected over this same period. The tracer-bearing aqueous solution was prepared in batches of one cubic meter at a time. One hundred kg of 1-ns sodium salt (1-naphthalenesulfonic acid sodium salt, CAS no: 130-14-3, molecular weight 230.22 g/mole) was dissolved in 1000 kg water and injected at a constant proportion to the gas-charged water using a Milton Roy dosing pump. The molar ratio between the DIC and DS, and the 1-ns tracer was 81,270 and 58880, respectively.

Following the approach of Matter et al. (2016), the fraction of the injected gas mineralization was computed by comparing measured aqueous DIC and DS concentrations in the sampled monitoring wells to those calculated assuming no reactions occurred in the subsurface. Concentrations of DIC and DS, assuming only the unreactive mixing of fluids ($m_{DIC,predicted}^{f,t}$ and $m_{DS,predicted}^{f,t}$), were determined from the measured concentrations of the injected non-reactive tracers using:

$$m_{i,predicted}^{f,t} = m_{i,background}^{f,t} + (m_{1-ns}^{f,t} - m_{1-ns,background}^{f,t})A \quad (3)$$

where A designates the molar ratio between the DIC or DS and tracer in the gas-charged injection water. The background concentrations of DIC and DS in the monitoring wells were calculated by averaging selected DIC and DS concentrations in the initial reservoir fluid before the arrival of gas-charged injection water to the monitoring wells (Table 4).

The background concentration for DIC was calculated to be 8.36 *mM*, 9.82 *mM*, and 18.1 *mM* in monitoring wells HE-31, HE-48 and HE-44. The corresponding values for DS were 1.27 *mM*, 1.38 *mM*, and 2.11 *mM* for wells HE-31, HE-48, and HE-44. The background concentration of 1-ns present in the geothermal system originates from the breakdown of other sulfonates used in previous tracer tests of the geothermal reservoir at Hellisheiði (Kristjánsson et al., 2016). The background concentration in the reservoir fluid ($m^{f,t}_{1-ns,background}$) in wells HE-31, HE-48, and HE-44 was 6.95×10^{-7} *mM*. Comparison of the observed and predicted DIC and DS concentrations in the monitoring wells allows for the calculation of fraction of gases mineralized in the subsurface. The fraction mineralized is calculated using the equation:

$$\text{Fraction } M\text{ineralized} = \frac{(m^{f,t}_{i,\text{predicted}} - m^{f,t}_{i})}{(m^{f,t}_{i,\text{predicted}} - m^{f,t}_{i,\text{background}})} \quad (4)$$

3. Results

The total measured dissolved inorganic carbon (DIC), methane (CH_4), total dissolved sulfur (DS), pH at 25 °C, and 1-ns tracer concentrations in the monitoring wells HE-31, HE-48, and HE-44 (Fig. 5)

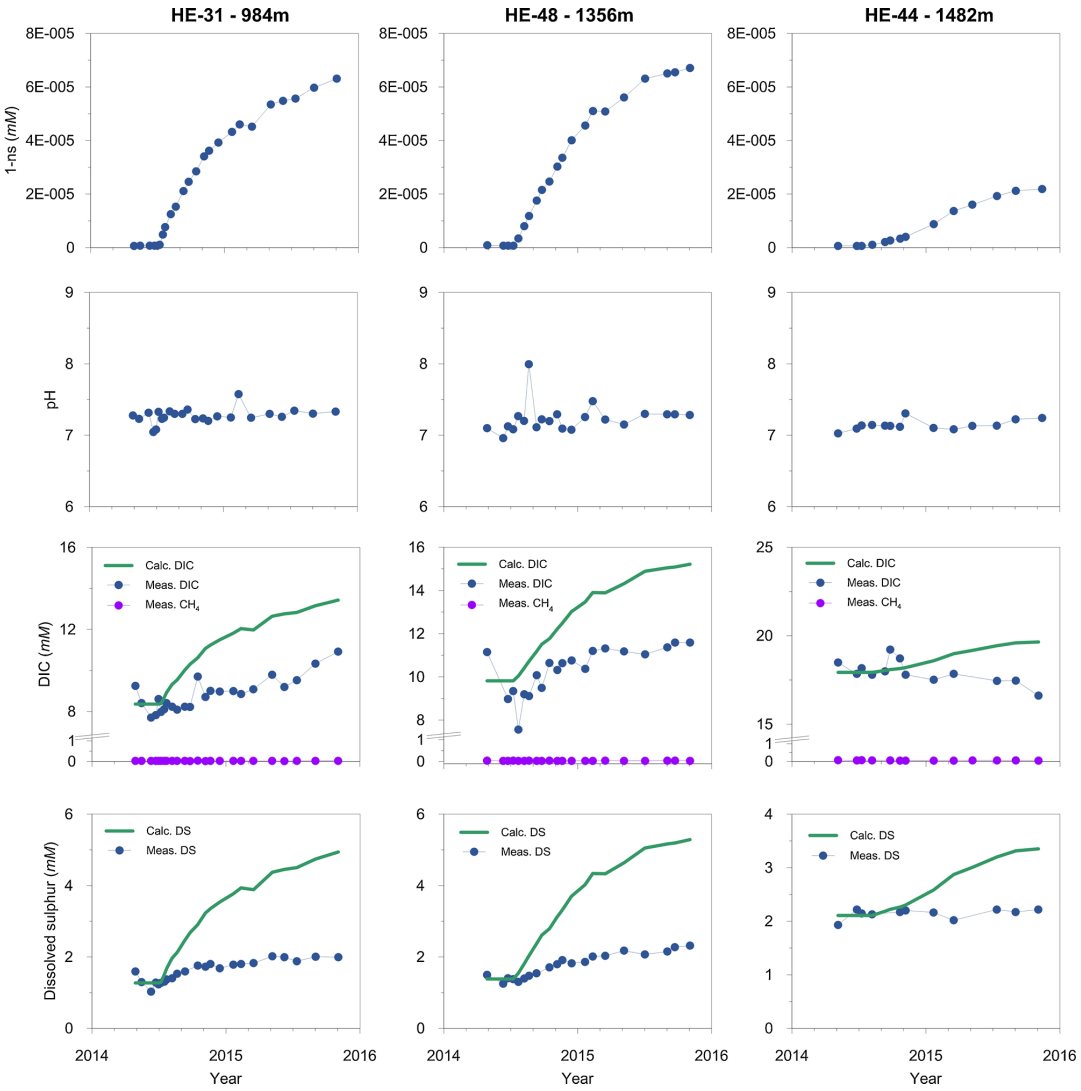

Fig. 5. The temporal chemical evolution of water samples collected from the HE-31, HE-48, and HE-44 monitoring wells located 984, 1356, and 1482 m, respectively, from the HN-16 injection well as indicated in the column headings. The top row of plots illustrates the measured dissolved 1-naftalenesulfonic acid (1-ns) tracer concentration. The second row of plots show the calculated pH of the sampled fluids at reservoir temperature. The third row of plots show the measured and calculated concentrations of dissolved inorganic carbon (DIC) and methane. The bottom row of plots depicts the measured and calculated total dissolved sulfur concentration (DS). Calculated values shown by the green lines were generated assuming only dilution and mixing affected the fluid compositions and the measured values of 1-ns. DIC and DS are shown as filled blue circles. The filled violet circles in the plots correspond to measured methane concentrations. The difference between the green and blue lines correspond to that fixed by chemical reactions occurring in the reservoir. (For interpretation of the references to colour in this figure legend, the reader is referred to the web version of this article.)

are listed in Table S-1. The first appearance of the 1-ns tracer was observed 17, 32, and 47 days after the beginning of the injection in wells HE-31, HE-48, and HE-44, respectively (Fig. 5). Due to subsurface mixing and dispersion, the average time for the tracer to flow from the injection well to monitoring wells HE-31, HE-48, and HE-44 (Fig. 2) is greater and determined to be 130, 163, and 272 days, respectively (Kristjánsson et al., 2016). The tracer concentrations in the monitoring well fluids continue to increase at the end of the study period as the flow system had not yet attained a steady-state concentration in response to the continuous injection of dissolved gases and tracer.

The fate of the injected gases was quantified using mass balance Eqs. (3) and (4). Results of these calculations, providing estimates of what the concentrations of DIC and DS in the sampled monitoring well fluids would be in the absence of chemical reactions, are listed in Table S-1 and shown in Fig. 5. These calculated values are substantially higher than those measured in these monitoring wells, suggesting a loss of DIC and DS along the subsurface flow path towards the monitoring wells. The only plausible mechanism for this difference is carbon- and sulfur-bearing mineral precipitation. The difference between the calculated and measured DIC and DS suggests that over 50% of the injected CO_2 and 76% of the injected H_2S were mineralized through water-gas-basalt interaction during the 130 to 272 days required for its transport from the injection to the monitoring wells (Table S-1, Fraction mineralized). Similar observations demonstrated the mineralization of injected CO_2 and H_2S during the original CarbFix project within two years at 20–50 °C (Matter et al., 2016; Snæbjörnsdóttir et al., 2017). Once mineralized, the risk of gas leakage to the surface is eliminated and a monitoring program of the storage site can be significantly reduced, thus enhancing storage security and potentially public acceptance.

An additional observation is that the permeability of the injection well was stable throughout the injection (Fig. 4), suggesting the long-term viability of these wells and this carbon storage approach. This later observation is consistent with the relatively low pH of the injected gas-charged injection water, which was undersaturated with respect to calcite, and most of the minerals present in the aquifer rocks.

4. Discussion

4.1. Injected gas mineralization and permeability

A significant result of this study is that the permeability of the target injection reservoir remained stable throughout the two-year injection despite the successful mineralization of much of the injected gases, likely as calcite and pyrite. There are two major reasons for this. First, the injected gas-charged fluids are acidic so that they are strongly undersaturated with respect to the basalts in the target aquifer. The undersaturation of this fluid leads to the dissolution of the host rock basalts in the vicinity of the injection well. Significant mineralization will only occur at a distance away from the injection well after heat exchange and sufficient dissolution of the host rock neutralizes the gas-charged water and saturates the formation water with respect to carbonate and sulfur minerals.

The second major reason for the stable permeability of the target reservoir over the 2-year injection period is likely the relatively small amount of mineral reaction compared to the size of the reservoir. The volume of calcite created by the mineral storage of one ton of CO_2 is 0.84 m^3; the volume of pyrite created by the mineral storage of one ton of H_2S is 0.70 m^3. As such, the total volume of calcite and pyrite created if all the gas injected during this study formed these minerals would be 5560 m^3. This compares to a reservoir volume of 6×10^8 m^3, determined assuming the target reservoir was 200 m in height, 200 m in width, and 1500 m in length. The volume of the precipitated calcite and pyrite would thus constitute only 0.009 vol percent of the reservoir. This compares with an estimated 8–10% porosity of the target reservoir basalts (Gunnarsson et al., 2011). The degree to which longer-term and or larger gas injections will alter permeability over time cannot be assessed at present, but it should be noted that the carbonation of basalts is a complex set of reactions that involve the dissolution of the host basalts and the potential precipitation of a large number of secondary phases in addition to calcite and pyrite (Stefánsson et al., 2011; Gysi, 2017; Snæbjörnsdóttir et al., 2018a). Moreover, the relationship between permeability and porosity, mineral dissolution, and mineral precipitation is complex and poorly understood at present (c.f. Oelkers, 1996; Jové Colón et al., 2004; Nogues et al., 2013; Noiriel et al., 2016; Beckingham, 2017). As such the long-term effect of this carbon and sulfur geologic storage approach might be best studied directly as long-term industrial-scale acid gas subsurface injection projects.

4.2. The cost of the described CCS approach

A major advantage of the CCS approach described above is its cost and safety relative to conventional technologies. The capture does not involve the separation of a pure and dry CO_2 phase; it captures all water-soluble gases in a single step by its dissolution into water, which is then directly injected into the subsurface at 9 bars absolute pressure. As a result, only water and electricity is needed for capture. The overall “on site cost” of this gas mixture capture, transport and storage at the CarbFix2 Hellisheiði site is US $24.8/ton (Fig. 6 and Table 4).

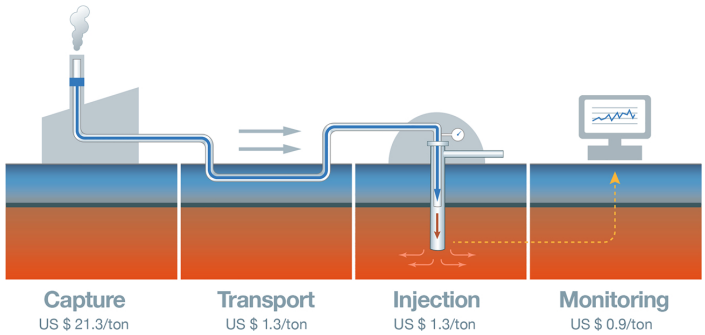

Fig. 6. Schematic illustration of the running cost of this integrated CCS solution at the CarbFix2 site. Costs are given in US$ per ton of gas mixture (CO_2 + H_2S) injected and assume “on- site” existing infrastructure, electricity cost and transport distance of 1.5 km as detailed in the text.

Table 4
Cost of mixed gas capture (CO_2 + H_2S) and storage at the CarbFix2 site.

	Case 1[a] (US $/ton)	Case 2[b] (US $/ton)	Case 3[c] (US $/ton)
Capture	21.3	21.3	42.1
Transport	1.3	1.3	1.3
Injection	1.3	4.1	4.1
Monitoring	0.9	0.9	0.9
Total CCS cost	24.8	27.6	48.4

[a] On site up-scaled cost at Hellisheiði power plant.
[b] On site up-scaled cost at Hellisheiði power plant including drilling a well for injection.
[c] On site up-scaled cost at Hellisheiði power plant including drilling a well and using average OECD electricity price for industry in 2014 (US $ 123,9/MWh) (IEA, 2016).

These cost calculations were based on "on-site" necessary capital expenditure (CapEx) and operating costs for capture, transport, injection, and monitoring, levelized to the total amount of gas injected for the time period in this study and assuming ISK/USD exchange rate of 130. All equipment and infrastructure were assumed to have a lifetime of 30 years and relevant cash flow projected for each year. Annual deprecation for property, plant, and equipment (PP&E) were assumed to be 3% and the effective tax rate 20%. Total cost per ton of mixed gas captured and injected over the 30-year lifetime was calculated by using the equivalent annual cost (EAC), where annual capture and injection rates were assumed to remain fixed at the current "up-scaled" capacity with 24 h year-round operation, apart from a two week annual maintenance stop. Lower tax payments due to operational losses for the project were considered as a revenue stream in the project's cash flow.

This overall up-scaled cost is dominated by that of gas mixture capture estimated to cost US $21.3/ton; a considerable part of this capture cost stems from compressing the gas and pure water to 6 bars and then further pressurizing the resulting gas-charged water to 9 bars prior to injection (Figs. 2 and 6). Note that this capture method also has the advantage of not using organic absorbents or solvents, such that it has less potential environmental influence. The on-site, up-scaled cost of transport and injection of the gas-charged fluid into the injection well is US $1.3/ton and US $1.3/ton, respectively; the bulk of this cost originates from the building of the additional infrastructure at the Hellisheiði site. The cost of injection, estimated here, excludes the drilling costs of the pre-existing wells at the CarbFix2 site. Estimates (Table 4) show that including the cost of drilling a suitable gas injection well at Hellisheiði would increase the cost of injection from US $1.3/ton to US $3.1–5.0/ton, depending on the depth of the well. The average of this additional cost is shown in Table 4. The cost of monitoring, estimated at US $0.9/ton, includes four soil gas flux measurements, injectivity, P–T, spinner and downhole camera measurements every five years, as well as bi-monthly sampling of the monitoring wells for five years after the start of injection and thereafter twice a year for the remaining 25 years of the estimated duration of this injection.

The pipe that transports the gas-charged water towards the injection well (Fig. 1), located at approximately 1.5 km distance from the power plant, is buried 1 m in the ground and only 1% of the total mass it transports is CO_2 and H_2S. The transport of the gas as a dissolved phase in condensate water elevates the cost significantly compared to conventional gas transport, where it is only necessary to transport pure dry gas. When settings require further transport of gas to injection sites, the cost of transport could be brought down by adding a degassing step after the gas scrubbing tower. The CO_2 gas could then be transported in smaller and lower grade pipes above surface, as the risk of water freezing of this anhydrous gas would be minimal. The CO_2 could then be re-dissolved in water at the injection site before or during injection.

4.3. Potential cost of this CCS approach at other sites

The overall cost and efficiency of the CCS approach described in this study will differ depending on the site, depth of injection well, composition of the exhaust gas to be treated, and the price of the energy used to capture the acid gases from the exhaust stream. Although it is not possible to consider all of these factors in estimating the costs of this CCS approach at other sites, it is possible to evaluate the effects of different energy costs and of a need to drill an injection well on the overall costs. Note that the "on site costs" of transport, injection and monitoring are not affected by the electricity price, only that of the acid gas capture.

The overall CCS cost at the CarbFix2 site based on three cost scenarios for a 1.5 km transport of gas mixture; 1) "on-site conditions", 2) adding the cost of a new injection well, and 3) taking into account the cost of new injection well and average OECD electricity price for industry in 2014 (IEA, 2016), is shown in Table 4. The three CCS cost estimates reported in Table 4, which range from US $25/ton to US $50/ton, are generally lower than cost estimates for conventional pure and dry CO_2 capture and storage (CCS), which range from US $38 to US $143/ton CO_2 (Global CCS Institute, 2011; Rubin et al., 2015). Our estimated CCS costs are also somewhat lower on average than the US $35 to US $65/ton recently estimated as the CCS cost at Chinese coal fire power plants (Hu and Zhai, 2017). The exact cost of adopting this CarbFix approach will vary site to site depending on a number of factors including gas composition, depth of target storage reservoir, and local energy costs (c.f. Rubin et al., 2015). The CCS costs using this CarbFix approach, however, would be offset by the co-fixation of sulfur through this process. As sulfur capture and storage can exceed US $300/ton (U.S. Department of Energy, 2013), this integrated method may provide the financial incentive for the general application of capturing and injecting water-soluble gas mixtures into reactive rocks.

The capture and storage of the mixed CO_2-H_2S gas at the Hellisheiði power plant using this CarbFix method may be particularly favorable compared to other sites due to the availability of a CO_2-rich gas stream, local permeable basalts, and abundant fresh water. The degree to which this or a similar approach will prove economically viable at other sites depends to a large extent on the composition of the exhaust gas and identity of the subsurface rock formations. The efficiency of CO_2 capture with other water-soluble gases in water diminishes with the decreasing CO_2 content of the exhaust gas. Consequently, the efficient capture of CO_2 and other water-soluble gases could require higher pressures in the scrubber for exhaust streams that are less concentrated in CO_2. This would increase capture costs, as these costs are dominated by the cost of pressurizing the exhaust gas-water stream. As the cost of capture is directly related to the pressure required in the scrubber, the optimization of scrubber pressure and water demand will need to be considered on a site by site basis.

There are many places around the world, however, which have both abundant water and permeable basalts, which may provide conditions for the further application of this CCS approach. Notably, the ocean floor is comprised mostly of basalts and adjacent to an inexhaustible supply of seawater (McGrail et al., 2006; Goldberg et al., 2008; Wolff-Boenisch et al., 2011; Gislason and Oelkers, 2014; Snæbjörnsdóttir et al., 2014), which may make the CCS methods described above favorable along many continental coastlines and on volcanic islands. For example, the subseafloor basalts of the Juan de Fuca ridge off the coast of the Pacific northwest of the United States have been reported to have porosities of > 10%, premeabilites estimated to range from 10^{-9} to 10^{-5} cm^2, and a potential pore volume of 780 km^3 (Goldberg et al., 2008). These authors concluded that this formation alone could store ~250 Gt of carbon as calcite. Moreover, the subsurface storage capacity of the porous basaltic rocks in Iceland has been estimated to be up to ~2500 Gt of CO_2 (Snæbjörnsdóttir et al., 2014), which is approximately 25 times that required prior to 2050 as part of an integrated effort to limit global warming to 2 °C (IEA, 2015). In addition, seawater

is commonly used in flue gas desulfuration (FGD), where seawater cooled fossil fueled power plants use the seawater to scrub sulfur dioxide from flue gas (Olkawa et al., 2003). The application of the CarbFix approach to will, however, need to account for 1) the lower solubility of CO_2 in seawater compared to that of fresh water; CO_2 is approximately 15% less soluble in seawater depending on the temperature and pressure (Weiss, 1974), and 2) the additional costs associated with the transport of gas to the coast for subseafloor injection. The mineralization of CO_2-charged seawater may be somewhat accelerated as the dissolution rates of basalt are somewhat enhanced in CO_2-charged seawater compared to CO_2-charged fresh water (Wolff-Boenisch et al., 2011). This more rapid basalt dissolution, likely does not lead to secondary mineral precipitation at temperatures less than 150 °C dissolution, as like its freshwater equivalent, CO_2-charged seawater is strongly undersaturated with respect to precipitating phases at these conditions. Note, however, that at temperatures in excess of 150 °C, anhydrite precipitation from injected seawater would be favored (Bischoff and Seyfried, 1978). The precipitation of anhydrite from the heating of CO_2-charged seawater as it is injected to high temperature basalts could pose a threat to the long-term injectivity of an injection well.

4.4. Carbon storage and waste water disposal

A critical factor in the application of this CarbFix approach for storing carbon by its mineralization in reactive rocks is the ability to inject large volumes of water into the subsurface. At a pressure of 25 bars, approximately 27 tons of pure water at 25 °C are required to dissolve each ton of CO_2 gas prior to or during its injection (Gislason et al., 2010, 2014). Large volumes of effluent water are, however, being injected into subsurface. There are currently 20–25 million tons of effluent water being injected into the subsurface basalts at Hellisheiði each year (Reykjavík Energy, 2016), sufficient for the dissolution and injection of close to one million tons of acid gases annually, or roughly 20 times the CO_2 emitted at the Hellisheiði power plant. The amount of waste and effluent water injected annually into the subsurface through industrial processes is far larger. It has been estimated that more than 3 Gt/y of oil field brines are brought to the surface in the US and UK alone (American Petroleum Institute and American Petroleum Institute, 2000; UK Oil and Gas Industry Association,2016). Reinjection is the primary disposal method. As such this may provide an opportunity to adopt some of the technology developed by this CarbFix method at other sites.

5. Conclusions

This study has demonstrated the efficiency and cost advantages of the capture and storage of mixed gas streams at the CarbFix2 site. Typical coal-fired power plant exhaust contains substantial quantities of oxidized sulfur and nitrogen gases, which are highly soluble in water (Freund et al., 2005). The simultaneous capture and storage of these gases with CO_2 may provide an additional economic incentive to make this CCS method a valuable contributor to the global effort to limit the increasing carbon concentration of the atmosphere.

The CCS approach described above also has the advantage of enhanced safety; the injected gas-charged water is less buoyant than the formation water, leading it to sink once injected into the subsurface. Moreover, this injection provokes the fast subsurface mineralization of much of the injected acid gases over month long time frames. As such, if it is possible to adapt this approach at other sites, its increased storage security may both lower monitoring costs and enhance public acceptance of CCS at other locations throughout the world.

Acknowledgments

We acknowledge funding from Reykjavik Energy; the European Commission through the projects CarbFix (EC coordinated action 283148), Min-GRO (MC-RTN-35488), Delta-Min (PITN-GA-2008-215360), and CO2-REACT (EC Project 317235) to E.H.O., S.R.G., and Reykjavik Energy; CarbFix2 (European Union's Horizon 2020 research and innovation program under grant number 764760); S4CE (European Union's Horizon 2020 research and innovation program under grant number 764810); Nordic fund 11029-NORDICCS; the Icelandic GEORG Geothermal Research fund (09-02-001) to S.R.G. and Reykjavik Energy; and the U.S. Department of Energy under award number DE-FE0004847 to J.M.M and M.S.; We thank Þ. A. Þorgeirsson, T. Kristinsson, H. Bergmann, S. S. Sigurðardóttir, V. Eiríksdóttir, C. Marieni and F. Jónsdóttir for helping with sample collection in the field and analysis.

Appendix A. Supplementary data

Supplementary material related to this article can be found, in the online version, at doi:https://doi.org/10.1016/j.ijggc.2018.08.014.

References

Alfredsson, H.A., Oelkers, E.H., Hardarsson, B.S., Franzson, H., Gunnlaugsson, E., Gislason, S.R., 2013. The geology and water chemistry of the Hellisheidi, SW-Iceland carbon storage site. Int. J. Greenh. Gas Control 12, 399–418.

American Petroleum Institute, 2000. Overview of Exploration and Production Waste Management Volumes and Waste Management Practices in the United States. American Petroleum Institute. http://www.api.org/environment-health-and-safety/environmentalperformance/~/media/Files/EHS/Environmental_Performance/ICF-Waste-Survey-of-EandP-Wastes-2000.ashx.

Aradottir, E.S.P., Gunnarsson, I., Sigfusson, B., Gunnarsson, G., Juliusson, B.M., Gunnlaugsson, E., Sigurdardottir, H., Arnarson, M.T., Sonnenthal, E., 2015. Toward cleaner geothermal energy utilization: capturing and sequestering CO_2 and H_2S emissions from geothermal power plants. Transp. Porous Media 108, 61–84.

Arnórsson, S., Sigurdsson, S., Svavarsson, H., 1982. The chemistry of geothermal waters in Iceland. 1. Calculation of aqueous speciation from 0°C to 370°C. Geochim. Cosmochim. Acta 46, 1513–1532.

Arnórsson, S., Bjarnason, J.Ö, Giroud, N., Gunnarsson, I., Stefansson, A., 2006. Sampling and analysis of geothermal fluids. Geofluids 6, 203–216.

Arnórsson, S., Stefánsson, A., Bjarnason, J.Ö., 2007. Fluid–fluid interactions in geothermal systems. Rev. Min. Geochem. 65, 259–312.

Beckingham, L.E., 2017. Evaluation of macroscopic porosity-permeability relationships in heterogeneous mineral dissolution and precipitation scenarios. Water Resour. Res. 53, 10217–10230.

Benson, S.M., Cook, P., Coordinating Lead Authors, Anderson, J., Bachu, S., Nimir, H.B., Basu, B., Bradshaw, J., Deguchi, G., Gale, J., von Goerne, G., Heidug, W., Holloway, S., Kamal, R., Keith, D., Lloyd, P., Rocha, P., Senior, B., Thomson, J., Torp, T., Wildenborg, T., Wilson, M., Zarlenga, F., Zhou, D., Authors, Lead, Celia, S.M., Gunter, B., Ennis King, J., Lindegerg, E., Lombardi, S., Oldenburg, C., Pruess, K., Rigg, A., Stevens, S., Wilson, E., Whittaker, S., 2005. Underground geological storage, IPCC special report on carbon dioxide capture and storage, chapter 5. Intergovernmental Panel on Climate Change. Cambridge University Press, Cambridge, U.K.

Bischoff, J.L., Seyfried Jr., W.E., 1978. Hydrothermal chemistry of seawater from 25 ° to 350°C. Am. J. Sci. 278, 838–860.

Bjarnason, J.Ö., 2010. The chemical speciation program WATCH, version 2.4. ISOR – Iceland Geosurvey, Reykjavík, Iceland. http://www.geothermal.is/sites/geothermal.is/files/download/watch_readme.pdf.

Blount, G., Gorensek, M., Hamm, L., O'Neil, K., Kervevan, C., 2017. CO_2 dissolved and aqueous gas separation. Energy Procedia 114, 2675–2681.

Burton, M., Bryant, S.L., 2009. Eliminating buoyant migration of sequestered CO_2 through surface dissolution: Implementation costs and technical challenges. SPE Reserv. Eval. Eng. 12, 399–407.

Duan, Z., Hu, J., Li, D., Mao, S., 2008. Densities of the CO_2-H_2O and CO_2-H_2O-NaCl systems up to 647 K and 100 MPa. Energy Fuels 22, 1666–1674.

Franzson, H., 1988. Nesjavellir: Permability in Geothermal Reservoir" (in Icelandic) OS-88046/JHD-09. Energy Authorities of Iceland, Reykjavik.

Franzson, H., Kristjansson, B.R., Gunnarsson, G., Björnsson, G., Hjartarson, A., Steingrimsson, B., Gunnlaugsson, E., Gislason, G., 2005. The Hengill-Hellisheidi geothermal field. Development of a conceptual geothermal model. Proc. World Geotherm. Congr.

Franzson, H., Gunnlaugsson, E., Árnason, K., Sæmundsson, K., Steingrímsson, B., Harðarson, B., 2010. Hengill geothermal system, conceptual model and thermal evolution. Proc. World Geotherm. Congr.

Freund, P., Bachu, S., Simbeck, D., Thambimuthu, K., Gupta, M., 2005. Properties off CO2 and carbon – based fuels. In: Metz, B., Davidson, O., Coninck, H., Loos, M., Meyer, L. (Eds.), IPCC Special Report on Carbon Dioxide Capture and Storage. Cambridge Univ. Press, pp. 383–398.

Gerdemann, S.J., Dahlin, D.C., O'Connor, W.K., 2002. Carbon dioxide sequestration by aqueous mineral carbonation of magnesium silicate minerals. Proceedings of the 6th International Conference on Greenhouse Gas Control Technologies.

Gislason, S.R., Oelkers, E.H., 2003. Mechanism, rates, and consequences of basaltic glass dissolution: II. An experimental study of the dissolution rates of basaltic glass as a function of pH and temperature. Geochim. Cosmochim. Acta 67, 3817–3832.

Gislason, S.R., Oelkers, E.H., 2014. Carbon storage in basalt. Science 344, 373–374.
Gislason, S.R., Wolff-Boenisch, D., Stefansson, A., Oelkers, E.H., Gunnlaugsson, E., Sigurdardottir, H., Sigfusson, B., Broecker, W.S., Matter, J.M., Stute, M., Axelsson, G., Fridriksson, T., 2010. Mineral sequestration of carbon dioxide in basalt: A pre-injection overview of the CarbFix project. Int. J. Greenh. Gas Control 4, 537–545.
Gislason, S.R., Broecker, W.S., Gunnlaugsson, E., Snæbjörnsdóttir, S.Ó., Mesfin, K.G., Alfredsson, H.A., Aradottir, E.S., Sigfusson, B., Gunnarsson, I., Stute, M., Matter, J.M., Arnarson, M.T., Galeczka, I.M., Guðbrandsson, S., Stockman, G., Wolff-Boenisch, D., Stefansson, A., Ragnheidardottir, E., Faathen, T., Gysi, A.P., Olssen, J., Didriksen, K., Stipp, S.L.S., Menez, B., Oelkers, E.H., 2014. Rapid solubility and mineral storage of CO_2 in basalt. Energy Procedia 63, 4561–4574.
Global CCS Institute, 2011. Economic Assessment of Carbon Capture and Storage Technologies: 2011 Update. https://hub.globalccsinstitute.com/sites/default/files/publications/12786/economic-assessment-carbon-capture-and-storage-technologies-2011-update.pdf.
Goldberg, D.S., Takahashi, T., Slagle, A.L., 2008. Carbon dioxide sequestration in deep-sea basalt. Proc. Nat. Acad. Sci. U. S. A. 105, 9920–9925.
Gudbrandsson, S., Wolff-Boenisch, D., Gislason, S.R., Oelkers, E.H., 2011. An experimental study of crystalline basalt dissolution from 2 < pH < 11 and temperatures from 5 to 75 °C. Geochim. Cosmochim. Acta 75, 5496–5509.
Gunnarsson, I., Arnórsson, S., 2000. Amorphous silica solubility and the thermodynamic properties of H_4SiO_4 in the range of 0 to 350 °C at P-sat. Geochim. Cosmochim. Acta 64, 2295–2307.
Gunnarsson, G., Arnaldsson, A., Oddsdóttir, A.L., 2011. Model Simulations of the Hengill area, Southwestern Iceland. Transp. Porous Media 90, 3–22.
Gunnlaugsson, E., 2012. The Hellisheidi geothermal project—financial aspects of geothermal development. Presented at Short Course on Geothermal Development and Geothermal Wells, UNU-GTP and LaGeo. . http://www.os.is/gogn/unu-gtp-sc/UNU-GTP-SC-14-12.pdf.
Gysi, A.P., 2017. Numerical simulations of CO_2 sequestration in basaltic rock formations: Challenges for optimizing mineral-fluid reactions. Pure App. Chem. 89, 581–596.
Gysi, A.P., Stefansson, A., 2012. CO_2-water-basalt interaction. Low temperature experiment and implications for CO_2 sequestration into basalts. Geochim. Cosmochim. Acta 81, 129–152.
Hebach, A., Oberhof, A., Dahmen, N., 2004. Density of water plus carbon dioxide at elevated pressures: Measurements and correlation. J. Chem. Eng. Data 49, 950–953.
Hu, B., Zhai, H., 2017. The cost of carbon capture and storage for coal-fired power plants in China. Int. J. Greenh. Gas Control 65, 23–31.
IEA, 2015. Energy Technology Perspectives–Mobilizing Innovation to Accelerate Climate Action International Energy Agency, Paris, France. http://www.iea.org/publications/freepublications/publication/energy-technology-perspectives-2015.html.
IEA, 2016. Electricity Information, 2016 ed. International Energy Agency. http://wds.iea.org/wds/pdf/Ele_documentation.pdf.
Jové Colón, C.F., Oelkers, E.H., Schott, J.S., 2004. Experimental investigation of the effect of dissolution on sandstone permeability, porosity, and reactive surface area. Geochim. Cosmochim. Acta 68, 805–817.
Kanakiya, S., Adam, L., Esteban, L., Rowe, M.C., Shane, P., 2017. Dissolution and secondary mineral precipitation in basalts due to reactions with carbonic acid. J. Geophys. Res. Solid Earth 122, 4312–4327.
Keleman, P.B., Matter, J., 2008. In situ carbonation of peridote for CO_2 storage. PNAS 105, 17295–17300.
Kervevan, C., Beddelem, M.-H., O'Neil, K., 2014. CO_2-dissolved: A novel concept coupling geologic storage of dissolved CO_2 and geothermal heat recovery—part 1. Assessment of the integration of an innovative low-cost, water based CO_2 Capture technology. Energy Procedia 63, 4508–4518.
Kervevan, C., Beddelem, M.-H., Galigue, X., Le Gallo, Y., May, F., O'Neil, K., Sterpenich, J., 2017. Main results of the CO2-DISSOLVED Project: First step toward a future industrial pilot combining geologic storage of dissolved CO_2 and geothermal heat recovery. Energy Procedia 114, 4086–4098.
Kristjánsson, B.R., Axelsson, G., Gunnarsson, G., Gunnarsson, I., Óskarsson, F., 2016. Comprehensive tracer testing in Hellisheidi Geothermal field in SW-Iceland. Proc. 41st Workshop on Geothermal Engineering.
Luhmann, A.J., Tutolo, B.M., Tan, C.Y., Moskowitz, B.M., Saar, M.O., Seyfried, W.E., 2017. Whole rock basalt alteration from CO_2-rich brine flow through experiments at 150 °C and 150 bar. Chem. Geol. 453, 92–110.
Maskell, A., Kampman, N., Chapman, H., Condon, D.J., Bickle, M., 2015. Kinetics of CO_2-fluid-rock reactions in a basalt aquifer, Sosa Springs, Idaho. Appl. Geochem. 61, 272–283.
Matter, J.M., Stute, M., Snæbjörnsdottir, S.Ó, Oelkers, E.H., Gislason, S.R., Aradottir, E.S., Sigfusson, B., Gunnarsson, I., Sigurdardottir, H., Gunnlaugsson, E., Axelsson, G., 2016. Rapid carbon mineralization for permanent disposal of anthropogenic carbon dioxide emissions. Science 352, 1312–1314.
McGrail, P.B., Schaef, H.T., Ho, A.M., Chien, Y.-J., Dooley, J.J., Davidson, C.L., 2006. Potential for carbon dioxide sequestration in flood basalts. J. Geoph. Res.; Solid Earth 111, B12201. https://doi.org/10.1029/2005JB004169.
Neveu, M., Desch, S.J., Castillo-Rogez, J.C., 2017. Aqueous geochemistry in icy world interiors: Equilibrium fluid, rock, and gas compositions, and fate of antifreezes and radionuclides. Geochim. Cosmochim. Acta 212, 324–371.
Nogues, J.P., Fitts, J.P., Celia, M.A., Peters, C.A., 2013. Permeability evolution due to dissolution and precipitation of carbonates using reactive trtsansport modeling in pore networks. Can. Water Resour. J. 49, 6006–6021.
Noiriel, C., Steefel, C.I., Yang, L., Bernard, D., 2016. Effects of pore-scale precipitation on permeability and flow. Adv. Water Resour. 95, 125–137.
Oelkers, E.H., 1996. Physical and chemical properties of rocks and fluids for chemical mass transport calculations. Rev. Min. Geochem. 34, 130–191.
Oelkers, E.H., Gislason, S.R., Matter, J.M., 2008. Mineral carbonation of CO_2. Elements 4, 333–337.
Olkawa, K., Yongsiri, C., Takeda, K., Harimoto, T., 2003. Seawater flue gas desulfurization: Its technical implication and performance result. Environ. Prog. Sustain. Energy 21, 67–71.
Parkhurst, D.L., Appelo, C.A.J., 2013. Description of Input and Examples for PHREEQC. Version 3–a Computer Program for Speciation, Batch-reaction, One-dimensional Transport, and Inverse Geochemical Calculations. U.S. Geological Survey Techniques. Methods Report. Book 6, Chapter A43, pp. 1–497. .
Patel, M.R., Eubank, P.T., 1988. Experimental densities and thermodynamic properties of carbon dioxide water mixtures. J. Chem. Eng. Data 33, 185–192.
Pham, V., Hai, T., Aagaard, P., Hellevang, H., 2012. On the potential for CO_2 mineral storage in continental flood basalts – PHREEQC batch and 1D diffusion-reaction simulations. Geochem. Trans. 13, 5. https://doi.org/10.1186/1467-4866-13-5.
Pool, M., Carrera, J., Vilarrasa, V., Silva, O., Ayora, C., 2013. Dynamics and design of systems for geological storage of dissolved CO_2. Adv. Water Resour. 62, 533–542.
Reykjavík Energy, 2016. Environmental Report 2016. . https://www.or.is/sites/or.is/files/or_environmental_report_2016.pdf.
Rose, P.E., Johnson, S., Kilbourn, P., Kastler, C., 2002. Tracer testing at Dixie Valley, Nevada using 1-naphtalene sulfonate and 2,6-napthalene disulfonate. Proc.26th Workshop on Geothermal Engineering. https://www.geothermal-energy.org/pdf/IGAstandard/SGW/2002/Rose.pdf?.
Rosenbauer, R.J., Thomas, B., Bischoff, J.L., Palandri, J., 2012. Carbon sequestration via reaction with basaltic rocks: Geochemical modeling and experimental results. Geochim. Cosmochim. Acta 89, 116–133.
Rubin, E.S., Davidson, J.E., Herzog, H.J., 2015. The cost of CO_2 capture and storage. Int. J. Greenh. Gas Control 40, 378–400.
Schaef, H.T., McGrail, B.P., Owen, A.T., Arey, B.W., 2013. Mineralization of basalts in the CO_2-H_2O-H_2S system. Int. J. Greenh. Gas Control 16, 187–196.
Schaef, H.T., Horner, J.A., Owen, A.T., Thompson, C.J., Lorring, J.S., McGrail, B.P., 2014. Mineralization of basalts in the CO_2-H_2O-SO_2-O_2 system. Environ. Sci. Technol. 48, 5298–5305.
Sigfusson, B., Gislason, S.R., Matter, J.M., Stute, M., Gunnlaugsson, E., Gunnarsson, I., Aradottir, E.S., Sigurdardottir, H., Mesfin, K.G., Alfredsson, H.A., Wolff-Boenisch, D., Arnarson, M.T., Oelkers, E.H., 2015. Solving the carbon-dioxide buoyancy challenge: The design and field testing of a dissolved CO_2 injection system. Int. J. Greenh. Gas Control 37, 213–219.
Skippen, G.B., 1980. Dehydration and decarbonation equilibria. In: Greenwood, H.J. (Ed.), Application of Thermodynamics to Petrology and Ore Deposits. Min. Soc. Canada Short Corse. Evergreen Press, Toronto Canada p. 66–83.
Snæbjörnsdóttir, S.Ó., 2011. The Geology and Hydrothermal Alteration at the Western Margin of the Hengill Volcanic System" MSc Thesis (in Icelandic). University of Iceland.
Snæbjörnsdóttir, S.Ó., Wiese, F., Fridriksson, T., Ármannsson, H., Einarsson, G.M., Gislason, S.R., 2014. CO_2 storage potential of basaltic rocks in Iceland and the oceanic ridges. Energy Procedia 63, 4585–4600.
Snæbjörnsdóttir, S.Ó., Oelkers, E.H., Mesfin, K., Aradóttir, E.S., Dideriksen, K., Gunnarsson, I., Gunnlaugsson, E., Matter, J.M., Stute, M., Gislason, S.R., 2017. The chemistry and saturation states of subsurface fluids during the in situ mineralization of CO_2 and H_2S at the CarbFix site in SW-Iceland. Int. J. of Greenh. Gas Control 58, 87–102.
Snæbjörnsdóttir, S.Ó., Gislason, S.R., Galeczka, I.M., Oelkers, E.H., 2018a. Reaction path modelling of in-situ mineralisation of CO_2 at the CarbFix site at Hellisheidi, SW-Iceland. Geochim. Cosmochim. Acta 220, 348–366.
Snæbjörnsdóttir, S.Ó, Tómasdóttir, S., Sigfússon, B., Aradóttir, E.S., Gunnarsson, G., Niemi, A., Basirat, F., Dessirier, B., Gíslason, S.R., Oelkers, E.H., Franzson, H., 2018b. The geology and hydrology of the CarbFix2 site, SW-Iceland. Energy Procedia 146, 146–157.
Stefánsson, A., Arnórsson, S., Gunnarsson, I., Kaasalainen, H., Gunnlaugsson, E., 2011. The geochemistry and sequestration of H_2S into geothermal system at Hellisheidi, Iceland. J. Volcanol. Geotherm. Res. 202, 179–188.
Takazo, S., Yoshizaki, M., Masaki, Y., Suzuki, K., Takai, K., Russell, M.J., 2013. Reactions between basalt and CO_2-rich seawater at 250 and 350 °C, 500 bars: implications for the CO_2 sequestration into the modern oceanic crust and the composition of hydrothermal vent fluid in the CO_2-rich early ocean. Chem. Geol. 359, 1–9.
Tao, Q., Bryant, S.L., 2014. Optimization of injection/extraction rates for surface-dissolution. SPE J. 19, 598–607.
Teng, H., Yamasaki, A., Chun, M.K., Lee, H., 2007. Solubility of liquid CO_2 in water at temperatures from 278 to 293 and pressures from 6.44 MPa to 29 MPa and densities of corresponding aqueous solutions. J. Chem. Thermodyn. 29, 1301–1310.
Trias, R., Menez, B., Campion, P., Zivanovic, Y., Lecourt, L., Lecoeuvre, A., Schmitt-Kopplin, P., Uhl, J., Gislason, S.R., Alfredsson, H.A., Mesfin, K.G., Snæbjörnsdóttir, S.Ó, Aradottir, E.S., Gunnarsson, I., Matter, J.M., Stute, M., Oelkers, E.H., Gerard, E., 2017. High reactivity of deep biota under anthroprogenic CO_2 injection into basalt. Nat. Commun. 8, 1063.
U.S. Department of Energy, 2013. More Economical Sulfur Removal for Fuel Processing Plants. Energy Efficiency & Renewable Energy. http://energy.gov/sites/prod/files/2013/11/f5/tda_sbir_case_study_2010.pdf.
UK Oil and Gas Industry Association, 2016. Oil & Gas UK: Environmental report. 58 pp. The UK Oil and Gas Industry Association Limited. http://oilandgasuk.co.uk/wp-content/uploads/2016/11/Environment-Report-2016-Oil-Gas-UK.pdf.
Weiss, R.F., 1974. Carbon dioxide in water and seawater: the solubility of a non-ideal gas. Mar. Chem. 2, 203–215.
Wolff-Boenisch, D., Gislason, S.R., Oelkers, E.H., Putnis, C.V., 2004. The dissolution of natural glasses at pH 4 and 10.6 and temperatures from 25 to 74 °C. Geochim. Cosmochim. Acta 68, 4843–4858.
Wolff-Boenisch, D., Gislason, S.R., Oelkers, E.H., 2006. The effect of crystallinity on dissolution rates and CO_2 consumption capacity of silicates. Geochim. Cosmochim. Acta 70, 858–870.
Wolff-Boenisch, D., Wenau, S., Gislason, S.R., Oelkers, E.H., 2011. Dissolution of basalts and peridotite in seawater, in the presence of ligands, and CO_2: Implications for mineral sequestration of carbon dioxide. Geochim. Cosmochim. Acta 75, 5510–5525.
Xiong, W., Wells, R.K., Menefee, A.H., Skemer, P., Ellis, B.R., Giammar, D.E., 2017. CO_2 mineral trapping in fractured basalt. Int. J. Greenh. Gas Control 66, 204–217.